Non-Newtonian Fluids in Complex Geometries

Stephen Chaffin

School of Mathematics and Statistics

University of Sheffield

This dissertation is submitted for the degree of

Doctor of Philosophy

Supervisor: Dr Julia Rees

27th August 2016

To Katie.

Declaration

I hereby declare that except where specific reference is made to the work of others, the contents of this dissertation are original and have not been submitted in whole or in part for consideration for any other degree or qualification in this, or any other university. This dissertation is my own work and contains nothing which is the outcome of work done in collaboration with others, except as specified in the text and Acknowledgements. This dissertation contains fewer than 65,000 words including appendices, bibliography, footnotes, tables and equations and has fewer than 150 figures.

Stephen Chaffin
27th August 2016

Acknowledgements

I would first like to thank the University of Sheffield for offering the GTA scholarship and equally for the friendly and fruitful environment that SOMAS is. I would also like to thank Professor W.B.J Zimmerman for helpful discussions along with the use of his servers and COMSOL licenses. And to my supervisor Dr J Rees for her time encouragement and support throughout these past few years. I would like to give a special mention to Alex Hague and Richard Hodgekinson for insightful, interesting (and often distracting) discussions, without which this thesis would not be the same. I would also like to thank my fellow office colleagues, in particular, Nabil Freij, for his delightful use of bubble machines, Freddie Mather, Schuyler Nicholson, Sam Bennett and Christopher Nelson for making my time at Sheffield all the more enjoyable.

On a deeper note, to my parents without whom I would never have been able to make it this far, thank you. And finally, to Katie Drabble, for being with me through the highs and lows, the long weekends and the messy rooms (although a lot of that was you)! Thank you for being there for me when I needed you.

Abstract

We consider shear-dependent viscous and viscoelastic fluids in three types of geometries namely; cross-slot, snail ball and driven corner. The flow field and the stress field are solved analytically in a Hele-Shaw cross-slot geometry for weakly viscoelastic fluids, which is then corroborated using a finite element model. The analytic model further investigates the effects of asymmetry in the inlet outlet channels and the resulting elongational flow field. We found that changing the geometry from the symmetrical case reduces the uniformity in the elongation rates.

For the snail ball system, two classes of solution are investigated: the rocking solution, and the runaway solution. It was found that the runaway solution still exists for both a power-law fluid and second order fluid models. The rocking solution is still possible for power-law fluid and a shear-thinning (thickening) fluid is predicted to travel less (further) than the Newtonian snail ball. The second order fluid does not allow the rocking solution but permits two constant rolling solutions, one stable and one unstable, which undergo a saddle-node bifurcation for sufficiently large viscoelastic effects.

In the driven boundary problem we analyse a Carreau fluid driven by a moving plate. The problem was divided into two types of behavoir: Newtonian fluid with weak power-law dependence and a power law fluid with weak Newtonian effects. In the latter case we find that there is a break-down due to zero shear which is resolved using matched asymptomatic analysis. It is found that there are two competing effects/boundary layers: transition to Newtonian behavior and translation of the point of zero shear.

In the finial section we analyze the effect of a mean field force on dumbbell dynamics under steady homogeneous velocity gradients. We find that the mean-field increases the extension of the dumbbells for both shear and elongational flow. The analysis demonstrates that there is a change in the singular extensional viscosity when the mean field term is present. Additionally, we find that the use of the Peterlin closure approximation for the spring forces leads to a dramatic over-estimation of the extension.

Table of contents

Chapter 1

Introduction

1.1 Overview

From the fuels which drive our cars to the food which we consume or the blood in our bodies the world is filled by a variety of often baffling, complex fluids. Bemusing effects can occur such as the tubeless siphon or stationary bubbles [85]. The mechanisms behind several of these phenomenon are still unexplained or much debated to this day, for instance the dramatic reduction of drag in turbulent flows with small polymer additives or discontinuities in the drag force on bubbles [104, 146]. However, perhaps the most frequent unsolved question which every student of rheology encounters is "*which equation should I use?*".

Classically, continuum mechanics has been split into two distinct fields, solid mechanics and fluid mechanics. However, such clear distinctions can become blurred on close inspection. For instance, over extremely small relaxation times, on the order of 10^{-13}s, even water can exhibit solid like behavior. Similarly, over geographic times scales even mountains appear to flow. For instance, the viscosity of granite has been estimated to be of the order of 10^{20}Pas [64].

However, the solid behavior of water and the fluid behavior of mountains are extremes and are not often of practical interest. There remains, though, a large variety of substances where both of these effects are appreciable. Such materials can be found ubiquitously in modern plastics and in the food industry. Consequently the field of rheology arose as a science in early mid 20th century[1], although one should note that certain rheological effects, such as temperature dependence, were known to the ancient Chinese and Egyptian cultures [132].

[1]The rod climbing phenomenon arose from investigation of flame-thrower propellants in WWII

As expected, the existence of a wide variety of materials comes with a broad spectrum of physical responses and thus mathematical models. This thesis will analyse generalized non-Newtonian fluids and non-linear viscoelastic fluids.

1.1.1 Conservation equations

Throughout this thesis we will be solving the two fundamental laws of mass and momentum conservation. As we will be studying fluids on a scale much larger than the mean free path of the fluid, we will use the continuum approximation which allows the conservation laws to be expressed as partial differential equations. We will also be considering flows where the speed of the fluid is small compared to the sound speed, in which case we can consider the fluid to be incompressible. For incompressible fluids mass conservation can be expressed succinctly by the solenoidal constraint

$$\nabla \cdot \mathbf{u} = 0, \tag{1.1}$$

where $\mathbf{u}$ is the velocity field. Momentum conservation can be written as

$$\rho\left(\frac{\partial \mathbf{u}}{\partial t} + (\mathbf{u} \cdot \nabla)\,\mathbf{u}\right) = \nabla \cdot \boldsymbol{\sigma}, \tag{1.2}$$

where $\boldsymbol{\sigma}$ is the stress tensor and ρ is the density. The stress tensor can be expressed as

$$\boldsymbol{\sigma} = -p\boldsymbol{\delta} + \boldsymbol{T}, \tag{1.3}$$

where p is the pressure, $\boldsymbol{\delta}$ is the unit tensor and $\boldsymbol{T}$ is the additional stress response due to the deformation. An additional equation, known as the constitutive relation, describes how the extra stress $\boldsymbol{T}$ couples to the deformation.

1.1.2 Simple Shear and Elongational flows

Under most circumstances it is impossible to solve equation (1.1) (1.2) and (1.3) by analytical methods alone. However if the velocity gradient is spatially homogeneous, one find that additional stress $\boldsymbol{T}$ is constant, and thus the constitutive equation decouples from the momentum equation. These types of flow are categorized into two class; shear and elongational flow, and understand of how a constitutive responds to these types of flows can allow one to understand and interpret how a particular model is responding to more complex flow field. For shear flow the velocity field, without loss of generality, can be written as $(u, v, w) = (\dot{\gamma} y, 0, 0)$. One is often interested in

shear flows as they occur naturally in pipe flows. In fact, any flow with a solid wall will induce some shear due to the no-slip condition. Constant shear flows are advantageous as the complex non-linear inertial terms are zero and the strain history of any fluid packet on a stream experiences is constant. The latter fact also remains true for elongational flows as well.

Elongational flows occur when a fluid element is undergoing a contraction in at least one direction and an expansion in the others. There are several classes of elongational flow that depend on the orientation of the contractions and expansions: uni-axial $(\dot{\varepsilon}, -\frac{1}{2}\dot{\varepsilon}, -\frac{1}{2}\dot{\varepsilon})$, bi-axial $(-\dot{\varepsilon}, \frac{1}{2}\dot{\varepsilon}, \frac{1}{2}\dot{\varepsilon})$ and planar $(\dot{\varepsilon}, -\dot{\varepsilon}, 0)$. One feature which is apparent with polymer solutions is that they have a much stronger tendency to resist being elongated than Newtonian fluids, this accounts for such phenomena as turbulent drag reduction in pipes [1], and upstream vortices in a contraction [128]. Elongational flows occur naturally during expansions and contractions and at stagnation points and more generally when velocity is changing in the direction of the streamline.

For elongational and shear flow the stress tensor $\boldsymbol{\sigma}$ can be obtained, however do the individual components of a stress tensor quantify the effects of a particular constitutive model? In reality it is found that it is much easier to interpret the physical effects through; the shear stress T_{12} and the first and second normal stress differences, N_1, N_2, which are given by

$$N_1 = T_{11} - T_{22}, \quad N_2 = T_{22} - T_{33}. \tag{1.4}$$

The first normal stress difference is typically positive[2] and significantly larger than the second normal stress difference, which is typically negative. The first normal stress difference physically manifests itself as a “hoop stress", which intuitively acts as a tension in the stream line and is directy responsible for rod-climbing and die-swell phenomena [142]. The second normal stress difference is often insignificant compared to the first normal stress difference, however, it can often be of importance in wire coating experiments [129].

[2]Liquid crystals are known to sometimes exhibit negative first normal stress differences [25].

1.2 Newtonian fluids

The first constitutive relation was proposed by Newton who suggested the force a fluid experiences is proportionate to the relative velocity between adjacent layers of fluid. Although Newton's relation was actually used to model an inter-planetary medium [132], the relation was found to be correct for most fluids and gave rise to the eponymous notion of a Newtonian fluid. It should be noted that it was not until the work of Navier, that we begin to see the modern concepts of viscosity, see [26] for an account of the history. Formally, a Newtonian fluid is one where the additional stress is proportional to the local rate of strain of the fluid:

$$\boldsymbol{T} = \mu \dot{\boldsymbol{\gamma}}, \tag{1.5}$$

where

$$\dot{\boldsymbol{\gamma}} = \nabla \mathbf{u} + \nabla \mathbf{u}^T, \quad \nabla \mathbf{u} = \begin{pmatrix} \frac{\partial u}{\partial x} & \frac{\partial v}{\partial x} \\ \frac{\partial u}{\partial y} & \frac{\partial v}{\partial y} \end{pmatrix}. \tag{1.6}$$

In (1.5) the constant of proportionality μ is the viscosity and $\dot{\boldsymbol{\gamma}}$ is the rate of strain tensor. As this relation holds for the most ubiquitously found fluids, i.e. water and air the field of Newtonian fluids is typically considered to be separate from rheology and often investigates the complex effects due to large inertial forces. Throughout this thesis we will only consider non-Newtonian fluids, which are simply defined as being any fluid where the relation (1.5) does not hold.

1.2.1 Generalized Newtonian model

Perhaps the most simple extension of the Newtonian concept is the notion of non-constant viscosity. Such models are known as generalized Newtonian fluids (GNF) and are studied in chapters 2,3. The viscosity of a Newtonian fluid is known to be an exponential function of temperature and even a function of pressure [18], although the dependence on pressure is much weaker than that for temperature. We refer to a non-Newtonian viscosity as one where the viscosity is a function of the local velocity gradient.

The viscosity must be independent of the coordinate system thus the viscosity cannot be directly a function of the components of the velocity gradient tensor. Instead it must be a function of one of the three invariants of the velocity gradient tensor, I=trace$\nabla\mathbf{u}$, II=trace$\nabla\mathbf{u}$-trace$\nabla\mathbf{u}^2$ and III=det($\nabla\mathbf{u}$). Immediately one can see that the viscosity is not a function of the first invariant as it is always zero by mass

conservation. The GNF relation is only expected to hold for sheared flows, although it does not necessarily capture the complexity from elongational flows, as such they are sometimes referred to as visco-inelastic fluids. As the third invariant is zero for pure shear-flows its dependency can be removed, although certain studies [97, 103] included the term for greater generality. Thus the viscosity in (1.5) can be replaced by

$$\mu = F(\dot{\gamma}), \tag{1.7}$$

where the second invariant can be replaced by the generlized shear rate $\dot{\gamma} = \sqrt{\frac{1}{2}\dot{\boldsymbol{\gamma}} : \dot{\boldsymbol{\gamma}}}$, where : denotes full index contraction. The functional form F of the shear-rate is free to be chosen. It has been found experimentally that for many fluids the functional viscosity behaves like the shear rate to some power. Often the apparent viscosity reduces with increasing shear, which is due to alignment of the micro-structure. In rare instances, for certain fluids the apparent viscosity increases (shear thickening). Such an effect can be physically attributed to the micro-structure of a solution locking against each other when shear is applied [1].

This observation resulted in the formation of the the power-law model and many derivatives there of including Carreau-Yosedia, Cross, Erying and Ellis models to name a few. Shear dependent behavior will clearly have effects such as required pressure drop needed to drive such a fluid at a fixed flow-rate. Surprisingly though Versluis et al. [140] found that shear thinning could be used to explain that the Kaye effect [69], which is the sporadic deflection of a poring stream for certain fluids.

It should be noted that GNF can also exhibit another non-Newtonian phenomenon, namely visco-plasticity. Certain fluids are not observed to flow until a critical yield stress is applied although there is some controversy about this description [92]. Such behavior is known as visco-plasticity. Some common yield models include the Bingham model (Newtonian with yield stress) and Herschel-Bulkley law (power law fluid with yield stress). Yield fluids occur widely in geological situations such as lava flows [44] or even glacial flows and snow avalanches, see Ancey [6] for a review.

1.3 Viscoelasticity

1.3.1 Linear viscoelasticity

The GNF model does allow for variable viscous behaviour, however there are many phenomena which cannot be described by such a law. One effect which clearly cannot be explained is hysteresis (or the apparent memory of fluids). One example of this can be found with silly putty [21]. One can form silly putty into a shape and it will retain its shape for certain length of time. However, given enough time under the influence of gravity, it will form a liquid puddle whereby it has "forgotten" the imposed shape. The GNF model depends only on the local velocity gradient and not on the previous history of the fluid. However, such memory effects are ubiquitous in solid mechanics in the form of elasticity, for instance an elastic band when stretched returns to its initial position after the applied forces are removed. The first model to incorporate these two effects was proposed by Maxwell where the additional stress was given by

$$\boldsymbol{T} + \lambda \frac{\partial \boldsymbol{T}}{\partial t} = \mu \dot{\boldsymbol{\gamma}}. \tag{1.8}$$

Here μ is a viscosity and λ denotes a relaxation time. The physics of Maxwells' model become clear if one consider extreme limits of λ. For $\lambda = 0$ the model gives simple Newtonian viscous behavior where the stress is proportional to the rate of strain. However, for large relaxation times we recover the relation $\lambda \to \infty$ one recovers $\boldsymbol{T} = G\boldsymbol{\gamma}$ where $G = \frac{\mu}{\lambda}$ is the modulus of elasticity. In this limit one finds that the stress is proportional to the strain which is well known to be Hooke's law. One can thus see how this model incorporates both elastic as well as viscous effects. Often polymer melts are embedded in a Newtonian solvent. An extension to Maxwell's model is Jeffreys' model, where the additional stress is decomposed such that Newtonian stress from the solvent is accounted for separately from the viscoelastic stress, i.e.

$$\boldsymbol{T} = \mu_s \dot{\boldsymbol{\gamma}} + \boldsymbol{T}_p, \tag{1.9}$$

where $\boldsymbol{T}$ satisfies equation (1.8). Many polymer solutions cannot be described by a single relaxation time and a single viscosity. This leads to a popular extension of the generalized Maxwell model, where $\boldsymbol{T} = \sum_{i=1}^{n} \boldsymbol{T}_i$, where each $\boldsymbol{T}_i$ satisfies equation (1.8) each with different parameters λ_i and μ_i.

Alternatively, a mechanical perspective to linear viscoelastic models can be sought by viewing the system as a superposition of dash-pots and linear springs. Whereas Maxwell's model can be considered a spring and a dash-pot in series, other linear

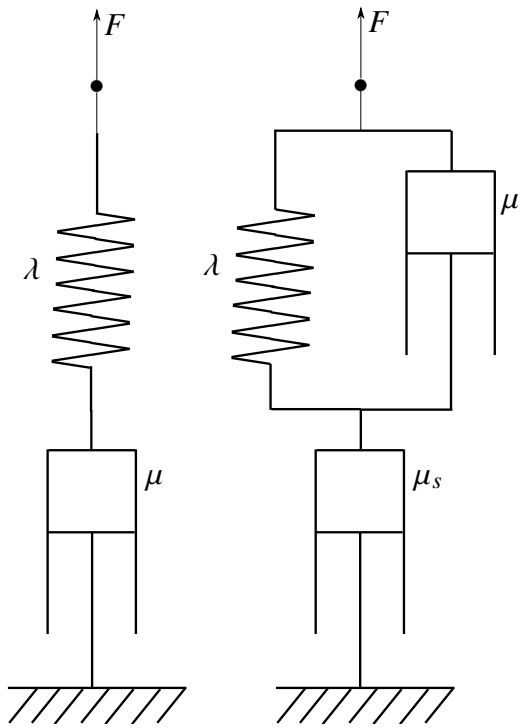

Fig. 1.1 A figure demonstrating a spring-dashpot construction model. The linear Maxwell model is presented on the left system, consisting of dashpot (bottom) and spring (top) in series. The Jeffrys' model analogue is presented on the right.

models such as Jeffreys model, Kelvin-Voigt model and generalized Maxwell model can similarly be interpreted as a system of string and dash-pots in series or parallel in various configurations.

The Maxwell model is in fact a subset of the generalized linear viscoelastic model which was first proposed by Boltzmann which assumes that the stress tensor can be written in the form

$$\boldsymbol{T} = \int_{-\infty}^{t} G(t-t')\dot{\boldsymbol{\gamma}}(t')dt'. \tag{1.10}$$

where the function $G(t-t')$ is the relaxation modulus, which gives the dependence of the stress tensor on the previous strain-rates. The function G, in effect, describes the memory for a linear visco-elastic fluid. For instance, for a Newtonian fluid $G(t-t') = \delta(t-t')$[3], which results in no dependence on the previous rates of strain. For Maxwell's model, $G(t-t') = \lambda^{-1}\mu e^{-\frac{(t-t')}{\lambda}}$, whereby the dependence on previous strain-rates fades exponentially with time.

[3]Here δ is the Dirac delta function.

1.3.2 Non-linear viscoelasticity

Linear viscoelasticity has the essential physics for modelling the correct behavior of polymer melts. However, the model is only able to predict behavior in relatively small deformations for quite dilute solutions. The problem can be found by considering the axiomatic approach first proposed by Oldroyd [95] and later by Noll et al. [93, 136] who expressed the fundamental axioms for a constitutive relation as principles of determinism, local action, coordinate invariance and material frame-indifference. The principle of determinism, in essence, states that the fluid is causal and the principle of local action that the fluid depends only on its close history. The principle of coordinate invariant states the equation should be independent of coordinates used. The principle of material indifference is of key importance and states the constitutive relation should be independent of the frame of reference of the observer i.e. objective.

Linear viscoelastic models, i.e. equation (1.10), do not possess objectivity, excluding the Newtonian case. For example in Bird et al. [15], for simple shear flow down a stationary pipe, an observer in a constantly rotating reference frame will observe that the shear stress on the wall of the channel is a function of shear rate and their angular velocity.

In order to keep the same structure as Maxwell's equation and introducing objective results in the non-linear Maxwell models which can be expressed as

$$\boldsymbol{T} + \lambda \frac{\delta \boldsymbol{T}}{\delta t} = \mu \dot{\boldsymbol{\gamma}}, \tag{1.11}$$

with the constraint that the derivative $\frac{\delta}{\delta t}$ is now objective. This leads to a surprising amount of freedom as to the choice of $\frac{\delta \boldsymbol{T}}{\delta t}$. However, several fundamental choices are

$$\frac{\delta \boldsymbol{T}}{\delta t} = \overset{\nabla}{\boldsymbol{T}} = (\mathbf{u} \cdot \nabla)\boldsymbol{T} - \nabla \mathbf{u}^T \cdot \boldsymbol{T} - \boldsymbol{T} \cdot \nabla \mathbf{u}, \tag{1.12}$$

$$\frac{\delta \boldsymbol{T}}{\delta t} = \overset{\triangle}{\boldsymbol{T}} = (\mathbf{u} \cdot \nabla)\boldsymbol{T} + \nabla \mathbf{u} \cdot \boldsymbol{T} + \boldsymbol{T} \cdot \nabla \mathbf{u}^T, \tag{1.13}$$

$$\frac{\delta \boldsymbol{T}}{\delta t} = \overset{\circ}{\boldsymbol{T}} = (\mathbf{u} \cdot \nabla)\boldsymbol{T} + \frac{1}{2}(\boldsymbol{\Omega} \cdot \boldsymbol{T} - \boldsymbol{T} \cdot \boldsymbol{\Omega}), \tag{1.14}$$

where the rotation tensor $\boldsymbol{\Omega}$ is given by $\nabla \mathbf{u} - \nabla \mathbf{u}^T$. The derivative represented by (1.12) is the most widely used and is the upper convective derivative or co-deformation derivative. The upper convective derivative denotes the rate of change experienced whilst deforming and translating with the fluid. The second (1.13) and third (1.14) derivative are the lower convective derivative and the Jaumann or

co-rotational derivative, which can be viewed as transforming and deforming and transforming and rotating with the fluid respectively. When equations (1.12), (1.13) and (1.14) are used in conjunction with the constitutive relation (1.11) one recovers the upper convective (UCM), lower convective (LCM), and co-rotating (CM) Maxwell models respectively.

The UCM is by far the most widely used as it is found to reproduce experimental observations more accurately. Notably, the second normal stress difference is found to be of the same order as the first normal stress difference for the LCM and CM [142]. In most fluids N_2 is of the order 10% of N_1. The UCM predicts zero second order stress difference. Such fluids are known as Wiessenberg fluids and are a much better approximation to the experimental observations. It is also found that several phenomena such as rod climbing [113] cannot be predicted by the LCM and CM respectively.

1.3.3 Non-dimensionalization

Throughout this work we will use the dimensionless mass momentum and conservation equations. This is advantageous as it allows one to reduce the number of input parameters needed for the system, and to identify which effects can be neglected. The UCM model is often extended to include the solvent viscocity, whereby this extended model is known as the Oldroyd B model. The procedure is the same as with Jeffreys' model, where the system of governing equations can be written as

$$\nabla \cdot \mathbf{u} = 0, \quad \rho\left(\frac{\partial \mathbf{u}}{\partial t} + (\mathbf{u} \cdot \nabla \mathbf{u})\right) = -\nabla p + \mu_s \nabla^2 \mathbf{u} + \nabla \cdot \boldsymbol{T}, \tag{1.15}$$

$$\boldsymbol{T} + \lambda \overset{\nabla}{\boldsymbol{T}} = \mu_p \dot{\boldsymbol{\gamma}}, \tag{1.16}$$

where μ_p represents the polymer viscosity. Let us suppose that the system has characteristic velocity and length scales U and L. We then introduce the dimensionless variables

$$\bar{x} = \frac{x}{L}, \quad \bar{y} = \frac{y}{L}, \quad \bar{t} = \frac{Ut}{L} \quad \bar{p} = \frac{U\left(\mu_p + \mu_s\right)}{L} p, \quad \bar{\boldsymbol{T}} = \frac{U\left(\mu_p + \mu_s\right)}{L} \boldsymbol{T}. \tag{1.17}$$

Equations (1.15), (1.16) can now be expressed as

$$\bar{\nabla}\cdot\bar{\mathbf{u}} = 0, \quad Re\left(\frac{\partial\bar{\mathbf{u}}}{\partial\bar{t}} + \left(\bar{\mathbf{u}}\cdot\bar{\nabla}\bar{\mathbf{u}}\right)\right) = -\bar{\nabla}\bar{p} + \mu_1\bar{\nabla}^2\bar{\mathbf{u}} + \bar{\nabla}\cdot\bar{\boldsymbol{T}},$$
$$\bar{\boldsymbol{T}} + W_e\overset{\nabla}{\bar{\boldsymbol{T}}} = \mu_2\bar{\dot{\boldsymbol{\gamma}}}. \tag{1.18}$$

where

$$Re = \frac{UL\rho}{\mu_s+\mu_p}, \quad W_e = \frac{U\lambda}{L}, \quad \mu_1 = \frac{\mu_s}{\mu_s+\mu_p}, \quad \mu_2 = \frac{\mu_p}{\mu_s+\mu_p}. \tag{1.19}$$

The dimensionless system contains three independent parameters: the Reynolds number Re, the Weissenberg number W_e and the viscosity fraction μ_1.[4]

The Reynolds number determines the strength of the inertial forces relative to the viscous forces. In the vast majority of Newtonian fluid dynamics problems the Reynolds number is large. However, as polymer melts are often extremely viscous and experiments are often run on small length scales, the Reynolds number can be often found to be much smaller than unity. Throughout the rest of this thesis we consider the Re to be small enough so that we can assume interia-less flow.

The parameter μ_1 is the ratio of the solvent viscosity to the total viscosity $\mu_p+\mu_s$. Moore et al. [91] point out that the parameter μ_1 physically represents the degree of coupling between the extra polymer stress and the velocity field. When $\mu_1 = 1$ the velocity field completely decouples from the extra stress. The strongest coupling is given for the case when $\mu = 0$.

The Weissenberg number, W_e, is the ratio of the characteristic relaxation time λ to advection time of the fluid $\frac{L}{U}$. For large Weissenberg numbers elastic effects are dominant whereas for small W_e the flow behavior is approximately Newtonian.

1.3.4 Second order fluid

If the Wiessenberg number is small compared to unity, one can look for a solution in the form

$$\boldsymbol{T} \sim \boldsymbol{T}_0 + W_e\boldsymbol{T}_1 + O(W_e^2). \tag{1.20}$$

Substituting (1.20) into (1.18) and comparing powers of W_e leads to

$$\boldsymbol{T}_0 = \mu_2\dot{\boldsymbol{\gamma}}, \quad \boldsymbol{T}_1 = -\mu_2 W_e\overset{\nabla}{\dot{\boldsymbol{\gamma}}}, \tag{1.21}$$

[4]The parameter μ_2 is not an independent parameter, as given μ_1, μ_2 can be found by $\mu_2 = 1-\mu_1$.

which gives the constitutive relation

$$\boldsymbol{T} = \mu_2 \dot{\boldsymbol{\gamma}} - \mu_2 W_e \overset{\nabla}{\dot{\boldsymbol{\gamma}}} . \tag{1.22}$$

The second order fluid model can be derived from the weak elastic limit of most models. In fact this is a special case of a perfect fluid or Riener-Rivilin fluid which can be generally written as

$$\mathbf{T} = \mu \dot{\boldsymbol{\gamma}} + \alpha_1 \dot{\boldsymbol{\gamma}} \cdot \dot{\boldsymbol{\gamma}} + 2\alpha_2 \overset{\nabla}{\dot{\boldsymbol{\gamma}}}, \tag{1.23}$$

We will discuss the shortcommings of the second order fluid model throughout the thesis, however the model should be thought of as a small correction on a Newtonian fluid. In-spite of this, the second order fluid model does introduce the same first normal stress for shear flow under constant elongational stress.

1.3.5 Giesekus-Tanner Theorem

In certain instances the velocity field for a Newtonian fluid gives a perfectly valid flow field for a second order fluid fluid. To see how this could be case consider the identity, which can be shown for an incompressible fluid,

$$\nabla \cdot \left(\overset{\nabla}{\dot{\boldsymbol{\gamma}}} + \dot{\boldsymbol{\gamma}} \cdot \dot{\boldsymbol{\gamma}} \right) = \frac{D\nabla^2 \mathbf{u}}{Dt} + (\nabla \mathbf{u} \cdot) \nabla^2 \mathbf{u} + \frac{1}{4} \nabla (\dot{\boldsymbol{\gamma}} : \dot{\boldsymbol{\gamma}}) . \tag{1.24}$$

For a Newtonian fluid, with velocity field $\mathbf{u}_N$ and rate of strain tensor $\dot{\boldsymbol{\gamma}}_N$ the velocity field satisfies

$$\nabla^2 \mathbf{u}_N = \nabla p_N, \tag{1.25}$$

where p_N is the Newtonian pressure field. After a little algebra one can show from (1.24)

$$\nabla \cdot \left(\overset{\nabla}{\dot{\boldsymbol{\gamma}}}_N + \dot{\boldsymbol{\gamma}}_N \cdot \dot{\boldsymbol{\gamma}}_N \right) = \nabla \left(\frac{Dp_N}{Dt} + \frac{1}{4} \dot{\boldsymbol{\gamma}}_N : \dot{\boldsymbol{\gamma}}_N \right) \tag{1.26}$$

Substituting a Newtonian velocity field into the momentum equation leads to the expression

$$\mu \nabla \cdot \dot{\boldsymbol{\gamma}}_N + 2\alpha_2 \nabla \cdot \left(\overset{\nabla}{\dot{\boldsymbol{\gamma}}}_N + \frac{1}{4} \dot{\boldsymbol{\gamma}}_N : \dot{\boldsymbol{\gamma}}_N \right) + \left(\alpha_1 - \frac{1}{2} \alpha_2 \right) \nabla \cdot (\dot{\boldsymbol{\gamma}}_N \cdot \dot{\boldsymbol{\gamma}}_N) = \nabla p. \tag{1.27}$$

From equations (1.24) and (1.25), the first two term on the left-hand side of (1.27) can be written as a potential of some scalar field. Thus the Newtonian field satisfies momentum conservation if either $2\alpha_1 = \alpha_2$, or the third term can be written as the

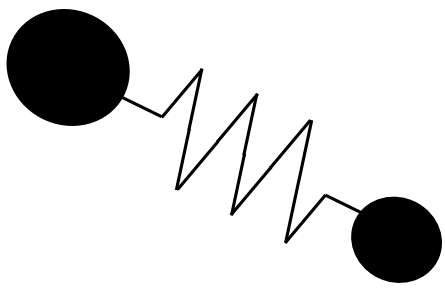

Fig. 1.2 Sketch of a simple dummbell, where two solid beads are attached by an elastic spring.

potential of some scalar field.

For the case $2\alpha_1 = \alpha_2$, leads to zero first normal stress difference and corresponds the second order fluid model obtained from perturbing the co-rotating Maxwell model, which generally produces unphysical behaviour.

For the second case, it can be shown that $\nabla(\dot{\boldsymbol{\gamma}} \cdot \dot{\boldsymbol{\gamma}})$ is the gradient of some potential for two classes of general flows, rectilinear flows i.e. $\mathbf{u} = (0, 0, w(x, y))$ and planar flows i.e. $\mathbf{u} = (u(x, y), v(x, y), 0)$. Therefore for rectilinear and planar flows the momentum equation (1.27) is satisfied, and thus the Newtonian velocity field solves the SOF system of equations.

1.4 Microscopic interpretation

The Oldroyd B model was first found by phenomenological argument, where one replaces the derivative in the linear Maxwell model with the upper convective derivative. However the physics behind the model are elusive. An alternative approach is to derive the theories from a molecular or 'structural' [58] approach. For instance Giesekus [41], found the UCM could be derived from a purely molecular interpretation.

The UCM can be recovered from considering a Newtonian fluid with a system of dumbbells, see Fig.1.2, suspended in the fluid. The first idea of using dumbbells can be dated back to Kuhn [77]. A dumbbell consists of two beads with different masses and radii, that are connected by a spring. One also assumes that the dumbbell is at

such a small length scale that the velocity gradient is homogeneous i.e.

$$\mathbf{u}(\boldsymbol{x}) \approx \mathbf{u}(\mathbf{0}) + \boldsymbol{\kappa} \cdot \boldsymbol{x}, \tag{1.28}$$

where $\boldsymbol{\kappa} = \nabla \mathbf{u}|_{\boldsymbol{x}=\mathbf{0}}$. It should be noted this assumption can be relaxed, see for instance [8]. Also, as a consequence of the small length scales, the viscous forces dominate inertial forces from the solvent. Intuitively the dominance of viscous forces over inertial forces can be argued as follows. Inertial forces act through the curvature in the streamlines, however at small scales this curvature is small. The equations of motion for the position of the center of mass $\boldsymbol{R}$ and the end-to-end vector (which is a vector connecting the two beads) $\mathbf{Q}$. When the inertia of the beads is ignored the system reduces to

$$\mathbf{0} = \left(\dot{\boldsymbol{R}} - \mathbf{u}(0) - \boldsymbol{\kappa} \cdot \boldsymbol{R}\right), \tag{1.29}$$

$$\mathbf{0} = -\zeta\left(\dot{\mathbf{Q}} - \mathbf{u}(0) - \boldsymbol{\kappa} \cdot \mathbf{Q}\right) - 2KT\frac{\partial \ln \psi}{\partial \mathbf{Q}} - 2\boldsymbol{F}^{(c)}. \tag{1.30}$$

The first terms in equations (1.29), (1.30) is simply Stokes' drag law with drag constant ζ, where the drag is proportional to the relative velocity between the fluid and bead. The second term in equation (1.30) is the entropic force term from Brownian motion, where K and T are the Boltzmann constant and the absolute temperature respectively. The entropic term arises to act to push the system towards its state of highest entropy [5]. The final term in (1.30) is the elastic force from the connecting spring.

The entropic force depends on the probability distribution ψ. Formally $\psi(\mathbf{Q})d\mathbf{Q}$ is the probability at time t that the end-to-end vector is in the interval $\mathbf{Q}$ to $\mathbf{Q} + d\mathbf{Q}$. The probability density function can be solved by the conservation law

$$\frac{\partial \psi}{\partial t} + \nabla_{\mathbf{Q}} \cdot \left(\dot{\mathbf{Q}}\psi\right) = 0, \tag{1.31}$$

where $\dot{\mathbf{Q}}$ is found from (1.30). Once the probability distribution is known the polymer contribution to the stress tensor from the polymer ($\boldsymbol{\tau}$) can be found from Kramer's law

$$\boldsymbol{\tau} = KT\boldsymbol{\delta} + \langle \mathbf{Q}\boldsymbol{F}^{c} \rangle. \tag{1.32}$$

[5] Physically the entropic force is not a force however the effect of small fluctuations in a system cumulatively act like a force.

It is of note that Kramer's law will only be applicable when the spring law $\boldsymbol{F}^{(c)}$ can be expressed. However, in certain models, such as rigid dumbbells, where the two beads are fixed by a rigid rod, $\boldsymbol{F}^{(c)}$ is not applicable. Alternatively one could use Giesekus's expression for the stress tensor, which is given by

$$\boldsymbol{\tau} = \frac{\zeta}{4} \langle \overset{\nabla}{\mathbf{QQ}} \rangle \,. \tag{1.33}$$

If we use the linear Hooke's law for the spring force i.e. $\boldsymbol{F}^{(c)} = H\mathbf{Q}$, then the UCM can be derived from equations (1.30), (1.31) and (1.32). Other constitutive equations can be similarly found from a structural interpretation. The Rouse Model [16] can be found from considering multiple chains. Even the Johnson Segalman model, which is normally derived from the superposition of the upper convective and lower convective derivative, can be derived from molecular arguments by introducing slip in the velocity between the flow and the bead [79].

1.5 Experimental considerations

The reader should note that this thesis is purely theoretical, however, the field of rheology relies on both experimentation and theory and as such we present an extremely brief overview of experimental methods.

1.5.1 Experimental methods

Experimentally, shear flow is relatively simple to generate and can be achieved by one wall moving with respect to a parallel wall with no applied pressure gradient. Several methods exist to generating shear-flow [145]. The most popular device is possibly a cone and plate rheometer where one measures the torque and the normal reaction force required to fix and rotate "the cone", relative to the plate, with the analyzed fluid sample acting as a lubricating layer. The physical measurements can be inverted to find the shear and normal stress exerted by the fluid sample and thus the material properties of the fluid. Parallel plate rheometers and concentric cylinders[6] work on a similar principle. Another common class of shear rheometers are capillary rheometers which measures pressure drop down a pipe. Shear rheometry is commonly extended to incorporate transient response of fluids by using "oscillator shear rheometry".

[6]Unlike cone and plate and parallel plate geometries concentric cylinders are not capable of measuring normal stresses

Pure steady elongational flow, however, is much more difficult to generate as the presence of walls will induce shear. However, there are several methods exist which involve cross slot (which will be discussed in chapter 2), four roll mill and converging channel geometries. However these methods only can produce elongation approximately over small regions of the device. Attaining consistent elongational results can be problematic, notably Keiller [70] found for the same Boger fluid that different elongational experiments produce vastly different results.

1.6 Overview of chapters

A more detailed introduction accompanies each of the chapters of this thesis but here we present a brief outline of the chapters.

- In chapter 2 we investigate a viscoelastic fluid in a cross-slot geometry. We will take the approach of solving the cross-slot analytically. However in order to make analytical progress we will perform the analysis for a second order fluid in a thin cross-slot. We also perform a full 3D finite element calculation to corroborate the result.

- In chapter 3 we will study a lubricating second order fluid in a new system the "snail ball". The work builds on that by Balmforth et al. [9] who studied the dynamics of the snail ball for a Newtonian fluid. We first study the behavior for a lubricating second order fluid and then progress to analyze the snail ball system for a generalized Newtonian fluid, specifically a power-law fluid.

- In chapter 4 we continue with the study of generalized Newtonian fluids, however, we consider the case of a Carreau fluid. The analysis is performed in Taylor's paint scraping geometry. The chapter further generalizes the Newtonian problem considered by Taylor [133] and the power-law case considered by Rielder and Schnedier [114].

- In chapter 5 we return to viscoelasticity. This chapter investigates concetration effects on a single dumbbell by using a mean-field force term proposed by

Schneggenburger et al. [121]. We extended the results of Schneggenburger to incorporate elongational flow, and analyze the effect of the pre-averaging closure assumption.

- In chapter 6, we present our conclusions and provide discussion as to how our results in this thesis fit into the literature as well as possible future work.

Chapter 2

Viscoelastic Hele-Shaw Flow in a Cross-Slot Geometry

Abstract

In this chapter a cross-slot geometry for which the height of the channel is small compared to the other channel dimensions is considered. The normal components of the viscoelastic stresses are found analytically for a second order fluid up to numerical inversion. The validity of the theoretical analysis was corroborated by comparison with numerical simulations based on a stabilized Galerkin Least Squares (GLS) finite element method using an Oldroyd B fluid. Close agreement was found between numerical predictions and analytical results for Weissenberg numbers (W_e) up to 0.2. Discrepancies observed between numerical and analytical results can be attributed to shortcomings in the second order fluid model. We further generalize the analytic second order fluid results to encompass the case where the inlet channel width is different from the outlet channel width. For such configurations it was found that uniformity of the elongation rate was reduced.

2.1 Introduction

Polymer melts, which are widely used in processing operations such as injection molding, mixing and extrusion, exhibit non-Newtonian properties. Due to the relaxation times involved and memory effects, the ability to accurately predict the velocity and stress fields is still a challenging problem.

The modeling of such viscoelastic fluids has proven to be difficult, both numerically and even more so analytically, even in the most simple of geometries. Analytical solutions are often presented under the assumption of constant velocity gradients, i.e. constant shear or elongation. Other solutions have been found, for example, an analytical solution for a FENE-P fluid was presented by Oliveira [96] and Rajagopal and Bhatnagar [109] found solutions for the flow of an Oldroyd B fluid, though exact analytical results often require the specification of a flow field such that the advection terms are zero. In this chapter we use perturbation methods to derive a semi-analytical result for a second order fluid in a Hele-Shaw cross-slot device. The Hele-Shaw approximation necessitates that the geometry must have one length

scale which is much smaller than the others. In our system the channel height is assumed to be much smaller than its width and thus the aspect ratio, δ, is small. This approximation has been used in numerous other studies, see for instance [35, 39]. A sketch of the full three-dimensional system is given in Fig.2.1. Mathematically, the system reduces to the two-dimensional system shown in Fig.2.2. Under the Hele-Shaw assumption one can perform an analysis of the stress under non-constant elongation. A finite element formulation for this flow configuration was also undertaken to consider the validity of the analytical results. Hele-Shaw flow only permits slip boundary conditions, although in reality there is a small layer, close to the solid wall, where the no-slip condition forces the velocity to drop to zero.

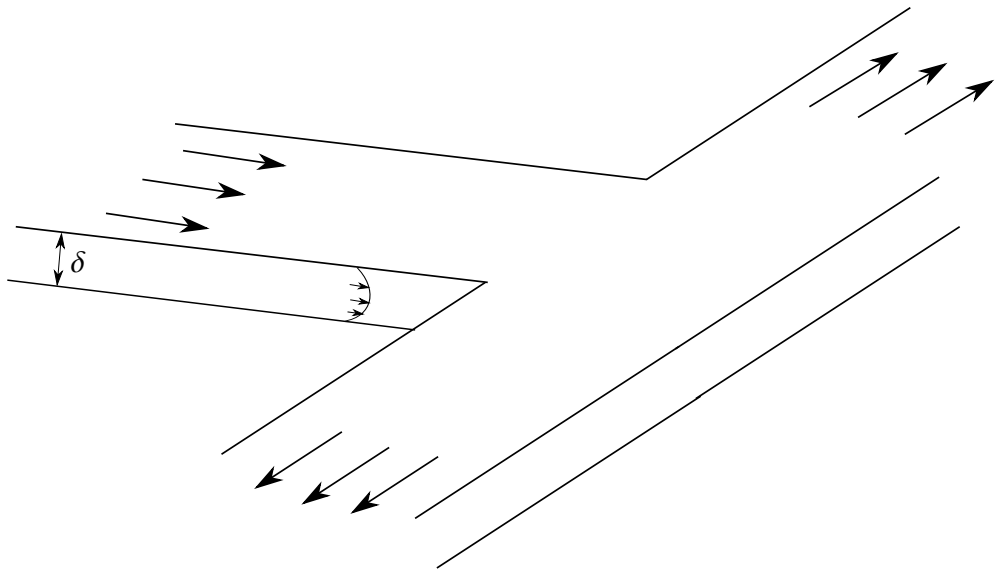

Fig. 2.1 Sketch of the three-dimensional geometry.

Experimental interest in the cross-slot geometry is focussed on investigating the extensional behavior of polymers motivated by the strong elongational nature of the flow in a cross-slot device. Birefringence techniques used in conjunction with numerical studies of extensional flows have been used effectively to assess the validity of constitutive models, however, studies of polymer melts have highlighted some inconsistencies due to end effects and beam deflections [102]. Recently, Scoulages et al. [2, 126] made three-dimensional birefringent measurements of flow in a lubricated cross-slot geometry in a study aimed at removing end effects. Achievement of this goal would lead to greater conformity with two-dimensional simulations without the compromise of using large aspect ratios. It may be possible to extend the results

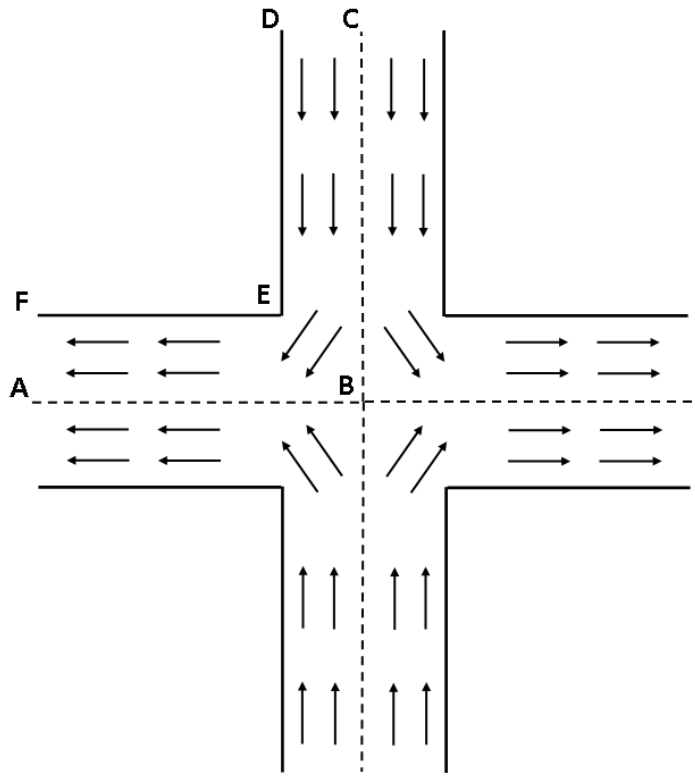

Fig. 2.2 The two-dimensional slice of the cross-slot geometry. The widths of the inlet section of the channel DC and the outflow channel FA are taken to be equal in section 4.

of this paper to a lubricated device without the need for small aspect ratios using the theory of Joesph [67, 68].

The cross-slot device does not produce pure extensional behavior throughout the flow field and the aim of generating purely extensional flows still proves challenging. Haward et al. [51] used numerical simulations to optimize the shape of corner regions in a cross-slot to produce a more homogeneous extensional flow field. This study was purely two-dimensional which can be difficult to realize experimentally due to end effects which arise from finite aspect ratios. Hele-Shaw flows may prove advantageous in achieving elongational homogeneous flow fields as the unwanted shear effects may be reduced. The shear induced from the horizontal walls is mainly located close to the boundary. Shear induced from the vertical walls could be reduced by considering the center plane.

The cross-slot device also exhibits strong bifurcating behavior with visco-elastic fluids [23, 50, 102, 116]. Sousa et al. [127] considered the effects of aspect ratio on

this instability. They found that for smaller aspect ratios the symmetry breaking bifurcation required a larger Weissenberg number, and that for sufficiently small aspect ratios, the symmetry breaking bifurcation was superseded by a transient bifurcation. Such an instability will not be considered in this study as we will assume symmetry of the device throughout. Bifurcations in cross-slot channels are not limited to non-Newtonian fluids. Poole et al. [106] found symmetry breaking birefringence for strongly inertial flows with Newtonian fluids, though the behavior of this bifurcation is inherently different to those caused by viscoelastic effects.

The aim of this investigation is to determine whether one can obtain analytic results for a viscoelastic fluid in a cross-slot device. This would be advantageous as performing three-dimensional simulations of viscoelastic fluids can prove costly in terms of both time and computational power. We will find later that our solution is not valid in the corner region. Viscoelastic effects in corner regions have been extensively studied. Analytical studies have addressed the dynamics of Oldroyd B and Upper Convective Maxwell (UCM) fluids flowing in a channel containing a sharp bend. Rernardy [112] used a similarity solution for the stress stream function and found that the stresses scaled $\sim r^{-\frac{2}{3}}$ in the corner region, where r is the distance from the corner. This work was subsequently generalized by Rallison and Hinch [110] to encompass a range of channel bend angles, and by Evans [36] who investigated the downstream effects. We refer to these studies to address the local corner effects. However, in this study we will focus predominantly on the stress effects along the line of symmetry along the outflow channel (the line AB in Fig.2.2), which is not in the vicinity of the corner.

The difficulty in generating formulations for analytical flows in such a geometry can be overcome by the use of complex potential theory, namely the Schwarz-Christoffel mapping (SCM) theorem. Taking advantage of the symmetry of the cross-slot device means that we need only consider one quadrant.

In this chapter, a finite element model is used to assess the validity of an approximate analytical solution for the flow of an inertialess Oldroyd B fluid in a three-dimensional cross-slot. We found that this problem exhibited numerical difficulties arising from the sharp corner. The problem, as first noted by Keunings [72], is that increases in the mesh resolution led to poorer convergence at high W_e when a sharp corner is present. As one often needs high mesh resolution in such corner regions this proves problematic. However, Singh and Leal [125] noted that this poor convergence

was due to insufficient mesh resolution in the azimuthal direction. We took this consideration in our numerical simulations.

In section 2 we describe the construction of the flow field. The governing equations and flow field are presented in section 3. For the case of inlet and outlet channels of equal width, the viscoelastic stress components and stagnation point pressure are analyzed in section 4. The effects of varying the ratio of the inlet and outlet channel width ratios are considered in section 5. The conclusions are summarized in section 6.

2.2 Construction of the flow field

Under the assumption of a small aspect ratio δ under zero Reynolds number for a Newtonian fluid, the mass and momentum conservation equations can be written as [10]

$$\mathbf{u}_{in} = -\frac{1}{2\mu}\bar{\nabla} p x_3 (d - x_3), \quad \frac{\partial p}{\partial x_3} = 0, \quad u_3 = 0, \quad \bar{\nabla} \cdot \mathbf{u}_{in} = 0 \tag{2.1}$$

except for a small region near the walls of order $O(\delta)$ where the no-slip condition dominates. Here $\mathbf{u}_{in} = (u_1, u_2)$ is the in-plane velocity, x_1 and x_2 are the in-plane coordinates. Likewise, u_3 is the out-of-plane component of the velocity where x_3 is perpendicular to x_1 and x_2. The variable p denotes the pressure, $\bar{\nabla}$ is the in-plane gradient operator and d denotes the channel height. In a plane with x_3 fixed, this is analogous to the commonly used potential flow problems for irrotational fluids whereby $\mathbf{u}_{in} = \bar{\nabla}\phi$, where ϕ is the velocity potential which acts analogous to pressure in our problem.

Potential flow theory can be used to find a solution for the flow in complex channel geometries by superposing fundamental solutions, such as sinks, sources, dipoles, etc. It is often advantageous to work in terms of the complex potential, w, which is given by

$$w(z) = \phi + i\psi, \tag{2.2}$$

where z is the complex variable $x_1 + ix_2$, and ψ is the stream-function for the in-plane velocity (u_1, u_2). It is easily shown that the derivative of (2.2) can be used to find the velocity components (u_1, u_2) from

$$\frac{dw}{dz} = u_1 - iu_2. \tag{2.3}$$

To construct the flow field as in Fig. 2.2, we make use of the SCM theorem [88]. The SCM theorem concerns the conformal transformation of the upper half-plane onto the interior of a simple polygon. This theorem states that for n points along the real axis $(\eta_1, \eta_2, \ldots, \eta_n)$ corresponding to the vertices of a simple polygon, such that $\eta_1 < \eta_2 < \cdots < \eta_n$, where $\theta_1, \theta_2, \ldots, \theta_n$ are the internal angles of the polygon, the transformation from the η-plane to the z-plane is given by

$$\frac{dz}{d\eta} = K(\eta-\eta_1)^{\frac{\theta_1}{\pi}-1}(\eta-\eta_2)^{\frac{\theta_2}{\pi}-1}\ldots(\eta-\eta_n)^{\frac{\theta_n}{\pi}-1}, \tag{2.4}$$

where K is a complex constant. If one chooses a map from the corners of a channel containing a right-angled bend, as shown in Fig.2.2, to the η-plane given by

$$A \to -\infty, \qquad B \to -a, \qquad C, D \to 0, \qquad E \to b, \qquad F \to +\infty, \tag{2.5}$$

then the SCM theorem gives

$$\frac{dz}{d\eta} = K\eta^{-1}(\eta+a)^{-\frac{1}{2}}(\eta-b)^{\frac{1}{2}}, \tag{2.6}$$

where a and b are positive non-zero real constants.

Here we explain the general idea behind how the SCM theorem works. First consider the conformal map $z = F(\eta)$ acting on the upper half plane. If $F'(\eta) \neq 0$ then one can readily show that arg(z)=arg($F'(\eta)$). Let us consider the effect at one vertex by considering the mapping of the real η axis under the transformation $F'(\eta) = (\eta - l)^{-b}$, where l is a point on the real axis in the η plane. For η on the real axis with $\eta < l$ we have arg($F(\eta)$)=$-i\pi b$, and for $\eta > l$ we have arg($F(\eta)$)=0. Hence in the z-plane we have an exterior angle $b\pi$ and interior angle $a\pi = \pi - \pi b$, thus $-b = -1 + a$.

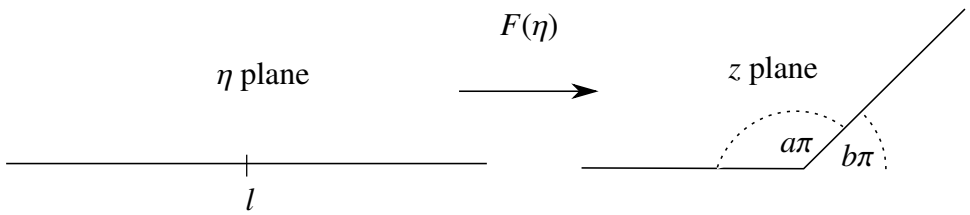

Fig. 2.3 Sketch demonstrating the SCM theorem for the map $F'(\eta) = (\eta - l)^{-b}$, from the η-plane (left) to the z-plane (right).

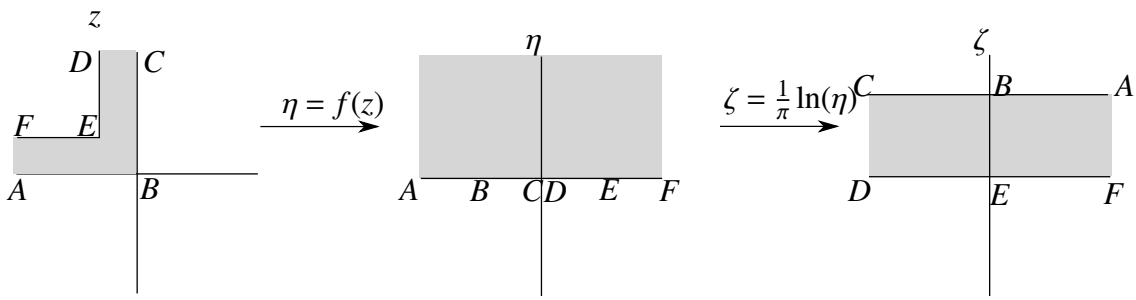

Fig. 2.4 Sketch demonstrating the conformal mapping. From left to right, mapping the z-plane onto the η-plane, and then the η-plane onto the ζ-plane.

Thus we have $\frac{dz}{d\eta} = F'(\eta) = (z-l)^{-1+a\pi}$. After noting that $a = \frac{\theta}{\pi}$, where θ is the internal angle and forming a product for multiple vertices leads to equation (2.4).

Upon integration, it should be remembered that the constant of integration will be complex. Initially the SCM theorem maps the cross-slot geometry onto the upper half infinite plane. This semi-infinite half plane can then be readily mapped onto an infinitely long rectangle of unit height using the transformation

$$\zeta = \frac{1}{\pi}\ln(\eta). \tag{2.7}$$

These mappings are shown graphically in Fig.2.4 which also depicts the mappings of the vertices. For the mapping onto the η-plane, the positive real η-axis maps to $\Im(\zeta) = 0$ and the negative real η-axis maps to $\Im(\zeta) = 1$. This can be seen by writing $\eta = re^{i\theta}$ for r, θ real. For the case where η lies on the positive real axis we have $\theta = 0$ and thus $\zeta(r) = \pi^{-1}\ln(r)$. Similarly, when η lies on the negative real axis, $\theta = \pi$ and hence $\zeta\left(re^{i\pi}\right) = \pi^{-1}\ln(r) + i$. The complex stream function for a uniform flow with constant flux Q_0 from C, D to A, F, in the ζ-plane, is given by

$$w(\zeta) = Q_0\zeta, \tag{2.8}$$

which can be written as

$$w(\eta) = \frac{U_0 h}{\pi}\ln(\eta), \tag{2.9}$$

where we have used the fact that for a channel of height h, and constant flow U_0 we can write $Q_0 = U_0 h$. Physically, in the η-plane, the complex potential w is analogous to a source with flux Q_0 around the origin, or in the z-plane to a flux source located infinitely far up the x_2-axis.

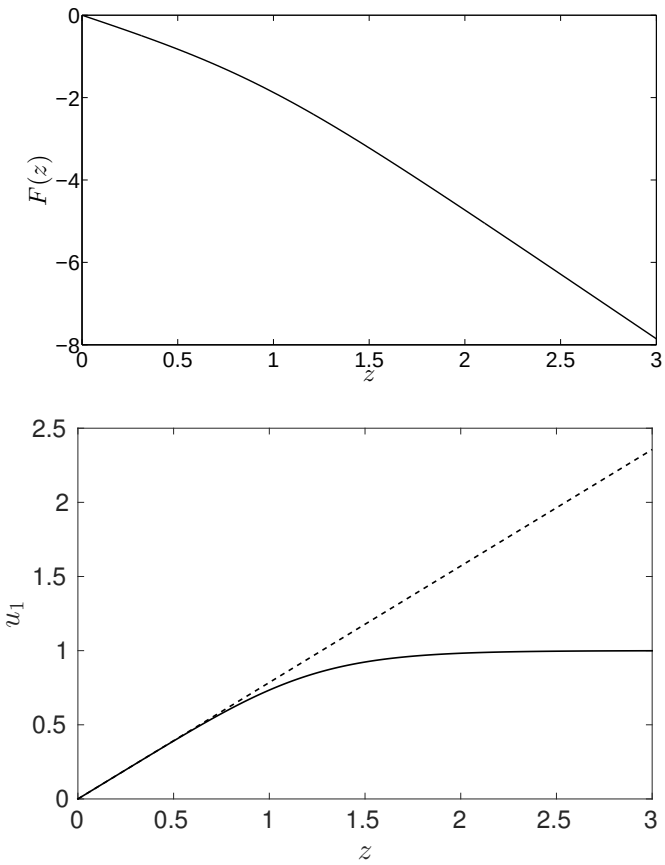

Fig. 2.5 (a) The inverse function $F(z)$ plotted against its argument. (b) The predicted velocity along the line of symmetry (solid line) together with that predicted by assuming purely elongational flow (dashed line), plotted against z.

Combining (2.6) and (2.9) gives

$$\frac{dw}{dz} = \frac{U_0 h}{\pi K} \frac{\sqrt{(\eta + a)}}{\sqrt{(\eta - b)}}. \tag{2.10}$$

The constants are determined by imposing the condition of a uniform flow stream at the channel inlet and outlet. This gives rise to

$$\frac{dw}{dz} \sim -U_0 \quad \text{as} \quad \eta \to \pm\infty, \tag{2.11}$$

$$\frac{dw}{dz} \sim U_0 i \quad \text{as} \quad \eta \to 0. \tag{2.12}$$

Constraints (2.11) and (2.12) can be used to determine the constants, giving

$$K = -\frac{h}{\pi}, \quad a = b = 1. \tag{2.13}$$

We note that there is an arbitrary degree of freedom for assigning the value of a and for convenience we set $a = 1$. By integrating (2.6) with the constants determined in (2.13) and making the substitution $\eta = \cosh(t)$ we find that

$$z(t) = -\frac{h}{\pi}\left(t + \tan^{-1}\left(\frac{1}{\sinh(t)}\right) - i\pi + \frac{\pi}{2}\right), \tag{2.14}$$

$$w(t) = \frac{U_0 h}{\pi}\ln(\cosh(t)), \tag{2.15}$$

where $t \in \mathbb{C}$ is a dummy variable. The constant of integration translates the geometry around the z-plane and is assigned such that the bottom corner is at the origin. Equations (2.14) and (2.15) form an implicit relation for the velocity field in the L bend geometry. Equation (2.14) can be inverted to give the result, $t = F(z)$, which is plotted in Fig. 2.5 along with the velocity profile along the center line of the channel. The stream lines are shown in Fig. 2.6. Note that the solution gives rise to a singularity in the corner region which makes the flow unphysical in this vicinity. We can analyze the local behavior of the stagnation point by performing a Taylor expansion around $t = i\pi$. Ignoring the constant term, for w is unique up to an additive constant,

$$w \sim \frac{U_0 h}{2\pi}(t - i\pi)^2 + O(t - i\pi)^4, \quad z \sim -\frac{2h}{\pi}(t - i\pi) + O(t - i\pi)^2. \tag{2.16}$$

We thus see that locally $w \sim \frac{U_0\pi}{8h}z^2$, from which, by considering the imaginary component, we can recover the stagnation point stream-function $\psi = \frac{U_0\pi}{4h}x_1x_2$, used in prior studies of stagnation points, see for instance [111, 134].

The solution near the corner point E is mapped to $t = 0$. Taking the limit around $t = 0$, we have $z \sim hi - \frac{h}{6\pi}t^3$, $w \sim \frac{1}{2}t^2$, thus we are left with $w \sim 2^{-\frac{1}{3}}3^{\frac{2}{3}}\pi^{\frac{2}{3}}h^{-\frac{2}{3}}(z - z_0)^{\frac{2}{3}}$, i.e. locally one recovers $\phi \propto r^{\frac{2}{3}}\cos\left(\frac{2}{3}\theta\right)$, $\psi \propto r^{\frac{2}{3}}\sin\left(\frac{2}{3}\theta\right)$, which is the potential flow solution around a corner, as to be expected.

2.3 Governing equations

We will calculate the viscoelastic stresses using the Hele-Shaw flow as an approximation to the fluid velocity. However to compare the validity of our approximation we will compare the result to the inertialess Oldroyd B equations (1.18). We chose the Oldroyd B model over the UCM because the addition of a small solvent viscosity can lead to considerably improved numerical stability [12]. However, one must bear in mind that the Oldroyd B model, in its relative simplicity, does predict physically

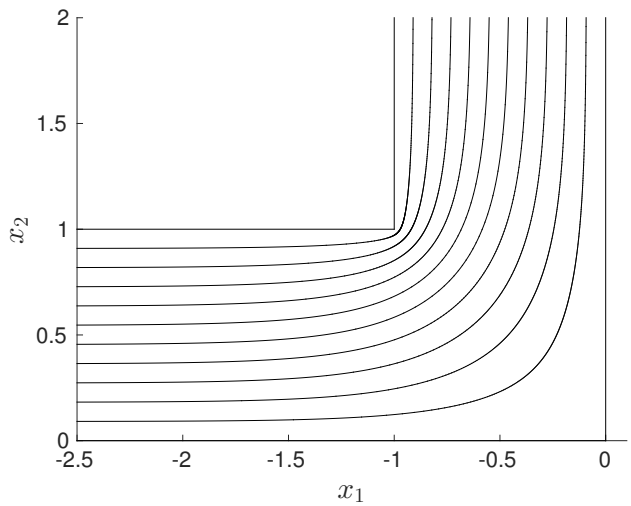

Fig. 2.6 Streamlines derived from conformal mapping analysis.

,

unrealistic behavior at high elongation rates, notably, the well-known phenomenon of singular extensional viscosity at a finite elongation rate. Fundamentally, this problem arises as the Oldroyd B model has a linear extensional law at a microscopic scale. This is often over come using models such as FENE-P, FENE-CR. Despite its limitations, the Oldroyd B model does reproduce complex viscoelastic behavior and is known to be a suitable choice for modeling Boger fluids [65]. Also, in general, most other more complex viscoelastic models reduce to the Oldroyd B model in certain parameter limits.

We will therefore solve the system of pdes in (1.18). Where the characteristic velocity U is taken to be the inlet velocity, the characteristic length L is the width of the channel. We will use the finite element software COMSOL Multiphysics. Numerical convergence can be difficult to achieve for the UCM and Oldroyd B models, especially for high Weissenberg numbers in the presence of large velocity gradients. Here we make use of the Galerkin least squares (GLS) method to stabilize the equations as originally proposed by Hughes et al. [61]. The scheme used here follows the procedure of Behr et al. [11] which was implemented in COMSOL by Craven et al. [24]. The GLS method is similar to the commonly used streamline up-wind Petrov-Galerkin method that is often used for integrating the Navier-Stokes equations, where the standard weak form of the equations is augmented with additional

stabilization terms:

$$
\begin{aligned}
&-\langle \nabla\cdot\mathbf{w}, p\rangle + \mu_1 \langle \dot{\boldsymbol{\gamma}}[\mathbf{w}], \dot{\boldsymbol{\gamma}}[\mathbf{u}]\rangle + \frac{1}{2}\langle \dot{\boldsymbol{\gamma}}[\mathbf{w}], \mathbf{T}\rangle + \langle \mathbf{q}, \nabla\cdot\mathbf{u}\rangle \\
&+ \langle \mathbf{S}, \mathbf{T}\rangle + \lambda \left\langle \mathbf{S}, \overset{\nabla}{\mathbf{T}} \right\rangle - \mu_2 \langle \mathbf{S}, \dot{\boldsymbol{\gamma}}[\mathbf{u}]\rangle + \sum_{elements} \tau_{mom} \langle\, \nabla q - \nabla\cdot\mathbf{S} \\
&- \mu_1 \nabla\cdot\dot{\boldsymbol{\gamma}}[\mathbf{w}]\,,\ \nabla p - \nabla\cdot\mathbf{T} - \mu_1 \nabla\cdot\dot{\boldsymbol{\gamma}}[\mathbf{u}]\,\rangle \\
&+ \sum_{elements} \rho\tau_{cont} \langle \nabla\cdot\mathbf{w}, \nabla\cdot\mathbf{u}\rangle + \sum_{elements} \tau_{cons} \left\langle \left[\mathbf{S} + \lambda\overset{\nabla}{\mathbf{S}} - \mu_2\dot{\boldsymbol{\gamma}}[\mathbf{w}]\right], \right. \\
&\left. \left[\mathbf{T} + \lambda\overset{\nabla}{\mathbf{T}} - \mu_2\dot{\boldsymbol{\gamma}}[\mathbf{u}]\right] \right\rangle,
\end{aligned}
\tag{2.17}
$$

under the convention $\dot{\boldsymbol{\gamma}}[\boldsymbol{g}] = \nabla\boldsymbol{g} + \nabla\boldsymbol{g}^T$. The terms $\tau_{cons}, \tau_{mom}, \tau_{cont}$ are the GLS parameters as defined as in [11]. Here $\mathbf{w}$, $\mathbf{S}$, q denote the test functions for the velocity field, extra stress tensor and the pressure field respectively. The test functions are taken to be Lagrange polynomials. It was found that the greatest stability could be achieved using cubic elements for the velocity field, and quadratic elements for the pressure field and for the extra stress tensor, though mixed elements are non-mandatory as the GLS formulation negates compatibility conditions on the order of the test functions. In the corner region, one would expect large velocity gradients which would give rise to a lack of convergence in the FEM model. The grid used for this study was composed of a mixed triangular, quadrilateral mesh comprising 20374 elements, which was then swept in the x_3 direction to form 5 mesh layers. The mesh was refined until the dependency of the solutions on the mesh size varied on the order 0.1%. Predictions of the flow fields within the cross-slot were obtained by solving equation (2.17) along with the boundary conditions. At the inlet uni-directional flow is imposed and solved numerically along with the stress field. Along the lines of symmetry we impose

$$
\mathbf{u}\cdot\mathbf{n} = 0, \quad (\boldsymbol{\sigma}\cdot\mathbf{n})\cdot\mathbf{t} = 0. \tag{2.18}
$$

Zero surface traction was imposed across the channel outlet, i.e.

$$
\boldsymbol{\sigma}\cdot\mathbf{n} = \mathbf{0}. \tag{2.19}
$$

Here the vectors $\mathbf{n}$ and $\mathbf{t}$ are the normal and tangential vectors respectively.

2.4 Weak Coupling Expansion

Thus far we have derived the velocity for a Newtonian fluid and have not considered any non-Newtonian effects. Of course if we can decouple the velocity field from non-Newtonian stress the problem simplifies dramatically. Common approaches to decoupling the non-Newtonian stress use a second order fluid and using the Gieskitus Tanner theorem [131] to decouple the flow field. However as the flow field is neither rectilinear nor planar we cannot directly use the GT theorem. There is however another limiting of the form which be may be of interest. If we take the approach of Moore et al. [91] one can assume that polymer viscosity μ_p is small in comparison to solvent viscosity i.e. $\mu_2 \ll 1$ in the dimensionless equation (1.18) and assume an expansion for the variables $u \sim u^{(0)} + \mu_p u^{(1)} + \ldots$, $p \sim p^{(0)} + \mu_p p^{(1)}$, and $\boldsymbol{T} = \mu_p \boldsymbol{T}^{(0)} + \mu_p^2 \boldsymbol{T}^{(1)}$. Substituting into (1.18) and taking leading order in μ_p gives

$$-\nabla p^{(0)} + \nabla^2 \mathbf{u}^{(0)} = \mathbf{0}, \quad \nabla \cdot \mathbf{u}^{(0)} = 0, \tag{2.20}$$

$$\boldsymbol{T}^{(0)} + \lambda\left(\left(\mathbf{u}^{(0)} \cdot \nabla\right)\boldsymbol{T}^{(0)} - \nabla \mathbf{u}^{(0)\,T}\boldsymbol{T}^{(0)} - \boldsymbol{T}^{(0)}\nabla \mathbf{u}^{(0)}\right) = \dot{\boldsymbol{\gamma}}^{(0)} \tag{2.21}$$

To leading order the velocity field completely decouples from the extra stress $\boldsymbol{T}^{(0)}$. Hence we can use the expression (2.2) to obtain $\mathbf{u}^{(0)}$ and solve equation (2.21) to obtain the extra stress. Unfortunately the velocity field and gradients are only implicitly a function of spacial coordinates, as t cannot be easily inverted to give a function of z. We can however locally invert t as a function of z using the inverse power series to give

$$t(z) \sim i\pi + \frac{\pi z}{2h} + \frac{\pi^3 z^3}{96h^3} - \frac{\pi^7 z^7}{143360h^7} + O(z^9) \tag{2.22}$$

Similarly we can find expansions for the velocity field and velocity gradient field. To do so it is useful to note the following expressions where $'$ denotes differentiation with respect to z:

$$w'(t) = U_0 \frac{\sinh(t)}{(-\cosh(t)+1)}, \quad w''(t) = -\frac{U_0 \pi}{h}\frac{\cosh(t)}{(1-\cosh(t))^2}. \tag{2.23}$$

Thus locally at $t = i\pi$ the velocity field and gradients can be written as

$$w'(t) \sim U_0\left(-\frac{1}{2}(t-i\pi) + \frac{1}{24}(t-i\pi)^3 - \frac{1}{240}(t-i\pi)^5\right) + O\left((t-i\pi)^7\right) \tag{2.24}$$

$$w''(t) \sim \frac{U_0\pi}{h}\left(\frac{1}{4} - \frac{1}{64}(t-i\pi)^4 + \frac{1}{192}(t-i\pi)^6\right) + O\left((t-i\pi)^8\right) \tag{2.25}$$

Combining with the local inversion (2.22), allows one to form a power series for the velocity and its gradient in terms of z explicitly

$$w'(z) = \frac{U_0 \pi z}{4h} - \frac{U_0 \pi^5 z^5}{1520 h^5} + O(z^9), \quad w''(z) = \frac{U_0 \pi}{4h} - \frac{U_0 \pi^5 z^4}{304 h^5} + O(z^8). \tag{2.26}$$

It is important to note that the constitutive equation (2.21) is now hyperbolic and can be solve along any given streamline. The choice of streamline can considerably simplify the problem and allow one concentrate at a point of physical interest. As cross-slots are not focused conventionally on shearing effects, we will consider the Oldroyd B fluid along the centre plane $x_3 = \frac{d}{2}$, where, by the x_3 symmetry, we can deduce that $T^{(0)}_{13} = T^{(0)}_{23} = T^{(0)}_{33} = 0$. Similarly as cross-slot devices primarily focus on the stagnation point we can further simplify the model by solving only along the streamline along the centre of the plane $z = \frac{d}{2}$, where again by symmetry $T^{(0)}_{12} = 0$. We are thus left with the simple decoupled ODE's for $T^{(0)}_{11}, T^{(0)}_{22}$

$$w' \frac{dT^{(0)}_{11}}{dz} - \left(2w'' - \frac{1}{\lambda}\right) T^{(0)}_{11} - \frac{2}{\lambda} w'' = 0, \quad w' \frac{dT^{(0)}_{22}}{dz} + \left(2w'' + \frac{1}{\lambda}\right) T^{(0)}_{22} + \frac{2}{\lambda} w'' = 0, \tag{2.27}$$

One can integrate the equations numerically however we continue to seek an approximate analytic result. Let us assume regularity in the $T^{(0)}_{11}, T^{(0)}_{22}$ i.e. that the stress can be expressed locally around the stagnation point like $T^{(0)}_{11} \sim a_0 + a_1 z + \ldots, T^{(0)}_{22} \sim b_0 + b_1 z + b_2 z^2$. Using the expression (2.26) with (2.27) and requiring a consistent balance $O(1)$ leads to $a_0 = \frac{2\pi U_0}{2h - \pi\lambda U_0}$, $b_0 = -\frac{2\pi U_0}{\pi\lambda U_0 + \lambda^{-1}}$. We can continue to find, to higher orders in z,

$$T^{(0)}_{11} = \frac{\pi U_0}{2h - \pi U_0 \lambda} + \frac{\pi^5 U_0 z^4}{128\left(\pi^2 U_0^2 \lambda^2 - 4h^2\right) h^3} + \ldots \tag{2.28}$$

$$T^{(0)}_{22} = -\frac{\pi U_0}{\pi U_0 \lambda + 2h} + \frac{\pi^5 U_0 z^4}{128\,(3\pi U_0 \lambda + 2h)\,(\pi U_0 \lambda + 2h)\, h^3} + \ldots \tag{2.29}$$

Although the above expansion is only valid locally around the stagnation point one can extend the series using continuous fraction approximation, but what form should the approximation take? From (2.15) we can see that $t \sim z$ and considering the Newtonian case, were $\boldsymbol{T} \propto w''$ which has exponential decay as $z \to \infty$. One cannot expect a polynomial fraction to decay as quickly as this, however we could produce quick polynomial decay as $z \to \infty$. We also expect the stress to be monotonically decreasing in z. We thus search for a Padé approximate in the form P^1_8. After

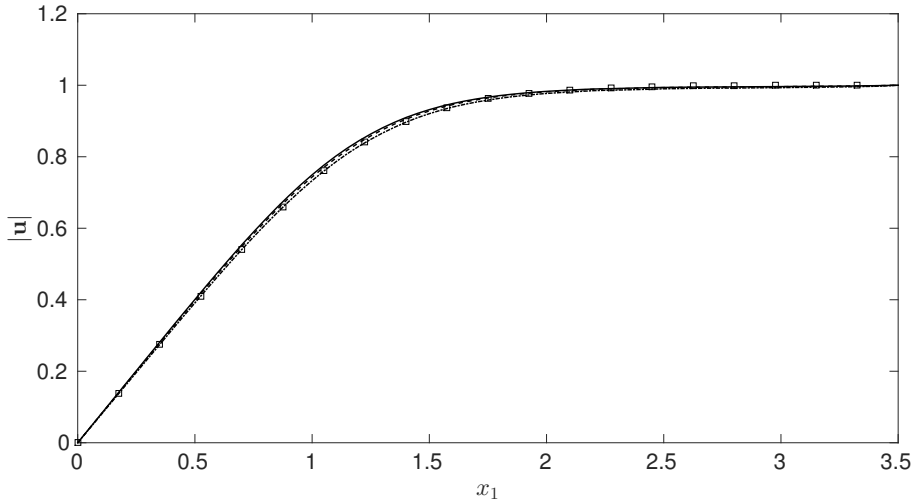

Fig. 2.7 The magnitude of the velocity along the centre line. The numerical result for $\mu_p = 0.5, \delta = 0.1$ for $\lambda = 0, 0.1$ and 0.2 are given by the solid and dashed and dot dashed lines respectively black. The Padé conformal mapping velocity filed is given by square markers.

rescaling by μ_p we find that the approximate simplifies to

$$T_{11} = \frac{A_0}{A_1 z^8 + A_2 z^4 + A_3}, \quad T_{22} = \frac{B_0}{B_1 z^8 + B_2 z^4 + B_3} \tag{2.30}$$

where the parameters for T_{11} are given by

$$A_0 = 144179200\mu_p \pi (3\pi\lambda + 2)(\pi\lambda + 2)^2, \quad A_1 = \pi^8 (\pi\lambda - 2)\left(6209\pi^2\lambda^2 - 6844\pi\lambda - 3324\right),$$
$$A_2 = -1126400\pi^4 (\pi\lambda - 2)(3\pi\lambda + 2)(\pi\lambda + 2), \quad A_3 = -14419200(\pi\lambda - 2)(3\pi\lambda + 2)(\pi\lambda + 2)^2.$$

Similarly for T_{22},

$$B_0 = 144179200\mu_p \pi (5\pi\lambda + 2)(3\pi\lambda + 2), \quad B_1 = \pi^8 (\pi\lambda + 2)\left(13641\pi^2\lambda^2 - 13492\pi\lambda - 3324\right),$$
$$B_2 = -1126400\pi^4 (5\pi\lambda + 2)(3\pi\lambda + 2)(\pi\lambda + 2), \quad B_3 = -144179200(\pi\lambda + 2)(3\pi\lambda + 2)^2.$$

Although one is mainly interested in the predicted stress, one should note that the Padé approximations for the stress can be used to explicit approximate the velocity field, instead of using the more cumbersome implicit description in equation (2.15). The velocity gradient can readily be obtained from considering the Newtonian case of

$$w''(z) \approx P_8^1 = f(z) = \frac{81920 U_0 \pi / h}{\left(\frac{\pi z}{h}\right)^8 + 1280\left(\frac{\pi z}{h}\right)^4 + 327680}. \tag{2.31}$$

We can integrate the above to give the expression for the velocity field

$$w'(z) = 81920U_0\left\{-\frac{1}{4(r_1-r_2)r_1^{\frac{3}{4}}}\ln\left(\frac{\pi z + r_1^{\frac{1}{4}}}{r_1^{\frac{1}{4}}-\pi z}\right)+\frac{1}{4(r_1-r_2)r_2^{\frac{3}{4}}}\ln\left(\frac{\pi z + r_2^{\frac{1}{4}}}{r_2^{\frac{1}{4}}-\pi z}\right)+\right. \tag{2.32}$$
$$\left.-\frac{1}{2(r_1-r_2)r_1^{\frac{3}{4}}}\tan^{-1}\left(\frac{\pi z}{r_1^{\frac{1}{4}}}\right)+\frac{1}{2(r_1-r_2)r_2^{\frac{3}{4}}}\tan^{-1}\left(\frac{\pi z}{r_2^{\frac{1}{4}}}\right)\right\},$$

here r_1, r_2 are the roots of the quadratic, in z^4, from the denominator (2.31), $r_1 = -640 + 128\sqrt{5}, r_1 = -640 - 128\sqrt{5}$. Although the velocity gradients decay exponentially for large z, whereas the approximation (2.31) predicts polynomial decay like z^{-8}. As the gradients in this regime are small the effect on the viscoelastic stress should be negligible. We can also investigate how well the weak-coupling assumption holds. The Padé approximation of the velocity field is compared to the finite element result in Fig.2.7 for $\lambda = 0, 0.1$ and 0.2. For increasing λ there is a slight reduction in the velocity gradient, as streamlines are deflected from the stagnation point due to hoop-stresses. Though this effect is small, even for $\mu_1 = 0.5$. The Padé flow field does slightly underpredict the velocity field near the stagnation point, however generally gives a good a prediction of the velocity field having only 0.2% error for large z.

2.4.1 Inversion of Normal Stress

As the approximate model captures the behaviour of full numerical model for the components T_{11}, T_{22}. However these components cannot be deduced directly from experiments. The first normal stress difference N_1 however is commonly found in birefringence experiments, which is given by, to $O(\mu_p)$,

$$N_1 = 2\mu_s\left(u_x^{(0)} - v_y^{(0)}\right) + \mu_p\left(T_{11}^{(0)} - T_{22}^{(0)}\right) + 2\mu_s\mu_p\left(u_x^{(1)} - v_y^{(1)}\right).$$

Where it is helpful to note, the elastic stress components at the stagnation point can be written as

$$T_{11}^{(0)} = \frac{\pi U_0}{2h - \pi\lambda U_0}, \quad T_{22}^{(0)} = -\frac{\pi U_0}{\pi\lambda U_0 + 2h}. \tag{2.33}$$

We can see that the normal stress difference depends on the corrected velocity $\mathbf{u}^{(1)}$ through the Newtonian stress, however for the sake of closure we will assume that contribution from elastic stress is larger than the contribution from Newtonian stress modified by the corrected velocity field.

Viscoelastic parameters are often found from fitting PDE simulations to the experimental data. As we now have an explicit expression for the normal stress difference along the centre line of the channel, we can invert to give the fluid parameters (μ_p, λ) in terms of measurables quantities. The question is what physical measurables to map the parameters to? The first normal stress difference at the stagnation point (N_{stag}) is readily observable and sensitive to the fluid parameters. For the second measurable quantity we will use the variance of the first normal stress difference along the centre line (V_{ar}). Although the integral can be evaluated analytically by use of the residue theorem the result is extremely transcendental, we thus expand the integral for small λ and recover the expression

$$V_{ar} = 2\int_0^\infty x^2 N_1 dx \approx \frac{U_0}{h}\left(6.43\mu_s + 10.76\frac{U_0\mu_p\lambda}{h}\right). \tag{2.34}$$

Similarly the normal stress at the stagnation point is given by, for small λ,

$$N_1 = \frac{2\pi U_0\left(\mu_s + \mu_p\right)}{h} + \frac{\mu_p \pi^3 U_0^3 \lambda^2}{2h^3}.$$

We can solve for small λ

$$\lambda = \frac{h}{10.76U_0\left(\mu_s + \frac{hN_1}{2\pi U_0}\right)}\left(\frac{hV_{ar}}{U_0} - 6.43\mu_s\right) \tag{2.35}$$

which can then be used for the expression for the polymer viscosity

$$\mu_p = \left(-\mu_s + \frac{hN_1}{2\pi U_0}\right)\left(1 - \frac{\pi^2 U^2 \lambda^2}{2h^2}\right). \tag{2.36}$$

2.4.2 Second Order Fluid

Thus far we have used a weak-coupling limit to solve our system approximately. Alternatively one could have used the second order fluid model to calculate the stresses, although this doesn't satisfy momentum conservation. In-spite of this the solution for a SOF is purely algebraic and readily solved without approximation. Use of the relation $w'(z) = u_1 - iu_2$, along with the Cauchy-Riemann equations and the property that w and all of its derivatives are harmonic functions, allows one to construct all of the partial derivatives of the velocity field by considering, in turn, the real $(\Re)$ and imaginary $(\Im)$ parts of (2.23). Upon doing so, one can obtain equations (2.37) and (2.38) for the normal stress components of the extra viscoelastic stress:

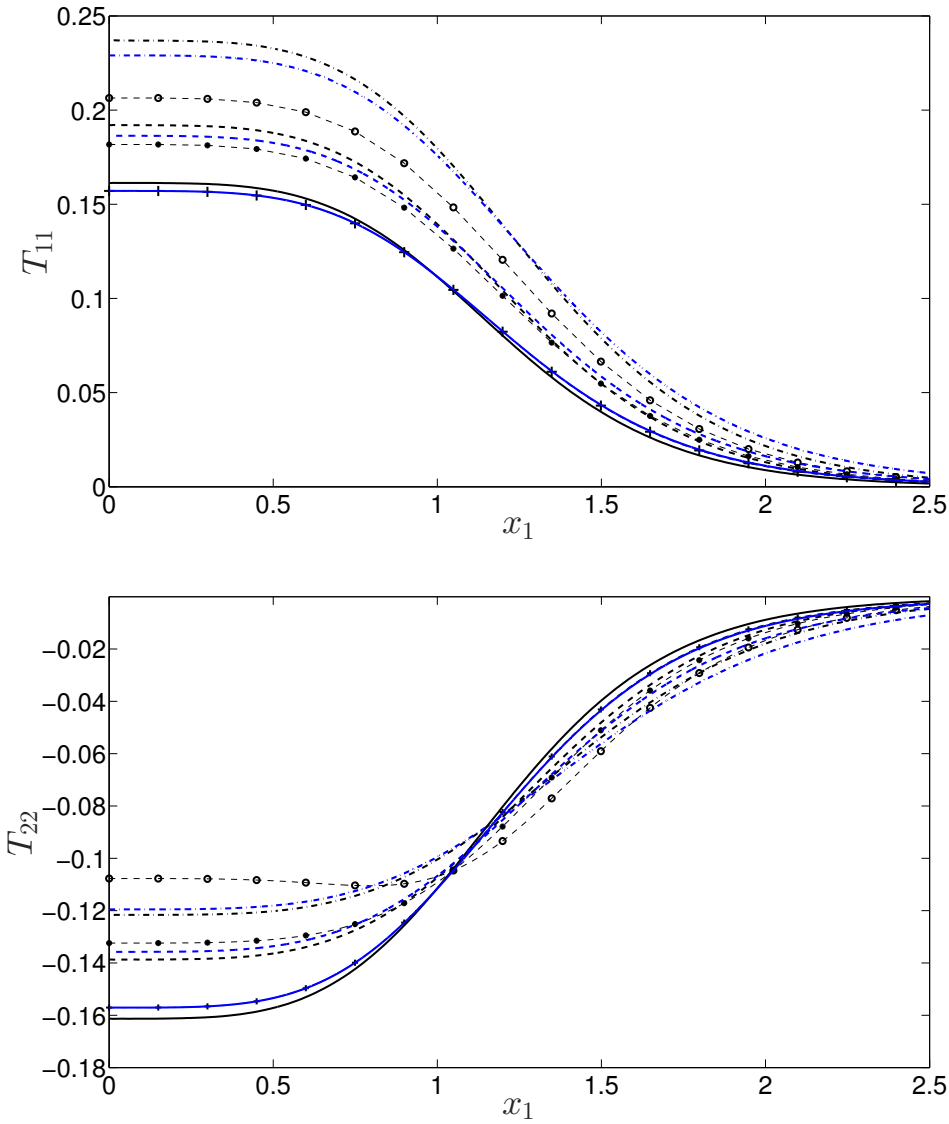

Fig. 2.8 Diagonal viscoelastic stress components with viscous ratio $\mu = 0.1$ and $\delta = 0.1$, (a) T_{11}, (b) T_{22}. The crossed, dotted and circular marked lines denote the analytic solution for $W_e = 0, 0.1$ and 0.2, whereas the solid, dashed and dash-dotted lines give the results for the FEM Oldroyd B model for $W_e = 0, 0.1$ and 0.2.

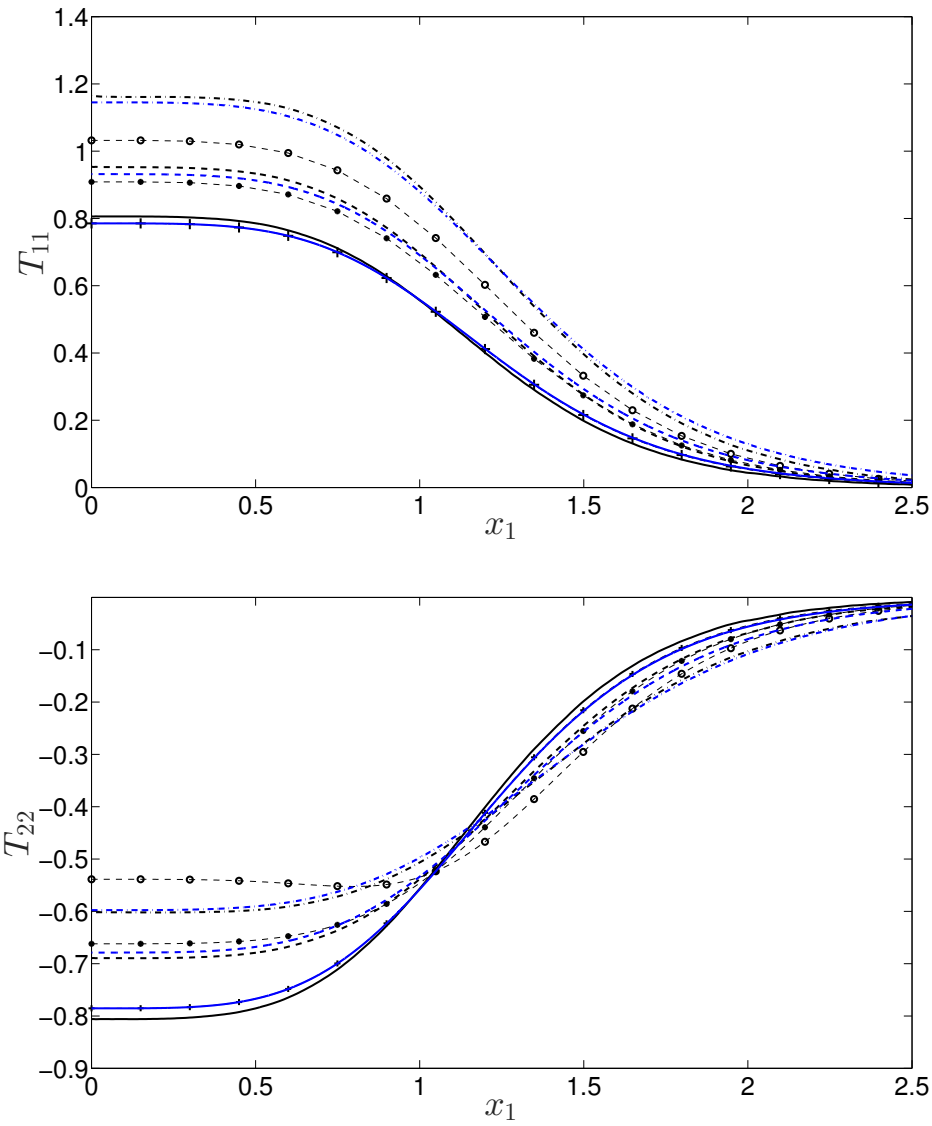

Fig. 2.9 Diagonal viscoelastic stress components with viscous ratio $\mu = 0.5$ and $\delta = 0.1$, (a) T_{11}, (b) T_{22}. The lines marked with crosses, dots and circles denote the SOF solution for $W_e = 0, 0.1$ and 0.2, respectively, whereas the solid, dashed and dash-dotted lines give the results for the FEM Oldroyd B model for $W_e = 0, 0.1$ and 0.2. The weak coupling Pad

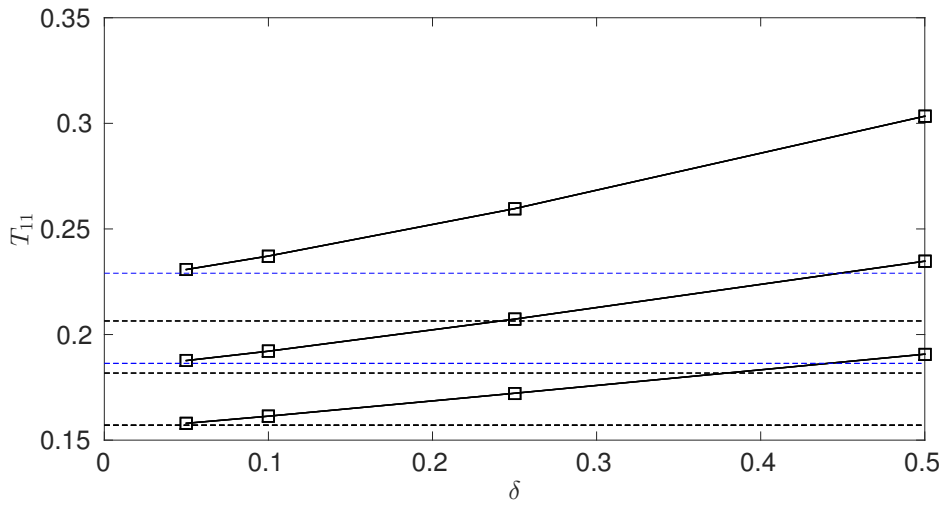

Fig. 2.10 T_{11} component of the extra stress at the stagnation point for $W_e = 0$ (bottom line), $W_e = 0.1$, $W_e = 0.2$ (top line) with $\mu = 0.1$ for varying δ. The Hele-Shaw ($\delta = 0$) solutions are given by the horizontal dashed lines where blue and black lines show the weak-coupling and second order fluid approximations respectively.

$$
\begin{aligned}
T_{11} =& 2\mu\Re\{w''(t)\} - 2W_e\mu\left(\Re\{w'(t)\}\Re\{w'''(z)\} + \Im\{w'(t)\}\Im\{w'''(t)\}\right) \\
&+ 4W_e\mu\left(\Re\{w''(t)\}^2 + \Im\{w''(t)\}^2\right), \qquad (2.37) \\
T_{22} =& -2\mu\Re\{w''(t)\} + 2W_e\mu\left(\Re\{w'(t)\}\Re\{w'''(t)\} + \Im\{w'(t)\}\Im\{w'''(t)\}\right) \\
&+ 4W_e\mu\left(\Re\{w''(t)\}^2 + \Im\{w''(t)\}^2\right). \qquad (2.38)
\end{aligned}
$$

We find that the discrepancy between the Hele-Shaw elongation rate and the FEM result at the stagnation point is of the order of 2% for an aspect ratio of $\delta = 0.1$. In Fig. 2.8 and Fig. 2.9, we can see that the behavior predicted by the complex potential theory is similar to that predicted by the finite element model however the weak-coupling approach does significantly better. The small error in the velocity gradient can easily be attributed to non-zero δ. The effects of changing the aspect ratio at the stagnation point are shown in Fig.2.10. This shows that in the limit of small δ, the FEM solution for $W_e = 0$ tends to the analytic solution. However, this is not true for non-zero W_e. This error is consistent with the use of a second order fluid model to approximate the Oldroyd B model. Even with an aspect ratio of $\delta = 0.05$ we find that the error is only 3% for $W_e = 0.1$. Unfortunately, however, the first normal stress difference is of order ${W_e}^2$ and thus cannot be predicted by the second order fluid but can be in the weak coupling approximation.

2.5 Unequal inlet and outlet channel widths

We now consider the geometry of the cross-slot as before, but relax the condition that the widths of the inlet channel (h) and outlet channel (l) are equal. As the cross-slot geometry is commonly used in experimental studies due to the region of pure elongational flow, we will investigate the effect that changing the aspect ratio will have on the elongation rates and normal stresses. We define the ratio of outlet to inlet channel widths as $\alpha = h/l$. Then, by mass conservation it follows that $\alpha U_0 = U_{\text{out}}$, where U_0 and U_{out} are the inflow and outflow velocities respectively. Using the source term as defined in equation (2.9), we can determine the boundary conditions at the outlet and inlet in the form:

$$\frac{dw}{dz} \sim -U_0\alpha \quad \text{as} \quad \eta \to \pm\infty, \tag{2.39}$$

$$\frac{dw}{dz} \sim U_0 i \quad \text{as} \quad \eta \to 0. \tag{2.40}$$

This enables us to determine the constants in equation (2.6) to be $K = -\frac{h}{\alpha\pi}, b = \alpha^2, a = 1$. This leads to

$$\frac{dw}{dz} = -U_0\alpha\sqrt{\frac{\eta+1}{\eta-\alpha^2}}, \tag{2.41}$$

$$\frac{dz}{d\eta} = -\frac{h}{\alpha\pi}\eta^{-1}(\eta+1)^{-\frac{1}{2}}(\eta-\alpha^2)^{\frac{1}{2}}. \tag{2.42}$$

Equation (2.42) can be solved to give

$$\begin{aligned} z(\eta) = &-\frac{h}{\alpha\pi}\ln\left(\frac{1}{2}(1-\alpha^2)+\eta+\sqrt{(\eta+1)}\sqrt{(\eta-\alpha^2)}\right) \\ &+\frac{hi}{2\pi}\ln\left(\left(-\alpha^2 i+\frac{1}{2}\left(1-\alpha^2\right)i\eta+\sqrt{\eta+1}\sqrt{\eta-\alpha^2}\right)^2\right)-\frac{hi}{2\pi}\ln(\eta^2) \\ &-\frac{h}{\alpha\pi}(1-\alpha i)\ln\left(\alpha^2+1\right), \end{aligned} \tag{2.43}$$

where the constant is again assigned such that $z = 0$ at $\eta = -1$. Using a Newton-Raphson scheme to find $\eta(z)$, we can plot the streamlines and the velocity profiles along the center line (Fig. 2.11). The velocity gradients can be obtained from the equation

$$\frac{d^2w}{dz^2} = -\frac{U_0\alpha^2\pi\eta\left(\alpha^2+1\right)}{2h\left(\eta-\alpha^2\right)^2}. \tag{2.44}$$

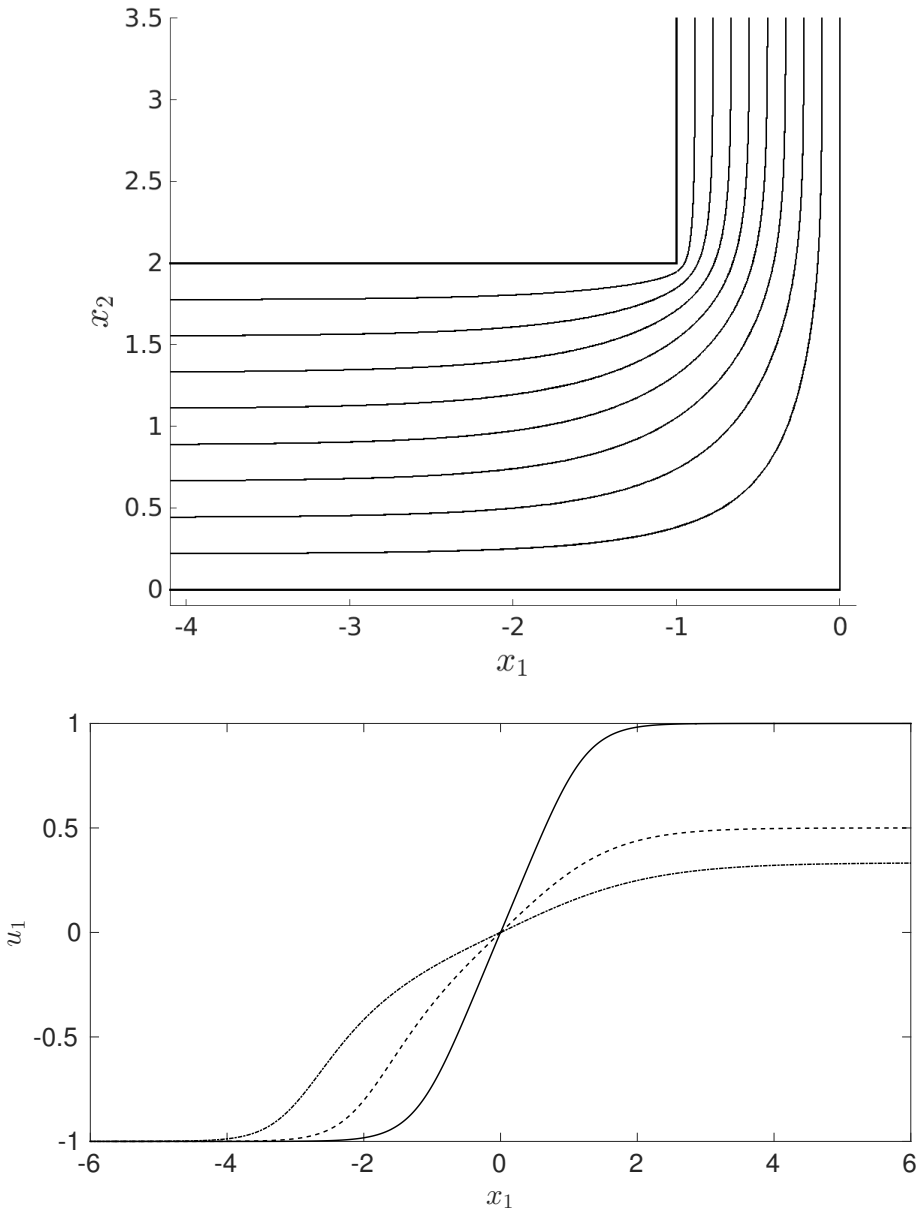

Fig. 2.11 (a) The streamlines for $\alpha = \frac{1}{2}$. (b) The velocity magnitude along the center line for $\alpha = 1, \frac{1}{2}, \frac{1}{3}$ which are denoted by the solid, dashed and dot-dashed lines respectively. The positive x values have the convention of being downstream of the stagnation point whilst the negative x values are upstream from the stagnation point.

Evaluating the above equation at the stagnation point gives a simple expression for the elongation rate for a given aspect ratio,

$$\dot{\varepsilon}_{stag} = \frac{U_0 \pi \alpha^2}{2h(1+\alpha^2)}. \tag{2.45}$$

We can thus expect the elongation rate to behave as α^2 for small α. We also obtain the result that the maximum elongation rate achievable at the stagnation point for potential flow is $\frac{U_0\pi}{2h}$. One might have expected the maximum elongation to become singular as the outlet channel is contracted, as the flow is being forced into an infinitely small contraction. This rather surprising result can be explained by observing that although the elongation rate does become singular, the maximum value does not occur at the stagnation point. For $\alpha > 1$ the maximum value occurs downstream of the stagnation point and for $\alpha < 1$ the maximum occurs upstream. From equation (2.44) we can see that the maximum occurs when $\eta = -\alpha^2$. When $\alpha = 1$, by the choice of mapping in (2.5), the location of maximum elongation rate coincides with the stagnation point. We can thus find the maximum elongation rate by substituting $\eta = -\alpha^2$ into equation (2.44) to give

$$\dot{\varepsilon}_{max} = \frac{U_0 \pi \left(\alpha^2 + 1\right)}{8h}, \tag{2.46}$$

where, in this case, the elongation rate does become singular as $\alpha \to \infty$ as expected.

For the asymmetric system we choose not to use the Weak-coupling approach. Although in the previous section it was shown to be superior to the SOF approach, the need for the Padé to capture the asymmetry leads to rather large expressions for the stress T_{11}, T_{12}. We introduce the effect of viscoelasticity by using the SOF approach, by using equations (2.37) and (2.38) to model the normal stress. The results are given in Fig.2.12. The elongation rate can be deduced from the Newtonian case, and it can be seen that the maximum elongation occurs upstream for $\alpha < 1$ and downstream for $\alpha > 1$. One can also see that viscoelasticity has a much smaller effect for $\alpha < 1$ owing to the much smaller velocity gradients. Downstream of the stagnation point these effects are negligible. Using the exact elongation rate gives normal stress components

$$T_{11} = \frac{U_0 \mu \pi \alpha^2}{(1+\alpha^2)h} + \frac{W_e \mu U_0^2 \pi^2 \alpha^4}{(1+\alpha^2)h^2}, \quad T_{22} = -\frac{U_0 \mu \pi \alpha^2}{(1+\alpha^2)h} + \frac{W_e \mu U_0^2 \pi^2 \alpha^4}{(1+\alpha^2)h^2}.$$

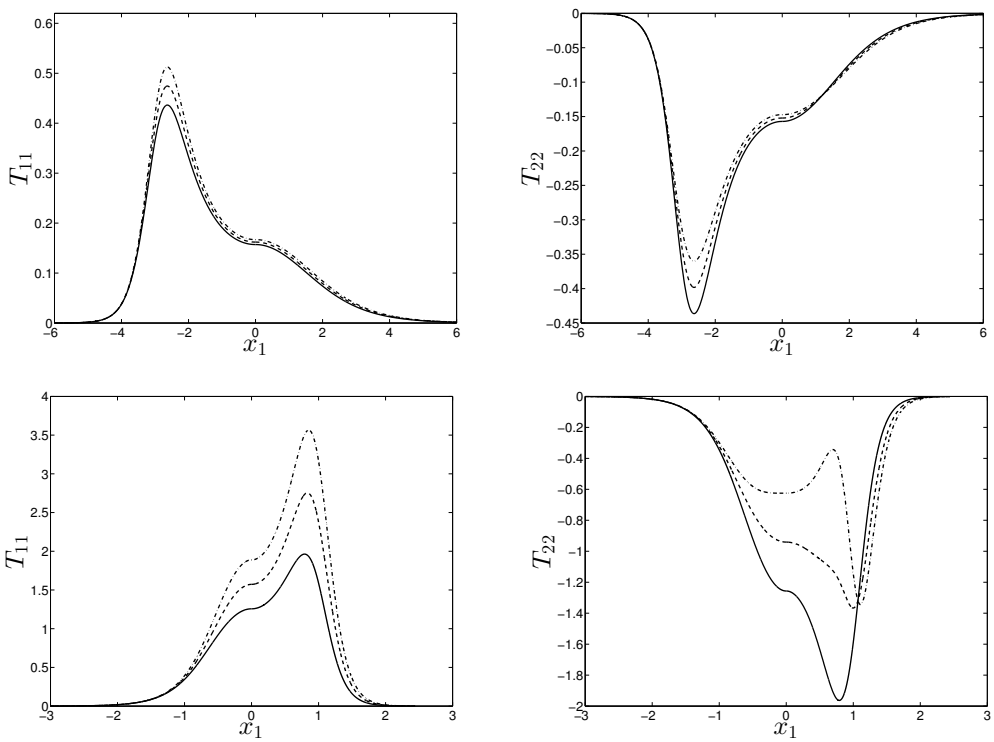

Fig. 2.12 The normal stress components (a) T_{11}, (b) T_{22} for $\alpha = \frac{1}{3}$, (c) T_{11}, (d) T_{22} for $\alpha = 2$. The polymer viscosity is taken to be $\mu = \frac{1}{2}$ and the results for $W_e = 0, 0.1$ and 0.2 are given by the solid, dashed and dot-dashed lines respectively.

Having derived an analytical velocity field we now consider whether or not greater uniformity of the elongation rate along the channel can be achieved by simply changing the aspect ratio. This is of key importance for extensional flow studies. Let us suppose that we wish to achieve a fixed elongation rate $\dot{\varepsilon}_0$ at the stagnation point, which, by equation (2.45), forces the condition $\frac{U_0\pi}{2h} = \frac{1+\alpha^2}{\alpha^2}\dot{\varepsilon}_0$. We now scale z by the inlet width h/π and w'' by $\dot{\varepsilon}_0$. The total curvature of the velocity field, S, is used as a metric for the uniformity of the elongation rate

$$S = \int_C |\kappa(z)| dz = \int_{-\infty}^{0} \left| \frac{w'''}{(1+w''^2)^{\frac{3}{2}}} \right| \frac{dz}{d\eta} d\eta, \tag{2.47}$$

where C is a contour traversing the center line which is readily converted into a real integral by using the mapping (2.5). Evaluation of the above integral leads to the expression

$$S = \frac{2\left(1+\alpha^2\right)^2}{\sqrt{\alpha^8 + 4\alpha^6 + 22\alpha^4 + \alpha^2 + 1}}. \tag{2.48}$$

S has a minimum value when $\alpha = 1$. Thus greater uniformity cannot be achieved by simply changing inlet-outlet aspect ratios.

2.6 Conclusions

We have derived the Hele Shaw flow solution for a two-dimensional cross-slot device. The principle result of the chapter is that the viscoelastic normal stresses derived using inviscid flow theory can be used to predict behavior that is shown to be quantitatively similar to that computed from a fully coupled numerical model. The theory requires the assumption of a second order fluid which is an approximation to the more complex Oldroyd B model. The diagonal stress components were derived and shown to be qualitatively similar to those predicted by numerical simulations, though the pressure at the stagnation point is systematically over-predicted. The results were then generalized to give an explicit solution for the normal stresses at the stagnation point for inlet and outlet channels of different widths. It was also proven that for a potential flow solution, changing the aspect ratio decreases the uniformity of the elongation rate, which is of experimental importance.

Chapter 3

A Toy Problem for Non-Newtonian Fluids: the Snail Ball.

Abstract

The theoretical dynamics of a simple toy, the snail ball, are investigated. The snail ball comprises a solid sphere contained within a larger hollow sphere separated by, conventionally, a highly viscous fluid. In this chapter we remove the constraint that the fluid be Newtonian. Specifically, we consider the two non-Newtonian effects: viscoelasticity (using a second order fluid model) and shear-dependent viscosity (using a power-law model). We find that for both models the “run-away" solution, where the system accelerates under the influence of gravity, still exists. However, in the case of a viscoelastic fluid, the rocking solution is found to be unstable but a new type of solution was discovered, which predicts that the toy descends down an inclined plane at a constant velocity. For the shear-dependent viscosity model the dynamical behavior of the snail ball was found to be similar to the Newtonian case, although for shear thinning (thickening) fluids, the rocking motion was less (more) damped than the Newtonian case. This leads to the prediction that a snail ball filled with a shear thinning fluid travels more slowly than one filled with a Newtonian fluid. Conversely, a snail ball containing a shear-thickening ball will travel more quickly than its Newtonian counterpart.

3.1 Introduction

A snail ball comprises a hollow sphere inside which is a solid sphere surrounded by a Newtonian fluid. When the device is released down an inclined plane rather surprising behavior is observed: the ball slowly descends and sporadically rocks to and fro. The dynamics of a snail ball fluid were first discussed in Balmforth et al. [9] and Vener [139]. Experimental results were also presented. The physical dynamics of the snail ball are well explained by Wagon [141] using purely geometrical arguments involving cycloids and the principle of minimum potential energy.

In this chapter we consider what happens to the behavior of such a device if the inner ball were to be immersed in (i) a viscoelastic fluid and (ii) a shear-dependent fluid. One would expect that in both scenarios the motion of the inner sphere would be quite different from that predicted by the Newtonian case. To make analytical

progress, both scenarios are considered under the assumption of a lubrication (small gap) approximation. Although not the focus of this study, dynamic mechanical systems such as a rolling ball viscometer [15] have been used to investigate viscometric properties and one could consider whether the snail ball system has the potential to be used for such a purpose, although the aim of this chapter is not focused on the practicalities of such a device. There is also a strong relationship between the dynamics of the snail ball and journal bearing problems. Non-Newtonian effects in journal bearing problems have been widely considered, including the investigation of shear dependent viscous effects [122]. Similarly, results can be found for other constitutive relations, for example, an analogous viscoplastic study is given in Pinkus [105]. As pointed out by Balmforth et al, when the inclined plane is parallel to the horizontal, the inner ball slowly sinks inside the outer ball with no rocking motion. We will refer to this case as the purely sedimenting solution. We will discuss this class of solution later.

We hope to capture the effects of a viscoelastic fluid by using a second order fluid (SOF) model. Though one could consider a SOF model as a constitutive relation in its own right, it is more widely regarded as an approximation of a more complex viscoelastic relation with predominantly viscous behavior with weak viscoelastic effects. However, issues remain regarding the model's physical validity, see for instance [40, 48]. In the SOF model for a static journal bearing system, for large eccentricity viscoelastic effects are found to dominate over viscous effects, which is indicative of the SOF model failing. Despite this, a numerical study of a journal bearing system for an Oldroyd B fluid by [115] found that the SOF model does perform reasonably well. A numerical study with the more complex Phan-Thien-Tanner model was given by [45] and found that the introduction of a slip parameter reduces the load bearing capacity of the fluid, which would have ramifications if introduced into the snail ball system. In spite of its shortcomings, the SOF model gains simplicity as the leading order dynamics can be expressed as a set of non-linear coupled ODEs.

We have chosen to model a shear-dependent viscosity fluid using a power-law constitutive relation. Unlike the Newtonian and SOF cases, due to the form of the non-linearity, the governing equations can not be presented so succinctly as a series of ODEs. This is to be expected as in journal bearing problems for the purely sedimentation case, citation, and for the non-squeezing case where the journal can rotate but no radial movement is allowed, the forces and torques acting on the system can only be expressed in an integral form.

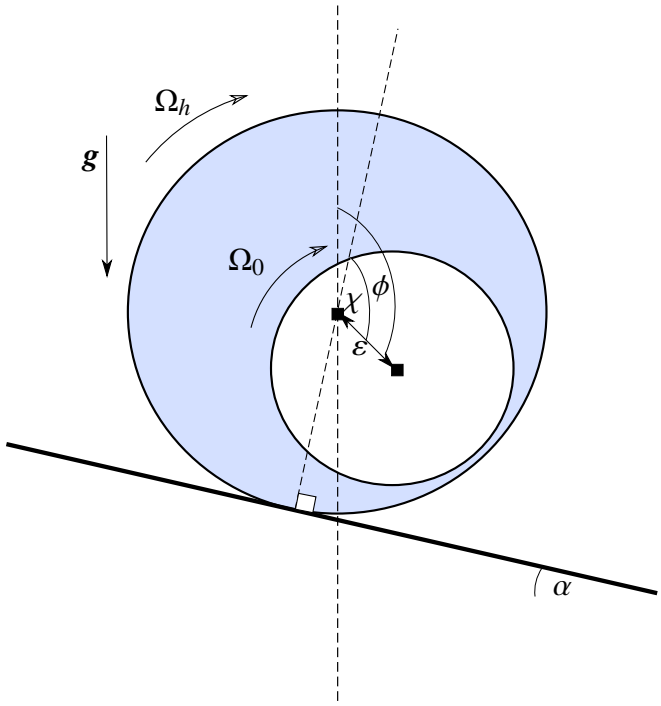

Fig. 3.1 Sketch of the snail ball system.

In spite of the unwieldiness of the lubricated power-law model several approximations can be utilized. One such method given by Safar [119] assumes that the flow can be approximated by the superposition of the power-law Couette flow and Poiseuille flow, though such a velocity profile does not satisfy the momentum equation. Similar approaches have been performed by Hwang [63] and Bird [15] though the latter used a variational argument to justify the result. We will later employ the approximation by Dien and Eldrod (DE) [33] to model the snail ball system. This choice was in part due to the fact that the DE approximation was derived from a more formal approach. In a previous study Ross et al. [118] found that DE theory was superior to Hwang's approximation for modeling a blade coating problem. We found that significant analytical progress could be made using the DE approximation under the assumption of large eccentricity. Analytical results are compared against numerical simulations. It is also of note that the power-law model can be applied to the purely sedimenting problem for large eccentricity without the need to call upon the DE approximation. A comparison is made between this problem and the DE snail ball problem.

3.1.1 Discussion of geometry

The set up of the geometry in our system is based upon that used by Balmforth et al. [9], which allows our results to be readily compared with the prior calculated Newtonian solution. The snail ball is again taken to be a “snail cylinder", where both the inner and outer balls are represented by an infinitely long inner cylinder. Such an approximation renders the problem to be two-dimensional. The system then reduces to the problem of solving the dynamics of an outer cylinder of radius b, which is infinitely thin, and an inner cylinder of radius a, with a solid core. Thus the gap length scale is $\delta = b - a$. Throughout the rest of this study δ is assumed to be small compared to the circumference, i.e. $\delta \ll a$, to justify the lubrication approximation. The position of the system at any point in time can be determined by finding the radial displacement between the center of masses, $\varepsilon(t)$, and the angle, $\chi(t)$, between the normal to the slope and the line connecting the center of mass of the inner and outer cylinders. We now let $\hat{\boldsymbol{\varepsilon}}$ be a unit vector pointing from the COM of the outer cylinder to the COM of the inner cylinder, and $\hat{\boldsymbol{\chi}}$ to be the right hand orthogonal unit vector to $\hat{\boldsymbol{\varepsilon}}$. These are given by

$$\hat{\boldsymbol{\varepsilon}} = \sin\chi \boldsymbol{i} + \cos\chi \boldsymbol{j}, \quad \hat{\boldsymbol{\chi}} = -\cos\chi \boldsymbol{i} + \sin\chi \boldsymbol{j}. \tag{3.1}$$

To describe the kinetics of the system completely, we further require the angular speed of the outer cylinder, Ω_h, and the inner cylinder angular speed, Ω_0.

To complete the description of the dynamics we will briefly describe the masses used in the derivation of the theory. Firstly, the fluid in the gap between the cylinders is assumed to have a constant density ρ. The other fluid parameters are defined according to which constitutive model is chosen. In the full derivation presented by Balmforth et al., several mass quantities appeared which we now briefly list. Firstly, let the mass of the inner cylinder be m_0, the mass of the outer cylinder be m_h, and the mass of the lubricating fluid be m_f. In order to express momentum conservation we define the total mass of the system as $M = m_0 + m_h + m_f$. Also, we denote $m_0'' = \pi a^2 \rho$ to be the displaced mass of the fluid and $m_0' = m_0 - m_0''$ to be the effective mass of the inner cylinder. Finally, we let $\mathcal{M} = m_0 + \frac{m_0''}{m_f}$ be the inertial mass of system defined in the reference frame where the centre of mass of the fluid is fixed.

3.2 Part I: viscoelastic system

3.2.1 Derivation of the governing equations

For most viscoelastic fluids the mass, momentum and constitutive equations can generally be written as

$$\nabla \cdot \boldsymbol{\sigma} = \mathbf{0}, \tag{3.2}$$

$$\nabla \cdot \mathbf{u} = 0, \tag{3.3}$$

$$\boldsymbol{\sigma} = -p\boldsymbol{\delta} - \boldsymbol{\tau}, \tag{3.4}$$

For the viscoelastic problem we consider a SOF in which $\boldsymbol{\tau}$ can be solely expressed in terms of the rate of strain tensor, $\dot{\boldsymbol{\gamma}}$. The stress tensor is then given by

$$\boldsymbol{\tau} = -\mu\dot{\boldsymbol{\gamma}}_{ij} + \alpha_1\dot{\boldsymbol{\gamma}}_{ip}\dot{\boldsymbol{\gamma}}_{pj} + 2\alpha_2\overset{\nabla}{\dot{\boldsymbol{\gamma}}}_{ij}, \tag{3.5}$$

where μ is the dynamic viscosity, and α_1 and α_2 are the retardation and relaxation times respectively.

If we assume that the gap between the cylinders is small, the radial derivative will dominate the components of the stress tensor. After keeping the leading order terms along with the mass conservation equation, the stress tensor simplifies to

$$\tau_{11} = -2\mu\frac{1}{a}\frac{\partial u}{\partial \theta} + \alpha_1\left(\frac{\partial u}{\partial r}\right)^2 - 4\alpha_2\left(\frac{\partial u}{\partial r}\right)^2, \tag{3.6a}$$

$$\tau_{22} = 2\mu\frac{1}{a}\frac{\partial u}{\partial \theta} + \alpha_1\left(\frac{\partial u}{\partial r}\right)^2, \tag{3.6b}$$

$$\tau_{12} = -\mu\frac{\partial u}{\partial r} + 2\alpha_2\left[v\frac{\partial^2 u}{\partial r^2} + \frac{1}{a}u\frac{\partial^2 u}{\partial \theta \partial r} + 2\frac{1}{a}\frac{\partial u}{\partial \theta}\frac{\partial u}{\partial r}\right] + 2\alpha_2\frac{\partial^2 u}{\partial r \partial t}. \tag{3.6c}$$

We now present a similar argument to that given by [120], and differentiate (3.4) leading to

$$\frac{1}{a}\frac{\partial \sigma_{22}}{\partial \theta} = \frac{\partial \tau_{12}}{\partial r} - \frac{1}{a}\frac{\partial}{\partial \theta}(\tau_{22} - \tau_{11}), \tag{3.7a}$$

$$\frac{\partial \sigma_{22}}{\partial r} = \frac{1}{a}\frac{\partial \tau_{12}}{\partial \theta}, \tag{3.7b}$$

where the pressure has been removed using the momentum equation (4.2). If we let $y = r - a$ and note that the characteristic length scale for y is δ, we see from (3.7a) that $\sigma_{22} \sim \delta^{-2}$. Hence the left-hand side of (3.7b) scales as δ^{-3}, whereas the right-hand

side scales as δ^{-1}. Thus to leading order σ_{22} is a function of θ only. We thus arrive at the equation,

$$\frac{1}{a}\frac{d\sigma_{22}}{d\theta} = -\mu\frac{\partial^2 u}{\partial y^2} + 2a^{-1}\alpha_2\left(u\frac{\partial^3 u}{\partial\theta\partial y^2} + \frac{\partial u}{\partial\theta}\frac{\partial^2 u}{\partial y^2} - \frac{\partial u}{\partial y}\frac{\partial^2 u}{\partial\theta\partial y}\right) + 2\alpha\frac{\partial^3 u}{\partial^2 y\partial t}, \tag{3.8}$$

which is solely expressed in terms of u. It is convenient to move to a frame of reference where the centers of the cylinders are fixed, which results in $U_0 = \Omega_0 - \dot{\phi}, U_h = \Omega_h - \dot{\phi}$. The velocity field, by the Giesekus Tanner theorem [131], can be shown to have the same form as that for the Newtonian case. Thus we seek a velocity field in the form

$$u = B(\theta)y\left(1 - \frac{y}{h}\right) + U_h\frac{y}{h} + U_0\left(1 - \frac{y}{h}\right), \tag{3.9}$$

where B acts analogous to the pressure in the Newtonian case. This velocity field gives $\frac{\partial^3 u}{\partial y^3} = 0$. Using this one can readily see from differentiating (3.8) with respect to y that σ_{22} is independent of y. If we recast the mass conservation equation (3.3) in integral form we have

$$\frac{1}{a}\frac{\partial}{\partial\theta}\left\{\int_0^h u dy\right\} = -h_t = \dot{\varepsilon}\cos\theta. \tag{3.10}$$

Here we use the subscript t to denote partial differentiation with respect to t, and $\cdot$ to denote the total derivative. We can integrate the above and use (3.9) to find

$$B(\theta) = 6ah^{-2}\dot{\varepsilon}\sin\theta - 3\bar{U}h^{-1} + \frac{\bar{U}C}{h^2}, \tag{3.11}$$

where $\bar{U} = U_h - U_0$ and C is a constant to be determined. Equations (3.8), (3.9) and (3.11) can be combined to give

$$\begin{aligned}\frac{d\sigma_{22}}{d\theta} &= 2ah^{-2}\mu\left(6ah^{-1}\dot{\varepsilon}\sin\theta - 3\bar{U} + \bar{U}Ch^{-1}\right) - \alpha_2\bar{U}^2C^2\frac{d}{d\theta}h^{-4} \\ &-12a\alpha_2\bar{U}\dot{\varepsilon}C\frac{d}{d\theta}\left(h^{-4}\sin\theta\right) + 4\alpha_2\bar{U}^2C\frac{d}{d\theta}h^{-3} - 36\alpha_2a^2\dot{\varepsilon}^2\frac{d}{d\theta}\left(h^{-4}\sin^2\theta\right) \\ &+24\alpha_2a\dot{\varepsilon}\bar{U}\frac{d}{d\theta}\left(h^{-3}\sin\theta\right) - 4\alpha_2\left(U_0^2 + U_0U_h + U_h^2\right)\frac{d}{d\theta}h^{-2} \\ &-4a\alpha_2\left\{h^{-2}\left(6ah^{-1}\dot{\varepsilon}\sin\theta - 3\bar{U} + \bar{U}Ch^{-1}\right)\right\}_t.\end{aligned} \tag{3.12}$$

The constant C can now be determined by the periodic constraint $\sigma_{22}(2\pi) = \sigma_{22}(0)$. When imposing this constraint it is helpful to introduce the scaled variable $\kappa = \delta^{-1}\varepsilon$. The only contributions come from the viscous term $\mu\dot{\gamma}$ and the elastic term $\frac{\partial\dot{\gamma}}{\partial t}$. Let

$\mathscr{F}$ be the integral of the viscous term over 2π. Then the periodic constraint becomes

$$\mu\mathscr{F} - 2\alpha_2 \frac{\partial}{\partial t}\mathscr{F} = 0, \tag{3.13}$$

where $\mathscr{F}$ is given by

$$\begin{aligned}\mathscr{F} &= 2a\mu\bar{U}\left(-3\int_0^{2\pi} h^{-2}d\theta + C\int_0^{2\pi} h^{-3}d\theta + \cancel{6\int_0^{2\pi} \dot{\varepsilon}\sin\theta h^{-3}d\theta}\right) \\ &= 2a\mu\bar{U}\left(-\frac{6\pi}{(1-\kappa^2)^{\frac{3}{2}}} + C\frac{\left(2+\kappa^2\right)\pi}{(1-\kappa^2)^{\frac{5}{2}}}\right),\end{aligned} \tag{3.14}$$

where one can see that the third term is zero as the integrand is odd and periodic over 2π. Equation (3.13) has solution $\mathscr{F} = \mathscr{F}_0 e^{2\alpha_2^{-1}\mu t}$. Thus

$$C = \frac{6\delta\left(1-\kappa^2\right)}{(2+\kappa^2)} + \frac{\left(1-\kappa^2\right)^{\frac{5}{2}}}{\bar{U}\,(2+\kappa^2)}\mathscr{F}_0 e^{\frac{t}{2\alpha}}. \tag{3.15}$$

We assume that $\mathscr{F}_0 = 0$, as otherwise the viscous force term will grow exponentially large in time. Then we can recover the same constraint as Balmforth [9] for the Newtonian system. If one were to fully determine σ_{22} an extra constraint would be needed in order to determine the constant term which arises from integrating (3.12). However, this is not needed as it contributes a purely isotropic term to the problem. There is a certain degree of controversy as to whether this is the correct condition to impose. As noted in Pinkus [105], for the Newtonian case the presence of large regions of negative pressure can arise and are an unphysical consequence of the periodic condition. To remove this problem a Sommerfeld boundary condition can be imposed where the pressure is set to zero over a portion of the domain. This type of condition was also imposed for the static system for a SOF by [59] to avoid large regions of negative normal stress. In our system we have imposed the classical periodic condition, however, it remains an open question as to whether or not changing to the Reynolds boundary condition will effect the dynamics in Newtonian as well as in non-Newtonian cases.

We are now in a position to calculate the forces exerted on the snail ball from the fluid. Let f_ε and f_χ be the forces parallel to the $\hat{\boldsymbol{\varepsilon}}, \hat{\boldsymbol{\chi}}$ directions respectively, then

$$f_\varepsilon = \int_0^{2\pi} \sigma_{11} \cos\theta d\theta = -\int_0^{2\pi} \frac{d\sigma_{11}}{d\theta} \sin\theta d\theta, \tag{3.16}$$
$$f_\chi = \int_0^{2\pi} \sigma_{11} \sin\theta d\theta = \int_0^{2\pi} \frac{d\sigma_{11}}{d\theta} \cos\theta d\theta.$$

Evaluating the integrals in (3.16), using $U_0 = a\Omega_0, U_h = a\Omega_h$ and $\bar{U} = a\bar{\Omega}$, gives

$$f_\varepsilon = -\frac{12a^2\delta^{-2}\dot{\kappa}\mu\pi}{(1-\kappa^2)^{\frac{3}{2}}} + \frac{36\pi a^2\bar{\Omega}^2\alpha_2\kappa^3\delta^{-2}}{(2+\kappa^2)^2(1-\kappa^2)^{\frac{3}{2}}} - \frac{36a^2\pi\alpha_2\dot{\kappa}^2\kappa\delta^{-2}}{(1-\kappa^2)^{\frac{5}{2}}}$$
$$-\frac{8\pi a^2\alpha_2\kappa\delta^{-2}\left(\Omega_0^2+\Omega_0\Omega_h+\Omega_h^2\right)}{(1-\kappa^2)^{\frac{3}{2}}} + 24a^2\delta^{-2}\pi\alpha_2\left\{\frac{\dot{\kappa}}{(1-\kappa^2)^{\frac{3}{2}}}\right\}_t, \tag{3.17}$$

$$f_\chi = \frac{12a^2\pi\delta^{-2}\bar{\Omega}\kappa\mu}{(1-\kappa^2)^{\frac{1}{2}}(2+\kappa^2)} - \frac{24\pi a^2\bar{\Omega}\delta^{-2}\alpha_2\dot{\kappa}}{(\kappa^2+2)(1-\kappa^2)^{\frac{1}{2}}} - 24a^2\pi\delta^{-2}\left\{\frac{\bar{\Omega}\kappa}{(1-\kappa^2)^{\frac{1}{2}}(2+\kappa^2)}\right\}_t. \tag{3.18}$$

Similarly, the torque on the inner cylinder, T_0, can be found from

$$T_0 = \int_0^{2\pi} \sigma_{12}\Big|_{y=0} dx = \frac{4\pi a\mu\delta^{-1}}{(1-\kappa^2)^{\frac{1}{2}}(2+\kappa^2)}\left[\left(1-\kappa^2\right)\Omega_h - \left(1+2\kappa^2\right)\Omega_0\right] + \frac{24\pi a\alpha_2\Omega_0\dot{\kappa}\kappa\delta^{-1}}{(1-\kappa^2)^{\frac{3}{2}}} \tag{3.19}$$
$$+4\pi a\mu\delta^{-1}\left\{\frac{\left[\left(1-\kappa^2\right)\Omega_h - \left(1+2\kappa^2\right)\Omega_0\right]}{(1-\kappa^2)^{\frac{1}{2}}(2+\kappa^2)}\right\}_t.$$

To evaluate the integrals one can use the list of integral identities presented in appendix A. The expressions (3.17), (3.18) and (3.19) reduce to Balmforth's solution in the limit as $\alpha_1 \to 0$ as to be expected. They also reduce to the fixed system described by Davies and Walter [27] when $\dot{\kappa} = 0$.

3.3 Governing equations

The snail ball system can be reduced to a system of non-linear differential equations for $\kappa, \phi, \Omega_0, \Omega_h$. We now use the momentum and angular momentum equations, as derived by Veneer [139]. The equations are defined in a frame of reference where

the center of mass of the fluid is fixed. The equations take the form

$$\mathcal{M}(\varepsilon\ddot{\chi}+2\dot{\varepsilon}\dot{\chi}) = \frac{m_0''}{a\pi\rho}f_\chi + m_0' g\sin\phi - m_0' b\dot{\Omega}_h\cos\chi, \tag{3.20}$$

$$\mathcal{M}\left(\ddot{\varepsilon}-\varepsilon\dot{\chi}^2\right) = \frac{m_0''}{a\pi\rho}f_\varepsilon - m_0' g\cos\phi - m_0' b\dot{\Omega}_b\sin\chi, \tag{3.21}$$

$$\frac{1}{2}m_0 a^2\dot{\Omega}_0 = \frac{m_0''}{\pi}T_0, \tag{3.22}$$

$$\frac{1}{2}m_0 a^2\dot{\Omega}_0 + (M+m_h)b^2\dot{\Omega}_h + \mathcal{M}\frac{d}{dt}\left(\varepsilon^2\dot{\chi}\right) + m_0' b\frac{d}{dt}(\varepsilon\sin\chi) + m_0' b\dot{\Omega}_0\varepsilon\cos\chi$$
$$= Mgb\sin\alpha + m_0' g\varepsilon\sin\phi. \tag{3.23}$$

Equations (4.2) and (4.6) are derived from momentum conservation on the inner cylinder in the $\hat{\boldsymbol{\varepsilon}},\hat{\boldsymbol{\chi}}$ directions respectively, with equations (3.22) and (3.23) resulting from angular momentum conservation of the inner cylinder and the entire system respectively. A full derivation can be found in Veneer [139]. Upon substituting equations (3.17)-(3.19), and introducing the time scale τ_0 and effective Wiessenberg number α,

$$\tau_0 = \frac{12am_0''\mu}{\rho m_0' g\delta^2}, \quad \alpha = \frac{\rho g m_0'\delta^2\alpha_2}{12am_0''\mu^2}. \tag{3.24}$$

Assuming that α is $O(1)$ we find that, after excluding the inertial terms, the momentum equations can be written as

$$\frac{\dot{\kappa}}{(1-\kappa^2)^{\frac{3}{2}}} - \frac{3\alpha\kappa^3\left(\Omega_0+\Omega_h-2\dot{\phi}\right)^2}{(2+\kappa^2)^2(1-\kappa^2)^{\frac{3}{2}}} + \frac{3\alpha\dot{\kappa}^2\kappa}{(1-\kappa^2)^{\frac{5}{2}}} +$$
$$\frac{2\alpha\kappa\left[\left(\Omega_h-\dot{\phi}\right)^2+\left(\Omega_0-\dot{\phi}\right)\left(\Omega_h-\dot{\phi}\right)+\left(\Omega_0-\dot{\phi}\right)^2\right]}{3(1-\kappa^2)^{\frac{3}{2}}} + \cos\phi - 2\alpha\left\{\frac{\ddot{\kappa}}{(1-\kappa^2)^{\frac{3}{2}}} + \frac{3\dot{\kappa}^2\kappa}{(1-\kappa^2)^{\frac{5}{2}}}\right\} = 0, \tag{3.25}$$

$$\frac{\left(\Omega_0+\Omega_h-2\dot{\phi}\right)(\kappa-2\alpha\dot{\kappa})}{(1-\kappa^2)^{\frac{1}{2}}(2+\kappa^2)} + \sin\phi - 2\alpha_2\left\{\frac{\left(\dot{\Omega}_0+\dot{\Omega}_h-2\ddot{\phi}\right)\kappa}{(1-\kappa^2)^{\frac{1}{2}}(2+\kappa^2)} + \frac{\left(\Omega_0+\Omega_h-2\dot{\phi}\right)\left(2\kappa^4-\kappa^2+2\right)\dot{\kappa}}{(1-\kappa^2)^{\frac{3}{2}}(\kappa^2+2)^2}\right\} = 0, \tag{3.26}$$

$$\frac{1}{2}\mathcal{H}\dot{\Omega}_0 = \frac{\left(1-\kappa^2\right)\left(\Omega_h-\dot{\phi}\right)-\left(1+2\kappa^2\right)\left(\Omega_0-\dot{\phi}\right)}{(1-\kappa^2)^{\frac{1}{2}}(2+\kappa^2)} - 2\alpha\left\{\frac{\left(1-\kappa^2\right)\left(\Omega_h-\dot{\phi}\right)-\left(1+2\kappa^2\right)\left(\Omega_0-\dot{\phi}\right)}{(1-\kappa^2)^{\frac{1}{2}}(2+\kappa^2)}-\right\}_t, \tag{3.27}$$

$$\mathcal{H}\dot{\Omega}_0 + \Lambda\dot{\Omega}_h = s + 6\kappa\sin\phi, \tag{3.28}$$

where $\Lambda = \frac{2(M+m_h)}{m_0}\mathcal{H}$ and $\mathcal{H} = \frac{\rho m_0' m_0 g \delta^3}{48 m_0''^2 \mu^2}$.

3.3.1 Sedimentation solution

The above system of non-linear ODEs simplifies substantially under the purely sedimenting system whereby $U_0 = U_h = \dot{\phi} = 0,\ s = 0,\ \phi = \pi$. This sedimenting solution, where the inner cylinder simply falls vertically onto the lower cylinder is governed by the first order non-linear ODE for κ:

$$\frac{\dot{\kappa}}{(1-\kappa^2)^{\frac{3}{2}}} + \frac{3\alpha\dot{\kappa}^2\kappa}{(1-\kappa^2)^{\frac{5}{2}}} - 2\alpha\left(\frac{\ddot{\kappa}}{(1-\kappa^2)^{\frac{3}{2}}} + \frac{3\dot{\kappa}^2\kappa}{(1-\kappa^2)^{\frac{5}{2}}}\right) = 1. \tag{3.29}$$

This simplifies to

$$\frac{\dot{\kappa}}{(1-\kappa^2)^{\frac{3}{2}}} - \frac{3\alpha\dot{\kappa}^2\kappa}{(1-\kappa^2)^{\frac{5}{2}}} - \frac{2\alpha\ddot{\kappa}}{(1-\kappa^2)^{\frac{3}{2}}} = 1. \tag{3.30}$$

The solution for $\alpha = 0$ was found by Goldman et al. [43], with initial condition $\kappa_0(0) = \mathcal{K}$, and is the sedimentation solution.

To further simplify the equations it is helpful to consider the limit as the two cylinders are almost touching. To do this we introduce the variable $\zeta = \sqrt{1-\kappa^2}$ which is the distance from touching. If we seek a solution of (3.38) for small ζ, and recalling that $\kappa \sim 1, \kappa_t \sim -\zeta\dot{\zeta}, \kappa_{tt} = -\zeta\ddot{\zeta} - \dot{\zeta}^2$, we recover

$$-\dot{\zeta}\zeta^{-2}\left(1 - 2\alpha\left(\frac{\ddot{\zeta}}{\dot{\zeta}} - \frac{\dot{\zeta}}{2\zeta}\right)\right) = 1. \tag{3.31}$$

3.3.2 Singularity in sedimentation problem

The ODE (3.31) bears a strong similarity to the expression given by Brindley et al. [19]:

$$\frac{\dot{h}}{h^3}\left(1 + \beta_2\left(\frac{\ddot{h}}{\dot{h}} - \frac{18\dot{h}}{5h}\right) + \frac{9}{10}\beta_3\frac{\dot{h}}{h}\right) = -1. \tag{3.32}$$

Here $\beta_2 = -\frac{1}{2}\Psi_1 = -2\alpha_2$ and $\beta_3 = \Psi_1 + \Psi_2 = (-4\alpha_2 + \alpha_1)$ are the first and second normal stress coefficients. Ψ_1 is, most often, positive and Ψ_2 negative with $|\Psi_2| \ll |\Psi_1|$. For the case of a Wiessenberg fluid $\Psi_2 = 0$. The expression (3.32) was derived for the evolution of the gap distance for two plates lubricated by a second order fluid, with the upper plate under constant load. The solution to (3.32) was found using a regular perturbation expansion by Brindley et al. . The solution, with initial

condition $h(0) = h_0$, is given by

$$h = h_\mu \left(1 + \frac{3\dot{h}_\mu}{5h_\mu} \left[\beta_2 - \frac{3\beta_3}{2} \right] \ln\left(\frac{h_\mu}{h_0} \right) \right), \tag{3.33}$$

where h_μ is the viscous solution given by

$$h_\mu = \frac{h_0}{\sqrt{1 + 2h_0^2 t}}. \tag{3.34}$$

We find that the solution exhibits a finite time singularity. This singularity can be seen to exist analytically. Let us search for a spontaneous singularity to equation (3.32) in the form $h \sim A\,[t-a]^{-r}$:

$$-A^{-2} r (t-a)^{2r-1} \left(1 + (t-a)^{-1} \left(\beta_2 \left(\frac{r(r+1)}{-r} + \frac{18}{5} r \right) - \frac{9}{10} \beta_3 r \right) \right) = 1. \tag{3.35}$$

Assuming $0 < r < 1$, the leading order term arises from the terms scaled by $(t-a)^{-1}$, which has an overall contribution $O((t-a)^{2r-2})$, rather than from the gravity term which is $O(1)$. Hence to leading order

$$\beta_2 \left(-1 + \frac{13}{5} \right) = \frac{9}{10} \beta_3 r. \tag{3.36}$$

Thus $r = \frac{5}{13\left(1 - \frac{9\beta_3}{26\beta_2}\right)}$ which, for a Wiessenberg fluid, gives $r = \frac{5}{22}$ and is consistent with $0 < r < 1$. This singularity is seen in Fig.3.2, and the singular behavior is shown to be like $-\frac{5}{22}$ in Fig.3.3.

As the numerical singular feature is clearly unphysical, we propose a regularisation of the model. We would like our regularization to maintain the following:

(i) When $\alpha_2 = \alpha_1 = 0$ one still recovers the Newtonian system.

(ii) Regularization should not permit spontaneous pole singularities for finite time.

(iii) One should recover the same behaviour as Brindley's perturbation result for the two plate problem for weak elasticity numerically.

(iv) Normal stress in shear flow should still behave proportionality to $\dot{\gamma}^2$.

From the analysis in equation (3.35) we can understand the singularity from a purely mathematical perspective. Mathematically, the second derivative allows one to formulate an equation for the free parameter r, which permits a leading order balance of momentum to leading order, at the expense of a singularity. So what is physically

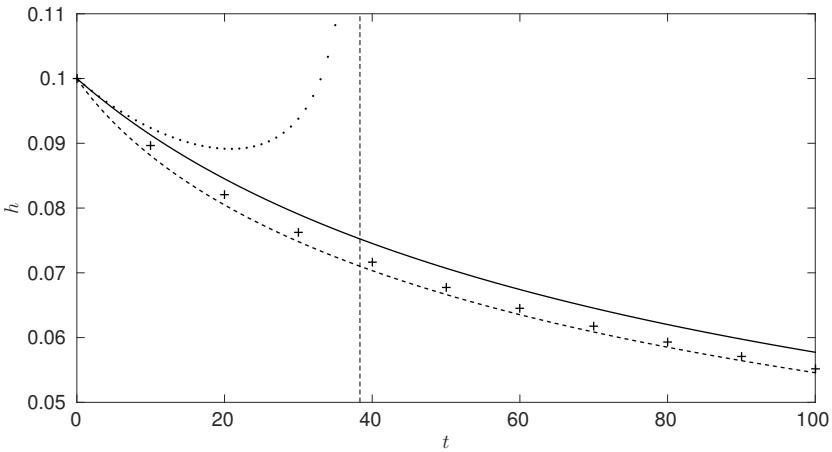

Fig. 3.2 The solid line is the Newtonian result. The dotted line is the singular numerical solution with $\beta_2 = -10$ in (3.32), with the vertical dashed line indicating the asymptote. The dashed line is the numerical solution (3.37), with the crosses indicating the perturbation solution.

happening at this singularity? The dominant terms in momentum balance, near the singularity, are both the elastic terms, in other words the elastic terms are self balancing. Clearly such an equilibrium is unphysical. Considering imposition (ii) and (3.35) leads one to note that the term $\frac{\partial \dot{\gamma}}{\partial t}$ must be regularized. For imposition (iii) to be true to leading order gravity and shear rate must both balance for all time, i.e. $\mu\dot{\boldsymbol{\gamma}} \sim \boldsymbol{g}$. Such a condition should stop only the elastic terms balancing themselves to leading order. We find that both of these condition can be reconciled if the rate of strain tensor in $\mu\frac{\partial \dot{\boldsymbol{\gamma}}}{\partial t}$ be replaced with $\frac{\partial \boldsymbol{g}}{\partial t}$, which is true to leading order. It should be noted that such an approach will clearly maintain imposition (i) and (iv).

If we implement this approach into (3.32) the ODE becomes

$$\frac{\dot{h}}{h^3}\left(1+\left(-\frac{3}{5}\beta_2+\frac{9}{10}\beta_3\right)\left(\frac{\dot{h}}{h}\right)\right) = -1. \tag{3.37}$$

This form describes the same perturbation series without allowing spontanous pole singularities. A comparison of the solutions of the ODEs (3.32) and (3.37), along with the perturbation series, is given in Fig.3.2.

So why have we concentrated on equation (3.32)? We find that this same singular phenomenon actually occurs in the snail ball system (3.31) and that such a phenomenon seems to occur in sedimenting SOF systems in general, and is not just a "snail ball problem".

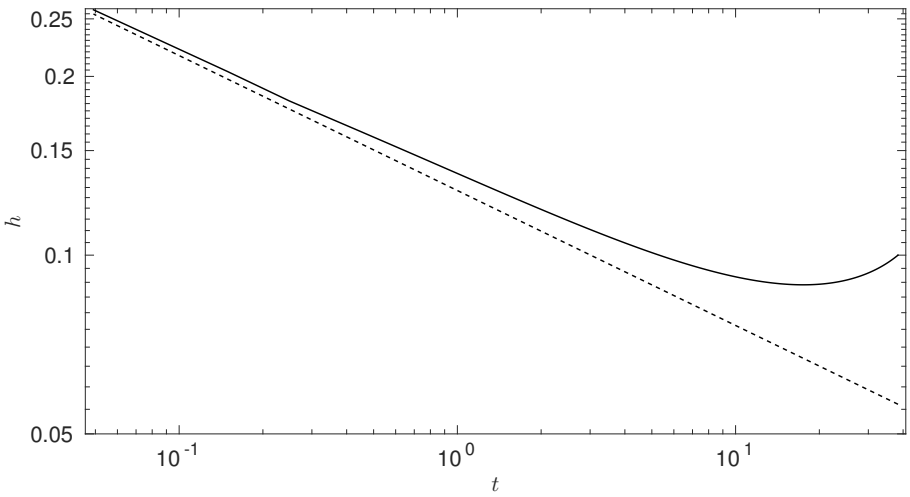

Fig. 3.3 The solid line is the singularity found from solving equation (3.32) with $h'(0) = 0.1, h''(0) = -10^{-3}$. The dashed line is the predicted pole behavior $(t-a)^{-\frac{5}{22}}$. The singularity occurs when $t = a \approx 38.35$.

However, one should remember that (3.31) is, in fact, an approximation to (3.30). Solving equation (3.30) numerically we find that the inner ball seems to oscillate between the top and bottom of the outer cylinder. This clearly does not satisfy energy conservation.

If one uses the regulization procedure the ODE becomes

$$\frac{\dot{\kappa}}{(1-\kappa^2)^{\frac{3}{2}}} + \frac{3\alpha\dot{\kappa}^2\kappa}{(1-\kappa^2)^{\frac{5}{2}}} = 1. \tag{3.38}$$

The solution for $\alpha = 0$ was found by Goldman Cox and Brenner [43], with initial condition $\kappa_0(0) = \mathcal{K}$, and is the sedimentation solution

$$\kappa_0(t) = \frac{t + \mathcal{K}/\sqrt{1-\mathcal{K}^2}}{\sqrt{1+\left(t+\mathcal{K}/\sqrt{1-\mathcal{K}^2}\right)^2}}. \tag{3.39}$$

In spite of its simplicity, no closed form analytical solution can be found for (3.38). We approach the problem instead by seeking a solution in the form of a regular perturbation series in α. It is of note that in the lubrication approximation we have already discarded terms of the order $O(\delta/a)$, hence to be clear, we are assuming that

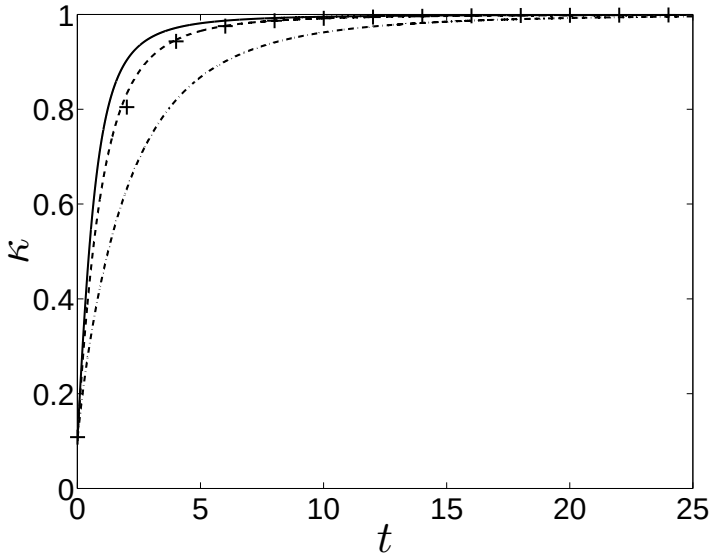

Fig. 3.4 The lines from bottom to top are the results with $\alpha = 0, 0.5, 5$, for $\mathcal{K} = 0.1$. The crosses are the first order perturbation results.

$1 \gg \alpha \gg \frac{\delta}{a}$, to keep the approximation orders consistent. To first order we find that

$$\kappa \sim \kappa_0(t) + \frac{3\alpha \ln\left(\frac{1-\kappa_0(t)^2}{1-\mathcal{K}^2}\right)}{2\left(1+\left(t+\mathcal{K}/\sqrt{1-\mathcal{K}^2}\right)^2\right)^{\frac{3}{2}}}. \tag{3.40}$$

The perturbation result along with a full numerical solution to equation (3.38) are presented in Fig.3.4 along with the perturbation series (3.40). As $\kappa_0(t) < 1$, if the solution is monotonically increasing ($\dot{\kappa} > 0$), with $\alpha > 0$, one can see that the correction term acts in the opposite direction to the viscous force and thus causes a quicker descent. Thus for positive first normal stress difference, the viscoelastic force acts so as to inhibit the inner cylinder from dropping to the base.

After this brief analysis of the sedimenting system one may suspect that the viscoelastic terms play “second fiddle" to the viscous terms. However, the terms in f_ε containing the angular velocities do not arise in the sedimenting system, and we will later find that these terms play an important role in the rocking system, completely changing the dynamics of the system.

3.4 Modified momentum equations

If one performs the replacement of the term $\frac{\partial\dot{\gamma}}{\partial t}$ in the momentum equations (3.25)-(3.28), one obtains:

$$\frac{\dot{\kappa}}{(1-\kappa^2)^{\frac{3}{2}}} - \frac{3\alpha\kappa^3\left(\Omega_0+\Omega_h-2\dot{\phi}\right)^2}{(2+\kappa^2)^2(1-\kappa^2)^{\frac{3}{2}}} + \frac{3\alpha\dot{\kappa}^2\kappa}{(1-\kappa^2)^{\frac{5}{2}}} + \frac{2\alpha\kappa\left[\left(\Omega_h-\dot{\phi}\right)^2+\left(\Omega_0-\dot{\phi}\right)\left(\Omega_h-\dot{\phi}\right)+\left(\Omega_0-\dot{\phi}\right)^2\right]}{3(1-\kappa^2)^{\frac{3}{2}}} + \cos\phi - 2\alpha\dot{\phi}\sin\phi = 0, \tag{3.41}$$

$$\frac{\left(\Omega_0+\Omega_h-2\dot{\phi}\right)(\kappa-2\alpha\dot{\kappa})}{(1-\kappa^2)^{\frac{1}{2}}(2+\kappa^2)} + \sin\phi + 2\alpha_2\dot{\phi}\cos\phi = 0, \tag{3.42}$$

$$\frac{1}{2}\mathcal{H}\dot{\Omega}_0 = \frac{\left(1-\kappa^2\right)\left(\Omega_h-\dot{\phi}\right)-\left(1+2\kappa^2\right)\left(\Omega_0-\dot{\phi}\right)}{(1-\kappa^2)^{\frac{1}{2}}(2+\kappa^2)} - \alpha H\ddot{\Omega}_0, \tag{3.43}$$

$$\mathcal{H}\dot{\Omega}_0 + \Lambda\dot{\Omega}_h = s + 6\kappa\sin\phi, \tag{3.44}$$

3.4.1 Steady rolling solution

For the case of a Newtonian fluid it was found by Balmforth et al. [9] that the system of equations permitted a steady state solution in which the snail ball rolls down the plane at a constant speed, defying experimental results. It was found, however, that this solution was unstable for all parameter regimes. We again found that equations (3.41-3.44) permitted a steady state solution. After a little algebra the steady state solution can be written as

$$\Omega_0 = \frac{s}{6}\kappa^{-2}\left(1-\kappa^2\right)^{\frac{3}{2}}, \quad \Omega_h = \frac{s}{6}\kappa^{-2}\left(1-\kappa^2\right)^{\frac{1}{2}}\left(1+2\kappa^2\right), \quad \sin\phi = -\frac{s}{6k}, \tag{3.45}$$

where κ^2 satisfies the 4th order polynomial (for $\kappa^2 \neq 1,0$):

$$36\kappa^4\left(1-\kappa^2\right)\left(s^2-36\kappa^2\right)+\alpha^2 s^4\left(2\kappa^4-\kappa^2+2\right)^2 = 0. \tag{3.46}$$

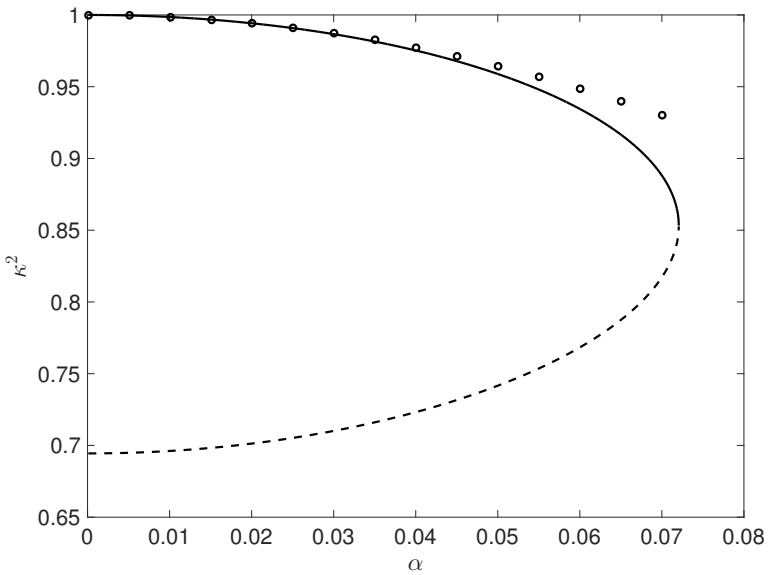

Fig. 3.5 The stable and unstable solutions are given by the solid and dashed lines respectively for $s = 5$. The circular markers indicate the approximate solution (3.48).

We find that there now exist two real steady state solutions to the system which for small, but non-zero α, are given approximately by

$$\kappa_1^2 \approx \left(\frac{s}{6}\right)^2 + s^4\alpha^2\left(\frac{s^4 - 18s^2 + 1296}{108s^2\sqrt{36 - s^2}}\right)^2, \tag{3.47}$$

$$\kappa_2^2 \approx 1 - \frac{s^4\alpha^2}{4(36 - s^2)}. \tag{3.48}$$

These can be deduced by iteration. The above solution is only valid for $s < 6$ as otherwise no real solutions exists. This is true for the Newtonian case as well. The first solution, κ_1, is the previous unstable Newtonian solution modified by viscoelastic effects. The second solution, κ_2, only arises in the presence of non-zero viscoelastic terms. A full numerical solution to equations (3.41) and (3.44) are presented in Fig.3.6 along with the steady solution given by equations (3.45) and (3.46).

By considering the limit of small s or α, for the second solution it can be seen that the inner cylinder “hovers" just above touching the outer cylinder as can be seen in Fig.3.7. The position of the stationary point increases in height for increasing slope or Weissenberg number. This can be seen by requiring the viscoelastic resistive force, which for small ζ behaves like $f_\varepsilon \sim \alpha\zeta^{-3}$, to balance out the gravitational force. Conversely, we find that the position of the unsteady solution decreases in height with increasing slope or Weissenberg number. Upon reaching a critical value of α

we find that the two states collide, and the unstable modified Newtonian solution and the stable viscoelastic steady state solution undergoes a saddle node bifurcation, hereafter no steady-state rolling solution exists.

A question remains concerning the physicality of this result, that the presence of a small amount of viscoelasticity can cause completely different behavior. We attribute this effect to the fact that the viscoelastic term grows much larger than the viscous term, which can result in anomalous behaviour of a SOF. What we are trying to suggest is that the introduction of viscoelasticity may result in a constant rolling solution, although this would need to be verified using a numerical study incorporating a more realistic viscoelastic model.

3.4.2 The rocking solution

Thus far we have found that the system permits a steady solution until a critical value of α is reached. However, we have not explored whether the possibility of the rocking solution, which was the main curiosity in the viscous case, is still permissible. Certainly, by direct substitution one can see that the solution $\kappa = 1, \Omega_a = \Omega_b = \dot{\phi}$, where the inner cylinder has made contact, is still a permissible solution to equations (3.41-3.44) where $\ddot{\phi}$ satisfies the harmonic oscillatory equation

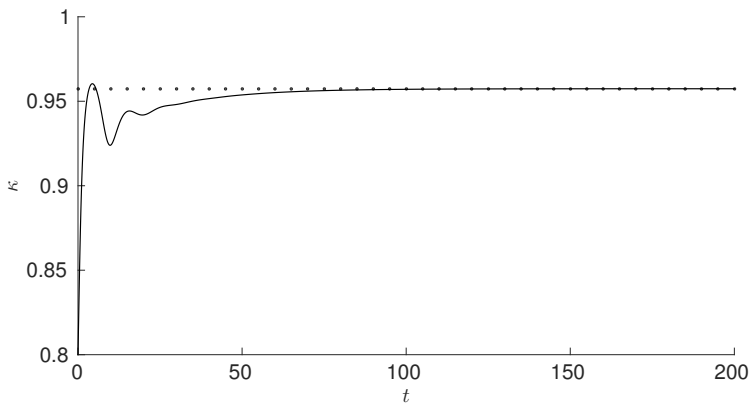

(a)

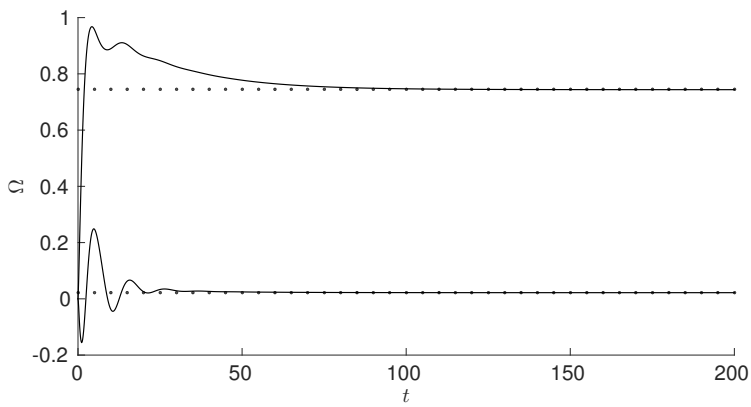

(b)

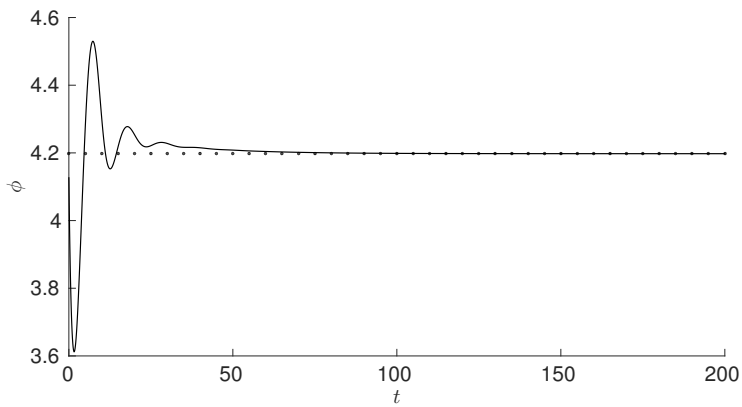

(c)

Fig. 3.6 The evolution (a) κ, (b) Ω_h (top line) and Ω_0 (bottom line), (c) ϕ for $\alpha = 0.065, \mathcal{H} = \Lambda = 6$, $s = 5$ with initial conditions $(\kappa(0), \Omega_0(0), \Omega_h(0), \phi(0)) = (.8, 0, 0, 4.1)$. The analytic steady state solution of (3.46) is marked by the dotted line.

$$(\mathcal{H} + \Lambda)\ddot{\phi} = s + 6\sin\phi. \tag{3.49}$$

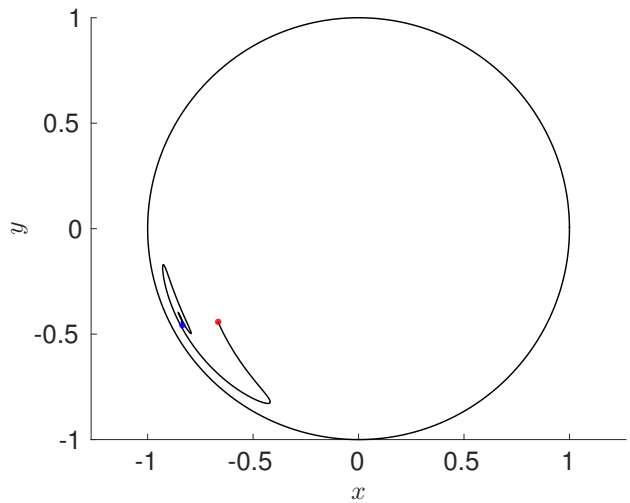

Fig. 3.7 The locus of the path of the inner cylinder for $\alpha = 0.065, \mathcal{H} = \Lambda = 6$, $s = 5$ with initial conditions $(\kappa(0), \Omega_0(0), \Omega_h(0), \phi(0)) = (.8, 0, 0, 4.1)$. The starting position is indicated by the red marker and the steady state position by the blue marker.

To analyze the rocking solution we expand for small ζ and keep the leading order contribution. In so doing equations (3.41-3.43) can be approximated to leading order as

$$\Omega_0 = \dot{\phi} - \frac{\zeta\mathcal{H}}{2}\left(\ddot{\phi} + 2\alpha\dddot{\phi}\right), \quad \Omega_h = \dot{\phi} + \zeta\left\{\frac{\mathcal{H}}{2}\left(\ddot{\phi} + 2\alpha\dddot{\phi}\right) - 3\sin\phi - 6\alpha\dot{\phi}\cos\phi\right\}. \quad (3.50)$$

Combining with equation (3.41) gives

$$\dot{\zeta}/\zeta - 3\alpha\left(\dot{\zeta}/\zeta\right)^2 = \frac{1}{3}\alpha\zeta^{-2}\left[\left(\Omega_h - \dot{\phi}\right)^2 + \left(\Omega_0 - \dot{\phi}\right)^2\right] + \zeta\cos\phi - 2\alpha\zeta\dot{\phi}\sin\phi. \quad (3.51)$$

From the above we can clearly see that the gravitation and viscoelastic terms have opposite signs. These drive the inner ball towards and away from touching the outer cylinder respectively. One can see from (3.50) that $\Omega_0 - \dot{\phi}$ and $\Omega_h - \dot{\phi}$ scale as ζ. Thus the first term on the right hand side scales as $O(1)$, whereas the second and third terms scale like $O(\zeta)$. Thus as $\zeta \to 0$, the resistive viscoelastic term becomes dominant over gravitational effects. Hence we deduce that

$$\dot{\zeta} = \frac{\left(1 \pm \sqrt{1 - \alpha^2\left(R_1^2 + R_2^2\right)}\right)\zeta}{6\alpha} + O(\zeta^2), \quad (3.52)$$

where

$$R_1 = \mathcal{H}\left(\ddot{\phi} + 2\alpha\dddot{\phi}\right), \quad R_2 = \mathcal{H}\left(\ddot{\phi} + 2\alpha\dddot{\phi}\right) - 6\sin\phi - 12\alpha\dot{\phi}\cos\phi. \quad (3.53)$$

The real component of $1 \pm \sqrt{1-\alpha^2\left(R_1^2+R_2^2\right)}$ is always positive. Therefore the ODE (3.52) has an unstable steady state at $\zeta = 0$ for all values of $\alpha > 0$.

Thus, the famous rocking solution is no longer attainable for positive normal stress differences.

In either case the predictions of the SOF in this limit must be treated with a degree of scepticism. Davies and Walters [27] remarked that in the limit of small gap one must take care to ensure that $\alpha_2\dot{\gamma}$ is small, which is required for the SOF to give physically realistic predictions. However, with decreasing gap size, the shear rate $\dot{\gamma}$ will increase. However, as mentioned previously, it seems reasonable to suggest that the behavior predicted by the SOF may be indicative of features which more complex models would produce.

3.5 Numerical solution

Equations (3.41)-(3.44) are solved using a second order implicit method in time with a Newton Raphson algorithm is employed to solve the implicit algebraic equations on each time step. The root is initially sought in the proximity of the Newtonian solution, but subsequently the solution at the previous time step is taken as the initial guess.

Depending on the initial position and the input parameters we find that the solution recovers either the predicted steady state solution see (Fig.3.6) or a “run away" solution where the system accelerates under the influence of gravity. We find that the solution often tends to the run away solution unless the initial conditions are close to the steady solution.

In the Newtonian run away solution, the position of the center of mass (COM) of the inner cylinder rapidly rotates around the COM of the outer cylinder. However, in the viscoelastic case we find that the COM of the inner cylinder migrates towards the COM of the outer cylinder. Physically, this could be considered to be due to any eccentricity in the inner cylinder yielding a region of higher shear, whereby the tensional forces restore the inner cylinder back to the center. We can see this effect

by assuming polynomial behavior for large time, i.e.

$$\Omega_0 \sim C_1 t^b, \quad \Omega_h \sim C_2 t^b, \quad \kappa \sim C_3 t^{-a}, \quad \phi \sim C_4 + C_5 t^{-c} \quad \text{as } t \to \infty. \tag{3.54}$$

Here $a, b, c > 0$ are *a priori* assumed to be greater than zero, and C_4 is a zero of the sin function. If we consider the system of equations (3.44)-(3.44), the long time behavior of the terms is shown in the underbrace:

$$\underbrace{\frac{\dot{\kappa}}{(1-\kappa^2)^{\frac{3}{2}}}}_{O(t^{-a-1})} - \underbrace{\frac{3\alpha\kappa^3\left(\Omega_0+\Omega_h-2\dot{\phi}\right)^2}{(2+\kappa^2)^2(1-\kappa^2)^{\frac{3}{2}}}}_{O(t^{-3a+2b})} + \underbrace{\frac{3\alpha\dot{\kappa}^2\kappa}{(1-\kappa^2)^{\frac{5}{2}}}}_{O(t^{-3a-2})} +$$

$$\underbrace{\frac{2\alpha\kappa\left[\left(\Omega_h-\dot{\phi}\right)^2+\left(\Omega_0-\dot{\phi}\right)\left(\Omega_h-\dot{\phi}\right)+\left(\Omega_0-\dot{\phi}\right)^2\right]}{3(1-\kappa^2)^{\frac{3}{2}}}}_{O(t^{-a+2b})} + \underbrace{\cos\phi}_{O(1)} - \underbrace{2\alpha\dot{\phi}\sin\phi}_{O(t^{-2c-1})} = 0, \tag{3.55}$$

$$\underbrace{\frac{\left(\Omega_0+\Omega_h-2\dot{\phi}\right)(\kappa-2\alpha\dot{\kappa})}{(1-\kappa^2)^{\frac{1}{2}}(2+\kappa^2)}}_{O(t^{b-a})} + \underbrace{\sin\phi}_{O(t^{-c})} + \underbrace{2\alpha_2\dot{\phi}\cos\phi}_{O(t^{-c-1})} = 0, \tag{3.56}$$

$$\underbrace{\frac{1}{2}\mathcal{H}\dot{\Omega}_0}_{O(t^{b-1})} = \underbrace{\frac{\left(1-\kappa^2\right)\left(\Omega_h-\dot{\phi}\right)-\left(1+2\kappa^2\right)\left(\Omega_0-\dot{\phi}\right)}{(1-\kappa^2)^{\frac{1}{2}}(2+\kappa^2)}}_{O(t^b)} - \underbrace{\alpha H\ddot{\Omega}_0}_{O(t^{b-2})}, \tag{3.57}$$

$$\underbrace{\mathcal{H}\dot{\Omega}_0}_{t^{b-1}} + \underbrace{\Lambda\dot{\Omega}_h}_{t^{b-1}} = \underbrace{s}_{O(1)} + \underbrace{6\kappa\sin\phi}_{O(t^{-a-c})}. \tag{3.58}$$

We can find a consistent balance if $b = 1, a = 2, c = 1$, for which the system reduces to an algebraic system

$$\frac{2\alpha C_3}{3}\left(C_1^2+C_1C_2+C_2^2\right) = -\cos C_4, \ \frac{C_3(C_1+C_2)}{2} = -C_5\cos C_4,$$
$$C_1 - C_2 = 0, \ \mathcal{H}C_1 + \Lambda C_2 = s. \tag{3.59}$$

Here $\sin(C_4) = 0$ thus $\cos C_4 = \mp 1$. We can solve the algebraic system to find the long time asymptotic behavior:

$$\Omega_0 \sim \Omega_h \sim \frac{st}{\mathcal{H}+\Lambda}, \ \kappa \sim \pm\frac{(\mathcal{H}+\Lambda)^2}{2\alpha s^2}t^{-2}, \phi \sim n\pi + \frac{(\mathcal{H}+\Lambda)}{2\alpha s}t^{-1} \quad \text{as } t \to \infty. \tag{3.60}$$

Here we have + sign for κ when n is odd and negative sign when n is even. We see that the rotation speed to leading order is independent of the fluid parameters as the

system acts as solid ball rolling down an inclined plane. The effect of viscoelasticity on the solution determines how quickly the centre point is reached. We can see this be observing that κ tends to zero quicker for larger α. The asymptotic solution is plotted in Fig.3.8 and Fig.3.9 along with the full numerical results. Perfect agreement is found for large times. The locus of the path taken by in the inner cylinder is shown in (3.10).

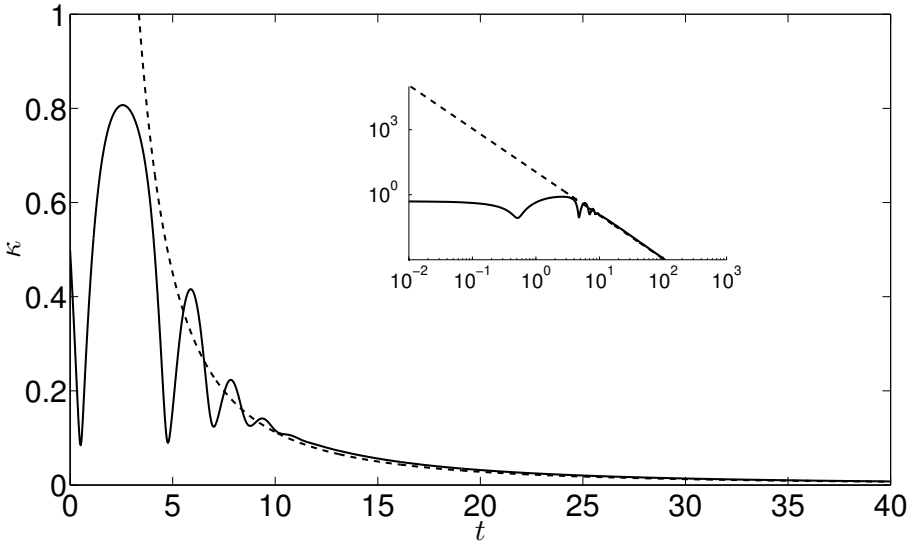

(a)

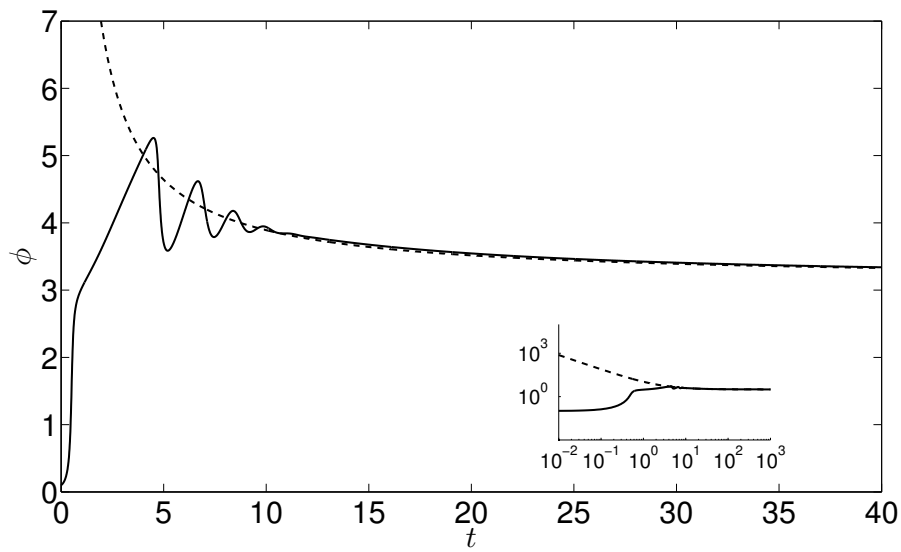

(b)

Fig. 3.8 The evolution of the variables κ (Fig.3.8a) and ϕ (Fig.3.8b). The initial condition is $\kappa = 0.5, \phi = \frac{5\pi}{6}$ with $\Omega_0 = \Omega_h = 0$ for $\alpha = 0.1, H = \Lambda = 6$ and $s = 8$. The solid line denotes the full numerical solution. The dashed line denotes the large time asymptotic behavior given in equation (3.60). Within each plot is a subplot showing the behavior on a logarithmic scale.

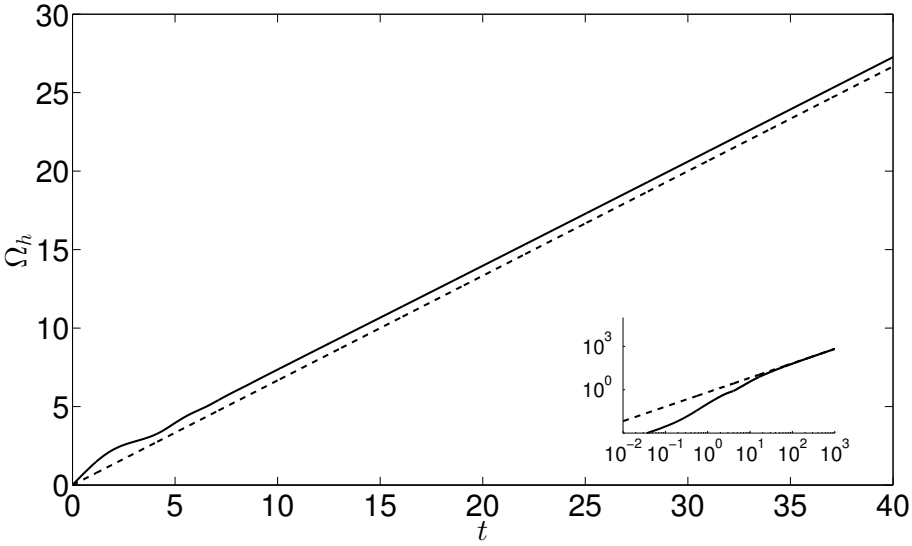

(a)

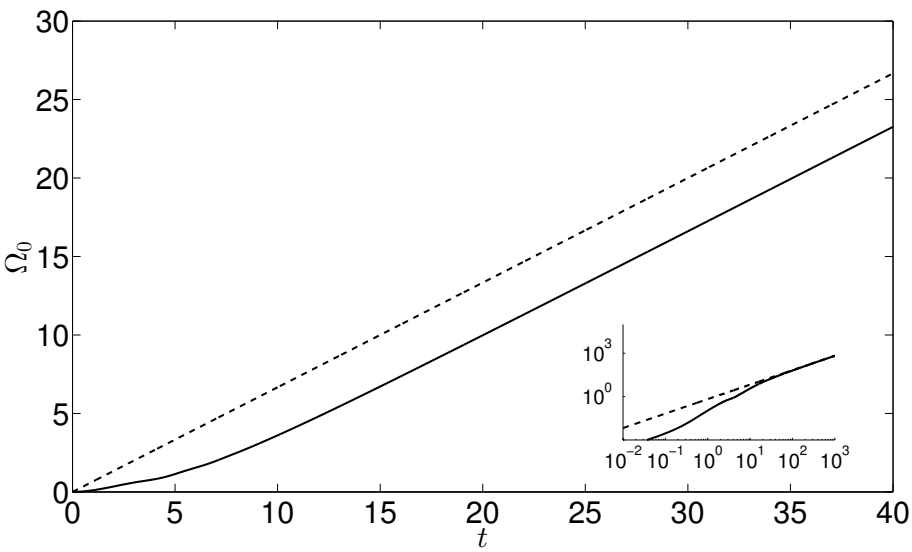

(b)

Fig. 3.9 The evolution of the variables Ω_h (Fig.3.9a) and Ω_0 (Fig.3.9b). The initial conditions are $(\kappa(0), \Omega_0(0), \Omega_h(0), \phi(0)) = (.5, 0, 0, 0.1)$ for $\alpha = 0.1, H = \Lambda = 6$ and $s = 8$. The solid line denotes the full numerical solution. The dashed line denotes the large time asymptotic behavior given in equation (3.60). Within each plot is a subplot showing the behavior on a logarithmic scale.

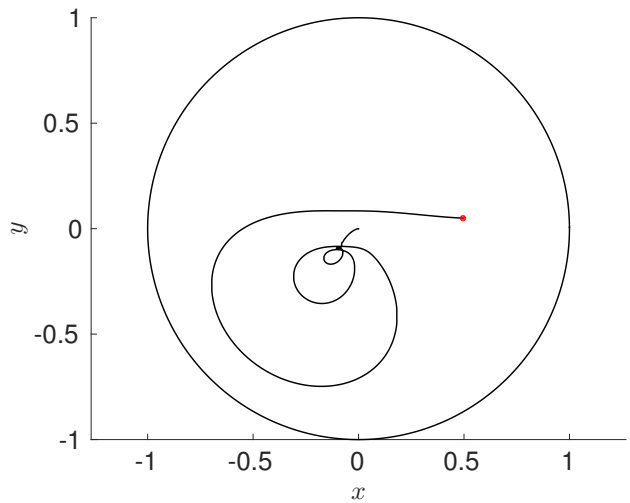

Fig. 3.10 The locus of the path that the inner cylinder takes for $\alpha = 0.1, \mathcal{H} = \Lambda = 6$, $s = 8$ with initial condition $(\kappa(0), \Omega_0(0), \Omega_h(0), \phi(0)) = (.5, 0, 0, 0.1)$. The starting position is indicated by the red marker.

3.6 Part II: Power-law system

3.6.1 Governing equations

In the previous section we derived the equations of motion for the case of a SOF which has simple viscoelastic effects. We now proceed by considering that the system is under the influence of a second non-Newtonian phenomenon, namely viscous shear dependency. For this we use the most common model, the power law (PL) fluid model. The PL model satisfies equations (3.2)-(3.4). However, $\boldsymbol{\tau}$ is given by a purely viscous response where

$$\boldsymbol{\tau} = \mu(\dot{\gamma})\dot{\boldsymbol{\gamma}}. \tag{3.61}$$

Note that here we have changed equation (3.4) to $\boldsymbol{\sigma} = -p\boldsymbol{\delta} + \boldsymbol{\tau}$ to abide by the normal sign convention associated with lubricated power-law fluids. The viscous shear-rate dependency is given by

$$\mu(\dot{\gamma}) = K\dot{\gamma}^{n-1} \approx K\left|\frac{\partial u}{\partial y}\right|^n. \tag{3.62}$$

Here K is the consistency and n is the power law index. We now present the governing equations in the form given by Hewitt and Balmforth [55]. Under the lubrication approximation, the shear rate to leading order is given by $\dot{\gamma} = u_y$ and equations (3.2), (3.4) become

$$\frac{\partial \tau}{\partial y} = a^{-1}\frac{\partial p}{\partial \theta}, \quad \frac{\partial p}{\partial y} = 0. \tag{3.63}$$

These can be integrated to give

$$\tau = \tau_0 + a^{-1} r \frac{\partial p}{\partial \theta}, \quad \text{or} \quad \tau = \tau_h + a^{-1}(r-h)\frac{\partial p}{\partial \theta}, \tag{3.64}$$

where τ_0 and τ_h are the shear stresses on the inner and outer cylinders respectively. It thus follows that

$$p_\theta = \frac{a}{h}(\tau_h - \tau_0). \tag{3.65}$$

Consequently, the momentum equation can be written as

$$U = U_h - U_0 = \int_0^h u_y dy = \frac{a}{p_\theta}\int_{\tau_0}^{\tau_h} G(\tau)d\tau = \frac{h}{\tau_h - \tau_0}(G_0(\tau_h) - G_0(\tau_0)), \tag{3.66}$$

where $G(\tau) = \text{sgn}(\tau)|\tau|^{\frac{1}{n}}$, which arises from inverting the constitutive law (3.61) and (3.62). We also use the notation $G_m = \int \tau^m G(\tau)d\tau$. Similarly, the mass conservation equation takes the same form as (3.10). After a little manipulation this can be written as

$$Q - q = \frac{hU}{2(\tau_h - \tau_0)} - \frac{h^2(G_1(\tau_h) - G_1(\tau_0))}{(\tau_h - \tau_0)^2}, \tag{3.67}$$

where Q is a function of t only and q is given by

$$q(\theta, t) = \int_0^\theta h_t d\theta + \frac{h}{2}(U_0 + U_h). \tag{3.68}$$

Equations (3.66) and (3.67) form a set of non-linear algebraic equations for τ_0 and τ_h, and must be solved for at each time step. In order to close the system we must also solve for Q which can be accounted for by including the periodic constraint

$$\int_0^{2\pi} p_\theta d\theta = \int_0^{2\pi} \frac{(\tau_h - \tau_0)}{h} d\theta = 0. \tag{3.69}$$

For given values $\kappa, \Omega_0, \Omega_h, \phi$ and $\dot{\kappa}, \dot{\phi}$ (which couple to the problem through q and U_0, U_h respectively), equations (3.66), (3.67) and (3.69) can be solved to give τ_0, τ_h and Q using the Newton Raphson method (see appendix 3.12 for details). The pressure can then be found from (3.65) which in turn allows one to find the forces on the inner and outer cylinders via:

$$T_a = \int_0^{2\pi} \tau_0 d\theta, \quad f_\varepsilon = \int_0^{2\pi} p\cos\theta d\theta = -\int_0^{2\pi} p_\theta \sin\theta d\theta, \tag{3.70}$$
$$f_\chi = \int_0^{2\pi} p\sin\theta d\theta = \int_0^{2\pi} p_\theta \cos\theta d\theta.$$

Thus the momentum equations become

$$0 = f_\chi + \sin\phi, \tag{3.71}$$

$$0 = f_\varepsilon - \cos\phi, \tag{3.72}$$

$$\frac{1}{2}\mathcal{H}_{PL}\dot{\Omega}_a = T_a, \tag{3.73}$$

$$\mathcal{H}_{PL}\dot{\Omega}_0 + \Lambda_{PL}\dot{\Omega}_h = s_{PL} + 6\kappa\sin\phi. \tag{3.74}$$

The scalings for $H_{PL}, \Lambda_{PL}, s_{PL}$ will be introduced later.

3.6.2 Dien and Elrod theory

For the above set of equations, analytic progress is rather impregnable. This in part is seen by the fact that for a PL fluid a Reynolds-like equation cannot be derived, except in cases where a strong symmetry exists, such as in the pure sedimenting solution, (see appendix (3.11)). The underlying problem is that the form of the velocity field is unknown. This problem does not arise for the SOF as the GT theorem allows one to readily find the velocity field. There are, however, several approximations that one can perform which allow the construction of a velocity field and ultimately a Reynolds equation. One method, as used by Safar [119] and Wang [63], is to assume that the velocity field takes the form of a linear superposition of a Couette flow plus a Poiseuille flow, although this assumption does not satisfy the momentum equation. A similar kind of approach is often used when performing a Rayleigh Ritz method [15]. Another method was proposed by Dien and Elrod, which was further expanded by [66]. This is where one assumes *a priori* that the velocity field is predominantly Couette-like and then performs a perturbation expansion around this.

The Dien and Eldrod solution requires that the velocity is predominantly Couette-like, which removes its usefulness for the purely sedimenting problem. This raises the question, “Is the flow within a snail ball Couette-like in nature?". We investigate this question by searching for clues in the Newtonian solution.

If we analyze the Newtonian solution we find that the squeeze term $\dot{\varepsilon} \sim O(\zeta^2)$ decays much more quickly than the velocity wall gradient difference $U_h - U_0 \sim O(\zeta)$. As the squeeze term generates purely non Couette-like flow, if this were a more dominant effect one may expect the DE equation to be invalid. We will assume, *a*

priori, that the leading order pressure contribution arises from the position where the gap length is at a minimum, though we will later see that this is indeed the case for power-law fluids for $n > 0.5$. For a rotating journal bearing embedded in a Newtonian fluid the system is shown to experience Couette flow on either side of the position of minimum gap length, and approximately Couette flow either side of this point. This is clearly indicated in the figure modified from Pinkus [105] shown in Fig.3.11. This is suggestive that the DE theory may be applicable.

With this in mind we use the (DE) Reynolds equation which is given by

$$\frac{\partial}{\partial x}\left\{\frac{h^{2+n}}{n}\frac{\partial p}{\partial x}\right\} = 6K(U_0+U_h)|U_h-U_0|^{n-1}h' + 12K|U_h-U_0|^{n-1}h_t. \tag{3.75}$$

One can think of this as the conventional Newtonian Reynolds equation, with the shear-rate in the viscosity term approximated by $\frac{U_h-U_0}{h}$. The derivation is given in appendix (3.13).

Integrating (3.75) gives

$$\frac{1}{n}h^{2+n}\frac{\partial p}{\partial \theta} = 6aK(U_0+U_h)|U_h-U_0|^{n-1}h + 2C_{PL}|U_h-U_0|^{n-1}(U_0+U_h) + 12a^2K|U_h-U_0|^{n-1}\int h_t d\theta, \tag{3.76}$$

where C_{PL} is some function of time and is analogous to the C in (3.11), where we now drop the PL subscript for convenience. Similarly, C must be determined from the periodic condition

$$3aK\int_0^{2\pi}\frac{1}{(1-\kappa\cos\theta)^{(1+n)}}d\theta - \frac{6a\dot{\varepsilon}}{U_0+U_h}\int_0^{2\pi}\frac{\sin\theta}{(1-\kappa\cos\theta)^{2+n}}d\theta + C\delta^{-1}\int_0^{2\pi}\frac{1}{(1-\kappa\cos\theta)^{2+n}}d\theta = 0. \tag{3.77}$$

In contrast to the Newtonian and SOF cases, the periodic condition for even the DE model is rather intractable. This is because the SOF had integer singularities which permitted the use of the residue theorem to obtain exact solutions to the integral. In the DE model, the non-integer powers result in the formation of branch cuts in the complex plane and a different approach must be used. As, to the best of the author's knowledge, exact solutions to the integrals are unobtainable, we approach the problem by evaluating the integrals asymptotically in the touching limit $\varepsilon \to 1$ or equivalently $\zeta \to 0$. Details of the asymptotics are given in appendix 3.9, but the physics of the simplification is a result of the dominant contribution to the forces and found to arise locally around $\theta = 0$, i.e. where the gap is smallest. The resulting

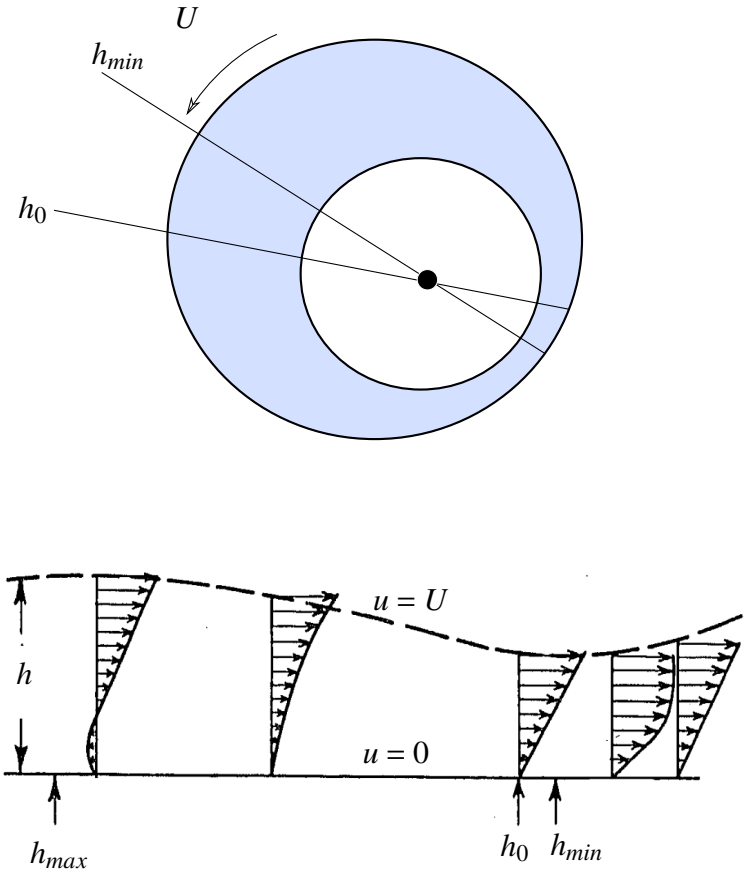

Fig. 3.11 Sketch of the journal bearing system described by Pinkus [105]. Unlike the snail ball, the inner cylinder is not free to move but fixed in place. The outer cylinder rotates with velocity U. The figure illustrates the velocity field. The minimum gap is height h_{min} and the local velocity is Couette like. Exact Couette flow occurs at h_0.

approximation for the periodic constraint can be written as

$$\frac{3aK2^{n+1}\pi^{\frac{1}{2}}\Gamma(n+\frac{1}{2})\zeta^{-2n-1}}{\Gamma(n+1)} + C\delta^{-1}\left(\frac{2^{n+2}\pi^{\frac{1}{2}}\Gamma\left(n+\frac{3}{2}\right)\zeta^{-2n-3}}{\Gamma(n+2)}\right) = 0, \tag{3.78}$$

where Γ is the Gamma function. The above approximation is only valid for $n > \frac{1}{2}$. When $n < \frac{1}{2}$ the contribution to the integrals around the singular point $\theta = 0$ is $O(1)$ which is the same order of contribution as that which arises from integrating around the entire circumference. The physical implications of this constraint are discussed later. Hence, to leading order

$$C = -\frac{3aK(n+1)\delta\zeta^2}{2\left(n+\frac{1}{2}\right)}. \tag{3.79}$$

The pressure gradient is thus given by

$$p_\theta \sim 6anKh^{-(2+n)}\Big\{(U_0+U_h)|U_h-U_0|^{n-1}h-12a^2K|U_h-U_0|^{n-1}\dot{\varepsilon}\sin\theta \tag{3.80}$$

$$-3aK(n+1)\delta\zeta^2/\left(n+\frac{1}{2}\right)(U_0+U_h)|U_h-U_0|^{n-1}\Big\}. \tag{3.81}$$

We will use (3.81) to approximate the forces given in (3.70). The component of the force in the $\hat{\boldsymbol{\varepsilon}}$ direction can be readily found to leading order:

$$f_\varepsilon = -12a^2K|U_h-U_0|^{n-1}n\dot{\varepsilon}\delta^{-1-n}\int_0^{2\pi}\frac{\sin^2\theta}{(1-\kappa\cos\theta)^{2+n}}d\theta$$

$$\sim \frac{3\cdot 2^{n+3}\cdot a^2|U_h-U_0|^{n-1}Kn\pi^{\frac{1}{2}}\Gamma(n+\frac{1}{2})\delta^{-1-n}\dot{\zeta}\zeta^{-2n}}{\Gamma(n+2)}. \tag{3.82}$$

However, difficulty arises in the evaluation of f_χ. Here f_χ is given by

$$f_\chi = -6aKn(U_h+U_0)|U_h-U_0|^{n-1}\delta^{-1-n}\int_0^{2\pi}\frac{\cos\theta}{(1-\kappa\cos\theta)^{1+n}}$$

$$+\frac{3aKn(n+1)\zeta^2(U_h+U_0)|U_h-U_0|^{n-1}\delta^{-1-n}}{\left(n+\frac{1}{2}\right)}\int_0^{2\pi}\frac{\cos\theta}{(1-\kappa\cos\theta)^{2+n}}d\theta. \tag{3.83}$$

To leading order, at the singularity, $\cos\theta\sim 1$, and we thus recover the periodic constraint (3.77). We therefore need to go to the next order to find the first non-zero contribution. One may initially expect that it is necessary to find the next order contribution to C from the periodic constraint (3.77). However, we find that this is not required. For a full calculation see Appendix 3.10, which explains how, to leading order, one can find that

$$f_\chi \sim \frac{3\cdot 2^n\pi^{\frac{1}{2}}(U_h+U_0)|U_h-U_0|^{n-1}aKn\Gamma(n-\frac{1}{2})\delta^{-1-n}\zeta^{-2n+1}}{\left(n+\frac{1}{2}\right)\Gamma(n+1)}. \tag{3.84}$$

We need only derive the torque term to complete the governing equations of the system. To do this we must recall that the DE theory assumes that the velocity field can be written as $u\sim u_0+u_1$, where u_0 is the Couette flow and u_1 is the pressure corrected velocity. It is found in the derivation presented in the appendix (3.13) that

$$u_0 = U_0\left(1-\frac{y}{h}\right)+U_h\left(\frac{y}{h}\right). \tag{3.85}$$

Likewise, u_1 can be shown to be given by

$$u_1 = -\frac{y(h-y)}{2a\mu_0}\frac{\partial p}{\partial \theta}. \tag{3.86}$$

Here μ_0 is the leading order contribution to the viscosity in equation (3.62) and μ_1 is the correction term. These are given by

$$\mu_0 = K\left|\frac{\partial u_0}{\partial y}\right|^{n-1}, \quad \mu_1 = (n-1)\,K\left|\frac{\partial u_0}{\partial y}\right|^{n-3}\frac{\partial u_0}{\partial y}\frac{\partial u_1}{\partial y}. \tag{3.87}$$

Hence the shear stress (3.61) can be expanded to give

$$\tau \approx \mu_0\frac{\partial u_0}{\partial y} + \mu_1\frac{\partial u_0}{\partial y} + \mu_0\frac{\partial u_1}{\partial y}. \tag{3.88}$$

Evaluating the above on the inner cylinder $y = 0$ leads to

$$\tau = \frac{K\,|U_h - U_0|^{n-1}\,(U_h - U_0)}{h^n} - \frac{nh}{2a}\frac{\partial p}{\partial \theta}, \tag{3.89}$$

from which we obtain

$$T_a = K|U_h - U_0|^n \mathrm{sgn}(U_h - U_0)\int_0^{2\pi}\frac{1}{h^n}d\theta \tag{3.90}$$
$$-\frac{n}{2}\int_0^{2\pi} h\cdot\frac{6KU^n h - 12a\dot{\varepsilon}\sin\theta - 3aK\,(n+1)\,\zeta^2/\left(n+\frac{1}{2}\right)U^n}{h^{2+n}/n}d\theta.$$

Again this integral can be evaluated to leading order in the touching limit to give

$$T_a = K\left\{\frac{2^n\pi^{\frac{1}{2}}\Gamma(n-\frac{1}{2})|U_h - U_0|^{n-1}K\delta^{-n}\zeta^{-2n+1}}{\Gamma(n)}\right\}\left((U_h - U_0) - \frac{3n\,(U_0 + U_h)}{(2n+1)}\right). \tag{3.91}$$

We thus see from equations (3.84) and (3.91) that the torque and force parallel to χ are weaker types of singularity than those in the ε direction given in (3.82). Also, it is of interest to note that as the singularity in equations (3.91) reduces to a logarithmic singularity. This can be seen as $\Gamma(x) \sim x^{-1}$ for small x, and $\frac{x^m-1}{m} \sim \ln(x)$ as $m \to 0$. Thus $\Gamma(n-\frac{1}{2})\zeta^{-2n+1} \sim \frac{2}{(2n-1)}\zeta^{-2n+1}$. For n fixed and ζ small $\frac{\zeta^{-2n+1}}{2n-1} \sim \frac{\zeta^{-2n+1}-1}{2n-1} \sim \ln\zeta$ as $n \to \frac{1}{2}$.

3.6.3 Touching power-law equations

We now introduce the natural time and parameter scalings:

$$\tau_0 = \left\{ \frac{3 \cdot 2^{n+3} n a^n K \delta^{-1-n} \Gamma(n+\frac{1}{2}) m_0''}{\pi^{\frac{1}{2}} \Gamma(n+2) \rho m_0' g} \right\}^{\frac{1}{n}}, \mathcal{H} = \frac{m_0 \Gamma(n) \pi^{\frac{1}{2}} \tau_0^{n-2} \delta^n}{2^{n+1} a^{n-2} m_0'' K \Gamma(n-\frac{1}{2})},$$
$$\Lambda = \frac{(M+m_h) b^2 \tau_0^{n-2} \pi^{\frac{1}{2}} \delta^n \Gamma(n)}{2^{n+1} a^{n-4} m_0'' K \Gamma(n-\frac{1}{2})}, \qquad s = \frac{6Mb \sin\alpha}{\rho m_0' a^{-4}}. \tag{3.92}$$

As the torque and internal forces can be found in closed forms for the touching limit under the DE approximation, we find that equations (3.71) through (3.74) reduce to

$$\frac{(n+1)\left(\Omega_h + \Omega_0 - 2\dot{\phi}\right)|\Omega_h - \Omega_0|^{n-1}}{8\left(n+\frac{1}{2}\right)\left(n-\frac{1}{2}\right)} + \zeta^{2n-1} \sin\phi = 0, \tag{3.93}$$

$$|\Omega_h - \Omega_0|^{n-1} \dot{\zeta} = \zeta^{2n} \cos\phi, \tag{3.94}$$

$$\frac{1}{2}\mathcal{H}\dot{\Omega}_0 = \frac{1}{2}|\Omega_h - \Omega_0|^{n-1}\left((\Omega_h - \Omega_0) - \frac{3n\left(\Omega_0 + \Omega_h - 2\dot{\phi}\right)}{(2n+1)}\right)\zeta^{-2n+1}, \tag{3.95}$$

$$\mathcal{H}\dot{\Omega}_0 + \Lambda\dot{\Omega}_h = \frac{2(2n-1)}{(n+1)}(s + 6\sin\phi) + \mathcal{O}(\zeta^2). \tag{3.96}$$

We can again see, as expected, that a rocking solution $\zeta = 0$, $\Omega_h = \Omega_0 = \dot{\phi}$, $(\mathcal{H}+\Lambda)\ddot{\phi} = \frac{2(2n-1)}{(n+1)}(s + 6\sin\phi)$ still exists, at least for $n > \frac{1}{2}$. We also recover the same condition for the Newtonian and SOF condition that rocking motion can only happen when $s < 6$. This can be seen by noting that as the solution is oscillating and smooth there must be a point where $\ddot{\phi} = 0$. At this point the boundedness of the sin function causes $s < 6$. It is important to note that in the system scalings in equations (3.92), the parameter s is found to be independent of n, and thus the maximum rocking angle is independent of the fluid rheology. This is consistent with the argument, as laid out by [141], which determined the dynamics by considering the snail ball as a solid ball with an off-centered mass. Assuming zero initial kinetic energy, if the slope is large enough so that the path traced out by the COM, which a cycloid, is continuously decreasing in height, the system will continue to roll down the hill. This argument is independent of the fluid which is reflected in the constraint. We now determine the

stability of such a system. We begin by writing the above as

$$\left(1-\frac{3}{n(2n+1)}\right)U_h-\left(1+\frac{3}{n(2n+1)}\right)U_0=|\Omega_h-\Omega_0|^{1-n}\mathcal{H}\dot{\Omega}_0\zeta^{2n-1}, \tag{3.97}$$

$$U_h+U_0=-\frac{8(n+\frac{1}{2})(n-\frac{1}{2})\sin\phi\cdot\zeta^{2n-1}}{(n+1)|\Omega_h-\Omega_0|^{n-1}}. \tag{3.98}$$

We can solve the above system to give

$$\Omega_0=\dot{\phi}+K_1|\Omega_h-\Omega_0|^{1-n}\zeta^{2n-1},\quad \Omega_h=\dot{\phi}+K_2|\Omega_h-\Omega_0|^{1-n}\zeta^{2n-1}. \tag{3.99}$$

Here

$$K_1=-\frac{1}{2}\mathcal{H}\ddot{\phi}+\frac{(2n-1)(n-1)}{n+1}\sin\phi, \tag{3.100}$$

$$K_2=\frac{1}{2}\mathcal{H}-\left(\frac{(5n+1)(2n-1)}{n+1}\right)\sin\phi. \tag{3.101}$$

To leading order, we can combine (3.96) and (3.99), to give

$$\sin\phi=\frac{(\mathcal{H}+\Lambda)(n+1)}{12(2n-1)}\ddot{\phi}-\frac{s}{6}. \tag{3.102}$$

Thus

$$K_1=-\frac{1}{2}\mathcal{H}\ddot{\phi}+\frac{(n-1)(\mathcal{H}+\Lambda)\ddot{\phi}}{12}-\frac{(2n-1)(n-1)s}{6(n+1)}, \tag{3.103}$$

$$K_2=\frac{\mathcal{H}}{2}\ddot{\phi}-\frac{(5n+1)(\mathcal{H}+\Lambda)}{12}\ddot{\phi}+\frac{(5n+1)(2n-1)s}{6(n+1)}. \tag{3.104}$$

For succinctness we express K_1, K_2 in the form

$$K_1=A_1\ddot{\phi}+B_1,\quad K_2=A_2\ddot{\phi}+B_2. \tag{3.105}$$

We can combine equations (3.99) to give

$$\Omega_h-\Omega_0=\mathrm{sgn}(K_1-K_2)\,|K_1-K_2|^{\frac{1}{n}}\zeta^{2-\frac{1}{n}}. \tag{3.106}$$

Thus equation (3.94) can be written as

$$\dot{\zeta}=\cos\phi\,|K_2-K_1|^{1-n}\zeta^{3-\frac{1}{n}}. \tag{3.107}$$

If we linearize around the center of the oscillation $\sin\phi = -\frac{s}{6}$, i.e. $\phi = \sin^{-1}(\frac{s}{6}) + \hat{\phi}$, then we can recover (3.107):

$$\dot{\zeta} = -\sqrt{1 - \frac{s^2}{36}} \left(\frac{n(2n-1)s}{(n+1)} \right)^{1-n} \zeta^{3-\frac{1}{n}}. \tag{3.108}$$

Before we continue with the analysis of the local behavior near the rolling solution, it is interesting to compare this result to that predicted by the pure-sedimenting solution. The analysis is performed in appendix D and we see, surprisingly, that $\dot{\zeta} \sim O\left(\zeta^2\right)$, whereas for the DE approximation, where the ball is placed on a sloped ramp, $\dot{\zeta} \sim O\left(\zeta^{3-\frac{1}{n}}\right)$. Interestingly the sedimentation descent rate has the same power as that expected for a Newtonian fluid. This difference arises as for the DE analysis which predicts that the viscosity behaves like $|\frac{U_h - U_0}{h}|^{n-1}$ and has no explicit pressure dependence, whereas for the sedimenting problem the viscosity is given by $(p'h)^{\frac{1}{n}-1}$. A non-linear dependence of the viscosity on the pressure like $p^{\frac{1}{n}-1}$ is required to give rise to the scaling $\dot{\zeta} \sim O\left(\zeta^2\right)$. What can clearly be seen is that both shear-dependent sedimenting problem differs vastly from the snail ball problem, and has its own unique features.

We can, however, conclude that in the ramped system the descent time is always shorter for shear-thinning fluids and longer for shear-thickening fluids than that expected for the purely sedimenting system. We attribute this to the shear induced effects from the difference in rotation of the speeds of the inner and outer shells, which are not present in the sedimenting solution. These effects result in greater shear thinning/thickening of the fluid and thus increasing/decreasing of the viscous resistive force compared to the Newtonian solution.

Continuing with the local analysis, for large t, equation (3.108) has solution

$$\zeta \sim \left(\left(2 - \frac{1}{n}\right) \left(\frac{n(2n-1)s}{n+1} \right)^{1-n} \sqrt{1 - \frac{s^2}{36}} t \right)^{\frac{n}{1-2n}}. \tag{3.109}$$

This solution can be compared with the numerical solution to equations (3.66), (3.67) and (3.69). It is shown to give good agreement in Fig. 3.12.

It is of note that the numerical system cannot be evolved for infinitely long time. We find that our numerical solution starts to fail when ζ is approximately of the order of the grid size. We thus cannot see if the solution would eventually touch the base as that would require an infinity refined grid with the current numerical scheme.

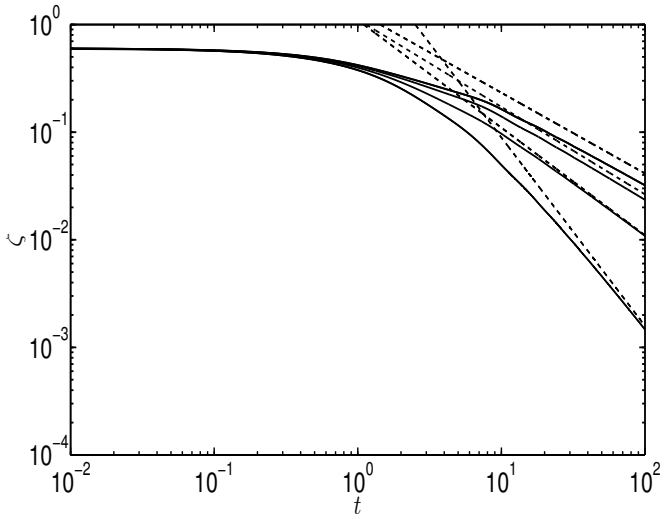

Fig. 3.12 Numerical results for ζ against time denoted by the solid line along with the touching asymptotic solution predicted by DE analysis. The curves are given, from bottom to top, for $n = 0.7, 1.0, 1.3, 1.5$.

For large n, we find that the descent predicted DE theory cannot decay any slower than $t^{-\frac{1}{2}}$. With decreasing n the solution decays more quickly, although the inner ball does not make contact in finite time.

3.6.4 The limit $n \to \frac{1}{2}$

The equations can be shown to produce exponential decay as $n \to \frac{1}{2}$. The parameters $\mathcal{H}$ and Λ in scalings (3.92) reduce to zero in the limit $n \to \frac{1}{2}$. To capture the limit of this behavior we introduce the finite parameters $\bar{\mathcal{H}} = \Gamma(n-\frac{1}{2})\mathcal{H}$, $\bar{\Lambda} = \Gamma(n-\frac{1}{2})\Lambda$, where $\bar{\mathcal{H}}$ and $\bar{\Lambda}$ are $O(1)$. Then equations (3.93)-(3.96) in the limit $n \to \frac{1}{2}$ become

$$-\frac{3}{16}\left(\Omega_h + \Omega_0 - 2\dot{\phi}\right)|\Omega_h - \Omega_0|^{-\frac{1}{2}} \ln\zeta + \sin\phi = 0, \tag{3.110}$$

$$|\Omega_h - \Omega_0|^{-\frac{1}{2}}\dot{\zeta} = \zeta^2 \cos\phi, \tag{3.111}$$

$$\frac{1}{2}\bar{\mathcal{H}}\dot{\Omega}_0 = -\frac{1}{2}|\Omega_h - \Omega_0|^{-\frac{1}{2}}\left(\frac{1}{4}\Omega_h - \frac{7}{4}\Omega_0 + \frac{3}{2}\dot{\phi}\right)\ln\zeta, \tag{3.112}$$

$$\bar{\mathcal{H}}\dot{\Omega}_0 + \bar{\Lambda}\dot{\Omega}_h = \frac{8}{3}(s + 6\sin\phi). \tag{3.113}$$

Following the same method as that on equations (3.97) and (3.98) we recover

$$U_0 + U_h = \frac{16}{3}|\Omega_h - \Omega_0|^{\frac{1}{2}} \sin\phi \ln\zeta^{-1}, \quad U_h - 7U_0 = -4\bar{\mathcal{H}}\dot{\Omega}_0|\Omega_h - \Omega_0|^{\frac{1}{2}} \ln\zeta^{-1}. \tag{3.114}$$

Solving and iterating for small ζ gives

$$\Omega_0 = \dot{\phi} + \left(\frac{14}{3}\sin\phi - \frac{1}{2}\bar{\mathcal{H}}\ddot{\phi}\right)|\Omega_h - \Omega_0|^{-\frac{1}{2}}\ln\zeta^{-1}, \tag{3.115}$$

$$\Omega_h = \dot{\phi} + \left(\frac{2}{3}\sin\phi + \frac{1}{2}\bar{\mathcal{H}}\ddot{\phi}\right)|\Omega_h - \Omega_0|^{-\frac{1}{2}}\ln\zeta^{-1}, \tag{3.116}$$

This can be rearranged to give

$$|\Omega_h - \Omega_0|^{\frac{1}{2}} = \left|\left(-4\sin\phi + \bar{\mathcal{H}}\ddot{\phi}\right)\ln\zeta^{-1}\right|. \tag{3.117}$$

Performing linearization as before and substituting into (3.111) gives

$$\dot{\zeta} = \frac{2s}{3}\sqrt{1 - \frac{s^2}{36}}\zeta\ln\zeta^{-1}. \tag{3.118}$$

Integrating the above gives

$$\zeta \propto \exp\left(-\left\{\frac{2s}{3}\sqrt{1 - \frac{s^2}{36}}t\right\}^{\frac{1}{2}}\right). \tag{3.119}$$

We thus see that the polynomial time decay is now replaced with, a more rapid, exponential decay.

3.6.5 Progression down the slope

Thus far we have described the decay rate of the inner cylinder. To further continue the analysis we investigate the stability of this rocking solution and investigate how shear thinning affects the distance travelled down the slope. We can see from equation (3.108) that $\dot{\zeta} \ll \zeta$ (for $n > \frac{1}{2}$), thus to leading order changes in ζ in time are small. Hence using (3.99) and (3.106), along with the chain rule, we can form the expression

$$\dot{\Omega}_0 = \ddot{\phi} + \frac{\partial}{\partial\ddot{\phi}}\left\{K_1|K_2 - K_1|^{\frac{1}{n}-1}\right\}\dddot{\phi}\zeta^{2-\frac{1}{n}}, \quad \dot{\Omega}_h = \ddot{\phi} + \frac{\partial}{\partial\ddot{\phi}}\left\{K_2|K_2 - K_1|^{\frac{1}{n}-1}\right\}\dddot{\phi}\zeta^{2-\frac{1}{n}}. \tag{3.120}$$

After linearization we get

$$\dot{\Omega}_0 = \ddot{\hat{\phi}} + \underbrace{\left\{A_1 |B_1 - B_2|^{\frac{1}{n}-1} + B_1 (A_1 - A_2)\left(\frac{1}{n} - 1\right)\mathrm{sgn}(B_1 - B_2)|B_1 - B_2|^{\frac{1}{n}-2}\right\}}_{Q_1} \dddot{\hat{\phi}}\zeta^{2-\frac{1}{n}},$$

$$\dot{\Omega}_h = \ddot{\hat{\phi}} + \underbrace{\left\{A_2 |B_1 - B_2|^{\frac{1}{n}-1} + B_2 (A_1 - A_2)\left(\frac{1}{n} - 1\right)\mathrm{sgn}(B_1 - B_2)|B_1 - B_2|^{\frac{1}{n}-2}\right\}}_{Q_2} \dddot{\hat{\phi}}\zeta^{2-\frac{1}{n}}. \tag{3.121}$$

Equation (3.96) reduces to

$$\ddot{\hat{\phi}} + \omega^2 \hat{\phi} = \Delta\zeta^{2-\frac{1}{n}} D \dddot{\hat{\phi}}, \tag{3.122}$$

where $\omega^2 = \frac{12(2n-1)}{(\mathcal{H}+\Lambda)(n+1)}\sqrt{1 - \frac{s^2}{36}}$, and $D = -\frac{\mathcal{H}Q_1 + \Lambda Q_2}{\mathcal{H}+\Lambda}$. We can now perform a multiple scales analysis on the problem. To perform the multiple scales analysis we are going to introduce an artificial scale Δ, with $\zeta^{2-\frac{1}{n}} = \Delta\zeta(t)^{2-\frac{1}{n}}$, where $\zeta(t)$ is found from (3.109). If the problem were non-linear, such as the famous Duffing oscillator (see for instance Bender and Orszag [13]), one would need to introduce a slowly varying time scale. However, as the problem is linear, one can use the much simpler WKB (Wentzel, Kramers, and Brillouin) method. Hereby we suppose that the solution for large time can be written in the form

$$\hat{\phi} \sim e^{\Delta^{-N} S_0 + \Delta^{-N+1} S_1 + \Delta^{-N+2} S_2}. \tag{3.123}$$

The parameter N can be found from equation (3.122) by using the method of dominant balance. A consistent scaling can be found when $N = 1$ where the third time derivative balances with the second time derivative. Substituting (3.123) into (3.122) then retaining leading order terms gives

$$S_0'^2 = D\zeta^{2-\frac{1}{n}} S_0'^3. \tag{3.124}$$

There are two solutions: $S_0' = 0$ and $S_0' = D^{-1}\zeta^{\frac{1}{n}-2}$. The first solution, $S_0' = 0$, has no component acting on the Δ^{-1} time scale and in fact we will find the oscillation to be to leading order. The other solution responds on the fast time scale Δ. This is to be expected as in the exact limit $\Delta = 0$, the additional initial condition from the third time derivative is redundant. Thus this quick time-scale is the scale over which the additional initial condition is of importance. As we are interested in the damping of the oscillating solution we will consider the case $S_0' = 0$. Thus to the next order we

have

$$S_1'' + S_1'^2 + \omega^2 = 0. \tag{3.125}$$

We see that there is a solution where $S_1 = \pm\omega i t$, which is the purely oscillating solution. Continuing to the next order gives

$$2S_1'S_2' + S_2'' = D\zeta^{2-\frac{1}{n}}\left(S_1'^3 + 3S_1''S_1' + S_1'''\right). \tag{3.126}$$

If we are interested in the behavior for large time, we assume that $S_1'' \ll S_2'$. Thus the system reduces to

$$S_2' = -\frac{1}{2}\omega^2 D\zeta^{2-\frac{1}{n}}(t). \tag{3.127}$$

Using (3.109) and then integrating gives

$$S_2 = -\mathscr{L}\ln(t), \quad \mathscr{L} = \frac{\omega^2 D}{2\left(2-\frac{1}{n}\right)\left(\frac{(n(2n-1)s}{n+1}\right)^{1-n}\sqrt{1-\frac{s^2}{36}}} = \frac{6n\left((n+1)\right)^{1-n}D}{\left(n\left(2n-1\right)s\right)^{1-n}(n+1)(\mathcal{H}+\Lambda)}. \tag{3.128}$$

Upon substituting this back into equation (3.123), and setting the artificial parameter $\Delta = 1$, for large time gives

$$\hat{\phi} \sim C_1 t^{-\mathscr{L}} e^{i\omega t} + C_2 t^{-\mathscr{L}} e^{-i\omega t}, \tag{3.129}$$

where C_1 and C_2 are arbitrary constants. The parameter D is rather cumbersome and as such it is difficult to discover the effects of introducing shear-dependent behavior. As we only expect the DE approximation to work for near Newtonian behavior, for greater insight one can instead Taylor expand around $n = 1$ to give the much more enlightening expression

$$\mathscr{L} = \frac{3\left(1+R^2\right)}{2\left(1+R\right)^2} + \frac{1}{2}\frac{\left(1-R+7R^2\right)}{\left(1+R\right)^2}(n-1). \tag{3.130}$$

Here the variable R is the ratio $\frac{\Lambda}{\mathcal{H}}$. The first term is equivalent to the Newtonian solution and is the same as that found by Balmforth et al. [9]. We can see that to first order $\mathscr{L}$ is independent of the slope parameter s and depends only on the ratio of the inner and outer moments of inertia. For a shear thickening fluid ($n > 1$) we find that the corrective term is always positive for all values of R and thus $\mathscr{L}$ is larger than that for the Newtonian case. Similarly, for the shear thinning case the value of $\mathscr{L}$ is smaller than when compared to the Newtonian case.

The variable $\mathscr{L}$ can be used to deduce the distance and speed at which a snail

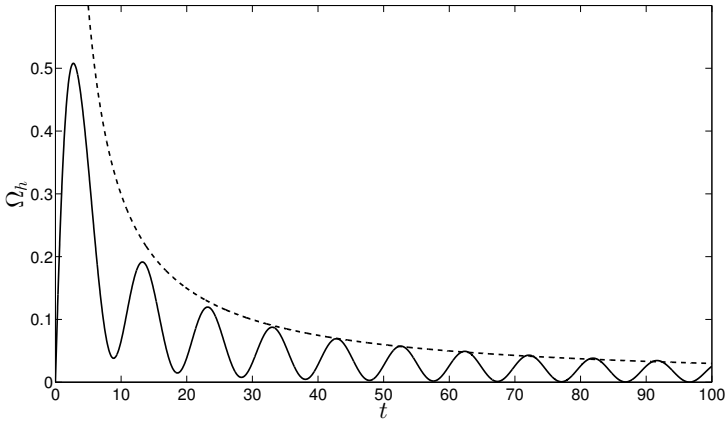

Fig. 3.13 The speed of the outer ball Ω_h for initial condition $s = 2.5, H = L = 5, n = 1.3$, with initial condition $(\kappa, \Omega_0, \Omega_h, \phi) = (0.8, 0, 0, 0.1)$. The decay predicted from equation (3.130) shown by the dashed line.

ball descends. The total distance travelled is given by the expression

$$D(t) = \int_0^t \Omega_h(t')dt'. \tag{3.131}$$

Balmforth et al. argued that when one filters the large time scales $\Omega_h \sim t^{-\mathscr{L}}$ once one filters out the fast oscillations. One can find that $D \sim t^{1-\mathscr{L}}$, so the distance travelled is thus a constant $t^{1-\mathscr{L}}$, where the constant comes from the contribution for non large t. As $\mathscr{L}$ is increased, for a shear thinning fluid the rolling speed of the ball is reduced. Conversely, for a shear thickening fluid the rolling speed of the ball increases.

It is also worth noting the boundedness of the parameter $\mathscr{L}$. As D behaves like $t^{1-\mathscr{L}}$ to leading order, if $\mathscr{L} < 1$ then the ball would make steady progress down the plane. For $\mathscr{L} > 1$ the distance the ball would travel would be finite. One can see after a little algebra that the parameter $\mathscr{L}$ is bounded by

$$\frac{3}{4} + \frac{7}{8}(n-1) < \mathscr{L} < \frac{3}{2} + \frac{7}{2}(n-1), \tag{3.132}$$

where the above inequality is only true for $O((n-1)^2)$. One finds that $\mathscr{L} < 1$ if

$$2 - \sqrt{3} - \frac{1}{2}\left(27 - 16\sqrt{3}\right)(n-1) < R < 2 + \sqrt{3} - \frac{1}{2}\left(27 + 16\sqrt{3}\right)(n-1). \tag{3.133}$$

From the above we see that the range R for which the solution makes steady progress is increased for a shear-thinning fluid, and decreased for shear a thickening fluid.

3.7 Discussion and conclusion

The behavior of the snail device has been investigated with two types of lubricating fluids. Firstly, for the case of a SOF, we found that the runaway solution is still permitted and the runaway condition is the same as that for a Newtonian fluid, which is consistent with the argument given by [141]. However, we find that the rocking solution is replaced with a constant steady rolling solution. The analysis suggests that this behavior occurs for any non-zero elasticity. Such behavior is probably due to shortcomings in the SOF model which occur when the elastic forces are more dominant than the viscous forces. To overcome this difficulty one must use a more versatile viscoelastic model, such as upper convective Maxwell-like models. We thus advise that this result must be taken with a degree of caution, and note that it may be possible that viscoelastic fluids may exhibit this kind of behavior.

For the power-law fluid the change in behavior is less dramatic. This is to be expected, as in similarity with the Newtonian system, the fluid only permits a viscous resistive force, only now the viscous response depends non-linearly on the shear rate. As with the SOF model the condition for the runaway solution remains unchanged and the rocking solution still exists. The frequency of the rocking solution remains unchanged as in the touching limit "$\zeta = 1$", the system is simply a weighted ball on an incline. However, the damping of such a rocking motion was changed which in turn was found to cause the speed of the snail ball to reduce if the fluid was shear thinning and to increase if it was shear thickening.

The descent time is similarly altered by the introduction of a shear dependent viscosity. For a shear-thinning fluid with $n > \frac{1}{2}$, the descent time is reduced compared to that of a Newtonian fluid. Similarly, for a shear thickening fluid the descent time is increased. This behavior was confirmed using the DE model. Physically, this is attributed to the extra shear induced from the rocking motion.

The behavior still remains unclear for $n < \frac{1}{2}$. It is interesting to note the strong similarity to the problem of the squeeze flow of a power-law fluid between two rigid spheres, where the leading order contribution to the vertical loading becomes non-local at $n = \frac{1}{3}$, (see Rodin [117]). We find this same phenomenon for the snail ball at $n = \frac{1}{2}$. Rodin found that for $n < \frac{1}{3}$ the gap is closed in finite time. Hence we speculate that for $n < \frac{1}{2}$ the inner cylinder will make contact with the outer cylinder although, this remains to be proven.

A final remark must be to focus on the practicalities of a non-Newtonian snail ball. Balmforth et al. [9] noted that the dynamics of the snail ball are heavily influenced by its surface roughness. This was found to lead to a constant rolling solution similar to that predicted by SOF. All of these non-Newtonian effects are thus valid only when the surface roughness is not significant.

3.8 Integrals for viscoelastic forces

In the derivation of equations (3.15), (3.17), (3.18) and (3.19) a variety of trigonometric integrals arose. As the results are non-trivial, for completeness we include a brief explanation of the derivations, preceeded by a list of the requisite integrals needed to perform the analysis. In the SOF analysis, integrals of the form

$$\int_0^{2\pi} \frac{\sin^2 x \cos x}{(1-\kappa\cos x)^5} dx \tag{3.134}$$

arose. The integrals needed for the Newtonian solution were first evaluated by Sommerfeld [105] using an adroit substitution. For our analysis we take the approach of using the Weierstrass substitution $s = \tan\frac{x}{2}$, whereby the integral is transformed to

$$\frac{8}{(1-\kappa)^5}\int_{-\infty}^{\infty} \frac{s^2\left(1-s^4\right)}{\left(1+\beta s^2\right)^5} ds, \tag{3.135}$$

where $\beta = \frac{1+\kappa}{1-\kappa}$. Let f be the complex function given by $f(z) = \frac{z^2(1-z^4)}{(1+\beta z^2)^5}$, where f has two poles of order 5 at $z = \pm\beta^{-\frac{1}{2}}i$. The residuals at the poles can be readily calculated and are given by $Res\{f\} = -\frac{5}{256}\beta^{-\frac{7}{2}}\left(\beta^2-1\right)$. Considering the complex integral along a contour C where

$$\oint_C f(z)dz = \int_{C_1} f(z)dz + \int_{C_2} f(z)dz, \tag{3.136}$$

where C_1 is the contour along the real line from $-R$ to R, and C_2 is the upper half circle which is parametrised by $z = Re^{i\theta}$. Equation (3.136) can be written as

$$\int_{-R}^{R} f(s)ds + \int_0^{2\pi} \frac{\left(R^2e^{2i\theta} - R^6e^{6i\theta}\right)}{\left(1+\alpha R^2e^{2i\theta}\right)^5} iRe^{i\theta}d\theta = \oint_C f(z)dz = 2\pi i Res\{f\}. \tag{3.137}$$

As $R \to \infty$ the second integral vanishes and we are left with the identity

$$\int_{-\infty}^{\infty} \frac{s^2\left(1-s^4\right)}{\left(1+\beta s^2\right)^5} ds = \frac{5\pi\left(\beta^2-1\right)}{128\beta^{\frac{7}{2}}}. \tag{3.138}$$

Substituting (3.138) into (3.135) and reintroducing $\beta = \frac{1+\kappa}{1-\kappa}$ we find:

$$\int_0^{2\pi} \frac{\sin^2 x\cos x}{(1-\kappa\cos x)^5} dx = \frac{5\pi\kappa}{4\left(1-\kappa^2\right)^{\frac{7}{2}}}. \tag{3.139}$$

A similar process can be performed to prove the following integrals

$$\int_0^{2\pi} \frac{\sin^2 x}{(1-\kappa\cos x)^3}dx = \frac{\pi}{(1-\kappa^2)^{\frac{3}{2}}}, \quad \int_0^{2\pi} \frac{\sin^2 x}{(1-\kappa\cos x)^4}dx = \frac{\pi}{(1-\kappa^2)^{\frac{5}{2}}},$$
$$\int_0^{2\pi} \frac{\sin^2 x}{(1-\kappa\cos x)^5}dx = \frac{\left(4+\kappa^2\right)\pi}{4\left(1-\kappa^2\right)^{\frac{7}{2}}}, \quad \int_0^{2\pi} \frac{\sin^4 x}{(1-\kappa\cos x)^5}dx = \frac{3\pi}{4\left(1-\kappa^2\right)^{\frac{5}{2}}},$$
$$\int_0^{2\pi} \frac{\sin^2 x\cos x}{(1-\kappa\cos x)^4}dx = \frac{\kappa\pi}{(1-\kappa^2)^{\frac{5}{2}}}, \int_0^{2\pi} \frac{\cos^2 x}{(1-\kappa\cos x)^3}dx = \frac{\left(1+2\kappa^2\right)\pi}{(1-\kappa^2)^{\frac{5}{2}}},$$
$$\int_0^{2\pi} \frac{\cos^2 x}{(1-\kappa\cos x)^4}dx = \frac{\left(1+4\kappa^2\right)\pi}{(1-\kappa^2)^{\frac{7}{2}}}, \int_0^{2\pi} \frac{\cos x}{(1-\kappa\cos x)^2}dx = \frac{2\kappa\pi}{(1-\kappa^2)^{\frac{3}{2}}}.$$
$$\int_0^{2\pi} \frac{\cos x}{(1-\kappa\cos x)^3}dx = \frac{3\kappa\pi}{(1-\kappa^2)^{\frac{5}{2}}}, \int_0^{2\pi} \frac{1}{1-\kappa\cos x}dx = \frac{2\pi}{\sqrt{1-\kappa^2}},$$
$$\int_0^{2\pi} \frac{\sin^2 x\cos x}{(1-\kappa\cos x)^5}dx = \frac{5\pi\kappa}{4\left(1-\kappa^2\right)^{\frac{7}{2}}}.$$

3.9 Asymptomatics for the touching solution

3.9.1 Case 1

Consider an integral of the form

$$\int_0^{2\pi} \frac{f(\theta)}{\left(1-(1-\frac{1}{2}\zeta^2)\cos\theta\right)^m}d\theta \tag{3.140}$$

as $\zeta \to 0$. If we naively try a regular perturbation approach we find that at $\theta = 0$ the leading order term in the dominator is 0. Clearly, this is incorrect as the dominator in (3.140) can never be singular. Hence let us consider some scale δ around the singular point ($\theta = 0$) and expand $\cos(\theta)$ and f. Assuming $f(0) \neq 0$, we have

$$\int_0^{\delta} \frac{2^m f(0)}{(\zeta^2+\theta^2)^m}d\theta \tag{3.141}$$

where the natural scaling for θ around the singular point is ζ, thus we introduce the scaling $\theta = \zeta\phi$. We can see that the local contribution is $O(\zeta^{-2m+1})$ whereas the global contribution from integrating around the circumference is $O(1)$. Thus for leading order we need only consider the singular contribution to leading order (if $m > \frac{1}{2}$). Continuing with the integration gives

$$2^m f(0)\zeta^{-2m+1}\int_0^{\frac{\delta}{\zeta}}\frac{1}{(1+\phi^2)^m}d\phi = 2^{m-1}f(0)\zeta^{-2m+1}\sum_{n=0}^{\infty}\int_0^{\frac{\delta}{\zeta}}(m)_n\frac{(-q)^{n-\frac{1}{2}}}{n!}du$$
$$= 2^m f(0)\zeta^{-2m+1}\phi\sum_{n=0}^{\infty}\frac{\left(\frac{1}{2}\right)_n(m)_n}{\left(\frac{3}{2}\right)_n}\frac{\left(-\phi^2\right)^n}{n!}. \tag{3.142}$$

Here we used the substitution $q=\phi^2$, and Taylor expanded around the origin. By comparing this to the ${}_2F^1$ hypergeometric function we find this is equivalent to

$$2^m f(0)\zeta^{-2m+1}X\,{}_2F^1\left(\frac{1}{2},m,\frac{3}{2},-X^2\right)\Bigg|_0^{\delta/\zeta} = 2^m f(0)\zeta^{-2m+1}\left(\delta\zeta^{-1}\right){}_2F^1\left(\frac{1}{2},m,\frac{3}{2},-(\delta/\zeta)^2\right), \tag{3.143}$$

which we evaluate at the limit as $\delta/\zeta\to\infty$. The limit requires the evaluation of a hyper-geometric function at ∞, which is outside of the radius of convergence of the ${}_2F^1$ function. Using the Euler hypergeometric transform (formula 15.3.7 of Abromvich and Steguns pg 559) which is given by

$${}_2F^1(a,b,c,z) = \frac{\Gamma(c)\Gamma(b-a)}{\Gamma(b)\Gamma(c-a)}(-z)^{-a}F(a,1-c-a,1-b+a,\frac{1}{z})+O((-z)^{-b}), \tag{3.144}$$

we can find that

$$\lim_{R\to\infty}2^m f(0)\zeta^{-2m+1}R\,{}_2F^1\left(\frac{1}{2},m,\frac{3}{2},-R^2\right) \tag{3.145}$$
$$= 2^m f(0)\zeta^{-2m+1}\lim_{R\to\infty}\frac{\Gamma\left(\frac{3}{2}\right)\Gamma\left(m-\frac{1}{2}\right)}{\Gamma(m)\Gamma(1)}\,{}_2F^1\left(\frac{1}{2},0,\frac{3}{2}-m,-\frac{1}{R^2}\right)+O(R^{-2m+1}). \tag{3.146}$$

We now require the constraint that $2m-1>0$. After a little manipulation one can recover

$$\int_0^{\pi}\frac{f(\theta)}{\left(1-(1-\frac{1}{2}\zeta^2)\cos\theta\right)^m}d\theta \sim \frac{f(0)2^{m-1}\pi^{\frac{1}{2}}\Gamma(m-\frac{1}{2})\zeta^{-2m+1}}{\Gamma(m)}. \tag{3.147}$$

As we have halved the singular point by cutting off at $z=0$, (as the singular point is approached from below as $\theta\to 2\pi$ or $\theta\to -0$ as well as from above), we must scale by 2 to get

$$\int_0^{2\pi}\frac{f(\theta)}{\left(1-(1-\frac{1}{2}\zeta^2)\cos\theta\right)^m}d\theta \sim \frac{2^m f(0)\pi^{\frac{1}{2}}\Gamma(m-\frac{1}{2})\zeta^{-2m+1}}{\Gamma(m)}. \tag{3.148}$$

3.9.2 Case 2

Let us suppose that we now consider the case where $f(0) = 0$ and $f'(0) = 0$. Performing a similar analysis to that used for Case 1 gives

$$\int_0^\pi \frac{f(\theta)}{(1-\varepsilon\cos\theta)^m} \sim 2^{m-1} f''(0)\zeta^{-2m+3} \int_0^\infty \frac{\phi^2}{(1+\phi^2)^m} d\phi \tag{3.149}$$

and

$$\int^X \frac{\phi^2}{(1+\phi^2)^m} d\phi = \frac{1}{3} X^3 \, {}_2F^1\left(\frac{3}{2}, m, \frac{5}{2}, -X^2\right). \tag{3.150}$$

Hence we can evaluate the limit to be

$$\frac{1}{3} \lim_{R\to\infty} R^3 \, {}_2F^1\left(\frac{3}{2}, m, \frac{5}{2}, -R^2\right) = \frac{\pi^{\frac{1}{2}}\Gamma(m-\frac{3}{2})}{4\Gamma(m)} \tag{3.151}$$

$$\tag{3.152}$$

for $2m-3 > 0$. We find that, assuming f is 2π periodic ,

$$\int_0^{2\pi} \frac{f(\theta)}{(1-\varepsilon\cos\theta)^m} d\theta = \int_{-\pi}^{\pi} \frac{f(\theta)}{(1-\varepsilon\cos\theta)^m} d\theta \sim \frac{2^{m-2} f''(0)\pi^{\frac{1}{2}}\Gamma(m-\frac{3}{2})\zeta^{-2m+3}}{\Gamma(m)}. \tag{3.153}$$

Moreover, generally one can show that for $n \in \mathbb{N}$

$$\int_0^\infty \frac{\phi^{2n}}{(1+\phi^2)^m} d\phi = \frac{\Gamma\left(n+\frac{3}{2}\right)\Gamma\left(m-n-\frac{1}{2}\right)}{(2n+1)\Gamma(m)}, \tag{3.154}$$

so long as $2m > 2n+1$.

3.10 Appendix: derivation of f_χ

We here present how the force f_χ can be calculated. The problem amounts to finding the leading order contribution of integrals of the form

$$\int_0^{2\pi} \frac{\cos\theta}{(1-\varepsilon\cos\theta)^m} = 2^{m+1}\zeta^{-2m+1} \int_0^\infty \frac{1-\frac{1}{2}\zeta^2\phi^2}{(1+\phi^2-\zeta^2 R)^m}$$
$$\approx 2^{m+1}\zeta^{-2m+1} \int_0^\infty \left\{ \frac{1}{(1+\phi^2)^m} + m\zeta^2 \frac{R}{(1+\phi^2)^{m+1}} - \frac{1}{2}\zeta^2 \frac{\phi^2}{(1+\phi^2)^m} \right\} d\phi, \tag{3.155}$$

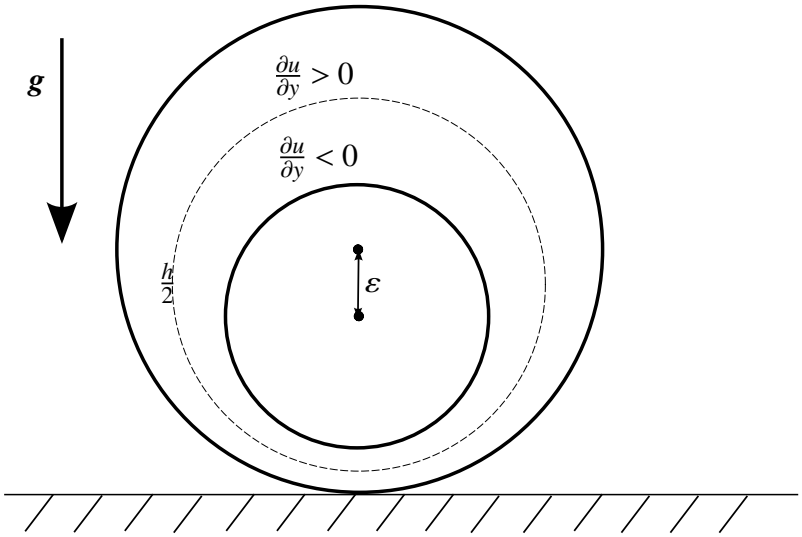

Fig. 3.14 Sketch of the sedimentation solution

where here we have let $R = -\frac{1}{24}\phi^4 - \frac{1}{4}\phi^2 + \frac{1}{8}$. For $m = 1+n$ let the first integral be given by I_0 and the next two terms by $\zeta^2 I_1$ and $\zeta^2 I_2$ respectively. For $m = n+2$ we similarly define J_0, J_1, J_2. Let us also assume that $C = C_0 + \zeta^2 C_1$. Then the periodic constraint (3.77) can be written as

$$(3aKI_0 + C_0 J_0) + \zeta^2 (3aKI_1 + C_0 J_1 + C_1 J_0) = 0. \tag{3.156}$$

The equation for f_χ, equation (3.83), can also be written as

$$\begin{aligned} f_\chi =& 2\Big(3aKI_0 + C_0 J_0 + \zeta^2 \{3aKI_1 + 3aKI_2 + C_0 J_1 + C_0 J_2 + C_1 J_0\}\Big) \\ =& 2\zeta^2 (3aKI_2 + C_0 J_2), \end{aligned} \tag{3.157}$$

where most of the terms cancel out due to (3.156). The integrals I_2 and J_2 can be evaluated to as in Appendix 3.9 to give (3.83).

3.11 Appendix: asymptotics for sedimenting solution.

To analyze the effects that the rocking motion has on the system we directly compare the results to that for the sedimenting case. Recall that the asymptotics for the rocking solution required the use of the DE approximation to form a Reynolds equation. However, for the purely sedimenting solution, the underlying assumption that the flow is a Couette flow is physically invalid. However, the velocity field is symmetric about the center line, whereby the no-slip conditions become $u = 0$ on $y = 0$. The strong symmetry of the system allows one to impose the symmetry condition $\frac{\partial u}{\partial y} = 0$

on $y = \frac{h}{2}$. In such instances the uncertainty as to the sign of the shear rate is removed and a Reynolds equation can be formed, see for instance [49]. Here we give the derivation of the momentum equation by Shukla and Prasad [122] but proceed by performing the touching limit approximation to allow comparison with the snail ball results. We can combine equations (3.61), (3.62) and (3.63) and integrate to give

$$\left|\frac{\partial u}{\partial y}\right|^{n-1} \frac{\partial u}{\partial y} = p'y + c, \tag{3.158}$$

for $\frac{h}{2} > y > 0$ and c being a function of x. By symmetry $\frac{\partial u}{\partial y} > 0$ and thus the $||$ can be ignored. Integrating further gives

$$\frac{\partial u}{\partial y} = \left|p'y + c\right|^{\frac{1}{n}-1} (p'y + c), \tag{3.159}$$

where c is a function of x only. Integrating again further gives

$$u = \frac{|p'y + c|^{\frac{1}{n}+1} - |c|^{\frac{1}{n}+1}}{p'(1 + \frac{1}{n})} + b, \tag{3.160}$$

where b is a function of θ. The undetermined functions of θ can be determined by applying no-slip conditions to give

$$u = \frac{|p'(y - h/2)|^{\frac{1}{n}+1} - |p'h/2|^{\frac{1}{n}+1}}{p'(1 + \frac{1}{n})}. \tag{3.161}$$

This leads to

$$u = (-p')^{\frac{1}{n}} \left\{ \frac{(h/2)^{\frac{1}{n}+1} - (h/2 - y)|^{\frac{1}{n}+1}}{(1 + \frac{1}{n})} \right\} \quad \text{for } 0 < y < \frac{h}{2}. \tag{3.162}$$

A similar expression can be found for $y > \frac{h}{2}$. Using the mass conservation constraint (3.10) one can form a Reynolds equation

$$\frac{1}{a}\frac{\partial}{\partial \theta}\left\{ \frac{2n}{2n+1}\left(-\frac{1}{aK}\frac{\partial p}{\partial \theta}\right)^{\frac{1}{n}} \left(\frac{h}{2}\right)^{2+\frac{1}{n}} \right\} = -h_t = \dot{\varepsilon}\cos\theta. \tag{3.163}$$

Integrating the above leads to

$$\frac{\partial p}{\partial \theta} = -aK\left(a\dot{\varepsilon}\frac{2n+1}{2n}\right)^n \left(\frac{h}{2}\right)^{-(2n+1)} \sin^n\theta, \tag{3.164}$$

where the constant term is zero as, by symmetry, there is no pressure gradient at $\theta = 0$. This is only valid in the regime where $\frac{\partial p}{\partial \theta} < 0$, i.e. $0 < \theta < \pi$. Thus, by symmetry $f_\chi = 0$ and

$$\begin{aligned} f_\varepsilon &= 2 \times a 2^{2n+1} K \left(a\dot{\varepsilon} \frac{2n+1}{2n} \right)^n \delta^{-(2n+1)} \int_0^\pi \frac{\sin\theta^{n+1}}{(1-\kappa\cos\theta)^{2n+1}} \\ &\approx a 2^{2n+2} K \left(-a\zeta\dot{\zeta} \frac{2n+1}{2n} \right)^n 2^{2n+1} \zeta^{-3n} \delta^{-(2n+1)} \int_0^\infty \frac{\phi^{n+1}}{(1+\phi^2)^{2n+1}} d\phi. \end{aligned} \tag{3.165}$$

The $\int \frac{\phi^{n+1}}{(1+\phi^2)^{2n+1}} d\phi = \frac{\phi^{n+2}}{n+2} {}_2F^1\left(\frac{n+2}{2}, 2n+1, \frac{n+4}{2}, -\phi^2\right)$. Again this must be evaluated outside the radius of convergence and the Euler transform must again be used, to give

$$\frac{\Gamma\left(\frac{n+4}{2}\right)\Gamma\left(\frac{3n}{2}\right)}{(n+2)\Gamma(2n+1)} {}_2F^1\left(\frac{n+1}{2}, -(n+1), \frac{1-3n}{2}, -\frac{1}{\phi^2}\right) + O\left(\phi^{-3n}\right). \tag{3.166}$$

Note here that the constraint $n > \frac{1}{2}$ is no longer required. Using (3.166) one can find that $\int_0^\infty \frac{\phi^n}{(1+\phi^2)^{2n+1}} d\phi = \frac{\Gamma\left(\frac{n+4}{2}\right)\Gamma\left(\frac{3n}{2}\right)}{(n+2)\Gamma(2n+1)}$. Thus the viscous resistive force f_ε balanced against the gravitational force in the momentum equation reduces to

$$\frac{a^{n+1} K 2^{4n+3} \Gamma\left(\frac{n+4}{2}\right)\Gamma\left(\frac{3n}{2}\right)}{(n+2)\Gamma(2n+1)} \left(-\dot{\zeta}\right)^n = \zeta^{2n}, \tag{3.167}$$

which leads to the result that $\dot{\zeta}$ is $O(\zeta^2)$. It is interesting to note that equation (3.165) differs from the spherical case given by Singh and Sinha [124] as the integral takes the form

$$f_\varepsilon \sim \int_0^\pi \frac{\sin(\theta)^{n+2}}{(1-\kappa\cos\theta)^{2n+1}} d\theta \tag{3.168}$$

with the extra power of sin arising from the additional dimension. This additional term has the consequence that the leading order asymptomatics for a load bearing force break at $n = \frac{1}{3}$, as noted by Rodin [117] and furthered by Lian et al. [80] .

3.12 Appendix: numerical algorithm.

On each iteration in time, for a given $\varepsilon, \dot{\varepsilon}, \Omega_0, \Omega_h, \phi$, to evolve equations (3.71) through (3.74) in time one is required to find the angular and normal forces acting on the system. To do this one need only calculate the pressure gradient and use equations (3.70) to calculate the forces. The pressure can readily be determined from

the inner wall shear stress τ_0 and the outer wall shear stress τ_h. This is found by solving equations (3.66), (3.67) and (3.69) for τ_0, τ_h and Q.

We can write (3.66), (3.67) and (3.69) as

$$F_i(\boldsymbol{\tau}_0, \boldsymbol{\tau}_h) = Q\mathbf{1}_i, \quad Z_i(\boldsymbol{\tau}_0, \boldsymbol{\tau}_h) = 0, \quad \int_0^{2\pi} f(\boldsymbol{\tau}_0, \boldsymbol{\tau}_h) d\theta = 0. \tag{3.169}$$

Here

$$F_i(\tau_0, \tau_h) = q(\theta_i, t) + \frac{h(\theta_i)U}{2(\tau_{h,i} - \tau_{0,i})} - \frac{h(\theta_i)^2 (G_1(\tau_{h,i}) - G_1(\tau_{0,i}))}{(\tau_{h,i} - \tau_{0,i})^2}$$
$$Z_i = \frac{h(\theta_i)}{\tau_{h,i} - \tau_{0,i}} (G_0(\tau_{h,i}) - G_0(\tau_{0,i})) - U, \quad f_i = \frac{\tau_{h,i} - \tau_{0,i}}{h(\theta_i)},$$

where $\mathbf{1}_i$ is a vector of ones. If we Taylor expand around the exact solution by replacing $\boldsymbol{\tau}_0 = \boldsymbol{\tau}_0^* + \Delta\boldsymbol{\tau}_0, \boldsymbol{\tau}_h = \boldsymbol{\tau}_h^* + \Delta\boldsymbol{\tau}_h$ and $Q = Q + \Delta Q$ and discretize with respect to θ we obtain

$$F_i^* + \sum_j \left\{ \frac{\partial F_i^*}{\partial \tau_{0,j}} \Delta\tau_{0,j} + \frac{\partial F_i^*}{\partial \tau_{h,j}} \Delta\tau_{h,j} \right\} = Q^* + \Delta Q, \tag{3.170}$$

$$Z_i^* + \sum_j \left\{ \frac{\partial Z_i^*}{\partial \tau_{0,j}} \Delta\tau_{0,j} + \frac{\partial Z_i^*}{\partial \tau_{h,j}} \Delta\tau_{h,j} \right\} = 0, \tag{3.171}$$

$$\int_0^{2\pi} f_i^* d\theta = -\sum_j \left\{ \int_0^{2\pi} \frac{\partial f_i^*}{\partial \tau_{0,j}} \Delta\tau_{0,j} + \frac{\partial f_i^*}{\partial \tau_{h,j}} \Delta\tau_{h,j} d\theta \right\}. \tag{3.172}$$

As F, Z, f, τ_0, τ_h are functions of θ, we have introduced the subscripts i, j to indicate that we are evaluating at the i/jth θ node. We have also used the shorthand notation $F_i^* = F_i(\boldsymbol{\tau}_0^*, \boldsymbol{\tau}_h^*)$ and similarly for Z_i^*. As F_i only depends on τ_i, then

$$\frac{\partial F_i^*}{\partial \tau_{hj}} = \frac{\partial F_{[i]}^*}{\partial \tau_{h\,[i]}} \delta_{[i]j} = \left(\frac{\partial F}{\partial \tau_h} \right)_{[i]} \delta_{[i]j} \tag{3.173}$$

with no summation implied with []. Thus we have

$$F_{[i]}^* + \left(\frac{\partial F^*}{\partial \tau_0} \right)_{[i]} \Delta\tau_{0,[i]} + \left(\frac{\partial F^*}{\partial \tau_h} \right)_{[i]} \Delta\tau_{h,[i]} = (Q^* + \Delta Q)\mathbf{1}_{[i]} \tag{3.174}$$

$$Z_{[i]}^* + \left(\frac{\partial Z^*}{\partial \tau_0} \right)_{[i]} \Delta\tau_{0,[i]} + \left(\frac{\partial Z^*}{\partial \tau_h} \right)_{[i]} \Delta\tau_{h,[i]} = 0, \tag{3.175}$$

$$\int_0^{2\pi} f_{[i]}^* d\theta = -\int_0^{2\pi} \left\{ \left(\frac{\partial f^*}{\partial \tau_0} \right)_{[i]} \Delta\tau_{0,[i]} + \left(\frac{\partial f^*}{\partial \tau_h} \right)_{[i]} \Delta\tau_{h,[i]} \right\} d\theta. \tag{3.176}$$

We can invert the linear system (3.174),(3.175), dropping [] notation to find

$$\begin{pmatrix} \Delta\tau_{0,i} \\ \Delta\tau_{h,i} \end{pmatrix} = J_i \begin{pmatrix} \left(\frac{\partial Z^*}{\partial \tau_h}\right)_i & -\left(\frac{\partial F^*}{\partial \tau_h}\right)_i \\ -\left(\frac{\partial Z_i^*}{\partial \tau_0}\right)_i & \left(\frac{\partial F^*}{\partial \tau_0}\right)_i \end{pmatrix} \begin{pmatrix} Q^* + \Delta Q - F_i^* \\ -Z_i^* \end{pmatrix}, \tag{3.177}$$

$$J_i = \left(\left(\frac{\partial F^*}{\partial \tau_0}\right)_i \left(\frac{\partial Z^*}{\partial \tau_h}\right)_i - \left(\frac{\partial F^*}{\partial \tau_h}\right)_i \left(\frac{\partial Z^*}{\partial \tau_0}\right)_i\right)^{-1}.$$

Hence dropping i for convenience and combining with (3.176) gives

$$-\int_0^{2\pi} f^* d\theta - \int_0^{2\pi} \left\{ \frac{J}{h}\frac{\partial f^*}{\partial \tau_0}\left(\frac{\partial Z^*}{\partial \tau_0} + \frac{\partial Z^*}{\partial \tau_h}\right)(Q - F^*) + \left(\frac{\partial F^*}{\partial \tau_0} + \frac{\partial F^*}{\partial \tau_h}\right) Z^* \right\} d\theta = \int_0^{2\pi} \frac{J}{h}\left(\frac{\partial Z^*}{\partial \tau_0} + \frac{\partial Z^*}{\partial \tau_h}\right) d\theta \Delta Q. \tag{3.178}$$

They key to (3.178) is that ΔQ is a function of time only and can be pulled out of the integral. Given an initial array containing the values of τ_0 and τ_h at the θ coordinate locations and an initial guess for Q. We can calculate the correction value ΔQ by equation (3.178). The further correction $\Delta\boldsymbol{\tau}_0, \Delta\boldsymbol{\tau}_h$ can be calculated from (3.177). The initial prediction for $\boldsymbol{\tau}_0, \boldsymbol{\tau}_h$ and Q is then updated and the process is iterated until a given tolerance is reached. As we are working with periodic functions we use the trapezoidal rule to calculate the integrals. We chose the trapezoidal rule over higher order methods such as Simpson's rule, due to its enchanting properties with perodic functions. Deeper insight into this numerical phenomenon can be found in the work by Trefethen et al. [135].

3.13 Derivation of the Dien Elrod approximation

We derive, in a non rigorous manner, the Dien Elrod approximation to give insight into to the inherent assumption. The assumption is that the velocity field can be written as

$$u \sim u_0 + u_1, p \sim p_1, \tag{3.179}$$

where $u_0 \gg u_1$ and u_1, p_1 are of the same order. Then the leading order and second order terms of the momentum equation can be written as

$$\left(\frac{\partial u_0}{\partial x}\right)^{n-1} = 0, \quad n\left(\frac{\partial u_0}{\partial y}\right)^{n-1} \frac{\partial u_1}{\partial y} = \frac{\partial p}{\partial x}, \tag{3.180}$$

whereby one can replace x with $a\theta$. We can solve the above subject to $u_0(0) = U_0, u_0(h) = U_h$ and $u_1(0) = 0, u_1(h) = 0$, which gives

$$u_0 = U_0\left(1 - \frac{y}{h}\right) + U_h\frac{y}{h}, \quad u_1 = -\frac{y(h-y)}{\mu_0}\frac{\partial p}{\partial x}, \tag{3.181}$$

and μ_0 is given in (3.87). Returning to the mass conservation equation (3.10) gives

$$\int_0^h \{u_0 + u_1\}\, dy = -h_t. \tag{3.182}$$

Using equations (3.181) and (3.182) gives rise to the DE equation

$$\frac{\partial}{\partial x}\left(\frac{1}{2}(U_0 + U_h)h^2 - \frac{h^3}{12n\mu_0}\frac{\partial p}{\partial x}\right) = -h_t. \tag{3.183}$$

Replacing μ_0 by its definition gives the DE equation (3.75).

Chapter 4

Carreau Fluid in a Wall Driven Corner Flow: an Inertialess Boundary Layer.

Abstract

Taylor's classical paint scraping problem provides a framework for analyzing wall-driven corner flow induced by the movement of an oblique plane. A study of the dynamics of an inertialess Carreau fluid in such a system is presented. New perturbation results obtained for large relaxation times, and for small relaxation times, are given. These are found to be valid close to, and far from, the corner respectively. When the relaxation time, Γ, is large a loss of uniformity arises in the solution near the region where the shear rate becomes zero, due to the presence of the two walls. We derive a new boundary layer equation, and find two regions of of sizes Γ^{-n} and Γ^{-2}, where n is the power-law index, where a change in behavior occurs. The shear rate is found to be proportional to the perpendicular distance from the line of zero shear. The point of zero shear moves in the order Γ^{-2} layer.

4.1 Introduction

Corner flows of both Newtonian and non-Newtonian fluids have been widely studied. Dean and Montagnon [31] and Moffatt [89] showed that for the flow of an inertialess Newtonian fluid, in plane polar coordinates (r,θ), the stream function $\psi(r,\theta)$ permits similarity solutions of the form $r^{\lambda} f(\theta)$. Dean and Montagnon identified the existence of a critical corner angle for which λ becomes complex. Later Moffatt interpreted these complex values as an infinite series of eddies of decreasing size. An experimental study by Taneda [130] revealed a series of decreasing eddies, thus confirming Moffatt's theoretical predictions.

Following Moffatt's work, Proudman and Asadullah [108] considered the case of two inertialess immiscible Newtonian fluids of different viscosities with a planar contact line and found that the limit to a one phase system differs from Moffat's solution. Later, Henriksen and Hassager [52] studied power-law fluids in a corner region, though due to physical constraints imposed on the power-law model, their results were limited to the parameter regime $0 < n < 2$, where n is the power-law exponent. Likewise, Keiller and Hinch [71] examined a system suspension of ridged

rods in a corner, but neglected the Brownian motion term of the constitutive equation in order to permit a similarity solution. They considered the aligned and unaligned orientations of the rods separately, but found that the solutions gave rise to unphysical eddies.

In this study we consider a two-dimensional incompressible fluid that occupies the region between two semi-infinite planes. One plane, aligned along $\theta = 0$, is moved with constant velocity U which drives the flow. The other plane is fixed at an angle α relative to the moving plane. In the vicinity of the corner, wall effects dominate the flow and inertial terms become negligible, though the inertial effects and thus creeping flow approximation can be used. The problem was first solved by Taylor [133], however, inertial effects were included in a study by Hancock et al. [47] by means of a perturbation expansion for the stream function. The corresponding three-dimensional case was later investigated by Hills and Moffatt [56]. The system has also been analyzed for the case of non-Newtonian fluids. Rielder and Schneider [114] found an exact solution for a power-law fluid in the creeping flow regime, and further considered the effects of leakage at the apex of the corner. Analysis of this geometry is not limited to power-law fluids but can be applied to other constitutive relations, see for instance [60, 123]. The power-law model has the unphysical feature of having zero or infinite shear viscosity in regions where the shear rate tends to zero depending upon whether n is greater than or less than 1. Often an alternative model is needed to obtain correct physical behavior. The most commonly used alternative is the Carreau model, where the kinematic viscosity, ν, is given by

$$\nu = \nu_\infty + (\nu_0 - \nu_\infty)\left(1 + \Gamma^2\dot{\gamma}^2\right)^{\frac{n-1}{2}}, \tag{4.1}$$

where $\dot{\gamma}$ is the generalized shear rate, Γ is the relaxation time and ν_∞ and ν_0 are the infinite shear and zero shear viscosities respectively. In the limit of low shear rates the viscosity approaches Newtonian behavior, thus overcoming the unphysical features of the power-law model. Throughout this chapter, for simplicity we take $\nu_\infty = 0$. In the interialess limit, when $\nu_\infty = 0$, a suitable scaling can be used to eliminate ν_0 from the governing equations.

A Carreau fluid exhibits increased complexity in a wall-driven corner flow. This arises because a Carreau fluid transitions from Newtonian behavior to power-law behavior in the geometry. Consequently, one finds that the physics does not permit a global self-similar solution, such as that which can be found for the case of a purely Newtonian fluid or the case of a purely power-law fluid. As no global solution exists,

our approach will be to consider the solution in two different domains: firstly, in the region far from the corner apex, where the shear rates are low and the solution is approximately Newtonian with a small power-law correction, and secondly, in the vicinity of the corner apex, where one has predominately power-law behavior coupled with a small Newtonian effect. It is worth noting that a global solution can be found for situations where the shear-rate has no radial dependence. This scenario occurs for the shear driven problem. The solution is presented in section (4.9.3).

4.2 Governing equations

The governing equations for the model are given by

$$-\frac{1}{\rho}\nabla p + \nabla\cdot\boldsymbol{\tau} = 0, \tag{4.2}$$

$$\nabla\cdot\mathbf{u} = 0, \tag{4.3}$$

where $\boldsymbol{\tau}$ is the viscous stress tensor which is given by $\boldsymbol{\tau} = \nu\dot{\boldsymbol{\gamma}}$, where $\dot{\boldsymbol{\gamma}} = \nabla\mathbf{u} + \nabla\mathbf{u}^T$ is the rate of deformation tensor. The kinematic viscosity, ν, is given by (4.1) with the generalized shear rate $\dot{\gamma}^2 = \frac{1}{2}\dot{\boldsymbol{\gamma}} : \dot{\boldsymbol{\gamma}}$. As we are considering a two-dimensional geometry we can remove the mass conservation constraint by introducing a stream function, ψ, whereby $(u, v) = (\frac{1}{r}\frac{\partial\psi}{\partial\theta}, -\frac{\partial\psi}{\partial r})$. Under this transform the shear rate and components of the stress tensor are given by

$$\tau_{rr} = -\tau_{\theta\theta} = 2\mu\frac{\partial}{\partial r}\left\{\frac{1}{r}\frac{\partial\psi}{\partial\theta}\right\}, \quad \tau_{r\theta} = \mu\left(\frac{1}{r^2}\frac{\partial^2\psi}{\partial\theta^2} - r\frac{\partial}{\partial r}\left\{\frac{1}{r}\frac{\partial\psi}{\partial r}\right\}\right), \tag{4.4}$$

$$\dot{\gamma}^2 = 4\left(\frac{\partial}{\partial r}\left\{\frac{1}{r}\frac{\partial\psi}{\partial\theta}\right\}\right)^2 + \left(\frac{1}{r^2}\frac{\partial^2\psi}{\partial\theta^2} - r\frac{\partial}{\partial r}\left\{\frac{1}{r}\frac{\partial\psi}{\partial r}\right\}\right)^2. \tag{4.5}$$

The pressure can be eliminated by taking the curl of equation (4.2) upon which we find that $\boldsymbol{\tau}$ must satisfy

$$r^{-1}\left(-\frac{1}{r}\frac{\partial^2\tau_{r\theta}}{\partial\theta^2} + \frac{\partial}{\partial r}\left\{\frac{1}{r}\frac{\partial}{\partial r}(r^2\tau_{r\theta})\right\} + \frac{1}{r}\frac{\partial^2}{\partial r\partial\theta}\{r(\tau_{\theta\theta} - \tau_{rr})\}\right) = 0. \tag{4.6}$$

The above equation is subject to no-slip and moving wall boundary conditions on the fixed and moving planes respectively, thus

$$\begin{aligned} \psi = 0, \quad \frac{1}{r}\frac{\partial\psi}{\partial\theta} &= U, \quad \text{on } \theta = 0, \\ \psi = 0, \quad \frac{\partial\psi}{\partial\theta} &= 0, \quad \text{on } \theta = \alpha. \end{aligned} \tag{4.7}$$

4.3 The Far Corner Approximation

We non-dimensionalize the system through scaling the velocity by U and r by a length scale L. For convenience we let $\tilde{\Gamma} = U^{-1}L\Gamma$ and hence forth suppress the $\sim$. We seek a solution in the form of a regular perturbation series

$$\psi \sim \psi_0 + \Gamma^2\psi_1 + \Gamma^4\psi_2 + \dots \tag{4.8}$$

in the limit as $\Gamma \to 0$. In this limit the natural expansion of the viscosity is given by

$$\left[1+\Gamma^2\dot{\gamma}^2\right]^{\frac{n-1}{2}} \sim 1 + \left(\frac{n-1}{2}\right)\dot{\gamma}^2\Gamma^2 + \frac{1}{2}\left(\frac{n-1}{2}\right)\left(\frac{n-3}{2}\right)\dot{\gamma}^4\Gamma^4 + O(\Gamma^6). \tag{4.9}$$

Substituting the expansion for the viscosity into the momentum equation (4.6) and imposing the boundary conditions (4.7) one can see that the zeroth order term reduces to the Newtonian system, which is given by the biharmonic equation. The solution is known to be given by [10]

$$\psi_0 = -rU\left(B\sin(\theta) + C\theta\cos(\theta) + D\theta\sin(\theta)\right), \tag{4.10}$$

where B, C, D are constants given by

$$B = \frac{-\alpha^2}{\alpha^2 - \sin^2(\alpha)}, \quad C = \frac{\sin^2(\alpha)}{\alpha^2 - \sin^2(\alpha)}, \quad D = \frac{\alpha - \sin(\alpha)\cos(\alpha)}{\alpha^2 - \sin^2(\alpha)}. \tag{4.11}$$

At $O(\Gamma)$ the momentum equation can be written as

$$\nabla^4\psi_1 = \kappa\nabla\times\nabla\cdot(\dot{\gamma}_0^2\dot{\boldsymbol{\gamma}}_0), \tag{4.12}$$

where $\kappa = \frac{n-1}{2}$, $\dot{\gamma}_0$ and $\dot{\boldsymbol{\gamma}}_0$ are the zeroth order terms of the shear rate and rate of deformation tensor, given by $\dot{\gamma}_0 = 2r^{-2}\left(C\sin(\theta) - D\cos(\theta)\right), \dot{\boldsymbol{\gamma}}_0 = \dot{\gamma}_0(\boldsymbol{e}_r\boldsymbol{e}_\theta + \boldsymbol{e}_\theta\boldsymbol{e}_r)$, where $\boldsymbol{e}_r, \boldsymbol{e}_\theta$ are unit vectors in the r, θ directions. Equation (4.12) can be expressed as

$$\nabla^4\psi_1 = 8\kappa r^{-5}\left\{\frac{\partial^2}{\partial\theta^2}\left[(C\sin\theta - D\cos\theta)^3\right] - 3\left(C\sin\theta - D\cos\theta\right)^3\right\}. \tag{4.13}$$

For ψ_1 to have consistent dimensions we seek a solution in the form $\psi_1 = r^{-1}f_1(\theta)$. Thus (4.13) reduces to

$$f_1^{iv} + 10f_1'' + 9f_1 = 8\kappa\left\{\frac{\partial^2}{\partial\theta^2}\left[(C\sin\theta - D\cos\theta)^3\right] - 3\left(C\sin\theta - D\cos\theta\right)^3\right\}, \tag{4.14}$$

subject to the boundary conditions $f(0) = f'(0) = f(\alpha) = f'(\alpha) = 0$. This can be simplified to

$$f_1(\theta) = (A_1 + B_1\theta)\cos(3\theta) + (C_1 + D_1\theta)\sin 3\theta + (E_1 + F_1\theta)\cos\theta + (G_1 + H_1\theta)\sin\theta, \tag{4.15}$$

$$\psi_1 = r^{-1}\{(A_1 + B_1\theta)\cos(3\theta) + (C_1 + D_1\theta)\sin 3\theta + (E_1 + F_1\theta)\cos\theta + (G_1 + H_1\theta)\sin\theta\}, \tag{4.16}$$

where

$$\begin{aligned} B_1 &= \frac{1}{2}\left(C^3 - 3CD^2\right)\kappa, \quad D_1 = \frac{1}{2}\left(3DC^2 - D^3\right)\kappa, \\ F_1 &= \frac{3}{2}\left(C^3 + D^2C\right)\kappa, \quad H_1 = \frac{3}{2}\left(D^3 + DC^2\right)\kappa. \end{aligned} \tag{4.17}$$

The constants A_1, C_1, E_1, G_1 are then derived from the boundary conditions. For simplicity we give the result for the case $\alpha = \pi/2$, for which

$$\begin{aligned} \psi_1 = \frac{\kappa}{r(\pi^2-4)^3}\Big\{&\left(8\pi^3 - 8(3\pi^2-4)\theta\right)\cos(3\theta) + \left(2\left(\pi^4 - 16\right) - 4\pi\left(\pi^2 - 12\right)\theta\right)\sin(3\theta) \\ &\left(-8\pi^3 + 24\left(\pi^2+4\right)\theta\right)\cos\theta + \left(-2\left(3\pi^4 + 16\right) + 12\left(\pi^2+4\right)\theta\right)\sin\theta\Big\}. \end{aligned} \tag{4.18}$$

Proceeding to find the second order contribution leads to the partial differential equation

$$\nabla^4\psi_2 = \nabla\times\nabla\cdot\left[\kappa\dot{\gamma}_1^2\dot{\boldsymbol{\gamma}}_0 + \kappa\dot{\gamma}_0^2\dot{\boldsymbol{\gamma}}_1 + \kappa_2\dot{\gamma}_0^4\dot{\boldsymbol{\gamma}}_0\right], \tag{4.19}$$

where $\kappa_2 = (n-1)(n-3)/8$, $\dot{\gamma}_1$, and $\dot{\boldsymbol{\gamma}}_1$ are the $O(\Gamma^2)$ terms of the shear rate and rate of deformation tensor and can be expressed as

$$\dot{\gamma}_1^2 = 2\Gamma^{-2}r^{-4}\left(f_0'' + f_0\right)\left(f_1'' - 3f_1\right), \quad \dot{\boldsymbol{\gamma}}_1 = r^{-3}\begin{pmatrix} -4f_1' & f_1'' - 3f_1 \\ f_1'' - 3f_1 & 4f_1' \end{pmatrix}, \tag{4.20}$$

respectively. We seek a solution in the form $\psi_2 = r^{-3}f_2(\theta)$, and the resulting ordinary differential equation (ODE) is

$$f_2^{iv}(\theta) + 34f_2'' + 225f_2 = N_1'' - 15N_1 - 8N_2'', \tag{4.21}$$

where

$$N_1 = 3\kappa\left(f_0'' + f_0\right)^2\left(f_1'' - 3f_1\right) + \kappa_2\left(f_0'' + f_0\right)^5, N_2 = -4\kappa\left(f_0'' + f_0\right)^2 f_1'. \tag{4.22}$$

Equation (4.21) could be solved analytically but as the solution is rather cumbersome we instead choose to solve it numerically to give $f_2(\theta)$. The above series suffers from lack of uniformity throughout the entire domain. If one considers the ratio of the first two terms, $\Gamma^2\psi_1/\psi_0 \sim \Gamma^2 r^{-2}$, it can be seen that the assumption $\Gamma^2\psi_1 \ll \psi_0$ fails when $r \sim \Gamma$. Physically, the loss of uniformity arises from the increase in shear rate as the apex of the corner is approached, thus the term $\Gamma^2\dot{\gamma}^2$ becomes significant in the viscosity expansion (4.9). Upon inspection, one can see that the solution is geometric in nature with r^{-2} acting analogous to a geometric ratio. Therefore, one might suspect that a rational fraction approximation might give a more uniform approximation. For simplicity we apply Shanks transform to the first three terms of the perturbation series, from which we obtain the following approximation of the stream function:

$$\psi_{Shank}(r,\theta) = f_0\left(\frac{f_0 f_1 - \Gamma^2 r^{-2}\left(f_2 f_0 - f_1^2\right)}{f_0 f_1 - \Gamma^2 r^{-2} f_2 f_0}\right). \tag{4.23}$$

The streamlines are given in Fig.4.1a for the case of a shear thinning fluid and Fig.4.1b for a shear thickening fluid. The Newtonian solution is plotted together with the first and second order perturbation terms and the Shanks transform. To prove the validity of the expansion the complete system of equations, i.e. equations (4.2), (4.3), is solved numerically using the finite element solver COMSOL Multiphysics. A Newtonian velocity field was imposed far from the corner with the moving and no-slip boundary conditions applied along the walls. Note that the first and second order terms quickly become invalid as the corner is approached, and thus only provide an appropriate correction from the zeroth order solution far from the corner. We see that the Shanks transform improves the convergence remarkably well for the shear thickening fluid even as the corner is approached, despite the underlying assumptions becoming invalid. However, for the shear thinning fluid, the Shanks transform does not perform as well. These results indicate that for shear thinning fluids the streamlines undershoot those of the Newtonian fluid, and that for shear-thickening fluids, the streamlines overshoot the Newtonian solution. A possible explanation for this is that as the viscosity of the system is reduced through shear thinning, the wall exerts a small shear stress on the fluid. A fluid element must be then be closer to the moving wall before it can be dragged off horizontally.

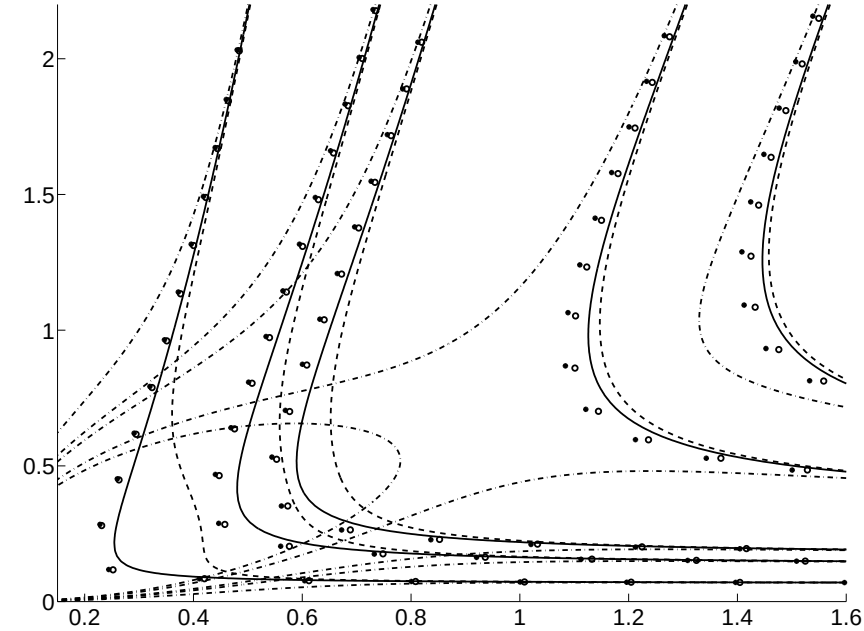

(a)

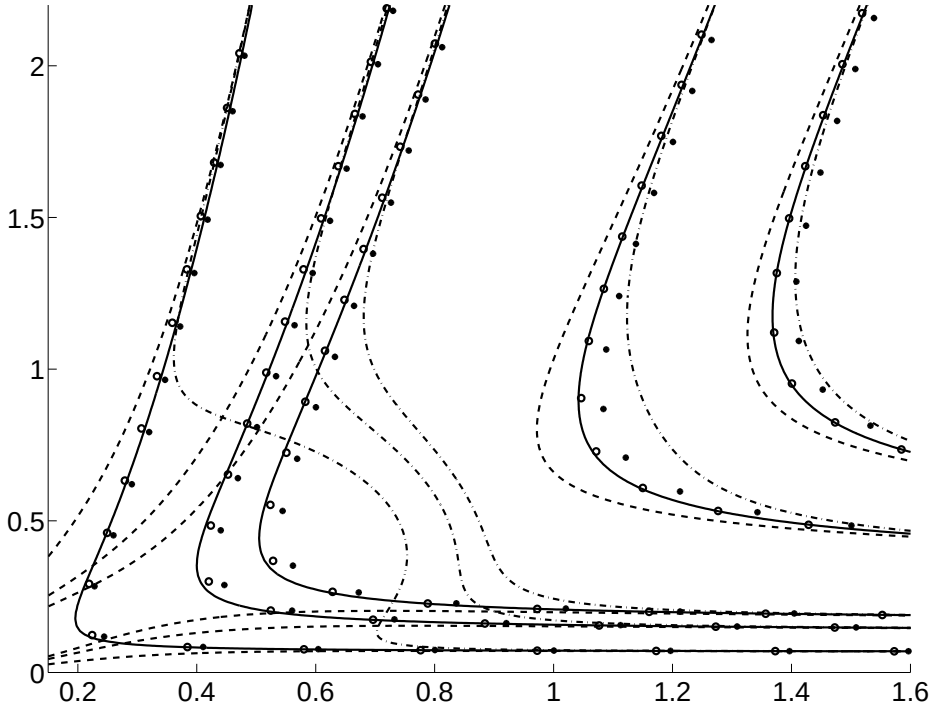

(b)

Fig. 4.1 A plot of the streamlines for $\Gamma = 0.6$ for (a) $n = 0.5$ and (b) $n = 1.7$ with a corner angle of $\alpha = \frac{\pi}{2}$. The first and second order perturbation solutions are given by the dashed and dot-dashed lines respectively. The exact numerical solution is denoted by the solid black line with the open circles and solid circles denoting the Shanks and Newtonian solutions respectively.

4.4 Near Corner Approximation

To further extend the domain in which analytic results can be found, we will now focus on the region closest to the corner where the shear rates are extremely large. We now consider the asymptotic series as $\Gamma \to \infty$. Although on first glance this may be regarded as a separate problem to the former case, where we considered the limit as $\Gamma \to 0$, this is not in fact the case. For the case of $\Gamma \to 0$, if one considers rescaling the radius by $r = \Gamma^2 \rho$ and stream function by $\psi \sim \Gamma^2 \Psi_0(\rho,\theta) + \Gamma^4 \Psi_1(\rho,\theta) + \dots$ such that ρ, Ψ are $\mathcal{O}(1)$, one would find that the problem is equivalent to the large Γ limit. As we expect the leading order behavior to be as a power-law fluid, the appropriate series expansions for the stream function and viscosity are

$$\psi \sim \psi_0 + \Gamma^{-2}\psi_1 + \Gamma^{-4}\psi_2 + \dots \tag{4.24}$$

and

$$\left[1 + \Gamma^2 \dot{\gamma}^2\right]^{\frac{n-1}{2}} \dot{\boldsymbol{\gamma}} \sim \Gamma^{n-1}\dot{\gamma}^{n-1}\dot{\boldsymbol{\gamma}} + \kappa\Gamma^{n-3}\dot{\gamma}^{n-3}\dot{\boldsymbol{\gamma}} + \dots \tag{4.25}$$

respectively. Comparing orders of Γ, the momentum equation gives

$$\nabla \times \nabla \cdot \left\{\dot{\gamma}_0^{n-1}\dot{\boldsymbol{\gamma}}_0\right\} = \mathbf{0}: \quad \text{at order } \mathcal{O}(\Gamma^{n-1}), \tag{4.26}$$

$$\nabla \times \nabla \cdot \left\{(n-1)\dot{\gamma}_1\dot{\gamma}_0^{n-2}\dot{\boldsymbol{\gamma}}_0 + \dot{\gamma}_0^{n-1}\dot{\boldsymbol{\gamma}}_1 + \kappa\dot{\gamma}_0^{n-3}\dot{\boldsymbol{\gamma}}_0\right\} = \mathbf{0}: \quad \text{at order } \mathcal{O}(\Gamma^{n-3}). \tag{4.27}$$

The zeroth order solution, ψ_0, was obtained previously by Rielder and Schneidier [114], where $\psi_0 = r g_0(\theta)$ and g_0 is given by the expression

$$g_0(\theta) = \left(1 - \frac{J_1(\theta)}{J_1(\alpha)}\right)\sin\theta + \frac{J_2(\theta)}{J_1(\alpha)}\cos\theta, \tag{4.28}$$

where

$$J_1(\theta) = \int_0^\theta |F(\theta')|^{\frac{1}{n}} \cos(\theta')d\theta', \quad J_2(\theta) = \int_0^\theta |F(\theta')|^{\frac{1}{n}} \sin(\theta')d\theta', \tag{4.29}$$

with

$$F(\theta) = \begin{cases} \sin(\sqrt{n(2-n)}(\theta - \theta_\infty)) & \text{for } n < 2, \\ \sqrt{(\theta - \theta_\infty)} & \text{for } n = 2, \\ \sinh(\sqrt{n(n-2)}(\theta - \theta_\infty)) & \text{for } n > 2. \end{cases} \tag{4.30}$$

The parameter θ_∞ is found by requiring that $J_2(\alpha) = 0$. The solution for g_0 can be obtained from analysis of the momentum equation which reduces to

$$n(n-2)|g_0 + g_0''|^{n-1}(g_0 + g_0'') = \left[|g_0 + g_0''|^{n-1}(g_0 + g_0'')\right]'', \tag{4.31}$$

where $'$ denotes differentiation with respect to θ. The solution for $g_0 + g_0''$ can be found readily to give

$$\operatorname{sgn}(g_0 + g_0'')|g_0 + g_0''|^n = \begin{cases} A\sin(\sqrt{n(2-n)}(\theta - \theta_\infty)) & \text{for } n < 2, \\ A(\theta - \theta_\infty) & \text{for } n{=}2, \\ A\sinh(\sqrt{n(n-2)}(\theta - \theta_\infty)) & \text{for } n > 2, \end{cases} \tag{4.32}$$

where $A^{-\frac{1}{n}} = J_1(\alpha)|n(n-2)|^{\frac{1}{2n}}$. Equations (4.28)-(4.29) can then be obtained by the method of variation of parameters and applying the constraints $g_0(0) = g_0(\alpha) = g_0'(\alpha) = 0$ and $g_0'(0) = 1$. We will now focus our attention on the perturbed partial differential equation (PDE) (4.27). On dimensional grounds we will seek a solution of the form $\psi_1 = r^3 g_1(\theta)$. One can examine the region where the series is valid prior to the calculation of g_1. If one assumes g_1 is $O(1)$, and as ψ_0 and ψ_1 increase as r and r^3 respectively, then the first order solution loses its uniformity again when ψ_0/ψ_1 is $O(1)$, i.e. when r is $O(\Gamma^{-1})$. We can see how this relates to the far from wall approximation by using the innermost scaling $r = \Gamma^2\rho$. In terms of the scaled system, the solution loses its uniformity when $r \sim \Gamma$, (that is $\rho \sim \Gamma^{-1}$). This corresponds to the same region as where the Newtonian solution loses uniformity. In effect, we have sandwiched the region of non-uniformity from above and from below. The zeroth and first order terms for the shear rate and rate of strain tensors can be written as

$$\dot{\gamma}_0 = r^{-1}\left|g_0 + g_0''\right|, \quad \dot{\boldsymbol{\gamma}}_0 = r^{-1}\begin{pmatrix} 0 & g_0 + g_0'' \\ g_0 + g_0'' & 0 \end{pmatrix},$$
$$\dot{\gamma}_1 = r \cdot \operatorname{sgn}\left\{\left(g_0'' + g_0\right)\right\} \cdot \left(g_1'' - 3g_1\right), \quad \dot{\boldsymbol{\gamma}}_1 = r\begin{pmatrix} 4g_1' & g_1'' - 3g_1 \\ g_1'' - 3g_1 & -4g_1' \end{pmatrix}. \tag{4.33}$$

Substituting (4.33) into the 1st order momentum equation (4.27) leads to the ODE

$$-\frac{d^2}{d\theta^2}\left\{n|g_0 + g_0''|^{n-1}(g_1'' - 3g_1) + \kappa_p|g_0 + g_0''|^{n-2}\right\} + 8(n-3)\frac{d}{d\theta}\left\{|g_0 + g_0''|^{n-1}g_1'\right\}$$
$$+(n-2)(n-4)\left\{n|g_0 + g_0''|^{n-1}(g_1'' - 3g_1) + \kappa_p|g_0 + g_0''|^{n-2}\right\} = 0, \tag{4.34}$$

where

$$\kappa_p = \operatorname{sgn}\left\{\left(g_0'' + g_0\right)\right\}\kappa. \tag{4.35}$$

g_1 is subject to the homogeneous conditions

$$g_1(0) = g_1'(0) = g_1(\alpha) = g_1'(\alpha) = 0. \tag{4.36}$$

Equation (4.34) has a regular singular point when $g_0 + g_0'' = 0$. From equation (4.32) it can be seen that this occurs when $\theta = \theta_\infty$. For convenience we now shift the coordinate system so that $\theta = \theta_\infty$ maps to $\theta = 0$. One would expect difficulties to arise in the formulation as $\dot{\gamma} \to 0$, as the expansion for the viscosity (4.25) will clearly fail. This problem is rectified later in this chapter. As no exact closed form analytical solution to equation (4.34) can be found except for special parameter choices (see appendix 4.9.1), we proceed by seeking the homogeneous solution to (4.34) and finding the inhomogeneous result by the method of variation of parameters. To find the general solution we will seek a series in the form

$$g_1(\theta) = \sum_{i=0}^{\infty} g_i(\theta)^{i+\beta}, \tag{4.37}$$

and use the series expansion

$$\begin{aligned} g_0 + g_0'' \sim \operatorname{sgn}(J_1(\alpha)\theta)|J_1(\alpha)|^{-1} n^{\frac{1}{2n}} |2-n|^{\frac{1}{2n}} |\theta|^{\frac{1}{n}} \Bigg[1 + \frac{(n-2)}{6}\theta^2 \\ - \frac{(n-2)^2(2n-5)}{360}\theta^4 \Bigg] + O\left(\theta^{6+\frac{1}{n}}\right) \quad \text{for } n \neq 2\,, \end{aligned} \tag{4.38}$$

which is obtained from equation (4.32). Substituting the series (4.37) and (4.38) into (4.34), one can see that for a non-trivial series expansion β must satisfy

$$\beta(\beta-1)(n\beta-(n+1))(n\beta-(2n+1)) = 0. \tag{4.39}$$

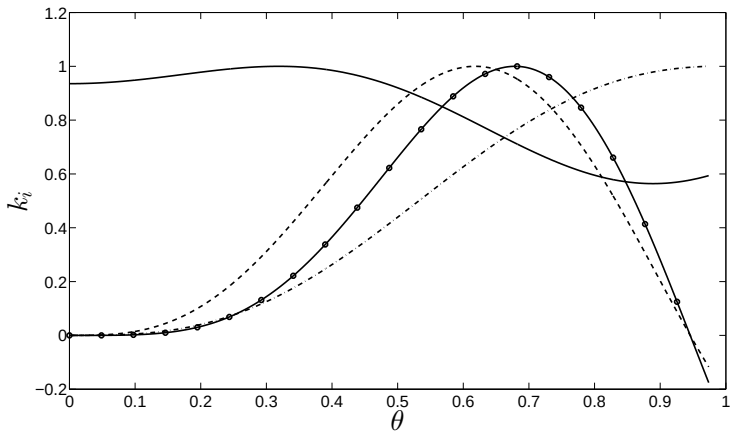

Fig. 4.2 The functions k_1, k_2, k_3 and k_4 for $n = 0.5$ and are given by the solid, dashed, dot-dashed and circular marker lines respectively.

The roots of (4.39) allow one to construct the four linearly independent solutions which can be written as (for $\frac{1}{n} \notin \mathbb{N}$,)

$$
\begin{aligned}
k_1 &\sim 1 + \frac{3}{2}\theta^2 + \frac{25n-51}{8(3n-1)}\theta^4 + \ldots, \\
k_2 &\sim \theta\left(1 + \frac{1}{6}\frac{(14n-27)}{(2n-1)}\theta^2 - \frac{128n^4 - 2136n^3 + 7258n^2 - 8001n + 2025}{120(2n-1)(3n-1)(4n-1)}\theta^4 + \ldots\right), \\
k_3 &\sim \theta^{1+\frac{1}{n}}\left(1 + \frac{1}{2}\frac{(n-2)(2n^2+33n+25)}{(2n+1)(3n+1)}\theta^2\right. \\
&\left. - \frac{(n-2)(48n^6 - 116n^5 + 220n^4 - 18095n^3 + 11362n^2 + 31171n + 8170)}{360(2n+1)(3n+1)(4n+1)(5n+1)}\theta^4 + \ldots\right), \\
k_4 &\sim \theta^{2+\frac{1}{n}}\left(1 - \frac{6n^3 - 53n^2 + 65n + 42}{6(3n+1)(4n+1)}\theta^2\right. \\
&\left. + \frac{336n^7 - 716n^6 - 6516n^5 + 47975n^4 - 93312n^3 + 16385n^2 + 11380}{360(2n+1)(3n+1)(4n+1)(5n+1)(6n+1)}\theta^4 + \ldots\right).
\end{aligned}
\tag{4.40}
$$

It is clear that the homogeneous solution is unphyiscal for $\theta < 0$ as for certain values of n the solution may be complex, moreover, the functions k_3 and k_4 are never smooth at the point $\theta = 0$. The way to overcome this is by separating the solution into two domains for $\theta > 0$ and $\theta < 0$, and then matching the solution across the boundary $\theta = 0$. The homogeneous equation, which can be seen by setting $\kappa_p = 0$ in equation (4.34), is invariant under the transformation $\theta \to -\theta$. We thus separate the solution

into

$$g_{homo} = \begin{cases} A^+k_1(\theta) + B^+k_2(\theta) + C^+k_3(\theta) + D^+k_4(\theta) & \theta > 0, \\ A^-k_1(-\theta) + B^-k_2(-\theta) + C^-k_3(-\theta) + D^-k_4(-\theta) & \theta < 0. \end{cases} \tag{4.41}$$

We later show that $A^+ = A^-, B^+ = -B^-, C^+ = C^-$ and $D^+ = -D^-$, the functions k_1, k_3 would not appear in the Poiseuille analysis due to symmetry. The homogenous functions are plotted in Fig.(4.2) up to θ_∞ for $\alpha = \pi/2$. The inhomogeneous solution can again be found by seeking a power-law solution. We find that

$$k_p = \operatorname{sgn}(\theta)|J_1(\alpha)|\left(n^{\frac{1}{2n}}|n-2|^{\frac{1}{2n}}\right)^{-1}\theta^{2-\frac{1}{n}}\left(-\frac{n}{2(2n-1)}\right.$$
$$\left.-\frac{\left(12n^4-60n^3+187n^2-81n+2\right)n(n-2)}{12(4n-1)(3n-1)(3n-2)(2n-1)}\theta^2+\dots\right). \tag{4.42}$$

The integer singularities can be resolved by the introduction of logarithmic terms, see appendix 4.9.4. Equation (4.42) gives the complete outer-solution, however, for matching over the boundary we need only consider the limit as $\theta \to 0$. To do this we keep the lowest order terms in θ for k_1 through k_4 and evaluate the integral (4.42). It is of note that the leading order behavior can be found more directly without obtaining the full solution. This is presented in the appendix. Evaluation of either method results in the expression

$$\psi_1 \sim \begin{cases} -\frac{n}{2(2n-1)}J_1(\alpha)\left(n^{\frac{1}{2n}}(n-2)^{\frac{1}{2n}}\right)^{-1}\Gamma^{-2}r^3\theta^{2-\frac{1}{n}} + \text{ homogeneous terms} & \text{as } \theta \to 0^+, \\ \frac{n}{2(2n-1)}J_1(\alpha)\left(n^{\frac{1}{2n}}(n-2)^{\frac{1}{2n}}\right)^{-1}\Gamma^{-2}r^3(-\theta)^{2-\frac{1}{n}} + \text{ homogeneous terms} & \text{as } \theta \to 0^-. \end{cases} \tag{4.43}$$

The asymptotic behavior of g_0 as $\theta \to 0$ can be found by solving (4.38) and keeping the first term on the left hand side of the series. The equation can be integrated to give a solution which can be written in terms of hyper-geometric functions. However, for the case of $\frac{1}{n} \notin \mathbb{N}$, if we take the leading order term in the Taylor series we find

$$g_0^{\pm} \sim r\sin(\theta+\theta_\infty) + C_0^{\pm}r\left((\pm\theta)^{2+\frac{1}{n}}+\dots\right), \quad \text{as} \quad \theta \to \pm 0, \tag{4.44}$$

where the first term, which arises from the homogeneous term in equation (4.32), does not contribute to the shear rate and $C_0^{\pm}$ is given by

$$C_0^{\pm} = \pm\frac{n^2\operatorname{sgn}(J_1(\alpha))}{(2n+1)(n+1)}|J_1(\alpha)^{-1}|n^{\frac{1}{2n}}(|n-2|)^{\frac{1}{2n}}. \tag{4.45}$$

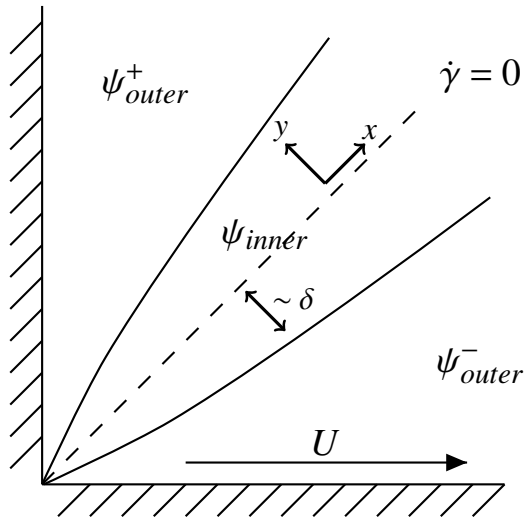

Fig. 4.3 Sketch of boundary layer system.

We can see that the stream function ψ behaves as $O(1)$ where the first order term has fractal powers of $\theta^{1+\frac{1}{n}}, \theta^{2-\frac{1}{n}}$. The stream function is uniformly valid if $\theta \to 0$ for $2 - \frac{1}{n} > 0$. However, the shear rate and thus the stress tensor, are not uniformly valid for any $n > 0$.

It is clear that the solution breaks down along the line $\theta = 0$ due to the shift from power law to Newtonian behavior. To analyze this change in physical behavior we assume that a boundary layer of unknown thickness exists around $\theta = 0$. We adopt Cartesian variables as polar coordinates offer no advantage, and make use of the "trick" proposed by Renardy [112]. We choose our Cartesian system such that x, y are parallel and perpendicular to the line $\theta = 0$ respectively (see Fig.4.3). Let us now suppose that the boundary layer has thickness δ which leads to the introduction of the scalings $y = \delta Y, x = X$. For the purpose of matching the outer solution, we note that the polar coordinates are related to the Cartesian coordinates by $r \sim X, \theta \sim \delta Y/X$. In the inner boundary layer the scaling of the stream function remains unknown, and we thus use an arbitrary scaling

$$\psi_{inner} = \Delta_0 \Psi + g(\theta_\infty) X + \delta g'(\theta_\infty) Y, \tag{4.46}$$

where X, Y, Ψ are $O(1)$ and the orders of δ and Δ_0 remain to be determined. The last two terms in equation (4.46) are included to account for the homogeneous term in equation (4.44). Physically these terms represent a constant velocity flowing into the boundary layer, but have no effect on the momentum equation. Using the afore-mentioned scalings it useful to note that the velocity gradients are now given

by

$$u_x = -v_y = -\Delta_0\delta^{-1}\Psi_{XY}, v_x = \Delta_0\Psi_{XX}, u_y = -\Delta_0\delta^{-2}\Psi_{YY}. \tag{4.47}$$

In reality the X derivatives should be small compared to the Y derivatives as no change in the velocity gradients occurs in the outer solution in this direction. In Cartesian variables the momentum equation (4.6) can be written as

$$\left(\frac{\partial^2}{\partial x^2} - \frac{\partial^2}{\partial y^2}\right)\tau_{xy} + \frac{\partial^2}{\partial x \partial y}\left(\tau_{yy} - \tau_{xx}\right) = 0. \tag{4.48}$$

Substituting (4.46) into (4.6) and keeping the lowest order terms, one finds

$$\nabla \times \nabla \cdot \left\{\left(1 + \Gamma^2\Delta_0^2\delta^{-4}\Psi_{YY}^2\right)^{\frac{n-1}{2}} \Delta_0\delta^{-2}\Psi_{YY}\mathbf{e}_x\mathbf{e}_y\right\} = \mathbf{0}. \tag{4.49}$$

We now argue that within this layer there must be a transition between Newtonian and non-Newtonian behavior. In the power-law region, the shear-dependent term $\Gamma^2\dot{\gamma}^2$ dominates the $+1$ term in the viscous equation (4.1), and likewise in the Newtonian case the $+1$ term dominates over the shear term, thus for a transition to occur we require that they are both of the same order. Hence $\Gamma\Delta_0\delta^{-2}$ must be $O(1)$, thus giving the first condition, $\Delta_0 = \Gamma^{-1}\delta^2$.

Substituting for Y and keeping the leading order terms gives

$$\left[\left(1 + \Psi_{YY}^2\right)^{\frac{n-1}{2}} \Psi_{YY}\right]_{YY} = 0, \tag{4.50}$$

which we will refer to throughout as “the boundary layer equation". We can readily see that this PDE permits similarity solutions of the form

$$\Psi = X^b\phi(X^{-\frac{b}{2}}Y). \tag{4.51}$$

The constant b is determined by requiring that the inner solution must match up to the outer solution $\psi = r\theta^{2+\frac{1}{n}} \sim \delta^{2+\frac{1}{n}}X^{-(1+\frac{1}{n})}Y^{2+\frac{1}{n}}$. This requires that b satisfies $b - \frac{b}{2}\left(2 + \frac{1}{n}\right) = -(1 + \frac{1}{n})$, which leads to $b = 2 + 2n$. The boundary layer equation subsequently becomes

$$\Psi = X^{2+2n}\phi(\chi), \quad \left[\left(1 + \phi''^2\right)^{\frac{n-1}{2}} \phi''\right]'' = 0, \tag{4.52}$$

where here $'$ denotes differentiation with respect to χ, where $\chi = X^{-(1+n)}Y$. This matching condition is satisfied if $\phi \sim \chi^{2+\frac{1}{n}}$ as $\chi \to \infty$. Integrating twice and setting

the constant term to be zero we have the non-linear second order ODE

$$\left[1+\phi''^2\right]^{\frac{n-1}{2}}\phi'' = A_b\chi. \tag{4.53}$$

Though no general closed form solution to the above equation can be found, the asymptotic behavior can be readily seen. First let us consider the case as $\chi \to \infty$, whereby the left-hand side of (4.53) must become large. This requires ϕ'' to become large and thus the +1 term becomes negligible, hence $\left[1+\phi''^2\right]^{\frac{n-1}{2}}\phi'' \approx (\phi'')^n$. Thus $\phi'' \sim \chi^{\frac{1}{n}}$ as $\chi \to \infty$ and hence $\phi \sim \chi^{\frac{1}{n}+2}$, which is the correct matching condition. For the inner solution as $\chi \to 0$ the left-hand side of equation (4.53) must be small and thus $\phi'' \ll 1$. Hence $\left[1+\phi''^2\right]^{\frac{n-1}{2}}\phi'' \approx \phi''$. Thus the inner behavior is as $\phi \sim \chi^3$. We can see the change in behavior by solving the boundary layer equation $\left(1+\phi''^2\right)^{\frac{n-1}{2}}\phi'' = \chi$ numerically. This was achieved by integrating $\phi'' = Z(x)$ using a second order finite difference scheme, where $Z(x)$ is the inverse function of $P(x) = \left(1+x^2\right)^{\frac{(n-1)}{2}}x$, which was found using the Newton Raphson method. The solution is shown in Fig.4.4, along with the inner and outer approximations. This permits us to examine the boundary layer behavior as the Newtonian limit is approached. If the fluid is everywhere Newtonian, there is no change in behavior and thus there must be no boundary layer. One might have expected that the size of the layer would tend to zero, however, we find its size in fact tends to Γ^{-1}. In the Newtonian limit we actually find the inner behavior χ^3, and the outer behavior $\chi^{2+\frac{1}{n}}$ coincide and thus no change in behavior is observable .

We can now see that behavior of the inner solution far from the boundary can be written in terms of the outer variables x, y as

$$\psi_{inner} \sim \Delta_0 X^{-(1+\frac{1}{n})}Y^{2+\frac{1}{n}} = \Delta_0\delta^{-(2+\frac{1}{n})}x^{-(1+\frac{1}{n})}y^{2+\frac{1}{n}}. \tag{4.54}$$

Thus, for the orders to match, we require that $\Delta_0 = \delta^{(2+\frac{1}{n})}$. By combining this with the first condition, $\Delta_0 = \Gamma^{-1}\delta^2$, we get the explicit scaling of the boundary layer $\delta = \Gamma^{-n}$ and $\Delta_0 = \Gamma^{-(2n+1)}$. Physically, we see that this new scaling is applicable when $\Gamma \sim \dot{\gamma}^{-1}$ as to be expected.

This scaling could alternatively have been deduced from looking at the form of the behavior of the outer solution. The behavior of the zeroth order term is as $r\theta^{2+\frac{1}{n}}$ and for first order term, is as $\Gamma^{-2}r^3\theta^{2-\frac{1}{n}}$ for $n < 2$. By considering the ratio of these

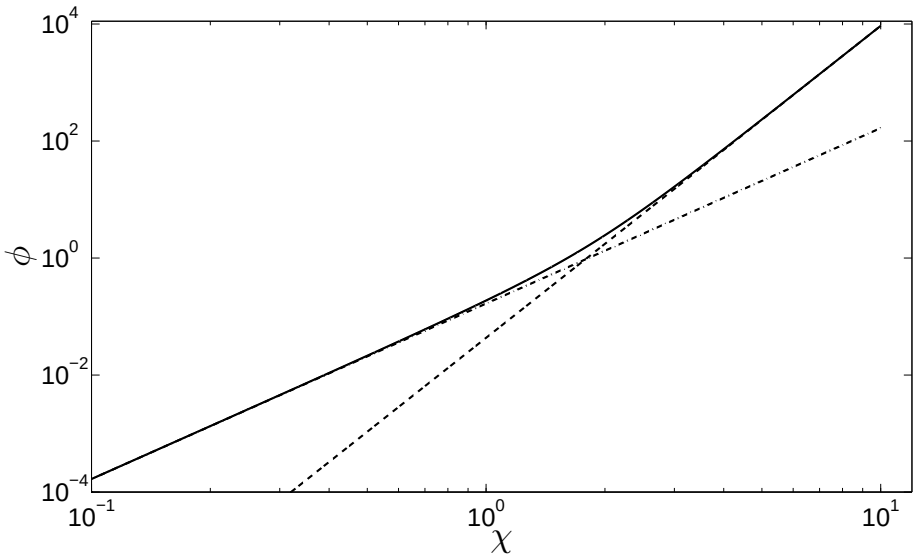

Fig. 4.4 Solution for $(1+\phi''^2)^{\frac{n-1}{2}}\phi'' = \chi$, given by the solid line with the inner, χ^3, and outer, $\chi^{2+\frac{1}{n}}$, behaviors given by the dot-dashed and dashed lines respectively for the case of $n = \frac{3}{10}$.

terms we see that the solution loses its uniformity when

$$\frac{r\theta^{2+\frac{1}{n}}}{\Gamma^{-2}r^3\theta^{2-\frac{1}{n}}} = \left(\Gamma^n r^{-n}\theta\right)^{\frac{2}{n}} = O(1). \tag{4.55}$$

As we consider r to be $O(1)$ this gives the required scaling for θ as $O(\Gamma^{-n})$. The scaling for ψ becomes apparent whilst expressing the first term in the outer series in terms of the scaled θ, i.e. if $\theta = \Gamma^{-n}\Theta$, then $\psi_0 = r\Gamma^{-(2n+1)}\Theta^{2+\frac{1}{n}}$. Likewise, one can see that the similarity variable appears as the ratio of the power-law and the viscous correction term.

The boundary layer occurs when $Y \sim \Gamma^{-n}$. The scaling suggests that as n grows large this boundary layer region becomes infinitely small, with the inner stream function scaling also becoming smaller, though we later find that for asymmetric flows an additional layer of width Γ^{-2} occurs which dominates for $n > 2$. This is discussed in section 4.6. However, as most fluids exhibit shear thinning properties, n is often $n < 1$ and consequently this layer would be much smaller than the Γ^{-n} layer.

4.5 Matching

4.5.1 Leading order

As two of the boundary conditions are applied in the region $\theta > 0$, and the other two in the region $\theta < 0$, to get a complete solution we must match the solutions over the boundary layer. We first consider the case of $n < 2$. The case of $n > 2$ is considered in section 4.6. The free parameters of the outer solution (4.43) can be matched to the inner solution, to obtain a solution defined across the whole domain. As the inner scaling can be derived from consideration of where the outer shear rate loses its uniformity, this is suggestive that the zeroth and first order terms in the outer series match to the lowest order in the inner series. We now formally match the leading order inner solution to the outer solutions. Considering the expansion for the outer solution (4.53) and using the series approximation for large ϕ'', we obtain

$$|\phi''|^{n-1}\phi'' + \frac{n-1}{2}|\phi''|^{n-3}\phi'' + \cdots = A_p\chi. \tag{4.56}$$

We can construct the inverse series, by means of iteration, to find

$$\phi'' = f(\chi) \sim \sum_{m=0}^{\infty} \beta_m \chi^{\frac{1}{n}-\frac{2m}{n}} \sim \operatorname{sgn}(A_p\chi)\left\{(|A_p\chi|)^{\frac{1}{n}} - \frac{n-1}{2n}(|A_p\chi|)^{-\frac{1}{n}}\right\} + O(\chi^{-\frac{3}{n}}), \tag{4.57}$$

which integrates to give

$$\phi = A + B\chi + \int_0^{\chi}\int_0^{\chi'} f(\chi'')d\chi''d\chi' \sim (A + Int_1) + (B + Int_2)\chi + \tag{4.58}$$

$$\frac{\operatorname{sgn}(\chi)n^2}{(n+1)(2n+1)}\operatorname{sgn}(A_p)|A_p|^{\frac{1}{n}}|\chi|^{2+\frac{1}{n}} - \frac{\operatorname{sgn}(\chi)n}{2(2n-1)}\operatorname{sgn}(A_p)|A_p|^{-\frac{1}{n}}|\chi|^{2-\frac{1}{n}} + \ldots \text{as } \chi \to \infty \tag{4.59}$$

where Int_1, Int_2 are the order 1 contributions which arise from the contribution to the integral for χ not large and are calculated numerically by

$$Int_2 = \int_0^{\infty}\left(f(\chi') - \operatorname{sgn}(A_p\chi')(|A_p\chi'|)^{\frac{1}{n}}\right)d\chi', \tag{4.60}$$

$$Int_1 = \int_0^{\infty}\left(\int_0^{\chi'} f(\chi'')d\chi'' - \sum_{m=0}^{1+\frac{1}{n}-\frac{2m}{n}<0} \frac{\beta_m}{\left(1+\frac{1}{n}-\frac{2m}{n}\right)}\chi^{1+\frac{1}{n}-\frac{2m}{n}} - Int_2\right)d\chi'. \tag{4.61}$$

Via Van Dyke's matching rule [57] if $A = -Int_1, B = -Int_2$ and $\operatorname{sgn}(A_p)|A_p|^{\frac{1}{n}} = J_1(\alpha)^{-1}n^{\frac{1}{2n}}(n-2)^{\frac{1}{2n}}$, or equivalently $A_p = \operatorname{sgn}(J_1(\alpha))|J_1(\alpha)^{-n}n^{\frac{1}{2}}(|n-2|)^{\frac{1}{2}}|$, and as

$\mathrm{sgn}(\theta) = \mathrm{sgn}(\chi)$, then the outer limit of ϕ is given by

$$\phi = \frac{n^2 \mathrm{sgn}(\theta) J_1(\alpha)^{-1} n^{\frac{1}{2n}} (n-2)^{\frac{1}{2n}}}{(n+1)(2n+1)} |\chi|^{2+\frac{1}{n}} - \frac{\mathrm{sgn}(\theta) n}{2(2n-1)} J_1(\alpha) \left(n^{\frac{1}{2n}} (n-2)^{\frac{1}{2n}} \right)^{-1} |\chi|^{2-\frac{1}{n}} + \dots \tag{4.62}$$

which matches exactly with the inner behavior of the inhomogeneous terms in the outer solution obtained previously (4.43),(4.44). Reverting back to polar coordinates allows one to incorporate the Newtonian effects to leading order expression by using the composite approximation to zeroth order with the expression

$$\psi_{comp} = r\left(g_0(\theta) - C_0^+ |\theta|^{2+\frac{1}{n}} \mathrm{sgn}(\theta) \right) + \Gamma^{-(2n+1)} r^{2+2n} \phi\left(\Gamma^n r^{-n} \theta \right). \tag{4.63}$$

The composite expansion gives an expression that is uniformly valid over the troublesome zero shear layer, though it is important to note that it does not resolve the loss of uniformity due to the radial decrease in shear rate.

4.5.2 Matching homogeneous terms: second internal boundary layer

To correctly apply the boundary conditions the constants A^+, B^+, C^+, D^+ must be matched to the corresponding terms in the lower domain, A^-, B^-, C^-, D^-. Using the aforementioned scaling leads one to look for an inner solution of the form

$$\begin{aligned} \psi_{inner} &= \sin(\theta_\infty) X + \Gamma^{-n} \cos(\theta_\infty) Y + \Gamma^{-(2n+1)} X^{2+2n} \phi \\ &+ \Gamma^{-2} \Psi_A + \Gamma^{-(n+2)} \Psi_B + \Gamma^{-(n+3)} \Psi_C + \Gamma^{-(2n+3)} \Psi_D, \end{aligned} \tag{4.64}$$

where Ψ_A,Ψ_B ,Ψ_C , Ψ_D map to k_1,k_2,k_3, k_4 respectively. We can instantly set $\Psi_A = A^+ X^3$ and $\Psi_B = B^+ X^2 Y$ which do not contribute to the leading order shear behavior and correctly match to the outer condition. Substituting into (4.50) and keeping the lowest orders we find that

$$\left[\left(1 + \phi''^2\right)^{\frac{n-1}{2}} \Psi_{C\,YY} + (n-1)\phi''^2 \left(1 + \phi''^2\right)^{\frac{n-3}{2}} \Psi_{C\,YY} \right]_{YY} = 0, \tag{4.65}$$

where Ψ_D also must satisfy (4.65). Equation (4.65) reduces to

$$\left[|Y|^{1-\frac{1}{n}} \Psi_{C\,YY} \right]_{YY} = 0, \quad \text{as} \quad Y \to \pm\infty, \tag{4.66}$$

$$\Psi_{C\,YYYY} = 0, \quad \text{as} \quad Y \to 0. \tag{4.67}$$

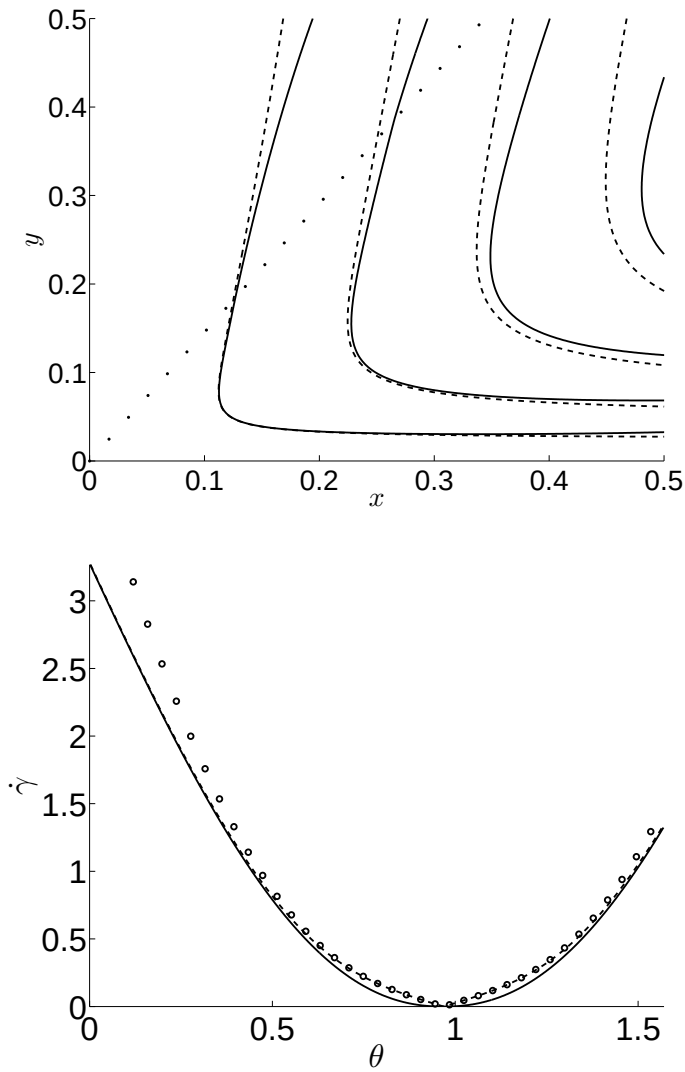

(a)

Fig. 4.5 In Fig.5(a) the composite streamline (dashed) along with pure power-law solution is shown, the line of zero shear is indicated by the dotted line. In Fig.5(b) shear rate along the contour $r = 1$ for $\Gamma = 5, n = 0.45, \alpha = \frac{\pi}{2}$ is plotted. The outer power-law solution (solid line), the inner boundary solution (circular markers) and the composite curve (dashed lines) are shown.

Let us now, without loss of generality, consider the limit as $Y \to 0^+$. Equation (4.66) is analogous to (4.86) and we can therefore write the general solution as

$$\Psi_C = \begin{cases} P_1 + P_2 Y + P_3 X^{2-\frac{1}{n}} Y^{1+\frac{1}{n}} + P_4 X^{1-\frac{1}{n}} Y^{2+\frac{1}{n}}, & \text{as} \quad Y \to \infty \\ P_1 + P_2 Y + \frac{(n+1)}{2n^2} P_3 X^{2-\frac{1}{n}} Y^2 + \frac{(n+1)(2n+1)}{6n^2} P_4 X^{1-\frac{1}{n}} Y^3 & \text{as} \quad Y \to 0, \end{cases} \tag{4.68}$$

where the X terms are added for convenience. To match with the outer conditions the only non-zero coefficient for Ψ_C is $P_3 = C^+$, and likewise $P_4 = D^+$ for Ψ_D.

We can again see that the uniformity for the inner shear rate breaks down as $Y \to 0$. Consider

$$\begin{aligned}\Psi_{YY} &= \Gamma^{-(2n+1)}\phi'' + \Gamma^{-2}\Psi_{A,YY} + \Gamma^{-(n+2)}\Psi_{B,YY} + \Gamma^{-(n+3)}\Psi_{C,YY} + \Gamma^{-(2n+3)}\Psi_{D,YY} \\ &= \Gamma^{-(2n+1)}A_b X^{-(1+n)}Y + \Gamma^{-(n+3)}\frac{(n+3)}{n^2}C^+X^{2-\frac{1}{n}} \\ &+ \Gamma^{-(2n+3)}D^+\frac{(n+1)(2n+1)}{n^2}X^{1-\frac{1}{n}}Y.\end{aligned}$$

The leading order shear rate behaves as $\Gamma^{-(2n+1)}Y$, whereas the homogeneous terms give rise to a shear rate $\Gamma^{-(n+3)}$. This results in a loss of uniformity when $Y \sim \Gamma^{n-2}$. This loss of uniformity arises because the point of zero shear no longer occurs when $Y = 0$, which is predicted by the pure power-law solution. Instead the point of zero shear has been shifted due to the presence of the anti-symmetric flow term. Physically this is to be expected as one would not anticipate a Carreau fluid to have exactly the same point of zero shear as a pure power-law fluid.

This leads one to consider another internal scaling. We therefore propose a second inner scaling whereby $Y = \Gamma^{n-2}\mathcal{Y}$, which can be written as $y = \Gamma^{-2}\mathcal{Y}$ in terms of the outer coordinates. As this innermost scaling does not change the inner boundary layer equation (4.67), one can simply express (4.64) in terms of this scaling. The solution can therefore be written as

$$\begin{aligned}\psi_{inner} = \sin(\theta_\infty)X + \Gamma^{-2}\left(A^+X^3 + \cos(\theta_\infty)\mathcal{Y}\right) + \Gamma^{-4}B^+X^2\mathcal{Y} + \\ \Gamma^{n-7}\left(\frac{n+1}{2n}C^+X^{2-\frac{1}{n}}\mathcal{Y}^2 + X^{2+2n}\mathcal{Y}^3\right) + \Gamma^{n-9}\frac{(n+1)(2n+1)}{6n^2}X^{1-\frac{1}{n}}D^+\mathcal{Y}^3,\end{aligned} \tag{4.69}$$

which is uniformly valid. Moreover, if one considers the alternative limit as $Y \to 0^-$, the same solution can be derived by symmetry, replacing A^+ by A^- and $\mathcal{Y}$ by $-\mathcal{Y}$, (excluding the $\cos(\theta_\infty)\mathcal{Y}$ term). In order for the solution to remain smooth we require that $A^+ = A^-, B^+ = -B^-, C^+ = C^-$ and $D^+ = -D^-$. We now have a smooth uniform approximation, which completes the matching.

The effect of the inner boundary layers is shown in Fig.4.6, where the shear rate is plotted for fixed r. The effect of the second inner layer of shifting the point of zero shear can be observed.

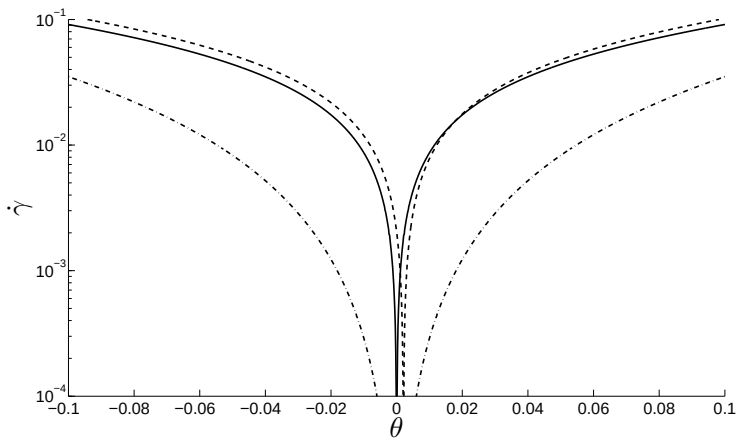

Fig. 4.6 The shear rate for the power-law fluid along $r = 1$ for $\Gamma = 5$, $n = 0.45$. The solid line is the zeroth order composite solution and the dashed line for the inclusion of the extra term. The pure power fluid is indicated by the dot dashed line.

4.6 Strong shear thickening fluids.

In the case of $n > 2$, the previous matching is no longer valid. This can be explained by considering the expression for the shear rate taking the first order terms in the outer series,

$$\dot{\gamma}_{outer} = C_0 r\theta^{\frac{1}{n}} + \Gamma^{-2} r^3 \left(C^+ \theta^{-1+\frac{1}{n}} - \frac{n-1}{2n} \Gamma^{-2} r^3 \theta^{-\frac{1}{n}} + O(1) \right). \tag{4.70}$$

The first term in the brackets arises from k_3 in the homogeneous solution (4.40), with the constant C^+ derived from the boundary conditions, and the second from the inhomogeneous term. For $n > 2$, as $\theta \to 0^+$, we see that the contribution from the homogeneous term is larger than that of the inhomogeneous term and the solution loses its uniformity before $y \sim \Gamma^{-n}$. From analysis of the ratio of the two terms we propose an inner scaling of the form $y = \Gamma^{-2} Y$, $\psi \sim \Gamma^{-4-\frac{2}{n}} \hat{\Psi}$. We can see from the previous solution that this new scaling is required as the innermost boundary layer (of thickness Γ^{-2}) is now larger than the previous outer layer (of thickness Γ^{-n}). Upon using this scaling and keeping only the first order terms one finds that the momentum equation reduces to

$$\left(\left(\hat{\Psi}_{YY} \right)^n \right)_{YY} = 0. \tag{4.71}$$

Integrating equation (4.71) gives

$$\hat{\Psi}_{YY} = \left(C_p^n Y + D_p\right)^{\frac{1}{n}} \sim \begin{cases} C_p Y^{\frac{1}{n}} + n^{-1} D_p C_p^{1-n} Y^{\frac{1}{n}-1} & \text{as} \quad Y \to \infty, \\ D_p^{\frac{1}{n}} + n^{-1} D_p^{1-\frac{1}{n}} C_p^n Y & \text{as} \quad Y \to 0, \end{cases} \tag{4.72}$$

where C_P and D_p can be functions of X, and we can immediately see that the zero shear rate no longer occurs at $Y = 0$. We now set $C_p = J_1^{-1} n^{\frac{1}{2n}} (n-2)^{\frac{1}{2n}} X^{-\left(1+\frac{1}{n}\right)}$ and $D_p = n C_p^{n-1} C^+ X^{2-\frac{1}{n}}$ and we match the other homogeneous solutions and the inhomogeneous term. Thus, we seek a solution of the form

$$\begin{aligned} \psi_{inner} = \sin(\theta_\infty) X + \Gamma^{-2} \cos(\theta_\infty) Y + \Gamma^{-4-\frac{2}{n}} \hat{\Psi} + \Gamma^{-2} \hat{\Psi}_A \\ + \Gamma^{-4} \hat{\Psi}_B + \Gamma^{-6-\frac{2}{n}} \hat{\Psi}_D + \Gamma^{-6+\frac{2}{n}} \hat{\Psi}_I, \end{aligned} \tag{4.73}$$

where $\hat{\Psi}_A, \hat{\Psi}_B$, and $\hat{\Psi}_D$ match to k_1, k_2 and k_4. We again set $\hat{\Psi}_A = A^+ X^3$ and $\hat{\Psi}_B = B^+ X^2 Y$ and note that $\hat{\Psi}_C$ is excluded as k_3 has already been matched in (4.72). The introduction of $\hat{\Psi}_I$ is required to match to the inhomogeneous term. The equation for $\hat{\Psi}_D$ and $\hat{\Psi}_I$ is given by

$$\left[\hat{\Psi}_{YY}^{n-1} \hat{\Psi}_{I\,YY} + \frac{(n-1)}{2} \hat{\Psi}_{YY}^{n-2} \left(1 + 2\hat{\Psi}_{YY} \hat{\Psi}_{I\,YY}\right)\right]_{YY} = 0, \tag{4.74}$$

$$\left[\hat{\Psi}_{YY}^{n-1} \hat{\Psi}_{D\,YY}\right]_{YY} = 0. \tag{4.75}$$

The additional +1 term for Ψ_I results from expanding the term in the constitutive equation for viscosity, $1 + \Gamma^2 \dot{\gamma}^2 \approx 1 + \Gamma^2 (\psi_{inner\,YY})^2$. For Ψ_I the cross term is $O(1)$, hence the inclusion of the +1 term in (4.74). If we again consider the limit as $Y \to \infty$, $\Psi_{YY} \sim C_p Y^{\frac{1}{n}}$, and equation (4.74) can be written as

$$\left[Y^{1-\frac{1}{n}} \hat{\Psi}_{I\,YY}\right]_{YY} = \left[-\frac{(n-1)}{2nC_p} Y^{1-\frac{2}{n}}\right]_{YY}. \tag{4.76}$$

The inhomogeneous term gives rise to a particular solution

$$\hat{\Psi}_I = -\frac{n}{(2n-1)} J_1 n^{-\frac{1}{2n}} (n-2)^{-\frac{1}{2n}} X^{\left(1+\frac{1}{n}\right)} Y^{2-\frac{1}{n}} \tag{4.77}$$

which correctly maps to the outer solution. To obtain the inner solution behavior of (4.74), we note that $\hat{\Psi}_{YY} \sim D_p^{\frac{1}{n}}$ as $Y \to 0$, and thus

$$\left[\hat{\Psi}_{I\,YY}\right]_{YY} = \left[-\frac{(n-1)}{2n} D_p^{\frac{1}{n}}\right]_{YY}, \tag{4.78}$$

hence the inner behavior of $\hat{\Psi}_I \sim -\frac{n-1}{4n} D_p^{\frac{1}{n}} Y^2$. The analysis for $\hat{\Psi}_D$ follows the same methodology that was applied to equations (4.66) and (4.67). Thus we obtain the inner solution

$$\psi_{inner} = \sin(\theta_\infty)X + \Gamma^{-2}\left(A^+X^3 + \cos(\theta_\infty)Y\right) + \Gamma^{-4}B^+X^3\mathcal{Y}$$
$$+\Gamma^{-4-\frac{2}{n}}\frac{1}{2}D_p^{\frac{1}{n}}Y^2 - \Gamma^{-6+\frac{2}{n}}\frac{n-1}{4n}D_p^{\frac{1}{n}}Y^2 + \Gamma^{-6-\frac{2}{n}}\frac{(n+1)(2n+1)}{6n^2}X^{1-\frac{1}{n}}D^+Y^3. \tag{4.79}$$

The above expression is uniformly valid, and the same matching conditions as before for $A^+, A^-, \ldots, D^-$ still apply. So what has happened to the layer of order Γ^{-n}? In fact it has been shifted to where $C_p^n Y + D_p = 0$ where $\Psi_{YY} \sim \bar{Y}^{\frac{1}{n}}$, and $\Psi_I \sim \bar{Y}^{-\frac{1}{n}}$ where $\bar{Y} = Y + D_p/C_p^n$. This breakdown is fixed in the sameway as before.

4.7 Decaying effects

In the far-field approximation we found that the Carreau effects decayed like r^{-1}, but a key question is whether or not this will be the dominant correction? The system will, near to the corner, have a behaviour which is power-law like. This will excite the Moffatt eigen-modes of $r^\lambda f(\theta)$ in the far field where $\lambda < 0$. Of course these modes might decay more slowly than the Carreau effects. The eigen-value, for a corner of angle α satifies (see Moffatt [90]

$$\sin(2\lambda\alpha) \pm \lambda \sin(2\alpha) = 0 \tag{4.80}$$

where $\pm$ is positive for an even mode and negative for an odd mode. The eigen-value must be found numerically and if we search for the leading order negative eigen-value are shown in figure. The all excited modes will strictly be less dominant than the Carreau correction for $\alpha < 1.1$. We also find that there is a very small regime $1.5695 < \alpha < 1.5702$ where in principle the modes decay quicker. However as λ is very close to -1 in this regieme it is not of physical interest.

4.8 Conclusions and discussions

We find that the solution for a Carreau fluid far from the corner can be readily calculated and that the result correctly predicts the overshoot and undershoot of streamlines for shear thinning/thickening behaviors respectively, though the solution is no longer valid for r of order $O(\Gamma)$. However, the far from wall approximation will eventually breakdown, due to the inertia terms becoming appreciably large.

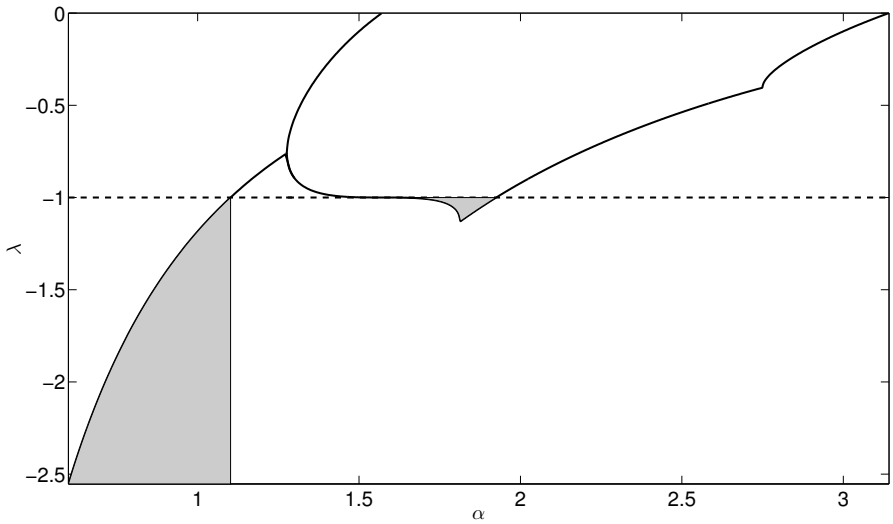

Fig. 4.7 Eigen values against α an even excitation, the shaded region indicates where the Carreau correction is applicable.

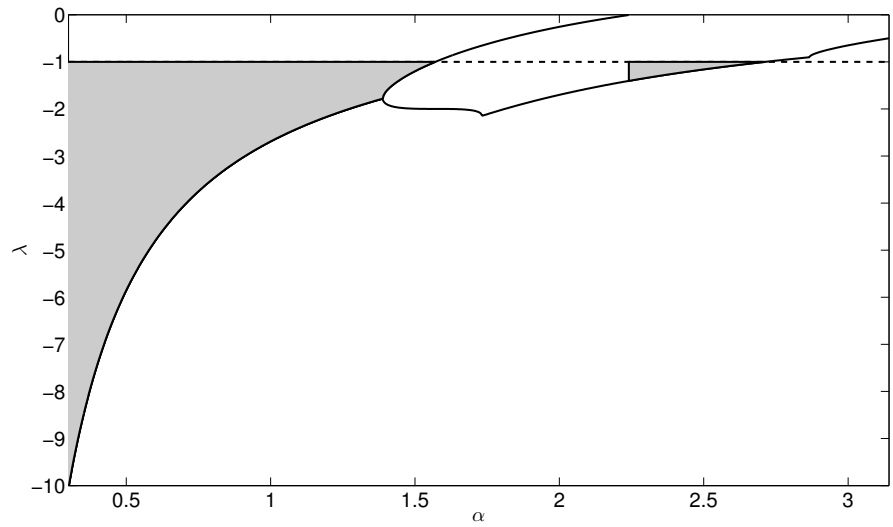

Fig. 4.8 Eigen values against α an odd excitation the Carreau correction is applicable.

In the limit of large Γ, that is highly shear dependent behavior, we found that the system can be modeled as a pure power-law solution in part of the domain. However, this solution breaks down and a novel new boundary layer equation is required to overcome this problem. The thickness of the region in which the solution breaks down is found to be of the order Γ^{-n} for $n < 2$, with another change in behavior at Γ^{-2}. In the case of $n > 2$ we find that only one layer occurs which is of thickness Γ^{-2}. This is suggestive that the stresses of shear thinning fluids with small power law index n near a region of low shear rates could vary dramatically from those predicted by a pure power law fluid.

It should be noted that there is an extra degree of freedom arising from distant disturbances. Let us now consider the far field Newtonian problem with a Carreau correction. The Carreau correction will only be important if disturbances near the corner decay more quickly then the Carreau correction. Such a disturbance can be written as a sum of terms of the form $r^{\lambda}h(\theta)$ where λ are the eigenvalues of the problem and $h(\theta)$ are the eigenfunctions. The eigenvalue parameters can be found in Moffatt [89]. Therefore we would require that $\Re(\lambda) < -1$. Similarly, for the near field problem, one requires that far field disturbances, which decay in accordance with the eigenvalues given in [52], decay more quickly than the decay rates predicted by Carreau correction, i.e. $3 < \Re(\lambda)$.

4.9 Appendix

4.9.1 Exact solution for power-law correction.

For the parameter choice $n = 3$ the general solution for the correction to the power-law equation (4.34) can be found in terms of tabulated functions. For $n = 3$, the governing equation simplifies to

$$\left(\frac{d^2}{d\theta^2}+1\right)\left\{3\left(g_0+g_0''\right)^2(g_1''-3g_1)+\kappa_p|g_0+g_0''|\right\}=0. \tag{4.81}$$

This can be solved by the same means as equation (4.31) which leads to the exact solution

$$g_1 = A\sinh(\sqrt{3}(\theta-\theta_\infty))+B\cosh(\sqrt{3}(\theta-\theta_\infty))+CI_1(\theta)+DI_2(\theta). \tag{4.82}$$

The functions I_1 and I_2 are given by:

$$I_1(\theta) = e^{-\sqrt{3}\theta}\int e^{\sqrt{3}\theta}\sinh^{-\frac{2}{3}}(\sqrt{3}(\theta-\theta_\infty))\sin(\theta-\theta_\infty)d\theta-$$
$$e^{\sqrt{3}\theta}\int e^{-\sqrt{3}\theta}\sinh^{-\frac{2}{3}}(\sqrt{3}(\theta-\theta_\infty))\sin(\theta-\theta_\infty)d\theta, \tag{4.83}$$
$$I_2(\theta) = e^{-\sqrt{3}\theta}\int e^{\sqrt{3}\theta}\sinh^{-\frac{2}{3}}(\sqrt{3}(\theta-\theta_\infty))\cos(\theta-\theta_\infty)d\theta$$
$$-e^{\sqrt{3}\theta}\int e^{-\sqrt{3}\theta}\sinh^{-\frac{2}{3}}(\sqrt{3}(\theta-\theta_\infty))\cos(\theta-\theta_\infty)d\theta. \tag{4.84}$$

4.9.2 Inner behavior of outer solution

The solution to equation (4.34) was obtained by use of Frobenius series, and is required to give the additional terms needed to describe the behavior far from $\theta = 0$. However, the leading order terms could be computed in a more direct manner, and as the equation appears later in the matching process we include it. If one considers the case where θ is small, then the second derivatives dominate equation (4.34). Keeping the highest order derivatives for the homogeneous and inhomogeneous parts one finds that

$$\frac{d^2}{d\theta^2}\left\{n|g_0+g_0''|^{n-1}g_1''+\kappa_p|g_0+g_0''|^{n-2}\right\} = 0. \tag{4.85}$$

Using only the first order term for $g_0''+g_0 = C_0\theta^{\frac{1}{n}}$, equation (4.85) reduces to,

$$\left[|\theta|^{1-\frac{1}{n}}g_1''\right]'' = -\frac{1}{n}\kappa_p C_0^{-1}\left(|\theta|^{1-\frac{2}{n}}\right)'', \tag{4.86}$$

which appears ubiquitously throughout the matching process. We can integrate (4.86) to give

$$g_1 = A+B\theta+C\theta^{1+\frac{1}{n}}+D\theta^{2+\frac{1}{n}}-\frac{n}{2(2n-1)}|J_1(\alpha)|\left(n^{\frac{1}{2n}}(|n-2|)^{\frac{1}{2n}}\right)^{-1}\mathrm{sgn}(\theta)|\theta|^{2-\frac{1}{n}}. \tag{4.87}$$

4.9.3 Shear driven problem

Although the driven corner problem is far more generally applicable, the boundary condition forces the stream function to behave as r, which precludes a self similar solution as the shear rate is radially dependent. However, if one considers the flow caused by constant shear stress, as performed by Moffatt [89] in the Newtonian case, there is no radial dependence on the shear rate and a global self similar solution can be found. We would be remiss in not presenting this solution. We now seek a

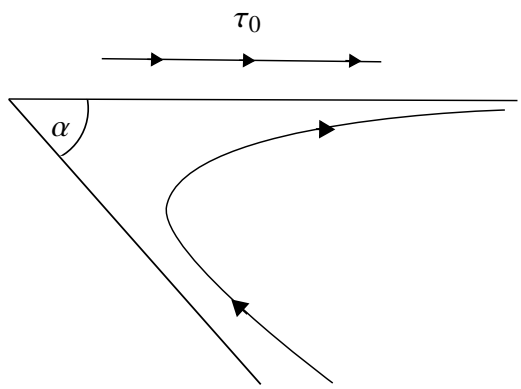

Fig. 4.9 Sketch of shear driven problem.

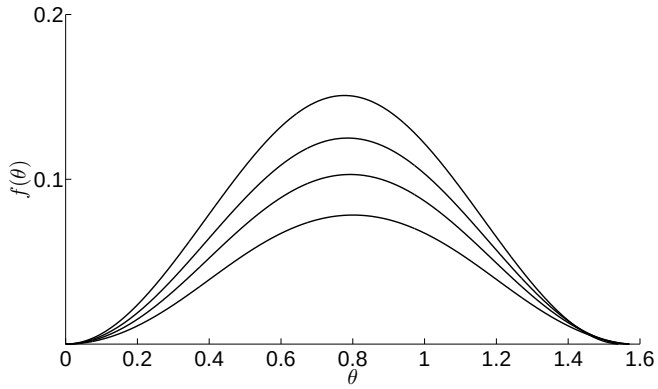

Fig. 4.10 The function f for the shear driven case. The results are shown, from bottom to top, for $n = 0.2, .5, 1, 2$ with $\Gamma = 1$.

solution of the form $\psi \sim \tau_0 \mu_0^{-1} r^2 f(\theta)$ whereby the stress tensor components reduce to

$$\tau_{rr} = 2\mu f' = -\tau_{\theta\theta}, \quad \tau_{r\theta} = \mu f'', \tag{4.88}$$

with the shear rate as given by equation (4.5),

$$\dot{\gamma} = \tau_0 \mu_0^{-1} \left(f''^2 + 4 f'^2 \right)^{\frac{1}{2}}, \tag{4.89}$$

whence the viscosity simplifies to

$$\mu = \mu_0 \left(1 + \left(\Gamma \tau_0 \mu_0^{-1} \right)^2 \left(f''^2 + 4 f'^2 \right) \right)^{\frac{n-1}{2}}. \tag{4.90}$$

The momentum equation (4.6), after introducing the appropriate non-dimensional scaling on Γ, reduces to the non-linear ODE

$$\frac{d^2}{d\theta^2}\left\{\left(1+\Gamma^2\left(f''^2+4f'^2\right)\right)^{\frac{n-1}{2}} f''\right\}+4\frac{d}{d\theta}\left\{\left(1+\Gamma^2\left(f''^2+4f'^2\right)\right)^{\frac{n-1}{2}} f'\right\}=0. \quad (4.91)$$

When equation (4.91) is solved subject to a constant shear stress being applied at some angle α and no slip on the bottom wall it gives the constrains

$$f(0)=f(\alpha)=f'(0)=0, \quad \left(1+\Gamma^2\left(f''(\alpha)^2+4f'(\alpha)^2\right)\right)^{\frac{n-1}{2}} f''(\alpha)=1. \quad (4.92)$$

As no analytic solution could be found we solve the above using the shooting method along with a Runge–Kutta 4 solver. The results are presented in Fig.4.10.

4.9.4 Integer singularities and logarithmic terms

We see that singularities occur in the first term of equation (4.42) when $n=\frac{1}{2}$ and in the second term when $n=\frac{1}{4},\frac{1}{3},\frac{3}{2}$ and $n=\frac{1}{2}$. Here we give some insight as to why these singularities occur. Consider the term

$$-\frac{d^2}{d\theta^2}\left\{n|g_0+g_0''|^{n-1}(g_1'')\right\}. \quad (4.93)$$

At leading order $g_1=\theta^{2-\frac{1}{n}}$, and $|g_0+g_0''|\sim\theta^{\frac{1}{n}}$ so we can obtain:

$$\frac{d^2}{d\theta^2}\left(\theta^{1-\frac{1}{n}}\cdot\left(2-\frac{1}{n}\right)\left(1-\frac{1}{n}\right)\theta^{-\frac{1}{n}}\right)=\left(2-\frac{1}{n}\right)\left(1-\frac{1}{n}\right)\left(1-\frac{2}{n}\right)\left(-\frac{2}{n}\right)\theta^{-1-\frac{2}{n}}. \quad (4.94)$$

Considering the next term in the Frobenius series where $g_1\sim\theta^{4-\frac{1}{n}}$, gives

$$\frac{d^2}{d\theta^2}\left(\theta^{1-\frac{1}{n}}\cdot\left(3-\frac{1}{n}\right)\left(4-\frac{1}{n}\right)\theta^{2-\frac{1}{n}}\right)=\left(2-\frac{2}{n}\right)\left(3-\frac{2}{n}\right)\left(3-\frac{1}{n}\right)\left(4-\frac{1}{n}\right)\theta^{1-\frac{2}{n}}. \quad (4.95)$$

We can see that the problem that arises at $n=\frac{1}{2}$ is that the derivative g' no longer behaves like $\theta^{1-\frac{1}{n}}$ but is in fact zero. The problem is resolved by the introduction of logarithmic terms. For simplicity we let $J=J_1(\alpha)$. Using the definition of κ_p in (4.35) we can then write the particular solution succinctly as

$$k_p(\theta)=\frac{3}{2}\kappa_p|J|\ln\theta+\frac{423\kappa_p|J|}{16}\theta^2+\frac{9\kappa_p|J|}{4}\theta^2\ln\theta+O(\theta^4). \quad (4.96)$$

Similarly problem occur when $n = \frac{1}{4}, n = \frac{1}{3}$, $n = \frac{2}{3}$. It can be readily seen that the solution can be expressed as a series in the form

$$
\begin{aligned}
n = \frac{1}{4} : g_1 &= -\frac{49\kappa_p|J|}{384}\theta^{-2} + \frac{68873371\kappa_p|J|}{2211840} - \frac{9947}{2560}\kappa_p|J|\ln\theta + O(\theta^2\ln\theta),\\
n = \frac{1}{3} : g_1 &= -\frac{5\sqrt{5}\kappa_p|J|}{18}\theta^{-1} - \frac{6589975}{1172242}\kappa_p\sqrt{5}|J|\theta + \frac{400}{81}\kappa_p\sqrt{5}|J|\theta\ln\theta + O(\theta^3\ln\theta),\\
n = \frac{2}{3} : g_1 &= \frac{8\sqrt{3}\sqrt[4]{2}|J|\kappa_p}{3}\theta^{\frac{1}{2}} - \frac{377546\sqrt{3}\sqrt[4]{2}|J|\kappa_p}{66015}\theta^{\frac{5}{2}} - \frac{448\sqrt{3}\sqrt[4]{2}\kappa_p|J|}{45}\theta^{\frac{5}{2}}\ln\theta + O(\theta^{\frac{9}{2}}\ln\theta).
\end{aligned}
\tag{4.97}
$$

Chapter 5

Mean Field Theory for Dumbbells in Shear and Elongational Flows.

Abstract

An analytic solution for the Fokker-Planck (FP) equation for FENE dumbbells augmented with a mean-field force term proposed by [76, 121] is found. The effect of finite extensibility under the Peterlin closure approximation is investigated for both elongational and shear flow. The solution was found analytically up to a system of transcendental equations. A closed form solution can be obtained for elongation flow for Hookean dumbbells, where the well-known result of infinite extension at an elongation rate of $\dot{\varepsilon} = \frac{1}{2\lambda}$ is modified by the mean field term. This result is compared to a finite element solution where the Peterlin closure approximation is relaxed. It was found that for both elongational and shear flow stress predictions, at smaller velocity gradients, are over predicted by the Peterlin model, with the effect becoming more pronounced with increasing concentration.

5.1 Introduction

Single bead springs models prove to be an effective way to construct consitutive equations for polymer melts. Perhaps the most widely used with success is finite extensible FENE dumbbell [143] which exhibits a viscous response, that arises from the Brownian motion, and an elastic response that arises from the spring.

However, single dumbbell models are just a simple approximation to polymer melts solutions. Authors have augmented dumbbell models to include additional physics such as internal viscosities [4, 5], additional hydrodynamic interactions [37, 83, 98] and aniostropic drag to name a few. Additional effects are included to achieve the allusive goal of attaining a computationally viable, constitutive model that can lead to improved predictions and greater understanding of single polymer experiments [32, 46, 62, 100].

The aim of this chapter is to investigate the mean field model proposed by Schneggenburger et al. [121] to account for concentration effects. The behavior of FENE dumbbells without mean field term is well known and has been extensively studied

[73, 138]. Schneggenbuger et al. investigated the model under uniform shear-flow conditions and found that reasonably good agreement between mean field predictions and data obtained from light scattering experiments. We will solve the mean-field term under the assumption that the flow field is purely extensional.

Concentration effects have previously been included interacting dumbbell model by Hess [54], or encapsulated dummbell theory of Bird DeAguiar [17] and DeAguiar [30] . It should be noted that the theory is only applicable in the limit of dilute solutions and will not capture the dynamics of highly concentrated solutions. For such solutions one must use the tube theory e.g. Doi and Edwards [34] and DeGennes [28, 29].

In section 5.2 we introduce the governing equations. In section 5.3 we characterize the effect of using mean field term and examining its effects under constant elongation. We further derive the probability density function for shear flow. In section 5.4 we investigate the effects of the Peterlin approximation in conjunction with the mean field term.

5.2 The governing equations

Throughout this work we will model the fluid as a suspension of dumbbells embedded in a Newtonian solvent. The dumbbells are considered to be single chained models, where two beads are connected via a spring. The behavior of the dumbbell can be completely described by finding the end-to-end vector $\mathbf{Q}$, which is a vector connecting the location of one of the beads with respect to the other. The governing equations are expressed solely in terms of the end-to-end vector, $\mathbf{Q}$. To form the equations which describe the evolution of $\mathbf{Q}$ one must propose an elastic law for the spring. In this study we will consider the FENE spring force, first proposed by Warner [144], which is given by

$$\mathbf{F}^c = \frac{H\mathbf{Q}}{1 - Q^2/Q_0^2}, \tag{5.1}$$

where H is a spring constant and Q_0 is the maximum allowable extension of the dumbbells. If one takes the limit $Q_0 \to \infty$ one recovers the linear Hookean spring law, which macroscopically recovers the Oldroyd B model. Another limit of importance is the point at which the end-to-end vector reaches its maximum extension. In such a limit the fluid acts analogous to a suspension of infinitely thin rigid rods. The FENE

spring force described in (5.1) is only an empirical approximation to the physically derived inverse Langevin operator [15], although other approximations have been used, for instance the Marko-Siggia force law [137], the Padé law [22], or improved closure approximation modifications such as the FENE-L model proposed by Lielens et al. [81, 82].

Once a spring law is defined the equation of motion for an individual dumbbell can be found. If one assumes that the velocity field is homogenous over the length scale of the polymer, then the evolution of $\mathbf{Q}$ is given by Langevin equation [16]

$$\mathbf{dQ} = \left(\boldsymbol{L}\cdot\mathbf{Q} - \frac{2}{\zeta}\left(\mathbf{F}^{c} + \mathbf{F}^{MF}\right)\right)dt + \sqrt{\frac{4kT}{\zeta}}\mathbf{dW}. \tag{5.2}$$

Here $\mathbf{F}^{c}$, $\mathbf{F}^{MF}$ are the spring and mean-field forces respectively, k is the Boltzmann constant and T is the absolute temperature, and ζ is the drag constant. The tensor $\boldsymbol{L}$ is the transpose of the velocity gradient given by $L_{ij} = \frac{\partial u_i}{\partial x_j}$. The Brownian term $\mathbf{dW}$ is a Wiener process whose components are independent Gaussian variables with mean zero and variance dt. The Langevin equation has an equivalent Fokker-Planck (FP) equation for the probability distribution $\psi(\mathbf{Q}, t)$. The evolution equation for ψ is given by the partial differential equation (PDE)

$$\frac{\partial\psi}{\partial t} = \nabla\cdot\left(-\boldsymbol{L}\mathbf{Q}\psi + \frac{2}{\zeta}\left(\mathbf{F}^{c} + \mathbf{F}^{MF}\right)\psi\right) + \frac{2kT}{\zeta}\nabla^{2}\psi, \tag{5.3}$$

$$\mathbf{u} = (\dot{\varepsilon}x, -\dot{\varepsilon}y) \tag{5.4}$$

with the convention of ∇ implying differentiation with respect to $\mathbf{Q}$. To study the mean-field effects we will consider the mean field force term. We use the form proposed by Kroger et al. [76, 121], which is given by

$$\mathbf{F}^{(MF)} = -\frac{kT}{Q_0^4} f \left\langle \overline{\mathbf{QQ}} \right\rangle \mathbf{Q}. \tag{5.5}$$

The mean field term is introduced to weakly model anisotropy from concentration effects due to intra and intermolecular interactions. The parameter f determines the strength of the mean field term and is a positive function of the concentration. For infinitely dilute solutions $f = 0$ and f increases with increasing concentration. In equation (5.5) $\overline{\mathbf{A}}$ is used to denote the deviatoric part of the symmetric decomposition of a tensor $\mathbf{A}$. Physically, the mean field term in equation (5.5) was motivated by the proposed mean field forces suggested for rod-like polymers [78]. This form has

the advantage that at equilibrium, when **QQ** is isotropic as there is no preferential direction, the mean field term becomes zero.

Unfortunately, if Q_0 is finite, when using the Warner spring force the system cannot be solved analytically. This is a consequence as one cannot form a closed constitutive equation with only the second moment, or radius of gyration tensor, $\langle \mathbf{QQ} \rangle$ [1]. One can form a closed system if the Hookean spring force, however in elongational flows one can expect the solution to be valid over a small range of elongation rates owing to dumbbells becoming infinitely extended.

The standard approach to overcome this closure problem is to replace the spring for in (5.1) with the pre-averaged Peterlin approximation [101]. Here Peterlin proposes that one can replace the non-linear Wagner spring force term by a self consistent average term given. This results in a spring force given by

$$\mathbf{F}^c \approx \frac{H\mathbf{Q}}{1 - \langle Q^2 \rangle / Q_0^2}, \tag{5.6}$$

This has the advantage that the non-linear finite extensibility term is now linear with respect to the microscopic variables. However the Peterlin expression is only approximation Wagner spring force.

5.3 Mean field force under elongation

We now seek an exact solution to (5.3) under homogeneous planar elongational flow with elongation rate $\dot{\varepsilon}$. Here we will use the convection that $\boldsymbol{L}$ is the velocity gradient tesnor, i.e. $L_{ij} = \frac{\partial u_i}{\partial x_j}$. Whence for purely planar elongation flow $\boldsymbol{L}$ is given by $L_{ij} = \dot{\varepsilon}\delta_{i1}\delta_{j1} - \dot{\varepsilon}\delta_{i2}\delta_{j2}$, where δ_{ij} is the Kronecker delta function. To find a steady state solution, we change the variable defined by $\psi = \chi \cdot \phi$, where $\phi = e^{\frac{\zeta}{4kT}\mathbf{L}:\mathbf{QQ}}$ and : denotes full index contraction. This form of solution is motivated by solutions of the Fokker Planck equation found for elongational flows in [16]. This removes the advective term and the FP equation reduces to

$$\nabla \cdot \left(\frac{2}{\zeta} \frac{H\mathbf{Q}\chi}{\left(1 - \langle Q^2 \rangle / Q_0^2\right)} - \frac{2fkT}{\zeta Q_0^4} f\left(\frac{n}{n^*}\right) \left\langle \overline{\mathbf{QQ}} \right\rangle \mathbf{Q}\chi \right) + \frac{2kT}{\zeta} \nabla^2 \chi = 0. \tag{5.7}$$

[1] where the factor of $\frac{1}{4}$ has been removed for convenience

As we are dealing for purely elongation we can assume *a priori* that the shear term $\langle \mathbf{QQ} \rangle_{12} = 0$. Then one can see that the tensor product term in (5.5) can be written as

$$\left\langle \overline{\mathbf{QQ}} \right\rangle_{ip} \mathbf{Q}_p = \left\langle \overline{\mathbf{QQ}} \right\rangle_{[ii]} \mathbf{Q}_{[i]}, \tag{5.8}$$

where [ ] implies no summation over the elements. We thus see that the spring force is now some scalar, at the microscopic level, multiplied by the end-to-end vector. This additional force is acting analogous to a Hookean spring with non constant H, i.e. it acts an anisotropic spring. We can use the result as derived in the Appendix, with anisotropic spring constants with $\varepsilon_1, \varepsilon_2$ chosen to be

$$\varepsilon_1 = -\varepsilon_2 = \frac{kT}{HQ_0^4} f \left\langle \overline{\mathbf{QQ}} \right\rangle_{11} \left(1 - \left\langle Q^2 \right\rangle / Q_0^2\right). \tag{5.9}$$

For ease of notation we let r, θ, x and y denote Q_r, Q_θ, Q_x and Q_y respectively and introduce the characteristic spring time given by $\lambda = \zeta/4H$. Upon doing so we can express ψ as

$$\psi(r,\theta) = J \exp\left\{-\frac{1}{2} W r^2 \left(1 - \varepsilon_1 \cos^2(\theta) - \varepsilon_2 \sin^2(\theta)\right)\right\} \exp\left\{\frac{H\lambda\dot{\varepsilon} r^2}{kT} (\cos^2(\theta) - \sin^2(\theta))\right\}. \tag{5.10}$$

The variables W and J are given by the expressions

$$W = \frac{H}{kT\left(1 - \langle r^2 \rangle / Q_0^2\right)}, J = \frac{H\sqrt{\left\{1 - \varepsilon_1 - 2\lambda\dot{\varepsilon}\left(1 - \langle r^2 \rangle / Q_0^2\right)\right\}\left\{1 - \varepsilon_2 + 2\lambda\dot{\varepsilon}\left(1 - \langle r^2 \rangle / Q_0^2\right)\right\}}}{2\pi kT\left(1 - \langle r^2 \rangle / Q_0^2\right)}. \tag{5.11}$$

For the case considered the anisotropic mean field force term has the property that $\varepsilon_1 = -\varepsilon_2$, we thus introduce the simplified notation that $\varepsilon = \varepsilon_1 = -\varepsilon_2$ for convenience. Physically ε is a measure of the anisotropy that arises solely due to the mean field effects and acts like an additional elongation rate. We must note that $\left\langle r^2 \right\rangle$ and ε are not free variables. They have a hidden dependency on ψ, and thus can be determined by the averaging conditions

$$\left\langle r^2 \right\rangle = \int_0^{2\pi} \int_0^{\infty} r^2 \psi(r, \theta; \langle r^2 \rangle, \varepsilon) r dr d\theta, \tag{5.12}$$

$$\frac{2HQ_0^4 \varepsilon}{kTf\left(1 - \langle r^2 \rangle / Q_0^2\right)} = \int_0^{2\pi} \int_0^{\infty} r^2 \left(\cos^2(\theta) - \sin^2(\theta)\right) \psi(r, \theta; \langle r^2 \rangle, \varepsilon) r dr d\theta. \tag{5.13}$$

Upon evaluation of the integrals, equations (5.12) and (5.13) give respectively the two transcendental equations,

$$\left\langle r^2 \right\rangle = \frac{2kT\left(1-\left\langle r^2\right\rangle/Q_0^2\right)}{H(1-\varepsilon-C_0)(1+\varepsilon+C_0)}, \tag{5.14}$$

$$\frac{HQ_0^4\varepsilon}{kTf\left(1-\langle r^2\rangle/Q_0^2\right)} = \frac{kT\,(\varepsilon+C_0)\left(1-\left\langle r^2\right\rangle/Q_0^2\right)}{H(1-\varepsilon-C_0)(1+\varepsilon+C_0)}. \tag{5.15}$$

The calculation can be simplified on using the scalings $\mathbf{Q}^* = \frac{\mathbf{Q}}{\sqrt{KT/H}}$, $t^* = \frac{t}{\lambda}, \dot{\varepsilon}^* = \lambda\dot{\varepsilon}$, $\psi^* = \frac{kT}{H}\psi$ and $f^* = \frac{k^2T^2}{H^2Q_0^4}f$. Under these scalings it is useful to note that the mean field, FENE-P force terms and FP equation (5.3) reduce to

$$\hat{\mathbf{F}}^c = \frac{1}{2}\frac{\mathbf{Q}^*}{1-\langle Q^2\rangle/b}, \quad \hat{\mathbf{F}}^{MF} = -\frac{1}{2}f^*\left\langle\overline{\mathbf{Q}^*\mathbf{Q}^*}\right\rangle\mathbf{Q}^*,$$

$$\frac{\partial\psi^*}{\partial t^*} = \nabla\cdot\left(-\boldsymbol{L}^*\mathbf{Q}^*\psi^* + \left(\hat{\mathbf{F}}^c+\hat{\mathbf{F}}^{MF}\right)\psi^*\right) + \frac{1}{2}\nabla^2\psi^*. \tag{5.16}$$

The new parameter $b = HQ_0^2/kT$ is the ratio of the flexible spring time $\frac{\zeta}{4H}$ to the characteristic rigid time $\frac{\zeta L^2}{12kT}$. Ottinger [99] indicated that physically b represents the number of monomers in the polymer. If one drops the * notation for convenience, we recover a system of non-linear algebraic equations

$$\left\langle r^2\right\rangle = \frac{2\left(1-\left\langle r^2\right\rangle/b\right)}{(1-\varepsilon-2\dot{\varepsilon}(1-\langle r^2\rangle/b))(1+\varepsilon+2\dot{\varepsilon}(1-\langle r^2\rangle/b))}, \tag{5.17}$$

$$\varepsilon = \frac{f\left(\varepsilon+2\dot{\varepsilon}\left(1-\left\langle r^2\right\rangle/b\right)\right)\left(1-\left\langle r^2\right\rangle/b\right)^2}{(1-\varepsilon-2\dot{\varepsilon}(1-\langle r^2\rangle/b))(1+\varepsilon+2\dot{\varepsilon}(1-\langle r^2\rangle/b))}. \tag{5.18}$$

As no analytic solution could be found we solved this system of equations using the Newton-Raphson method whereby the starting solution is updated upon each iteration. The system was solved for constant b with varying $\dot{\varepsilon}^*$ and f^*. It was found that the solution becomes unstable with increasing f^*, as was reported in [121] under conditions of homogeneous shear flow, with the effect being magnified for increasing b. The solution shows that the elliptical factor ε increases initially until a peak is reached, whereby from then on it decreases. The change in behavior occurs because the finite extensibility becomes the dominant force with increasing elongation rate. Finite extensibility becomes apparent if one considers taking the Oldroyd limit ($b \to \infty$). It is well known that for the case of $\dot{\varepsilon}^* = \frac{1}{2}$ the solution becomes singular in such a limit.

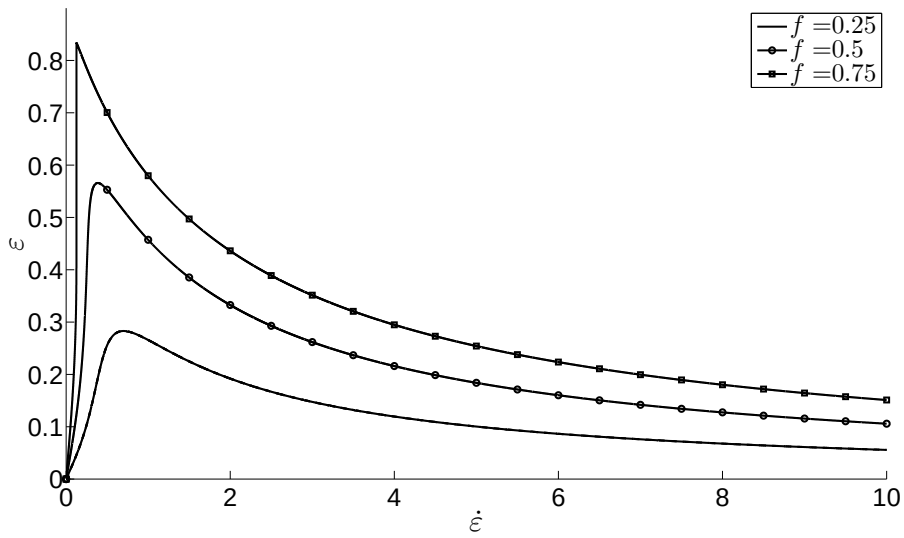

Fig. 5.1 Numerical solution for ε against non-dimensional elongation rate $\dot{\varepsilon}$ using the Newton-Raphson method. Results are given for $f = 1, 5, 10$ and 15 with extensibility parameter $b = 10$.

If one formally considers the limit of $b \to \infty$, equation (5.18) can be expressed as a cubic in ε given by

$$\varepsilon^3 + 4\dot{\varepsilon}\varepsilon^2 + \left(-1 + 4\dot{\varepsilon}^2 + f\right)\varepsilon + 2\dot{\varepsilon}f = 0. \tag{5.19}$$

The correct solution can be recovered by seeking the root which gives rise to no anisotropy from the MF force at zero concentration, i.e. $\varepsilon = 0$ at $f = 0$. Hence within the Hookean regime the probability distribution and radius of gyration can be found exactly. The solution is given by

$$\psi(r,\theta) \propto e^{-\frac{1}{2}r^2(1-(\varepsilon+2\dot{\varepsilon})\cos(2\theta))}, \tag{5.20}$$

$$\left\langle r^2 \right\rangle = \frac{2}{1-(\varepsilon+2\dot{\varepsilon})^2}, \tag{5.21}$$

$$\varepsilon = -\frac{1}{2}\left(s^+ + s^-\right) - \frac{4\dot{\varepsilon}}{3} - i\frac{\sqrt{3}}{2}\left(s^+ - s^-\right), \tag{5.22}$$

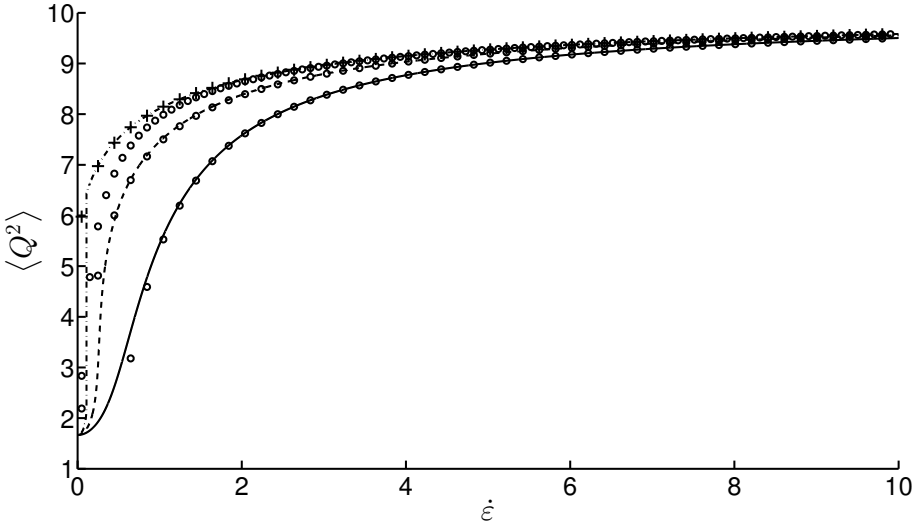

Fig. 5.2 The solution expanded around $\theta = 0$ compared to the exact numerical solution for $f = 0$ (lower curve), $0.5, 0.75$ (upper curve) for $b = 10$ is given by the solid line. The Padé approximation (5.32) is given by the circular markers, with the exact solution indicated by + for the case $f = 0.75$.

where $s^{\pm}$ is given by [2]

$$s^{\pm} = \frac{1}{3}\sqrt[3]{-18\dot{\varepsilon} + 8\dot{\varepsilon}^3 - 9\dot{\varepsilon}f \pm 3\sqrt{-3 + 24\dot{\varepsilon}^2 + 9f - 48\dot{\varepsilon}^4 + 60\dot{\varepsilon}^2 f - 9f^2 - 3\dot{\varepsilon}^2 f^2 + 3f^3}}. \tag{5.23}$$

The analytic solution (5.21) to (5.22) is plotted in Fig.5.3 for $f = 0.1$ along with the curves $b = 10, 50, 100$ and 1000. As expected we can see that the $b = 1000$ term conforms almost identically with the Hookean solution, though one can see a slight deviation near the infinity extension asymptote. One expects regular consistent behaviour of the root when the discriminant of the polynomial is less than zero i.e. (5.19)

$$-48\dot{\varepsilon}^4 + \left(24 + 60f - 3f^2\right)\dot{\varepsilon}^2 + 3f^3 - 3 + 9f - 9f^2 < 0. \tag{5.24}$$

We find that the point at which this condition fails coincides with the dumbbells becoming infinitely extended. It is of note that the inequality at $f = 0$ recovers the well known inequality $|\dot{\varepsilon}| < \frac{1}{2}$. The discriminant expression is rather opaque as to the effect of introducing the parameter f. However, as one expects f to be less than one, a regular perturbation for small f indicates that the critical elongation rate is

[2] As we are dealing with multiple roots we need a consistent definition. Thus we define the root $\sqrt[n]{w}$ to be defined under the convention of $r'^{\frac{1}{n}} e^{\frac{\phi'}{n} i}$ where r' and ϕ' are the modulus and argument of w respectively.

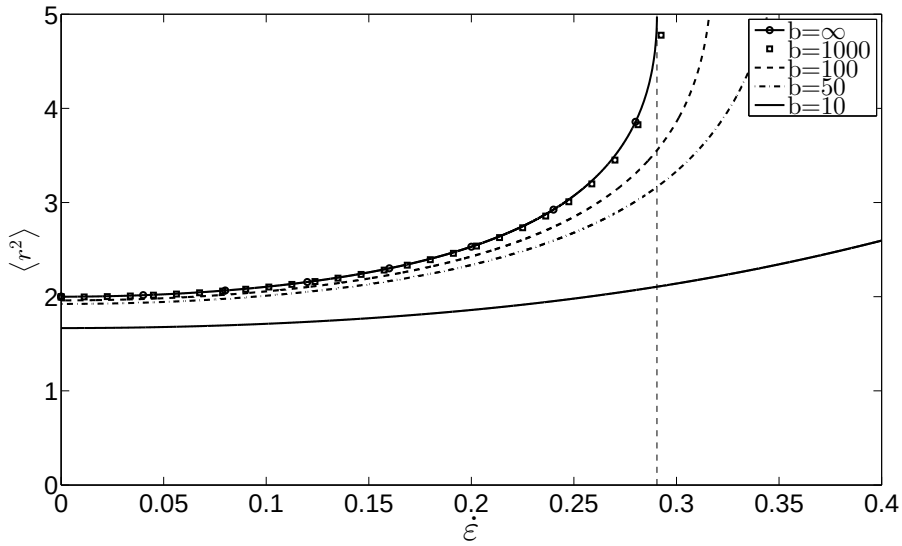

Fig. 5.3 The exact analytic solution for Hookean dumbbells ($b = \infty$) denoted by the circled solid line, with $f = 0.1$, compared to the Newton Raphson results with finite extensiblity parameter given by $b = 10, 50$, 100 and 1000 given by the solid, dot dashed, dashed curves and squares respectively.

approximately $\dot{\varepsilon}_c \approx \frac{1}{2} - \frac{\sqrt{2}}{2} f^{\frac{1}{2}}$. We see that the critical infinite extension elongation rate decreases for increasing concentration and change is like the square-root of the concentration parameter.

We also see that f must satisfy the inequality $f < 1$. This inequality can be deduced as the critical elongation rate would be zero when $f = 1$, which is clearly un-physical. Since the proposed MF model is only valid for dilute solutions, we propose that this breakdown occurs as the solution is too concentrated to be modelled accurately by the mean field term.

5.3.1 Maximum extension solution

We previously obtained results for the Hookean regime, or equivalently, the effect of the mean field term far from the maximum extension. We can, however, give an exact solution which is valid near the region of large elongation rates which, for ease, we will informally call the outer solution, although it is not an outer solution in a strict matched asymptotic sense. Physically, at large elongation rates, the dumbbell will be stretched along axis of extension. Thus the probability density function will be largely located around $\theta = 0$. Therefore, after Taylor expansion around $\theta = 0$, the

probability density function can be approximated by

$$\psi = Je^{-\frac{1}{2}r^2\left((1-\langle r^2\rangle/b)^{-1}(1-\varepsilon_r)+2(1-\langle r^2\rangle/b)^{-1}\varepsilon_r\theta^2\right)}. \tag{5.25}$$

For ease of notation we let $\varepsilon_r = \varepsilon + 2\dot{\varepsilon}\left(1-\left\langle r^2\right\rangle/b\right)$. As we have exponential decay in ψ any contribution far from the origin is assumed to be negligible. As such, we can extend the upper bound of the integral from 2π to ∞. Thus J is given by

$$J = \left\{\int_0^\infty d\theta \int_0^\infty re^{-\frac{1}{2}r^2(A+B\theta^2)}dr\right\}^{-1} = 2\pi^{-1}\cdot\sqrt{AB}, \tag{5.26}$$

where $A = \left(1-\left\langle r^2\right\rangle/b\right)^{-1}(1-\varepsilon_r)$, $B = 2\left(1-\left\langle r^2\right\rangle/b\right)^{-1}\varepsilon_r$. Equation (5.12) becomes

$$\left\langle r^2\right\rangle = J\int_0^\infty d\theta \int_0^\infty r^3 e^{-\frac{1}{2}r^2(A+B\theta^2)}dr = A^{-1}, \tag{5.27}$$

which can be rearranged to give

$$\left\langle r^2\right\rangle = \frac{b}{1+b(1-\varepsilon_r)}, \tag{5.28}$$

which reduces the problem to solely finding a solution for ε_r. Addition of the term $2\dot{\varepsilon}\left(1-\left\langle r^2\right\rangle/b\right)$ to equation (5.13) allows one to formulate the equation for ε_r:

$$\begin{aligned}\varepsilon_r &= \frac{1}{2}Jf\left(1-\left\langle r^2\right\rangle/b\right)\int_0^\infty d\theta\left(1-2\theta^2\right)\int_0^\infty r^3e^{-\frac{1}{2}r^2(A+B\theta^2)}dr + 2\dot{\varepsilon}\left(1-\left\langle r^2\right\rangle/b\right),\\ &= f\frac{(2\varepsilon_r-1)(1-\left\langle r^2\right\rangle/b)^2}{2\varepsilon_r(1-\varepsilon_r)} + 2\dot{\varepsilon}\left(1-\left\langle r^2\right\rangle/b\right).\end{aligned} \tag{5.29}$$

Using equations (5.28) and (5.29) allows one to formulate a quartic polynomial, given in equation (5.30), for ε_r thus reducing the problem to solving the quartic

$$\begin{aligned}2b^2\varepsilon_r^4 - (4b^2(1+\dot{\varepsilon})+4b)\varepsilon_r^3 + \left(2b^2+8b^2\dot{\varepsilon}+2fb^2+4b\dot{\varepsilon}+4b+2\right)\varepsilon_r^2\\ -\left(4b^2\dot{\varepsilon}+3fb^2+4b\dot{\varepsilon}\right)\varepsilon_r + fb^2 = 0.\end{aligned} \tag{5.30}$$

The correct root is identified by requiring the dumbbell to tend to its finite extension as the elongation rate increases. It is readily seen from (5.28) that this condition translates to $\varepsilon_r \to 1$ as $\dot{\varepsilon} \to \infty$. The exact solution to the polynomial (5.30) which satisfies the condition is readily obtainable, though tedious, thus for completeness it is given in the appendix (see equations (5.56) and (5.57)). Instead one can search for a solution in the form of a perturbation for large $\dot{\varepsilon}$. By performing a fixed point

iteration we find that

$$\varepsilon_r = 1 - \frac{1}{2b}\dot{\varepsilon}^{-1} + \frac{b^2 f - 2b + 2}{8b^2}\dot{\varepsilon}^{-2} - \frac{b^4 f^2 - 2b^3 f + 6b^2 f + 4b^2 - 12b + 4}{32b^3}\dot{\varepsilon}^{-3} + O(\dot{\varepsilon}^{-4}). \tag{5.31}$$

We can thus see how, the mean-field effects decay like $\dot{\varepsilon}^{-2}$ for large elongation rates. The solution (5.31) unfortunately has extremely poor convergence. This can be improved by, instead of presenting the solution as a series of polynomial, expressing the solution as a series of continuous fractions i.e. the Padé approximation. After equating the Taylor expansion of the Padé approximate we recover

$$P_2^2 = \left[1; \frac{1}{2b}; \frac{1}{4}(bf-2); \frac{b^2 f + bf - 2}{2b(bf-2)}\right], \tag{5.32}$$

where here we have used the notation for the truncated continuous fraction

$$[d_0; d_1; \ldots; d_n] = \frac{d_0}{1 + \frac{d_1 \dot{\varepsilon}^{-1}}{1 + \frac{\cdots}{1 + d_n \dot{\varepsilon}^{-1}}}}. \tag{5.33}$$

The solution in equation (5.32) is far more succinct and usable than the exact solution (5.56), (5.57). The truncated Padé approximation vastly improves the convergences, and for the case $f = 0.5$ the approximation the Padé approximation has a 1% error at an elongation rate of $\dot{\varepsilon} = 0.5$. Without delving deeply into the analysis of the Padé approximation, the improved convergence arises as the naive Taylor series must converge in a unit disc in the complex plane, whereas the Padé approximate can converge in the complex plane with a branch cut at the branch points. For an excellent discussion and overview into the Padé approximation see [13].

The Padé approximation is plotted in Fig.5.2. The solution conforms almost exactly with the numerical solution for $\dot{\varepsilon}$ approximately greater than 1. When $f = 0.75$ there appears to be a significant deviation in the result. The exact root of the polynomial (5.30) is shown to perform much better and hence this is a failing of the Padé approximation as opposed to that incurred in the integral approximation (5.25).

5.3.2 Mean field force under shear

We now go on to show that a similar result can be obtained under shear flow conditions. It is noted that Kroger et al. [121] investigated shear flow by means of solving the constitutive equation for the second moment, which is the most utilitarian quantity of interest. However at no extra computational cost one could obtain ψ

which allows computation of any macroscopic variable. Unlike elongation flow, it is clear that the term $\langle \mathbf{QQ} \rangle_{12}$ will be non-zero and thus a different approach must be taken. First though, we begin by discussing the solution of the FP equation for Hookean dumbbells with no mean-field dependence, under shear flow. Under shear-flow the velocity gradient $\boldsymbol{L}$ is now given by $L_{ij} = \dot{\gamma}\delta_{i1}\delta_{j2}$. The FP equation for such a flow can be shown [16] to have solution

$$\psi_{SR} \propto \exp\left\{ -\frac{H}{2kT} \frac{\left(x^2 - 2\lambda\dot{\gamma}xy + (1+2\lambda^2\dot{\gamma}^2)y^2\right)}{1+\lambda^2\dot{\gamma}^2} \right\}. \tag{5.34}$$

We thus anticipate that the solution is of the same form as (5.36), and seek a solution in the form

$$\exp\left(-\frac{H(Ax^2 + Bxy + Cy^2)}{2kT(1 - \langle Q^2 \rangle / Q_0^2)} \right). \tag{5.35}$$

Under such an assumption we need not restrict ourselves to pure shear flow but can consider introducing a mixed elongational and shear flow. Thus we will consider the most general homogenous velocity gradient field whereby the velocity is given by $u = \dot{\varepsilon}X + \dot{\gamma}_1 Y$ and $v = -\dot{\varepsilon}Y + \dot{\gamma}_2 X$. Here the notation X, Y is used to emphasize that these are Cartesian variables and not the shorthand notation for $\mathbf{Q}$. Substitution of this trail solution into the FP equation leads to

$$\nabla \cdot \left[-\dot{\varepsilon}\boldsymbol{q}\psi - \begin{pmatrix} \dot{\gamma}_1 \\ \dot{\gamma}_2 \end{pmatrix} \circ \boldsymbol{q}'\psi + \frac{2H\mathbf{Q}\psi}{\zeta(1 - \langle Q^2 \rangle / Q_0^2)} + \frac{2kT}{\zeta}\nabla\psi \right] = 0 \tag{5.36}$$

where we use the notation $\boldsymbol{q} = (x, -y)$, $\boldsymbol{q}' = (y, x)$ and introduce the notation $\circ$ to denote arraywise multiplication. After substitution of our trial solution we are left with the expressions

$$A = \frac{(1 - 2\dot{\gamma}_1\dot{\gamma}_2\lambda^2 + 2\lambda^2\dot{\gamma}_2^2 - 2\lambda\varepsilon)}{(1 + \dot{\gamma}_1^2\lambda^2 - 2\lambda^2\dot{\gamma}_1\dot{\gamma}_2 + \dot{\gamma}_2^2\lambda^2)}, \quad B = \frac{-2\lambda((\dot{\gamma}_1 + \dot{\gamma}_2) + 2\varepsilon(\dot{\gamma}_2 - \dot{\gamma}_1)\lambda)}{(1 + \dot{\gamma}_1^2\lambda^2 - 2\lambda^2\dot{\gamma}_1\dot{\gamma}_2 + \dot{\gamma}_2^2\lambda^2)},$$
$$C = \frac{(1 - 2\lambda^2\dot{\gamma}_1\dot{\gamma}_2 + 2\lambda^2\dot{\gamma}_1^2 + 2\lambda\varepsilon)}{(1 + \dot{\gamma}_1^2\lambda^2 - 2\lambda^2\dot{\gamma}_1\dot{\gamma}_2 + \dot{\gamma}_2^2\lambda^2)}. \tag{5.37}$$

We can now decompose the mean field term into terms of two basis vectors, $\boldsymbol{q}$ and $\boldsymbol{q}'$, which separates the mean field force term into a shear-like component and an elongation-like component. The mean field term in (5.5) decomposes into $\mathbf{F}^{(MF)} = -\frac{kT}{2Q_0^4} f\left(\left\langle x^2 - y^2 \right\rangle\right)\boldsymbol{q} - \frac{kT}{Q_0^4} f\langle xy \rangle \boldsymbol{q}'$. Using this decomposition we can write

the FP equation as

$$\nabla\cdot\left[-\frac{kT}{\zeta Q_0^4}f\left(\left\langle x^2-y^2\right\rangle\right)\boldsymbol{q}\psi-\begin{pmatrix}\dot{\gamma}+\frac{2kT}{\zeta Q_0^4}f\langle xy\rangle\\ \frac{2kT}{\zeta Q_0^4}f\langle xy\rangle\end{pmatrix}\circ\boldsymbol{q}'\psi+\frac{2H\mathbf{Q}\psi}{\zeta(1-\langle Q^2\rangle/Q_0^2)}+\frac{2kT}{\zeta}\nabla\psi\right]=0, \tag{5.38}$$

which is analgous to the $f=0$ solution with modified shear rate $\dot{\gamma}_1=\dot{\gamma}+\dot{\gamma}_2,\dot{\gamma}_2=\frac{2kTf}{\zeta Q_0^4}\langle xy\rangle$ and modified elongation rate $\dot{\varepsilon}=\frac{kTf}{\zeta Q_0^4}\left\langle x^2-y^2\right\rangle$. Using the solution (5.37) allows one to write the parameters A,B,C as

$$\begin{aligned}
A&=\frac{1-\dot{\gamma}\lambda\Gamma\left(1-\left\langle r^2\right\rangle/Q_0^2\right)^2-\Theta\left(1-\left\langle r^2\right\rangle/Q_0^2\right)}{1+\lambda^2\dot{\gamma}^2\left(1-\langle r^2\rangle/Q_0^2\right)^2},\\
B&=\frac{-2\dot{\gamma}\lambda\left(1-\left\langle r^2\right\rangle/Q_0^2\right)-2\Gamma\left(1-\left\langle r^2\right\rangle/Q_0^2\right)+2\dot{\gamma}\lambda\Theta\left(1-\left\langle r^2\right\rangle/Q_0^2\right)^2)}{1+\lambda^2\dot{\gamma}^2\left(1-\langle r^2\rangle/Q_0^2\right)^2},\\
C&=\frac{1+2\dot{\gamma}^2\lambda^2\left(1-\left\langle r^2\right\rangle/Q_0^2\right)+\dot{\gamma}\lambda\Gamma\left(1-\left\langle r^2\right\rangle/Q_0^2\right)^2+\Theta\left(1-\left\langle r^2\right\rangle/Q_0^2\right)}{1+\lambda^2\dot{\gamma}^2\left(1-\langle r^2\rangle/Q_0^2\right)^2},
\end{aligned} \tag{5.39}$$

where $\Theta=\frac{kTf}{HQ_0^4}\left\langle x^2-y^2\right\rangle/2$ and $\Gamma=\frac{kTf}{HQ_0^4}\langle xy\rangle$. One can readily see that in the limit as f tends to zero (i.e. $\Theta,\Gamma\to 0$) and $Q_0\to\infty$ that we recover the standard Hookean solution (5.36). The normalization constant J can be expressed readily by $J=\frac{H\sqrt{4AC-B^2}}{4\pi kT\left(1-\langle r^2\rangle/Q_0^2\right)}$. The consistency conditions for the system naturally give rise to an equivalent set of equations as derived by Schneggenburger [121] et al. who used a change of basis method. The two conditions (5.12) and (5.13) still hold, however, as no anzats is used regarding A_{12} the extra degree of freedom is accounted for by an additional consistency condition

$$\left\langle r^2\right\rangle=J\int r^2\psi(r,\theta;\left\langle r^2\right\rangle,\Gamma,\Theta)rdrd\theta, \tag{5.40}$$

$$\frac{HQ_0^4}{kTf}\Gamma=J\int_0^{2\pi}\int_0^{\infty}r^2\sin(\theta)\cos(\theta)\psi(r,\theta;\left\langle r^2\right\rangle,\Gamma,\Theta)rdrd\theta, \tag{5.41}$$

$$\frac{HQ_0^4}{kTf}\Theta=\frac{1}{2}J\int_0^{2\pi}\int_0^{\infty}r^2\left(\cos^2(\theta)-\sin^2(\theta)\right)\psi(r,\theta;\left\langle r^2\right\rangle,\Gamma,\Theta)rdrd\theta. \tag{5.42}$$

Use of the aforementioned scalings, with the shear rate scaling analogous to the elongation rate (i.e. $\dot{\gamma}^*=\dot{\gamma}\lambda$), leads one to the system of equations (with the star notation droppped),

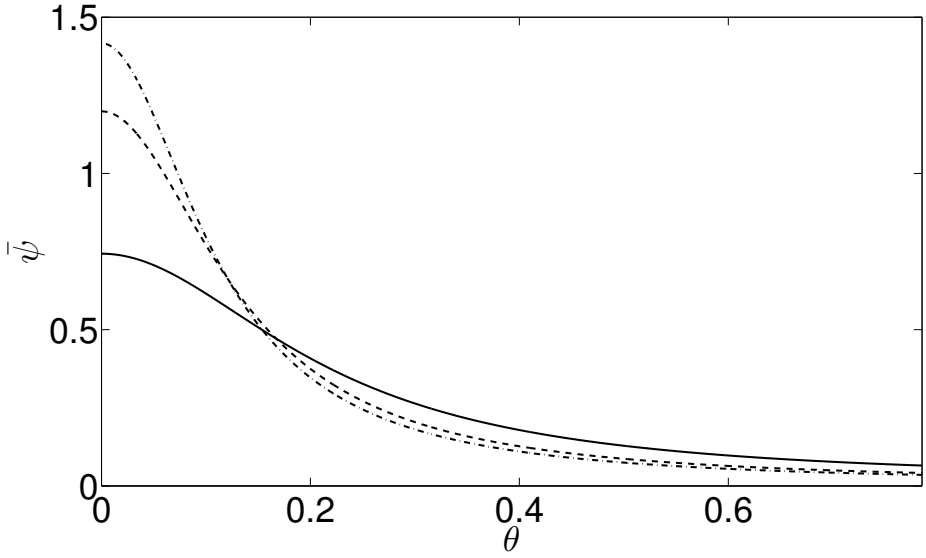

(a)

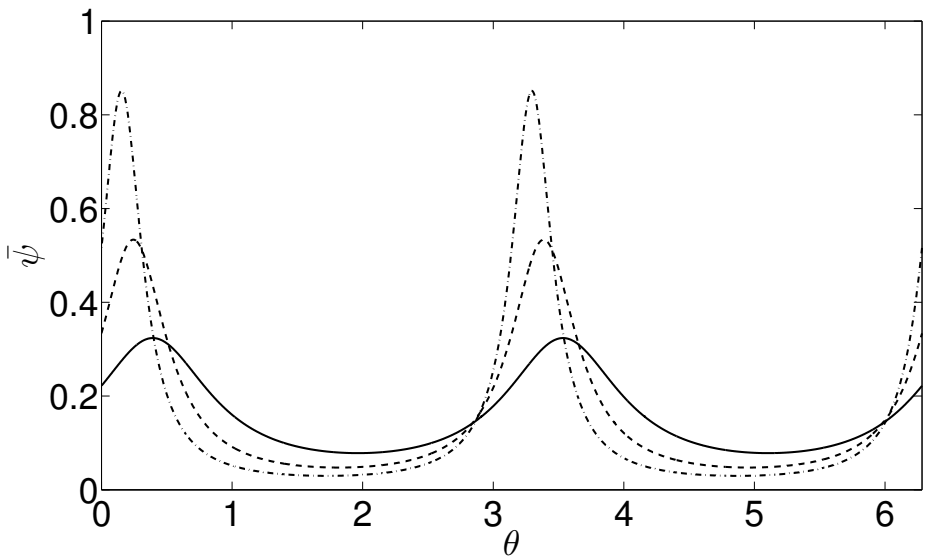

(b)

Fig. 5.4 In (a) the radially averaged probability distribution for elongational flow with $\dot{\varepsilon} = 1$ with $f = 0, 0.5$ and 0.75 which are denoted by the solid, dashed and dot-dashed lines respectively. In (b) the radially averaged distribution $\bar{\psi}$ in the upper quadrant $0 < \theta < \frac{\pi}{4}$. In (b) the contour $\psi = 0.5$ is plotted.

$$\left\langle r^2 \right\rangle = \frac{2\left(1 + \dot{\gamma}^2 \left(1 - \left\langle r^2 \right\rangle / b\right)^2\right)\left(1 - \left\langle r^2 \right\rangle / b\right)}{\left(1 - (1 - \langle r^2 \rangle / b)^2 \left(\Gamma^2 + \Theta^2 + 2\dot{\gamma}\Gamma\right)\right)}, \tag{5.43}$$

$$\Gamma = \frac{f\left(\dot{\gamma}+\Gamma-\dot{\gamma}\Theta\left(1-\left\langle r^2\right\rangle/b\right)\right)\left(1-\left\langle r^2\right\rangle/b\right)^2}{\left(1-(1-\langle r^2\rangle/b)^2\left(\Gamma^2+\Theta^2+2\dot{\gamma}\Gamma\right)\right)}, \tag{5.44}$$

$$\Theta = \frac{f\left(\dot{\gamma}^2\left(1-\left\langle r^2\right\rangle/b\right)+\Theta+\dot{\gamma}\Gamma\left(1-\left\langle r^2\right\rangle/b\right)\right)\left(1-\left\langle r^2\right\rangle/b\right)^2}{\left(1-(1-\langle r^2\rangle/b)^2\left(\Gamma^2+\Theta^2+2\dot{\gamma}\Gamma\right)\right)}, \tag{5.45}$$

which are again solved by the Newton-Raphson method. One can readily see that for elongation flow increasing f leads to greater stretching of the dumbbell and for shear leads to greater orientation of the dumbbell along the flow. We will now proceed in comparing the results to the full non-linear FENE model.

The expansion for small $\dot{\gamma}$ was previously been obtained by [121], however the effect for large shear was not considered. To consider the effects of large shear we first write the equations [5.43-5.45] as

$$\left\langle r^2\right\rangle\left(1-\Delta^2 A\right) = 2\left(1+\dot{\gamma}^2\Delta^2\right)\Delta, \quad \Gamma\left(1-\Delta^2 A\right) = f\left(\dot{\gamma}+\Gamma+\Theta-\dot{\gamma}\Theta\Delta\right)\Delta^2,$$
$$\Theta\left(1-\Delta^2 A\right) = f\left(\dot{\gamma}^2\Delta+\Theta+\dot{\gamma}\Gamma\Delta\right)\Delta^2, \tag{5.46}$$

where we use the notation $\Delta = \left(1-\left\langle r^2\right\rangle/b\right)$, $A = \Gamma^2+\Theta^2+2\dot{\gamma}\Gamma$. We know to leading order for high shear that the dumbbell will be fully extended, i.e. $\left\langle r^2\right\rangle \sim \langle b\rangle$. We will thus assume leading order polynomial behavior in the shear rate for the variables like $\Delta \sim \dot{\gamma}^{-a_1}, \Gamma \sim \dot{\gamma}^{-a_2}, \Theta \sim \dot{\gamma}^{-a_3}$. We can find a consistent balance if $a_1 = \frac{2}{3}, a_2 = \frac{1}{3}, a_3 = 0$, and expanding further to give the first few terms gives

$$\left\langle r^2\right\rangle \sim b - 2^{-\frac{1}{3}}b^{\frac{4}{3}}\dot{\gamma}^{-\frac{2}{3}} + \frac{2^{\frac{1}{3}}b^{\frac{2}{3}}\left(2+b+b^2 f\right)}{6}\dot{\gamma}^{-\frac{4}{3}} + O(\dot{\gamma}^{-\frac{6}{3}})$$
$$\Theta \sim \frac{bf}{2} - \frac{2^{\frac{2}{3}}b^{\frac{1}{3}}f(2+b)}{4}\dot{\gamma}^{-\frac{2}{3}} + O\left(\dot{\gamma}^{-\frac{4}{3}}\right),$$
$$\Gamma \sim 2^{-\frac{2}{3}}b^{\frac{2}{3}}f\dot{\gamma}^{-\frac{1}{3}} - \frac{f}{12}\left(b^2 f+4b+8\right)\dot{\gamma}^{-1} + O(\dot{\gamma}^{-\frac{4}{3}}).$$

The series has much better convergence than that for elongation flow and could be improved using the Padé approximation. We see that concentration effects increase the radius of gyration, and the effects decay as $\dot{\gamma}^{-\frac{4}{3}}$, which is a much slower decay than for the elongation case which decay as $\dot{\varepsilon}^{-2}$. One can also show that the concentration effects as $b^2 f$, and thus for larger b concentration dependence is increased. An interesting feature of shear flows is that degree of shear changes the orientation dumbbells. For elongational flow the dumbbell always aligns along the

axis of extension and compression. The orientation angle, as defined by [53], is given by

$$\chi = \frac{\pi}{4} - \frac{1}{2}\tan^{-1}\left(\Gamma\Theta^{-1}\right) \sim \frac{\pi}{4} - 2^{-\frac{2}{3}} b^{\frac{2}{3}} \dot{\gamma}^{-\frac{1}{3}} + \frac{1}{12}(bf-2)\dot{\gamma}^{-1}. \tag{5.47}$$

As $\dot{\gamma} \to \infty$ we find that the angle or orientation is $\frac{\pi}{4}$ as to be expected and the dominant effect is the finite extension force. We see that the mean-field term decays as $\dot{\gamma}^{-1}$ and the mean-field term has opposite sign to the finite extension effect. Hence the mean field term resists orientation of the dumbbell.

5.4 FENE soultion

An analytical solution for the FENE dumbbell model with a mean field term was found up to the solution of a system of transcendental equations. However, the solution necessitated the use of the Peterlin approximation in order to obtain a tractable solution. We now relax this assumption and include the full non-linear FENE force term and investigate the consequences of such an assumption. A direct solution of the FP equation is found for the non-linear system using an iterative finite element scheme.

Initially the Peterlin approximation seems rather good, and removes the unwanted infinite elongation that occurs with Hookean Spring models. However, the Peterlin approximation does introduce subtle consequences. Firstly, as discussed by Herrchen and Öttinger [86], the Peterlin approximation only imposes a constraint on the averaged value of the end-to-end vector and not an upper-bound, hence dumbbells can exist which have length greater than Q_0. Secondly, the effect of the Peterlin approximation is non-local. The distribution for the FENE-P model is Gaussian whereas the FENE model cannot have a chain length greater than the maximum extension which gives compact support. The difference in the FENE-P model has previously been shown to effect the transient response as well [74]. In this study we limit our investigation to only steady state however the effects of the transient consequences of the mean field term could be a topic for further study.

Under purely elongation flow, the FP equation is solved on the upper quadrant of a circle of radius $\sqrt{b}$ to reduce the computational domain. Symmetry boundary conditions are imposed along the x and y axes and the Dirichlet condition $\psi = 0$ is applied on the boundary $r = \sqrt{b}$, which causes zero probability of the dumbbell

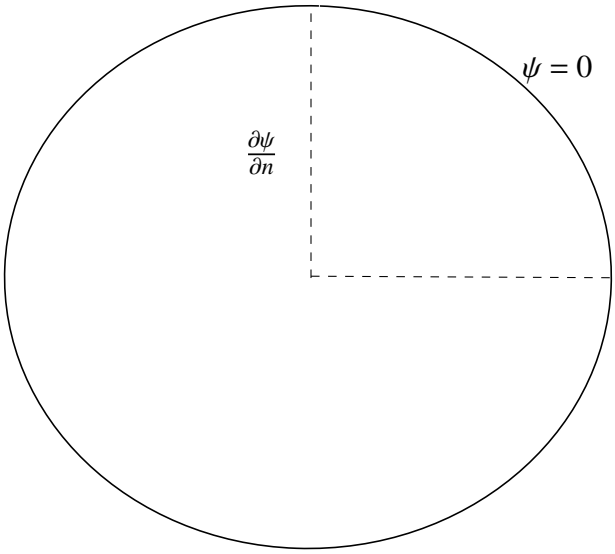

Fig. 5.5 The finite element domain for the non-linear FENE model. The dashed line indicates the truncated geometry used for pure elongational flow.

being fully extended. Unfortunately, for the pure shear case, such a strong symmetry does not exist, and the FP equation must be solved over the entire circular domain. As such a system has purely homogeneous boundary conditions, one would recover the trivial zero solution. In order to overcome this we added an inhomogeneity along the boundary $r = \sqrt{b}$ by setting ψ equal to an arbitrary constant. Then after normalization of ψ by scaling by its Zustandsumme leads to ψ at the boundary scaling approximately to zero.

Comparison of the finite element scheme to the exact analytical solution, for $f = 0$, which is given by $N \int r^2(1 - r^2/b)^{b/2} e^{\dot{\varepsilon} r^2 \cos(2\theta)} d\Omega$ see [15] where N is the appropriate normalization constant and shown in Fig.5.8a. In Fig.5.8a the analytical solution is indicated by the circular markers and is seen to be in excellent agreement with the results given by the finite element solution. Using the previous scaling, whilst dropping the * for convenience, the steady FP equation with the inclusion of a mean field term at steady state for elongation flow is given by

$$\nabla \cdot \left[-\dot{\varepsilon}(x\boldsymbol{e_x} - y\boldsymbol{e_y})\psi + \frac{1}{2}\left(\frac{\boldsymbol{x}}{1 - r^2/b} - f\left\langle \overline{\mathbf{QQ}} \right\rangle \boldsymbol{x} \right)\psi \right] + \frac{1}{2}\nabla^2\psi = 0, \tag{5.48}$$

where $\boldsymbol{e_x}$ and $\boldsymbol{e_y}$ are the unit vectors in the x and y directions respectively. The above equation gives rise to the weak form (again under the anzats $\langle \mathbf{QQ} \rangle_{12} = 0$).

We can express (5.48) in weak form as

$$\int_\Omega \left\{ \nabla \cdot \left(-\dot{\varepsilon}(x\boldsymbol{e_x} - y\boldsymbol{e_y})\psi + \frac{1}{2}\left(\frac{\boldsymbol{x}}{1 - r^2/b} - f\left\langle \overline{\boldsymbol{xx}} \right\rangle \boldsymbol{x} \right)\psi \right) - \frac{1}{2}\nabla v \cdot \nabla \psi \right\} dV + \frac{1}{2}\int_{\partial\Omega} v \nabla \psi \cdot \mathbf{dS} = 0, \tag{5.49}$$

where v are the shape functions, which are taken to be linear Lagrange polynomials and with an incorporated triangular mesh. The integration is performed using a forth order Gauss quadrature. It is of note that equation (5.49) does not account for the following two constraints. Firstly that $\int_\Omega \psi dV = 1$, and secondly, upon scaling of ψ, the condition of $\left\langle \overline{\mathbf{QQ}} \right\rangle = \int \overline{\mathbf{QQ}} \psi dV$, the latter of which introduces non-linearity in ψ. We approach these conditions by means of a fixed point iterative scheme whereby one iterates the system until a default tolerance is reached:

$$\mathscr{L}(\psi, v; \dot{\varepsilon}, \left\langle \overline{\mathbf{QQ}} \right\rangle_n) = 0, \tag{5.50}$$

$$\psi^* = \frac{\psi}{\int_\Omega \psi dV}, \tag{5.51}$$

$$\left\langle \overline{\mathbf{QQ}} \right\rangle_{n+1} = \int_\Omega \overline{\mathbf{QQ}} \psi^* d\mathbf{Q}, \tag{5.52}$$

where $\mathscr{L}\left(\psi, v; \dot{\varepsilon}, \left\langle \overline{\mathbf{QQ}} \right\rangle\right)$ denotes the left-hand side of (5.49). Equation (5.48) can be similarly formed and solved for the case of pure shear flow. The advective term is the only part which changes and $\langle \boldsymbol{QQ} \rangle_{12}$ is found through the iterative scheme.

The probability density function ψ is plotted for the FENE solution for the case of pure elongational in Fig.5.6. The effects of the addition concentration are, as expected, similar to those for the Peterlin case where the concentration term acts analogous to elongation and gives rise to increased probability of larger extensions of the dumbbells. The effect is similar, although less dramatically seen, for the case of pure shear flow as shown in Fig.5.7.

The direct comparison against the Peterlin approximation by solution of (5.17) and (5.18) is shown in Figs.5.8 and 5.9. Fig.5.8 plots the radius of gyration for varying elongation rates with and without the Peterlin closure approximation. Similar results for shear flow are shown in Fig.5.9.

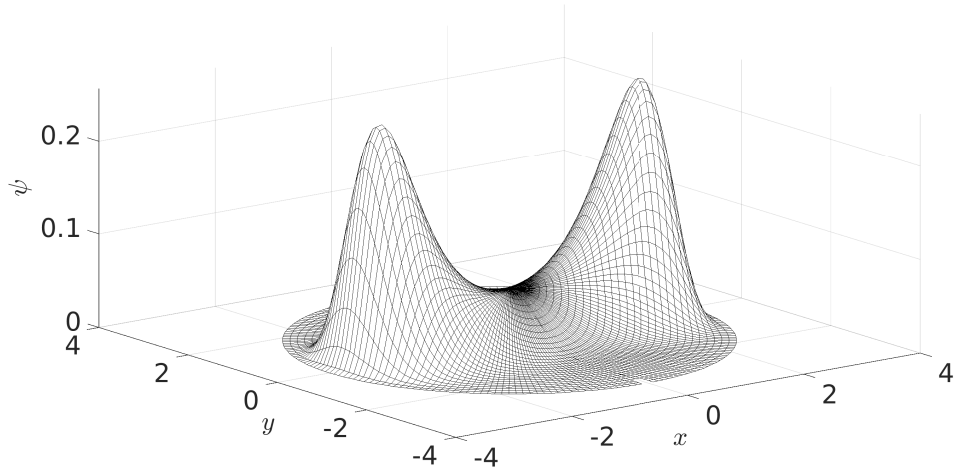

(a)

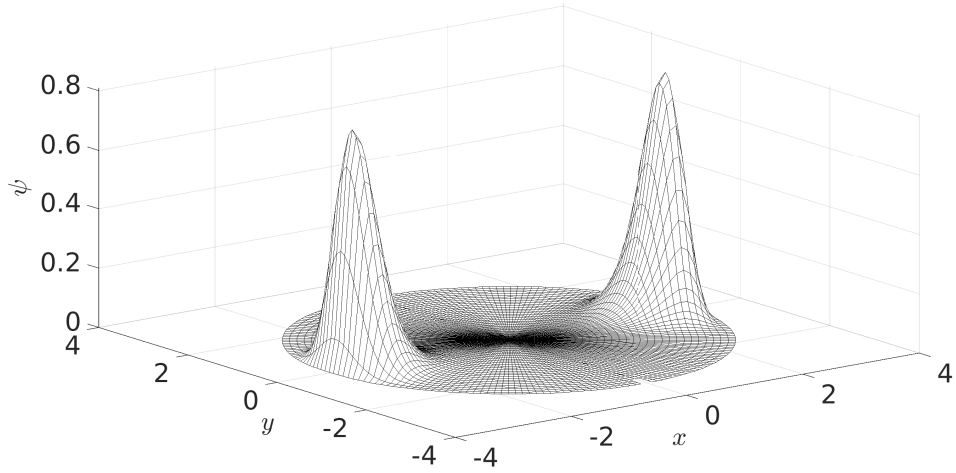

(b)

Fig. 5.6 The probability density function ψ for the full non-linear FENE solution for $\dot{\varepsilon} = 1$ for $f = 0$ (in (a)) and $f = 0.5$ (in (b)) with $b = 10$.

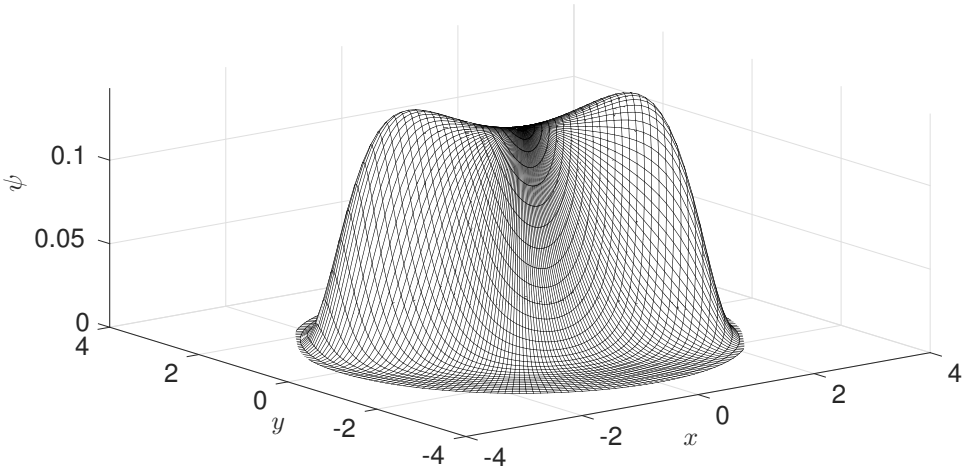

(a)

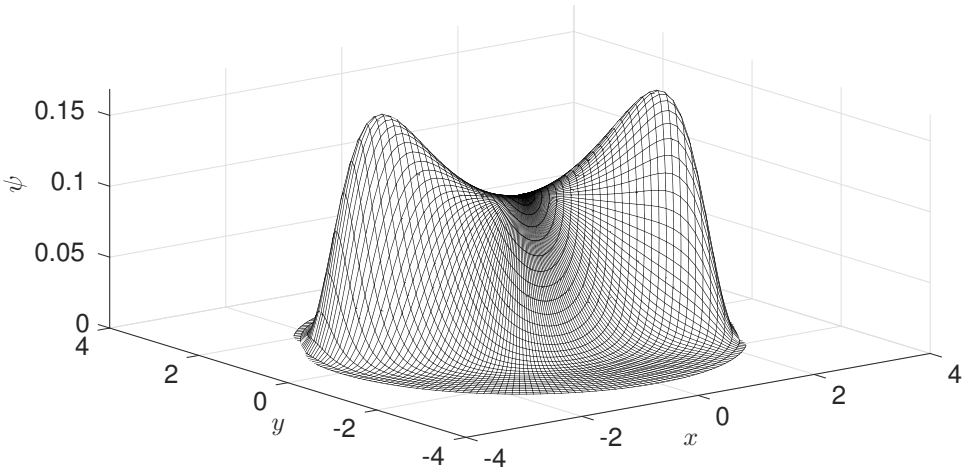

(b)

Fig. 5.7 The probability density function ψ for the full non-linear FENE solution for $\dot{\gamma} = 2$ for $f = 0$ (in (a)) and $f = 0.5$ (in (b)) with $b = 10$.

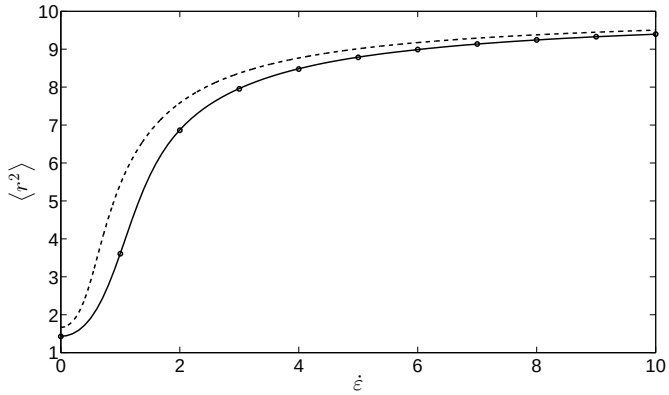

(a) $f = 0$

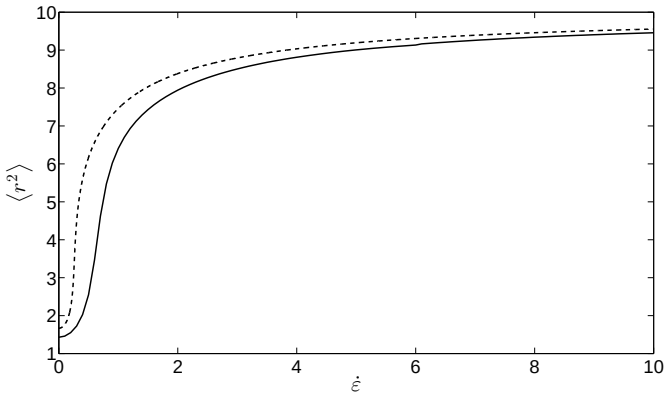

(b) $f = 0.5$

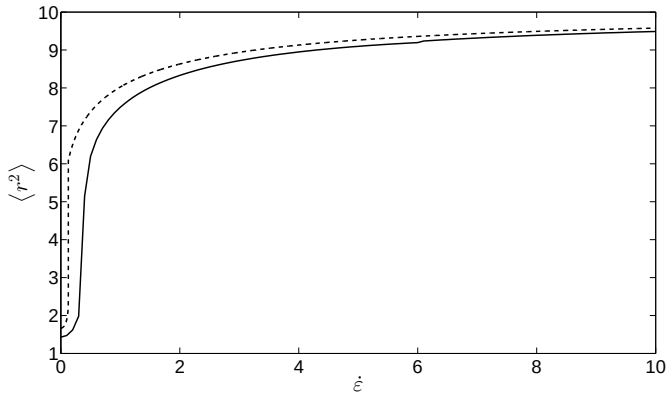

(c) $f = 0.75$

Fig. 5.8 Numerical solution for $\langle r^2 \rangle$ against non-dimensional elongation rate $\dot{\varepsilon}$ for the FENE-P (dashed lines) and FENE (solid lines) for varying f. Circular markers indicate exact analytic solution.

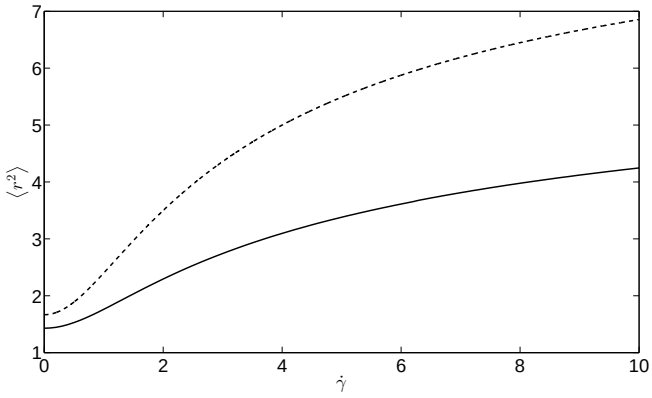

(a) $f = 0$

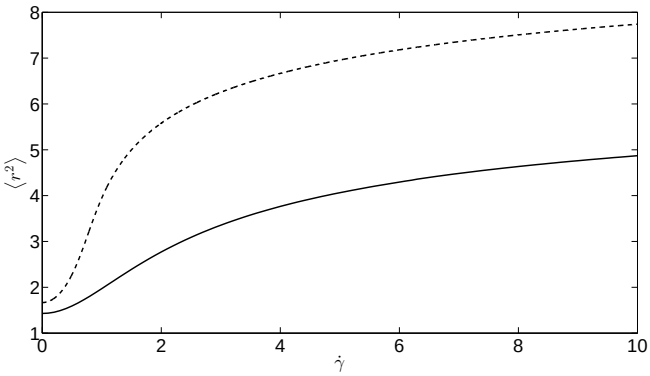

(b) $f = 0.5$

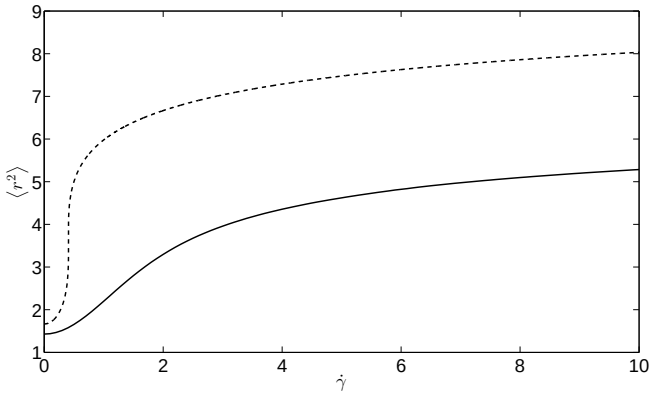

(c) $f = 0.75$

Fig. 5.9 Numerical solution for $\left\langle r^2 \right\rangle$ against non-dimensional shear rate $\dot{\gamma}$ for the FENE-P (dashed lines) and FENE (solid lines) for varying f.

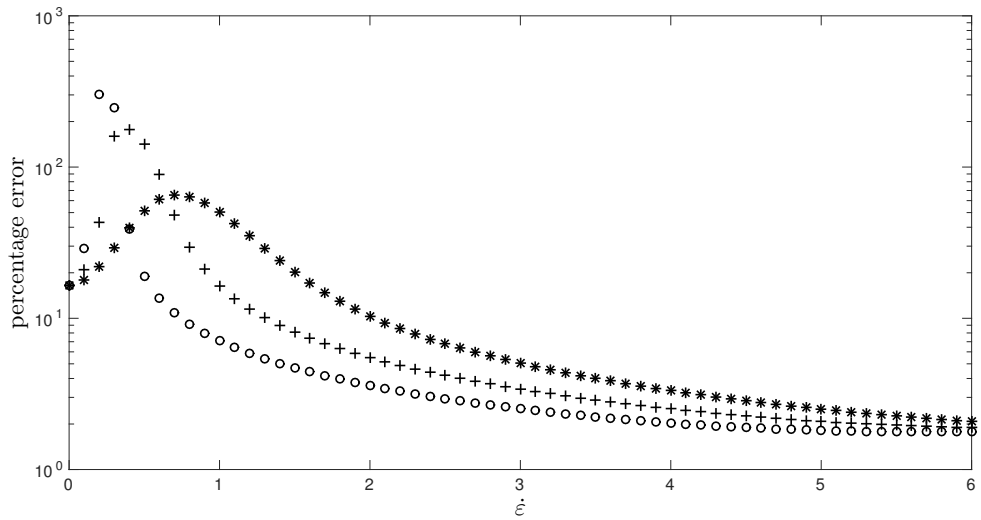

Fig. 5.10 The error between the FENE-P and FENE models against elongation rate. The results are shown for $f = 0, 0.5$ and 0.75 and are denoted by the starred, crossed and circular markers respectively.

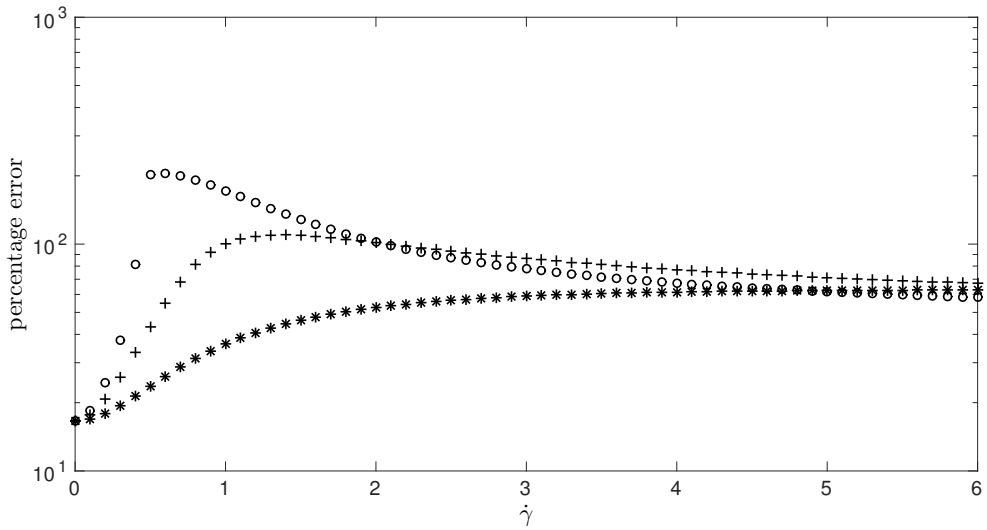

Fig. 5.11 The percentage error for the radius of gyration between the FENE-P and FENE models against shear rate. The results are shown for $f = 0, 0.5$ and 0.75 and are denoted by the starred, crossed and circular markers respectively.

5.5 Results and discussion

We find from Fig.5.8 that the Peterlin approximation for large elongation rates the behavior is very similar to FENE model, although the Peterlin approximation does systematically overestimate the radius of gyration.

To investigate the error induced from the FENE-P approximation we plot the error between the approximations against elongation rates in Fig 5.10. For the case $f = 0$ the over-estimation can be explained as the finite extension imposed on only the average extension. We also find that the greatest error occurs for moderately small elongation rates. We find that the magnitude of the error is increases and the peak error occurs at a lower elongation rate for increasing values of f. This error is due to large gradients of the radius of gyration, with respect to the elongation rate, as can be seen in Fig 5.8. These large gradients are due to the infinite extension. These gradients are eventually smoothed when the finite extensibility constraint starts to dominate. The positional change in the maximum error seems to be in accordance with finite extension occurring at a lower elongation for increasing f, as found from (5.24).

For shear flow with $f = 0$, the error increases monotonically with shear rate. However, with the introduction of the mean field term the peak error occurs at a finite shear rate. The effect of increasing f is the similar, but less pronounced, to the effect seen with elongational flows, where the magnitude of the error increases and occurs at a lower shear rate.

5.6 Conclusions

The principle result of the chapter was the derivation of solutions to the Fokker-Planck equation with the addition of a mean field term for both shear and elongation flows. We found that the results under elongation were amenable to analytical analysis. For a linear spring force the distribution can be found exactly and for near full extensional flows an exact solution was found to be expressed as the root of a quartic equation.

We further investigated the effect the closure assumption on the spring force has on the model. The PDF was found numerically using a finite element scheme. We found that the closure assumption in conjunction with the mean field term led to

dramatic over estimation of the extension of the dumbbell at moderate values of the elongation and shear rate.

For future work the theoretical predictions are reproducible experimentally. It would be of interest to investigate whether the model parameters, fitted to extensional flow date, are consistent with shear flow data. Unfortunately, extensional rheometry is experimentally more difficult than its shear counterpart. And as the mean field term is only valid for relatively dilute suspensions, this may limit the experiment to birefringence techniques used in cross-slot [38, 87, 94], four roll mill [107] or converging channel geometries [20, 84]. It should be noted that even for dilute solutions, filament stretching techniques were found to be stable by Godin et al. [42] thereby extensional techniques such as FiSER (filament stretching extension rheometer) [14] or CaBER (capillary break-up extensional rheometer) [7] may also prove to be viable alternatives.

Throughout this chapter we have only considered mean-field effects under steady shear and steady elongation conditions. This leaves the area of transient shear and elongation open to further study.

5.7 Appendix

5.7.1 Perturbation expansion for elongational flow

Here we outline how one can obtain the solution to the FP equation for mean field terms. The results can be obtained by calculating the equilibrium state of Hookean dumbbells with no mean field force, but assuming that the additional force behaves as a Hookean dumbbell with an anisotropic spring constant. We note that we do not propose this as a dumbbell model, but it provides a useful basis for solving the mean field model and possibly other additional forces which behave in a similar fashion. In this approach H is scaled by $1-\varepsilon_1$ and $1-\varepsilon_2$ in the x and y directions respectively where $\varepsilon_1, \varepsilon_2$ are general functions of macroscopic variables only. Using the scalings to give (5.16), such a system at equilibrium has FP equation given by

$$\frac{\partial}{\partial x}((1-\varepsilon_1)x\psi) + \frac{\partial}{\partial y}((1-\varepsilon_2)y\psi) + \nabla^2\psi = 0. \tag{5.53}$$

The solution for the Hookean case, i.e. isotropic spring constant ($\varepsilon_1 = \varepsilon_2 = 0$), is given by the Gaussian $\psi \propto e^{-\frac{1}{2}r^2}$, see e.g. Bird [16]. Using this distribution whilst considering the case $\varepsilon_1 = 0$ leads one to seek a solution in the form of a regular

perturbation series in ε_2 given by

$$\psi \sim e^{-\frac{1}{2}r^2}\left(1+\varepsilon_2\psi_1+\varepsilon_2^2\psi_2+\dots\right). \tag{5.54}$$

From substitution of (5.54) into (5.53) one can find a solution for the nth order $\psi_n = \frac{1}{2^n n!} r^{2n}\sin^{2n}(\theta)$, which is the series expansion of $e^{\frac{1}{2}r^2\sin^2(\theta)}$. Using the inherent symmetry of the system allows one to see that the exact solution is given by

$$\psi \propto e^{-\frac{1}{2}r^2\left(1-\varepsilon_1\cos^2(\theta)-\varepsilon_2\sin^2(\theta)\right)}. \tag{5.55}$$

5.7.2 Exact outer solution

Here we give the correct root the cubic polynomial given in equation (5.30) using the technique outlined in [3]. In the case as $f = 0$ the problem simplifies dramatically due to it becoming a cubic. Due to its lengthiness, the solution is expressed as a series of substitutions for compactness. Let

$$\begin{gathered}
A_2 = b^{-1}\left(4b+8b\dot{\varepsilon}+4+4b\dot{\varepsilon}^2+4\dot{\varepsilon}+fb+3fb\dot{\varepsilon}+3f\right),\\
A_1 = -(2b^2)^{-1}(2b^2+8b^2\dot{\varepsilon}+2fb^2+4b+2),\\
A_0 = -(4b)^{-2}\left(16b+32b\dot{\varepsilon}+24fb+16b\dot{\varepsilon}^2+8fb\dot{\varepsilon}+bf^2+8fb\dot{\varepsilon}^2+16f\dot{\varepsilon}\right),\\
q = \frac{3A_1-A_2^2}{9}, \quad r = \frac{1}{6}(A_1A_2-3A_0)-\frac{1}{27}A_2^3,\\
s_\pm = \left(r\pm\left(q^3+r^2\right)^{\frac{1}{2}}\right)^{\frac{1}{3}}, \quad U = -\frac{1}{2}(s_++s_-)+\frac{A_2}{3}+\frac{i\sqrt{3}}{2}(s_+-s_-).
\end{gathered} \tag{5.56}$$

The solution is then given by

$$\varepsilon_r = -\left(\frac{a_3}{4}+\frac{1}{2}\left(\frac{a_3^2}{4}+U-a_2\right)^{\frac{1}{2}}\right)-\frac{1}{2}\sqrt{\frac{a_3}{2}+\left(\frac{a_3^2}{4}+U-a_2\right)^{\frac{1}{2}}-2U-4\left(\frac{U^2}{4}-a_0\right)^{\frac{1}{2}}}, \tag{5.57}$$

where a_i is the component in front of ε_r^i in the polynomial (5.30) scaled by $2b^2$. However for ease of calculation the Pad/'e solution (5.32) is more usable.

Chapter 6

Conclusions

To the author's knowledge, we have produced a first analytical attempt to describe the cross-slot device. As such we found analytical expressions for the stress and velocity fields throughout the cross-slot. These expressions can be written succinctly at the stagnation point, where, given a flow-rate and channel height, the stresses and elongation rates simplify dramatically. It should also be noted that small channel heights can prove difficult numerically when modelling due to the large gradients and the necessary mesh size needed to resolve them. Having an analytical result results in a much simpler exercise to calculate stresses. Such results maybe of use as a rough estimate in experimental design in cross-slot devices. The method could similarly be applied to other geometries. A natural extension of the work would be to study the stability of the potential second order fluid result. Stability of a cross-slot has been greatly studied and there are currently two proposed mechanisms [146] for asymmetric bifurcation. It would be interesting to see whether or not the potential theory could predict the asymmetric instability or the transient instability in [127].

It must be noted that the analytical study necessitated two approximations small channel height and small W_e. The small channel height can be physically realised and is often easier to impose on a geometry than large channel heights needed for conventional two dimensional flows. The small channel assumption also neglects a small region, near the solid boundary walls, with extremely high shear. The second assumption small W_e number is an imposing factor, and limits the range of applicability to relativity slow flows.

We then proceed with lubricating flows, however we apply the result to a different, transient, system. The work is based on extending that done by Balmforth et al. [9], who studied a snail ball with a Newtonian lubricant and found two permissible solutions, the rocking and runaway solutions. We attempt to answer the question: "what happens to a snail ball with a non-Newtonian lubricating fluid?". The initial part of the study focussed on the same model used in chapter 2; the second order fluid model. We found that the runaway solution still exists and that the sufficient condition needed for the runaway solution is unchanged. Physically, this is consistent with the argument put-forth by Wagon [141]. The rocking solution, however, is no longer achievable. This is because there is now a tensional force which grows significantly large with decreasing gap distance. This leads to the formation of a new constant rolling solution.

The second order fluid analysis suggests that the constant rolling solution occurs for any non-zero elasticity, which we suspect to be erroneous. However, the general

behavior of an elastic fluid suspending the inner ball due to Hoop stresses maybe realizable. Certainly a more complex model will be needed to investigate this problem further. It should also be noted that if the steady rolling solution is producible experimentally, it may be difficult to distinguish this effect from the steady rolling behavior due to surface roughness.

The second order fluid only captures one non-Newtonian effect: viscoelasticity with constant normal stress coefficients. This does not incorporate viscous shear dependency. This effect was introduced to the problem by using the power-law model to represent the lubricating fluid. Consistently with the SOF and Newtonian models, the condition for the runaway solution remains unchanged. However, unlike the SOF the rocking solution still exists.

In the rocking system, the key influence of introducing shear-thinning is that it reduces the forces acting on the inner ball. This effect is thought to be due of the decrease in viscosity which results from the shear induced by the rocking motion. Using the DE approximation, we found that a shear-thinning snail ball will travel slower than its Newtonian counterpart. For shear thickening fluids the opposite effect can be found, i.e. the forces on the inner ball increase and the ball will travel quicker than the Newtonian case.

We continue with the analysis of generalized Newtonian fluids where we consider the effects in Taylor's paint scraping problem using a Carreau fluid. When a Carreau fluid is used, we find that the complexity of the problem increases dramatically as the system is no longer self similar, unlike the Newtonian and power-law cases.

To analyze the system, we consider two different regions: far from the corner where Newtonian effects are strong; and near to the corner where shear dependent behaviour is dominant. The far field problem could be solved analytically using a regular perturbation expansion for the stream function. As the perturbation series suffered from extremely poor convergence, we performed a Shanks' transform to improve the range of convergence. The results were then corroborated by a finite element model.

In the near corner approximation the regular perturbation expansion was found to be no-longer valid throughout the domain. This is because there is a region in the geometry where the shear-rate drops to zero. The problem is addressed using

matched asymptotics and we found that two effects were presented: the transition to Newtonian due to drop in shear rate which behaves like Γ^{-n}; a positional shift in the point of zero shear from the power-law position which behaves like Γ^{-2}.

The near corner behavior cannot be easily modelled numerically and as such we believe that the perturbation series opens up the problem to analysis. One numerical problem is the shear-stress becomes singular as the corner is approached. There is a more fundamental problem as to what is happening in the far field. There is no apparent boundary condition to impose on the flow in the far field. This, however, leads to the question of which effect will be dominate in the near corner, the Carreau correction or the effects of the far-field boundary condition.

In the final chapter of this thesis, we conclude with an investigation of the mean-field term proposed by Kroger et al. [76, 121]. The solution was solved by using a Fokker Planck formulator and the predictions for shear-flow are consistent with Kroger's original approach. The results were then extended to elongational flows and the mean field term results in increased extension of the dumbbells. If the model is to be used in numerical studies with elongational flows, the need for finite extensibility becomes more severe, as the singular extensional viscosity occurs at a much lower elongation rate than without the mean-field term.

The need for finite extension requires using a closure assumption, whereby we employ the widely used Peterlin assumption [101]. It was found that the Peterlin assumption, with the mean field term, can lead to a dramatic over-estimation (on the order of 100%) of the extension of the dumbbells for both elongation and shear rates at low to moderate values.

It should be noted that the proposed mean-field term is only a simple model to introduce concentration effects. Prior investigations, such as [75] have found that certain models do not produce consistent results across both shear and elongational flows. It would be of interest to see how well the mean-field model performs extension and investigate whether this is consistent with the results obtained from shear flow.

References

[1] Lecture 1 introduction: E.J. Hinch. http://www.damtp.cam.ac.uk/user/hinch/teaching/whoi/lecture01.ps.

[2] A. Abedijaberi, J. Soulages, M. Kröger, and B. Khomami. Flow of branched polymer melts in a lubricated cross-slot channel: a combined computational and experimental study. *Rheol. Acta*, 48(1):97–108, 2009.

[3] M. Abramowitz and I.A. Stegun. *Handbook of Mathematical Functions*. Dover, New York, fifth edition, 1964.

[4] S.A. Adelman and K.F. Freed. Microscopic theory of polymer internal viscosity: Mode coupling approximation for the rouse model. *The Journal of Chemical Physics*, 67(4), 1977.

[5] G. Allegra. Internal viscosity in polymer chains: A critical analysis. *The Journal of Chemical Physics*, 84(10), 1986.

[6] C. Ancey. Plasticity and geophysical flows: A review. *Journal of non-Newtonian fluid mechanics*, 142(1-3):4–35, MAR 16 2007. Workshop on Viscoplastic Fluids, Banff, CANADA, OCT 22-27, 2005.

[7] S.L. Anna and G.H. McKinley. Elasto-capillary thinning and breakup of model elastic liquids. *Journal of Rheology*, 45(1), 2001.

[8] J.H. Aubert and M. Tirrell. Macromolecules in nonhomogeneous velocity gradient fields. *The Journal of Chemical Physics*, 72(4), 1980.

[9] N. J. Balmforth, J. W. M. Bush, D. Vener, and W. R. Young. Dissipative descent: rocking and rolling down an incline. *Journal of Fluid Mechanics*, 590:295–318, 11 2007.

[10] G.K. Batchelor. *An Introduction to Fluid Mechanics*. Cambridge University Press, 1967.

[11] M. Behr, D. Arora, M. Coronado, and M. Pasquali. Stablilized finite element modelling of Oldroyd-B viscoelastic flow. *Proc of the Third M.I.T. Conference on Computational Fluid and Solid Mechanics, Massachusetts Institute of Technology, Cambridge, USA*, pages 135–308, 2005.

[12] M. Behr, D. Arora, and M. Pasquali. *Stabilized finite element methods of GLS type for Oldroyd-B viscoelastic fluid*. ECCOMAS, 2004.

[13] C.M. Bender and S.A. Orszag. *Advanced Mathematical Methods for Scientists and Engineers I: Asymptotic Methods and Perturbation Theory*. Advanced Mathematical Methods for Scientists and Engineers. Springer, 1999.

[14] A. Bhardwaj, E. Miller, and J.P. Rothstein. Filament stretching and capillary breakup extensional rheometry measurements of viscoelastic wormlike micelle solutions. *Journal of Rheology*, 51(4), 2007.

[15] R. Byron Bird, Charles F. Curtiss, Robert C. Armstrong, and Ole Hassager. *Dynamics of Polymeric Liquids, Fluid Mechanics (Dynamics of Polymer Liquids Vol. 1)* . Wiley-Interscience, volume 1 edition, June 1987.

[16] R.B. Bird, C.F. Curtiss, R.C. Armstrong, and O. Hassager. *Dynamics of Polymeric Liquids, Kinetic Theory (Dynamics of Polymer Liquids Vol. 2)* . Wiley-Interscience, volume 2 edition, June 1987.

[17] R.B. Bird and J.R. Deaguiar. An encapsulated dumbbell model for concentrated polymer solutions and melts.1. theoretical development and constitutive equation . *Journal of non-Newtonian fluid mechanics*, 13(2):149–160, 1983.

[18] P.W. Bridgman. Theoretically interesting aspects of high pressure phenomena. *Reviews of modern physics*, 7(1):0001–0033, JAN 1935.

[19] G. Brindley, J.M. Davies, and K. Walters. Elastico-viscous squeeze films. part i. *Journal of Non-Newtonian Fluid Mechanics*, 1(1):19 – 37, 1976.

[20] G. Chauveteau, M. Moan, and A. Magueur. Thickening behaviour of dilute polymer solutions in non-inertial elongational flows. *Journal of Non-Newtonian Fluid Mechanics*, 16(3):315 – 327, 1984.

[21] W.M. Christopher. *Rheology principles, measurements and applications*. VCH publishers inc, 1994.

[22] A. Cohen. A padé approximant to the inverse langevin function. *Rheologica Acta*, 30(3):270–273, 1991.

[23] K. D. Coventry and M. R. Mackley. Cross-slot extensional flow birefringence observations of polymer melts using a multi-pass rheometer. *J. Rheol.*, 52(2):401–415, 2008.

[24] T .J. Craven, J .M. Rees, and W .B .J. Zimmerman. Stablilized finite element modelling of Oldroyd-B viscoelastic flow. *COMSOL User Converference 2006 Birmingham*, 2006.

[25] P. K. Currie. The first normal-stress difference in shear of nematic liquid crystals. *Molecular Crystals and Liquid Crystals*, 73(1-2):1–6, 1981.

[26] O. Darrigol. *Worlds of Flow*. Oxford University Press, 2005.

[27] M.J. Davies and K. Walters. The behaviour of non-newtonian lubricants in journal bearings- a theoretical study. *The Rheology of Lubricants*, pages 65–80, 1979.

[28] P. G. de Gennes. Reptation of a polymer chain in the presence of fixed obstacles. *The Journal of Chemical Physics*, 55(2), 1971.

[29] P.G. de Gennes. *Scaling Concepts in Polymer Physics*. Cornell University Press, 1979.

[30] J.R. Deaguiar. An encapsulated dumbbell model for concentrated polymer-solution and melts .2. calculation of material functions and experimental comparisons. *Journal of non-Newtonian fluid mechanics*, 13(2):161–179, 1983.

[31] W. R. Dean and P. E. Montagnon. On the steady motion of viscous liquid in a corner. *Mathematical Proceedings of the Cambridge Philosophical Society*, 45:389–394, 7 1949.

[32] R. DelgadoBuscalioni. Dynamics of a single tethered polymer under shear flow. *AIP Conference Proceedings*, 913(1), 2007.

[33] I. K. Dien and H. G. Elrod. A generalized steady-state reynolds equation for non-newtonian fluids, with application to journal bearings. *J. of Lubrication Tech*, 105(3):385–390, 1982.

[34] M. Doi and S.F. Edwards. *The Theory of Polymer Dynamics*. Oxford University Press, 1990.

[35] S. Drost and J. Westerweel. Hele-shaw rheometry. *J. Rheol.*, 57(6), 2013.

[36] J. D. Evans. Re-entrant corner flows of the upper convected maxwell fluid. *Proc.: Math., Phys. Eng. Sci*, 461(2053):pp. 117–142, 2005.

[37] J. Farago, H. Meyer, J. Baschnagel, and A. N. Semenov. Hydrodynamic and viscoelastic effects in polymer diffusion. *Journal of physics condensed matter*, 24(28), JUL 18 2012.

[38] R.S. Farinato. Elongational flow birefringence of poly(styrene sulphonate). *Polymer*, 29(1):160 – 167, 1988.

[39] P. Fast, L. Kondic, M.J. Shelley, and P. Palffy-Muhoray. Pattern formation in non-Newtonian Hele-Shaw flow. *Physics of fluids*, 13(5):1191–1212, MAY 2001.

[40] R.L. Fosdick and K.R. Rajagopal. Anomalous features in the model of "second order fluids". *Archive for Rational Mechanics and Analysis*, 70(2):145–152, 1979.

[41] H. Giesekus. Die elastizität von flüssgkeiten. *Rheol Acta*, 5:29 – 35, 1966.

[42] M. Goldin, J. Yerushal, R. Pfeffer, and R. Shinnar. Breakup of a laminar capillary jet of a viscoelastic fluid. *Journal of fluid mechanics*, 38(4):689–711, 1969.

[43] A.J. Goldman, R.G. Cox, and H. Brenner. Slow viscous motion of a sphere parallel to a plane wall—i motion through a quiescent fluid. *Chemical Engineering Science*, 22(4):637 – 651, 1967.

[44] R.W. Griffiths. The dynamics of lava flows. *Annual review of fluid mechanics*, 32:477–518, 2000.

[45] D.R. Gwynllyw and T.N. Phillips. The influence of oldroyd-b and {PTT} lubricants on moving journal bearing systems. *Journal of Non-Newtonian Fluid Mechanics*, 150(2–3):196 – 210, 2008.

[46] C. Haber, S.A. Ruiz, and D. Wirtz. Shape anisotropy of a single random-walk polymer. *Proceedings of the National Academy of Sciences of the United States of America*, 97(20):pp. 10792–10795, 2000.

[47] C. Hancock, E. Lewis, and H. K. Moffatt. Effects of inertia in forced corner flows. *Journal of Fluid Mechanics*, 112:315–327, 11 1981.

[48] O. Hassager, R.C. Armstrong, and R.B. Bird. Limitation on the use of the retarded motion expansion. *Journal of Non-Newtonian Fluid Mechanics*, 34(2):241 – 245, 1990.

[49] O. Hassager and T.L. Lauridsen. Singular behavior of power-law fluids in hele shaw flow. *Journal of Non-Newtonian Fluid Mechanics*, 29:337 – 346, 1988.

[50] D.G. Hassell, D. Auhl, T.C.B. McLeish, and M.R. Mackley. The effect of viscoelasticity on stress fields within polyethylene melt flow for a cross-slot and contraction-expansion slit geometry. *Rheol. Acta*, 47(7):821–834, September 2008.

[51] S.J. Haward, M. Oliveira, M.A. Alves, and G.H. McKinley. Optimized cross-slot flow geometry for microfluidic extensional rheometry. *Phys. Rev. Lett.*, 109:128301, Sep 2012.

[52] P. Henriksen and O. Hassager. Corner flow of power law fluids. *Journal of Rheology (1978-present)*, 33(6), 1989.

[53] S. Hess. Rheological properties via nonequilibrium molecular dynamics: From simple towards polymeric liquids. *Journal of Non-Newtonian Fluid Mechanics*, 23:305 – 319, 1987.

[54] W. Heß. Molecular theory for moderately concentrated polymer solutions in shear flow. *Rheologica Acta*, 23(5):477–488, 1984.

[55] I.J. Hewitt and N.J. Balmforth. Viscoplastic lubrication theory with application to bearings and the washboard instability of a planing plate. *Journal of Non-Newtonian Fluid Mechanics*, 169–170:74 – 90, 2012.

[56] C.P. Hills and H. K. Moffat. Rotary honing: a variant of the taylor paint-scraper problem. *Journal of Fluid Mechanics*, 418:119–135, 9 2000.

[57] E.J. Hinch. *Perturbation Methods*. Cambridge University Press, 1991. Cambridge Books Online.

[58] E.J. Hinch and L.G. Leal. Constitutive equations in suspension mechanics 1. general formulation. *Jounral of fluid mechanics*, 71(OCT14):481–495, 1975.

[59] P. Huang, Z.H. Li, Y.G. Meng, and S.Z. Wen. Study on thin film lubrication with second-order fluid. *Journal of trilogy-transactions of the ASME*, 124(3):547–552, JUL 2002.

[60] Y.N. Huang, R.K. Bhatnagar, and K.R. Rajagopal. Flow of a non-newtonian fluid between intersecting planes of which one is moving. *Rheologica Acta*, 32(5):490–498, 1993.

[61] T.J.R. Hughes, L.P. Franca, and G.M. Hulbert. A new finite element formulation for computational fluid dynamics: Viii. The Galerkin/least-squares method for advective-diffusive equations. *Comput. Methods Appl. Mech. Eng.*, 73(2):173 – 189, 1989.

[62] J.S. Hur, E.S.G. Shaqfeh, and R.G. Larson. Brownian dynamics simulations of single dna molecules in shear flow. *Journal of Rheology*, 44(4), 2000.

[63] S. S Hwang. Non-newtonian liquid blade coating process. *J. Fluids Eng*, 104:469 – 474, 1982.

[64] H. Itô and S. Sasajima. A ten year creep experiment on small rock specimens. *International Journal of Rock Mechanics and Mining Sciences & Geomechanics Abstracts*, 24(2):113 – 121, 1987.

[65] D.F. James. Boger fluids. *Annu. Rev. Fluid Mech.*, 41(1):129–142, 2009.

[66] M . W. Johnson and S. Mangkoesoebroto. Analysis of lubrication theory for the power law fluid. *Journal of Tribology*, 115, 1993.

[67] D.D. Joseph. Bernoulli equation and the competition of elastic and inertial pressures in the potential flow of a second-order fluid. *J. Non-Newtonian Fluid Mech.*, 42(3):385 – 389, 1992.

[68] D.D Joseph, T. Funada, and J. Wang. *Potential Flows of Viscous and Viscoelastic Fluids*. Cambridge University Press, 2007.

[69] A. Kaye. A bouncing liquid stream. *Nature*, 197(487):1001–&, 1963.

[70] R.A. Keiller. Modelling of the extensional flow of the m1 fluid with the oldroyd equation. *Journal of Non-Newtonian Fluid Mechanics*, 42(1):49 – 64, 1992.

[71] R.A. Keiller and E.J. Hinch. Corner flow of a suspension of rigid rods. *Journal of Non-Newtonian Fluid Mechanics*, 40(3):323 – 335, 1991.

[72] R. Keunings. On the high Weissenberg number problem. *J. Non-Newtonian Fluid Mech.*, 20(0):209 – 226, 1986.

[73] R. Keunings. On the peterlin approximation for finitely extensible dumbbells. *Journal of Non-Newtonian Fluid Mechanics*, 68(1):85 – 100, 1997.

[74] R. Keunings. On the peterlin approximation for finitely extensible dumbbells. *Journal of Non-Newtonian Fluid Mechanics*, 68(1):85 – 100, 1997.

[75] S. A. Khan and R. G. Larson. Comparison of simple constitutive equations for polymer melts in shear and biaxial and uniaxial extensions. *Journal of Rheology*, 31(3), 1987.

[76] M. Kroger. *Models for Polymeric and Anisotropic Liquids*. Springer, 2005.

[77] W. Kuhn. Concerning the shape of thread shapes molecules in solution. *Kolloid-Zeitschrift*, 68(1):2–15, Jul 1934.

[78] N. Kuzuu and M. Doi. Constitutive equation for nematic liquid crystals under weak velocity-gradient derived from a molecular kinetic equation . *Journal of the physical society of Japan*, 52(10):3486–3494, 1983.

[79] R.G. Larson. *Constitutive Models with Nonaffine Motion*. Butterworths Series in Chemical Engineering. Butterworth-Heinemann, 1988.

[80] G. Lian, Y. Xu, W. Huang, and M.J. Adams. On the squeeze flow of a power-law fluid between rigid spheres. *Journal of Non-Newtonian Fluid Mechanics*, 100(1–3):151 – 164, 2001.

[81] G. Lielens, P. Halin, I. Jaumain, R. Keunings, and V. Legat. New closure approximations for the kinetic theory of finitely extensible dumbbells1. *Journal of Non-Newtonian Fluid Mechanics*, 76(1–3):249 – 279, 1998.

[82] G. Lielens, R. Keunings, and V. Legat. The fene-l and fene-ls closure approximations to the kinetic theory of finitely extensible dumbbells. *Journal of Non-Newtonian Fluid Mechanics*, 87(2–3):179 – 196, 1999.

[83] H.B. Ma and M.D. Graham. Theory of shear-induced migration in dilute polymer solutions near solid boundaries. *Physics of fluids*, 17(8), AUG 2005.

[84] M. R. Mackley and A. Keller. Flow induced polymer chain extension and its relation to fibrous crystallization. *Philosophical Transactions of the Royal Society of London A: Mathematical, Physical and Engineering Sciences*, 278(1276):29–66, 1975.

[85] A.B. Metzner. Behavior of suspended matter in rapidly accelerating viscoelastic fluids- Uebler effect. *Aiche Journal*, 13(2):316–&, 1967.

[86] M.H. and H.C. Öttinger. A detailed comparison of various fene dumbbell models. *Journal of Non-Newtonian Fluid Mechanics*, 68(1):17 – 42, 1997.

[87] M.J. Miles and A. Keller. Conformational relaxation time in polymer solutions by elongational flow experiments: 2. preliminaries of further developments: chain retraction; identification of molecular weight fractions in a mixture. *Polymer*, 21(11):1295 – 1298, 1980.

[88] L.M. Milne-Thomson. *Theoretical Hydrodynamics*. Academia, 1962.

[89] H. K. Moffatt. Viscous and resistive eddies near a sharp corner. *Journal of Fluid Mechanics*, 18:1–18, 1 1964.

[90] H. K. Moffatt. Viscous and resistive eddies near a sharp corner. *Journal of Fluid Mechanics*, 18:1–18, 1964.

[91] M.N.J. Moore and M.J. Shelley. A weak-coupling expansion for viscoelastic fluids applied to dynamic settling of a body. *Journal of Non-Newtonian Fluid Mechanics*, 183–184(0):25 – 36, 2012.

[92] Q.D. Nguyen and D.V. Boger. Measuring the flow properties of yield stress fluids. *Annual review of fluid mechanics*, 24:47–88, 1992.

[93] W. Noll. On the continuity of the solid and liquid fluid states. *Journal of rational mechanics and analysis*, 4(1):3–81, 1955.

[94] J.A. Odell, A. Keller, and M.J. Miles. Assessment of molecular connectedness in semi-dilute polymer solutions by elongational flow. *Polymer*, 26(8):1219 – 1226, 1985.

[95] J. G. Oldroyd. On the Formulation of Rheological Equations of State. *Royal Society of London Proceedings Series A*, 200:523–541, February 1950.

[96] P. J. Oliveira. An exact solution for tube and slit flow of a FENE-P fluid. *Acta Mech.*, 158(3-4):157–167, 2002.

[97] P.J. Oliveira and F.T. Pinho. A qualitative assessment of the role of a viscosity depending on the third invariant of the rate-of-deformation tensor upon turbulent non-newtonian flow. *Journal of Non-Newtonian Fluid Mechanics*, 78(1):1 – 25, 1998.

[98] H.C. Öttinger. A model of dilute polymer solutions with hydrodynamic interaction and finite extensibility. i. basic equations and series expansions. *Journal of Non-Newtonian Fluid Mechanics*, 26(2):207 – 246, 1987.

[99] H.C. Öttinger. *Stochastic preocesses in polymetric fluids*. Springer -Verlag, 1996.

[100] T.T. Perkins, D.E. Smith, and S. Chu. Single polymer dynamics in an elongational flow. *SCIENCE*, 276(5321):2016–2021, JUN 27 1997.

[101] A. Peterlin. Hydrodynamics of macro-molecules in a velocity field with longitudinal gradient . *Journal of polymer science part B-polymer letters*, 4(4PB):287–&, 1966.

[102] G.W.M. Peters, J.F.M. Schoonen, F.P.T. Baaijens, and H.E.H. Meijer. On the performance of enhanced constitutive models for polymer melts in a cross-slot flow. *J. Non-Newtonian Fluid Mech.*, 82:387–427, 1999.

[103] C.J.S. Petrie. Extensional viscosity: A critical discussion. *Journal of non-Newtonian fluid mechanics*, 137(1-3):15–23, AUG 30 2006.

[104] S.B. Pillapakkam, P. Singh, D. Blackmore, and N. Aubry. Transient and steady state of a rising bubble in a viscoelastic fluid. *Journal of fluid mechanics*, 589:215–252, OCT 25 2007.

[105] O. Pinkus and B. Sternlicht. *Theory of hydrodynamic lubrication*. McGraw-Hill, 1961.

[106] R.J. Poole, G.N. Rocha, and P.J. Oliveira. A symmetry-breaking inertial bifurcation in a cross-slot flow. *Comput. Fluids*, 93(0):91 – 99, 2014.

[107] D.P. Pope and A. Keller. Alignment of macromolecules in solution by elongational flow; a study of the effect of pure shear in a four roll mill. *Colloid and Polymer Science*, 255(7):633–643, 1977.

[108] I. Proudman and M. Asadullah. Steady viscous flow near a stationary contact line. *Journal of Fluid Mechanics*, 187:35–43, 2 1988.

[109] K.R. Rajagopal and R.K. Bhatnagar. Exact solutions for some simple flows of an oldroyd-b fluid. *Acta Mech.*, 113(1-4):233–239, 1995.

[110] J .M. Rallison and E .J. Hinch. The flow of an Oldroyd fluid past a reentrant corner: the downstream boundary layer. *J. Non-Newtonian Fluid Mech.*, 116(2–3):141 – 162, 2004.

[111] J.M. Rallison and E.J. Hinch. Do we understand the physics in the constitutive equation? *J. Non-Newtonian Fluid Mech.*, 29(0):37 – 55, 1988.

[112] M. Renardy. A matched solution for corner flow of the upper convected Maxwell fluid. *J. Non-Newtonian Fluid Mech.*, 58(1):83 – 89, 1995.

[113] Y.Y. Renardy. Spurt and instability in a two-layer johnson-segalman liquid. *Theoretical and Computational Fluid Dynamics*, 7(6):463–475, 1995.

[114] J. Riedler and W. Schneider. Viscous flow in corner regions with a moving wall and leakage of fluid. *Acta Mechanica*, 48(1-2):95–102, 1983.

[115] G.W. Roberts and K. Walters. On viscoelastic effects in journal-bearing lubrication. *Rheologica Acta*, 31(1):55–62, 1992.

[116] G .N. Rocha, R. J. Poole, M. A. Alves, and P J. Oliveira. On extensibility effects in the cross-slot flow bifurcation. *J. Non-Newtonian Fluid Mech.*, 156(1–2):58 – 69, 2009.

[117] G.J. Rodin. Squeeze film between two spheres in a power-law fluid. *Journal of Non-Newtonian Fluid Mechanics*, 63(2–3):141 – 152, 1996.

[118] A. B. Ross, S. K. Wilson, and B. R. Duffy. Blade coating of a power-law fluid. *Physics of Fluids*, 11(5):958–970, 1999.

[119] Z.S. Safar. Dynamically loaded bearings operating with non-newtonian lubricant films. *Wear*, 55(2):295 – 304, 1979.

[120] W.G. Sawyer and J.A. Tichy. Non-Newtonian lubrication with the second-order fluid. *Journal of tribology-transactions of the ASME*, 120(3):622–628, JUL 1998.

[121] C. Schneggenburger, M. Kröger, and S. Hess. An extended {FENE} dumbbell theory for concentration dependent shear-induced anisotropy in dilute polymer solutions. *J. Non-Newtonian Fluid Mech.*, 62(2–3):235 – 251, 1996.

[122] J.B. Shukla, K.R. Prasad, and P. Chandra. Effects of consistency variation of power law lubricants in squeeze films. *Wear*, 76(3):299 – 319, 1982.

[123] A. M. Siddiqui, A. R. Ansari, A. Ahmad, and N. Ahmad (late). On taylor's scraping problem and flow of a sisko fluid. *Mathematical Modelling and Analysis*, 14(4):515–529, 2009.

[124] C. Singh and P. Sinha. Non-newtonian squeeze films in journal bearings. *Wear*, 70(3):311 – 319, 1981.

[125] P. Singh and L.G Leal. Finite element simulation of flow around a $\frac{3\pi}{2}$ corner using the {FENE} dumbbell model. *J. Non-Newtonian Fluid Mech.*, 58(2–3):279 – 313, 1995.

[126] J. Soulages, T. Schweizer, D.C. Venerus, J. Hostettler, F. Mettler, M. Kröger, and H.C. Öttinger. Lubricated optical rheometer for the study of two-dimensional complex flows of polymer melts. *J. Non-Newtonian Fluid Mech.*, 150(1):43 – 55, 2008.

[127] P. C. Sousa, F. T. Pinho, M. S. N. Oliveira, and M. A. Alves. Purely elastic flow instabilities in microscale cross-slot devices. *Soft Matter*, 11:8856–8862, 2015.

[128] P. Szabo, J.M. Rallison, and E.J. Hinch. Start-up of flow of a FENE-fluid through a 4:1:4 constriction in a tube. *Journal of non-Newtonian fluid mechanics*, 72(1):73–86, SEP 1997.

[129] Z. Tadmor and R.B. Bird. Rheological analysis of stabilizing forces in wire-coating dies. *Polymer engineering and science*, 14(2):124–136, 1974.

[130] S. Taneda. Visualization of separating stokes flows. *Journal of the Physical Society of Japan*, 46(6):1935–1942, 1979.

[131] R.I. Tanner. Plane creeping flows of incompressible secondorder fluids. *Physics of Fluids*, 9(6):1246–1247, 1966.

[132] R.I. Tanner and K. Walters. *Rheology: An Historical Perspective*. Elsevier Science, 1998.

[133] G.I. Taylor. On scraping viscous fluid from a plane surface. *Miszellaneen der Angewandten Mechanik, year = 1952, pages = 313-315,*.

[134] B. Thomases and M. Shelley. Emergence of singular structures in Oldroyd-B fluids. *Phys Fluids*, 19(10), 2007.

[135] L.N. Trefethen and J. A.C. Weideman. The exponentially convergent trapezoidal rule. *SIAM Review*, 56(3):385–458, 2014.

[136] C. Trussel and K. Walters. *The Non-Linear Field Theories of Mechanics*. Springer-Verlag, 1965.

[137] P.T. Underhill and P.S. Doyle. Accuracy of bead-spring chains in strong flows. *Journal of Non-Newtonian Fluid Mechanics*, 145(2–3):109 – 123, 2007.

[138] A .P .G. van Heel, M .A. Hulsen, and B .H .A .A. van den Brule. On the selection of parameters in the FENE-P model. *J. Non-Newtonian Fluid Mech.*, 75(2–3):253 – 271, 1998.

[139] D.P. Vener. *Rocking and rolling down an incline : the dynamics of nested cylinders on a ramp*. PhD Thesis M.I.T, 2006.

[140] M. Versluis, C. Blom, D. van der Meer, K. van der Weele, and D. Lohse. Leaping shampoo and the stable kaye effect. *Journal of Statistical Mechanics: Theory and Experiment*, 2006(07):P07007, 2006.

[141] S. Wagon. The geometry of the snail ball. *Mathematics Magazine*, 83(4):276–279, 2010-10-01T00:00:00.

[142] K. Walters. *An Introduction to Rheology*. Elsevier Science, 1989.

[143] H.R. Warner. Kinetic-theory and rheology of dilute suspension of finite extendable dumbbells . *Industrial & engineering chemistry fundamentals* , 11(3):379–&, 1972.

[144] H.R. Warner. Kinetic theory and rheology of dilute suspensions of finitely extendible dumbbells. *Industrial and Engineering Chemistry Fundamentals*, 11(3):379–387, 1972.

[145] R.W. Whorlow. *Rheological techiniques*. Ellis Horwood, 1992.

[146] H.J. Wilson. Open mathematical problems regarding non-Newtonian fluids. *NONLINEARITY*, 25(3):R45–R51, MAR 2012.